Dissertation zur Erlangung des Doktorgrades der
Fakultät für Chemie und Pharmazie der
Ludwig-Maximilians-Universität München

Excited State Dynamics in Novel Energy Conversion Materials

Alexander Biewald

aus

Gräfelfing, Deutschland

2024

Erklärung

Diese Dissertation wurde im Sinne von §7 der Promotionsordnung vom 28. November 2011 von Herrn Prof. Achim Hartschuh betreut.

Eidesstattliche Versicherung

Diese Dissertation wurde eigenständig und ohne unerlaubte Hilfe erarbeitet.

München, 22. November 2024 Alexander Biewald

Eingereicht am	13. August 2024
1. Gutachter	Prof. Achim Hartschuh
2. Gutachter	Prof. Thomas Bein
Mündliche Prüfung am	17.Oktober 2024

Abstract

The photophysical properties of light-absorbing semiconducting materials are of significant interest, as these materials are essential for light-induced energy conversion processes such as those in solar cells. This work investigates photo-induced excited state dynamics in semiconductors using confocal microscopic measurement techniques, focusing specifically on the radiative photoluminescent decay of both static and diffusing excited states.

The thesis begins with an introduction to the physical description of excited states in materials, comparing their characterization in semiconductors to that in molecules. Additionally, the excited state can represent a mobile state, driven by a chemical potential. A subsequent chapter explains the dynamics of diffusion combined with photophysical decay, linking measured data with diffusion functionality through various numerical and analytical approaches. Chapter three is introducing the confocal microscope and the implemented advanced time-resolved and spectroscopy techniques. Furthermore, a detailed description of the signal generation is given determining the measured photo luminescence. The final section explains the numerical analysis of the measured data. These foundational chapters serve to introduce the main projects discussed in this work.

In methyl ammonium lead iodide ($MAPbI_3$) thin films, the diffusive transport of excited ambipolar charge carriers is hindered by optical phonons and lattice fluctuations. Additionally, the disorder induced by phase transitions in thin films was found to halt this transport. In ceasium formamidium lead triiodide ($CsFAPbI_3$) quantum dot films, restructuring of the clustering improved photophysical properties and consequently enhanced power conversion efficiency. For lead-free perovskite systems, the inferior solar cell performance was attributed to strong localization of excited states due to coupling to lattice phonons and immobile defect states. The novel approach using wurster-benzodithiophene-dialdehyde covalent-organic-framework (WBDT COF) highly crystaline thin films, a tunable material composed solely of organic molecules, exhibited semiconductor-like behavior, with disorder identified as a critical factor influencing excited state diffusive transport. Finally, measurements on rare-earth-ion metallic-organic-frameworks (REI MOFs) revealed a non-parametric downconversion process in ytterbium 2,5-dihydroxy-1,4-benzoquinone metallic-organic-frameworks (DHBQ MOFs), demonstrated through second-order time correlation function analysis of emitted photons.

Contents

1 Introduction

Dear reader, welcome to my thesis. I will guide you through my topic and scientific projects. The thesis begins with three theoretical sections. The first chapter focuses on photo physics, describing the physical model of the excited states in semiconductors. The second chapter is dedicated to diffusion and related phenomena, which are central to this work. The third chapter discusses the instrumentation and generation of the measured signals. These three chapters provide insights into our experiments, their limitations, and the information they reveal. They lead over to the scientific work summarized in the final chapter. The most important publications are attached, providing detailed information on the performed studies. Many wonderful people involved in these projects, since scientific research requires teamwork, especially as questions become more complex and challenging to solve. The talent and knowledge of different scientists are needed to address these problems. It is often not possible to answer everything, and new questions frequently arise during research. This can make it difficult to justify this work and scientific research in a fast-paced, capitalistic, and populist world that demands easy answers to easy questions. Our world is complex, and we face significant problems in the future, one of which is climate change caused by industrialization and the release of CO_2 over the past 200 years through the burning of fossil fuels[1]. This is a major driving force behind climate change, though there are other influences as well. We are using our resources intensively, and the increasing demand for energy is exacerbating climate change.

This thesis does not offer a complete solution but provides a small piece of knowledge as a contribution to the basic understanding of photoactive semiconductor materials. This highlights the complexity of the world, as each person can only investigate a tiny specific part of a scientific field. The focus of this thesis is on understanding the underlying photophysics in novel photoactive crystalline semiconductor materials using an optical microscope. The microscope allows us to resolve the photoexcited states both spatially and temporally. I believe that scanning novel photoactive semiconductors is still important, even though silicon already provides relatively good solar cells, albeit with high production energy costs. The transition has just begun, and we still mainly use fossil fuels or nuclear power plants. A single solution for generating energy is not sufficient. Nature shows us that variety is beneficial in facing different environmental impacts. This motivates me to investigate new light-harvesting materials that convert photon energy into different forms. Potential applications include solar cells, improved photocatalytic reactions, or entirely different uses. Regardless of the application, a deep understanding is required. This work offers a small piece of basic understanding and results for a few novel solid-state materials, with the hope that it contributes to research in a meaningful way. This motivation is idealistic and not easily measurable as a success, as it is a small puzzle piece in a larger picture. The future will determine its usefulness.

2 General Photophysics- Solid State- versus Molecule-Model

This work focuses on the investigation of photoactive crystalline solid-state thin films. It is essential to distinguish between different types of thin-film samples. The first type is a printed, spin-coated, or drop-casted thin film of nanoparticles or quantum dots. Before forming a thin layer on a substrate, the nanoparticles are in solution and are stabilized by surface groups. In the film, the nanoparticles form a closely packed layer, but structurally, they remain separated from each other. The next film category is a thin crystallite layer. Here, individual crystallites form grain boundaries at their borders. These films can be created by spin-coating, printing, or other solution-based techniques. The third class comprises films made of two-dimensional materials, either through exfoliation or as crystalline films of two-dimensional sheets detached by surface linkers. All these different films are treated as two-dimensional systems since most films are only a few nanometers thick. Solution-based films, in particular, range between 50-500 nm, and exfoliated samples of two-dimensional materials can be as thin as a monolayer. Therefore, these solid films behave as two-dimensional emitters because they are much thinner than the Rayleigh length of the microscope objectives used, which is on the order of micrometers. The origin of the observed signal is influenced by how it is generated inside the material via photophysical processes and how it can be observed via the setup. The latter point will be discussed in the setup chapter. Since the word exciton among other terms, can be used in different contexts, I think it is important to carefully define the notation used in this work. So let's take a closer look at the solid-state physics and molecular physics perspectives. In general, for the measurements performed here, after laser excitation, the emitted light from an excited state of a solid-state sample is measured. This emitted light is called photoluminescence (PL). So, what is this excited state?

2.1 Band Model

In the model description of a semiconductor, the valence electrons are delocalized over the periodic crystal structure spanned by positively charged ions. This spanned crystal lattice fulfills all symmetry properties. These ions are atom centers or larger molecules. Let's write down the full Hamiltonian operator for this many-body problem[2, 3, 4].

$$H = \quad H_{el} + H_{ion} + H_{el-ion} + H_{ex} \tag{2.1}$$

H_{el} represents the energy contribution from the electrons, and H_{ion} from the ions. H_{el-ion} sums up all interactions between electrons and ions, and the last term H_{ex} includes all external fields that disturb the system, although it is set to zero for completeness. However, we cannot find an analytic solution for this Hamiltonian operator, so we need to make some simplifications and assumptions. Each energy term of the electrons depends on the mass m, momentum p, charge e and coordinate $\boldsymbol{r}$. The independent electron term is then the sum of the kinetic energy of each electron and the potential energy of the interacting electrons. The potential term is approximated by the sum over all two-particle

interactions. Similarly, for the ions, the energy terms depend on momentum P, mass M and the potential term V is a function of the coordinate $\boldsymbol{R}$.

$$\begin{aligned} H_{el} &= H_{el,kin} + H_{el-el} = \sum_k \frac{p_k^2}{2m} + \frac{1}{2}\sum_{k,k'} \frac{e^2}{|\boldsymbol{r}_k - \boldsymbol{r}_{k'}|} \\ H_{ion} &= H_{ion,kin} + H_{ion-ion} = \sum_i \frac{P_i^2}{2M_i} + \frac{1}{2}\sum_{i,i'} V_{ion}(\boldsymbol{R}_i - \boldsymbol{R}_{i'}) \\ H_{el-ion} &= \sum_{k,i} V_{el-ion}(\boldsymbol{r}_k - \boldsymbol{R}_i) \end{aligned} \tag{2.2}$$

The interaction term between electrons and ions is also approximated by a sum over two-particle interactions involving one electron and one ion. Given that the mass M of ions is much larger than the mass m of electrons, we can adopt an adiabatic approach where the ions are treated as fixed potentials surrounded by the faster-moving electrons. Thus, all the potential energies of the ions are combined into a periodic potential V. The potential experienced by the electrons depends solely on the electron coordinates $\boldsymbol{r}$. In addition to the Coulomb interaction among electrons, the total Hamiltonian includes a spin-dependent electronic energy term.

$$H = \sum_k \frac{p_k^2}{2m} + \sum_k V(\boldsymbol{r}_k) + \frac{1}{2}\sum_{k,k'} \frac{e^2}{|\boldsymbol{r}_k - \boldsymbol{r}_{k'}|} + H_{spin} \tag{2.3}$$

The second assumption is that the overall wave function Φ consists of n one electron wave functions ϕ. Each one-electron wave function also depends on the spin of the electron, ensuring that the wave functions are antisymmetric under exchange. The n one-electron wave functions form an antisymmetric n-particle electron wave function.

$$\Phi(\boldsymbol{r}_1, ..., \boldsymbol{r}_n, \sigma_1, ..., \sigma_n) = \underbrace{(n!)^{-1/2}\sum_p (-1)^{P_p} P}_{\mathcal{A}} \cdot \phi_1(\boldsymbol{r}_1, \sigma_1) \cdot \phi_2(\boldsymbol{r}_2, \sigma_2) ... \phi_n(\boldsymbol{r}_n, \sigma_n) \tag{2.4}$$

P is one of the $n!$ permutations and P_p is the parity. The wave function for an electron in a periodic potential can be solved by the Bloch states:

$$\phi(\boldsymbol{r}) = e^{i\boldsymbol{k}\boldsymbol{R}} u(\boldsymbol{r}) \tag{2.5}$$

In the ground state, the description of a moving single-electron wave through the crystal is analogous to the description of a localized single electron around each ion. In the following, the Bloch states are used as an approach to solve the many-body problem. Using the variational principle, the Hamiltonian 2.3 can be diagonalized by solving the Schrödinger equation. The electron-electron interaction is treated as a weak perturbation. Furthermore, due to the Pauli exclusion principle, the electrons are indistinguishable, and there are $N!$ possible distributions for N electrons, each with equal probability. Permuting electrons among these terms may introduce a sign change due to the antisymmetric nature of the wave functions. The overall wave function over all possible combinations takes the form of a Slater determinant. All individual electron wave functions $\phi_j(\boldsymbol{r}, \sigma)$ are orthogonal to each other. The final Hamiltonian operator includes a term for the free-moving electron in the periodic potential, a term for the Coulomb interaction, and a contribution from the exchange of electrons. Due to the orthogonality of the individual wave functions, only

electrons with the same spin need to be considered, hence it suffices to use only the local coordinates $\boldsymbol{r}$ in the Hamilton operator:

$$E_j\phi_j(\boldsymbol{r}) = \left(-\frac{\hbar^2}{2m}\Delta + V(\boldsymbol{r})\right)\phi_j(\boldsymbol{r}) + \cdots \underbrace{\sum_{k\neq j}\int e^2\frac{|\phi_k(\boldsymbol{r}')|^2}{|\boldsymbol{r}-\boldsymbol{r}'|}\,d\tau'\phi_j(\boldsymbol{r})}_{\text{Coulomb Term}} - \underbrace{\sum_{k\neq j}^{equal\ Spin}\int e^2\frac{\phi_k^*(\boldsymbol{r}')\phi_j(\boldsymbol{r}')}{|\boldsymbol{r}-\boldsymbol{r}'|}d\tau'\phi_k(\boldsymbol{r})}_{\text{Exchange Term}} \tag{2.6}$$

This approach to the semiconductor system is also known as the Hartree-Fock equation. With the concept of Bloch states, it is possible to construct the conduction and valence bands. Here, individual electrons are delocalized over the whole crystal, moving as waves through it. From this fundamental description of electrons in the crystal lattice, we now move to the description of excitons. An exciton is a bound pair of an electron and a "hole" (an absence of an electron). When an electron is excited from the ground state, it leaves behind a hole. In the second quantization of quantum mechanics, this pair forms a quasi-particle known as an exciton.

2.1.1 Frenkel exciton

Let us start with a localized exciton bound to its atom or molecule. The one-electron wave functions in the Hartree-Fock approximation are localized around their respective atoms or molecules within the crystal structure. Furthermore, we assume that the individual wave functions do not strongly overlap with each other. This implies that in this scenario, the exciton is very localized and strongly bound to its origin[2, 3, 4, 5, 6]. Therefore, we can write the wave function for the excited state as the product of all ground state electrons $\phi_k(\boldsymbol{r},\sigma)_0$ and all excited state electrons $\phi_k(\boldsymbol{r},\sigma)_1$.

$$\Phi_0 = \mathcal{A}\prod_{k=1}^{n}\phi(\boldsymbol{r},\sigma)_0 \;\rightarrow \Phi_1 = \mathcal{A}\prod_{k=1}^{m-1}\phi_k(\boldsymbol{r},\sigma)_0 \cdot \underbrace{\phi_m(\boldsymbol{r},\sigma)_1}_{\text{excited electron}} \cdot \prod_{k=m+1}^{n}\phi_k(\boldsymbol{r},\sigma)_0 \tag{2.7}$$

The excited state can be in an ith energy level. Thus, the total energy is the sum of the single-electron energy eigenvalues in the ground state, with an additional contribution from an excited state.

$$E_1 = E_0 + \sum_i e^{i\boldsymbol{k}\boldsymbol{R_i}}E_i^1 \tag{2.8}$$

A good example would be a molecular crystal, where the excited state is localized at the molecule. Moreover, the mobility is not expected to be high, since the overlap of the wave functions is only small. A hopping transport mechanism is anticipated.

2.1.2 Wannier exciton

In the case of a bound delocalized electron and hole, we need to change the description. Both particles are coupled via Coulomb interactions to each other, and the strength depends on the surrounding dielectric media[2, 3, 4, 5, 7]. Thus, there is no longer interaction with a specific atomic or molecular position. The Hamiltonian is the sum of the kinetic

energy terms for both particles and the Coulomb potential energy:

$$\left(-\frac{\hbar^2}{2m_e^*}\Delta_e - \frac{\hbar^2}{2m_h^*}\Delta_h - \frac{e^2}{\varepsilon|\boldsymbol{r}_e - \boldsymbol{r}_h|}\right)|\Phi\rangle = E\,|\Phi\rangle \tag{2.9}$$

This Hamiltonian is similar to the one from the Hydrogen model. The energy eigenvalues are:

$$E_{exciton} = -\frac{\mu e^4}{2\hbar^2\varepsilon^2 n^2} + \frac{\hbar^2 K^2}{2(m_e^* + m_h^*)} \tag{2.10}$$

The exciton energy is a function of the quantum number n, where n is an element of the natural numbers representing the nth excited energy state. In addition to the excited energy, the exciton also has kinetic energy. The total energy balance is then the sum of the ground state energy of electrons E_0, the energy needed to create a charge pair E_{gap} to overcome the bandgap, and the exciton energy.

$$E_{nlm} = \underbrace{E_0}_{\text{zero energy}} + \underbrace{E_{Gap} - \frac{\mu e^4}{2\hbar^2\varepsilon^2 n^2}}_{\text{energy creating 1 exciton}} + \underbrace{\frac{\hbar^2 K^2}{2(m_e^* + m_h^*)}}_{\text{kinetic exciton energy}} \tag{2.11}$$

Generally, in the literature, such excitons are discussed as being much larger and delocalized over several ionic crystal lattice centers. Therefore, these types tend to be more mobile and often exhibit coherent, band-like transport. However, in the case of 2D materials, the binding can be very large due to the field lines extending out of the material, resulting in smaller excitons, that are not localized to a single atomic center but still exhibit coherent transport after excitation. For example, in monolayered transition metal dichalcogenides, the Bohr radii are $1 - 2nm$[8], which is comparable with the expected size of a Frenkel exciton. The actual mobility of excitons can differ from that of single excited electrons or holes. The dispersion relation, which describes the curvature of the energetic bands and hence the effective mass, can differ for excitons compared to electrons and holes. The more curved the bands are, the more mobile the excitons are due to their lower effective mass. If the binding energy of the exciton is lower than the thermal excess energy, the exciton can dissociate into single excited holes and electrons. These excited charges will move together as unbound ambipolar charge carriers, since having individual moving species would create an electric potential that is energetically unfavorable. A perfect example demonstrating this effect is methylammonium lead iodide, as discussed later.

2.1.3 Polaron

After introducing excitons, we now turn to the description of a polaron[5, 9]. A polaron is an excited electron or hole that is additionally coupled to a vibrational mode, a phonon. The description of the excited state must extend to include additional interaction terms. Returning to the Hamiltonian 2.2 , let us include the interaction terms of the phonons. Here, the Hamiltonian of the potential energy of the atomic centers $H_{ion-ion}$ is a sum of their equilibrium positions $H^0_{ion-ion}$ and some phonon energy H_{phonon}, which represents vibrational modes of the lattice or molecules.

$$\begin{aligned} H_{ion-ion} &= H^0_{ion-ion} + H_{phonon} \\ H_{el-ion} &= H^0_{el-ion} + H_{phonon-el} \end{aligned} \tag{2.12}$$

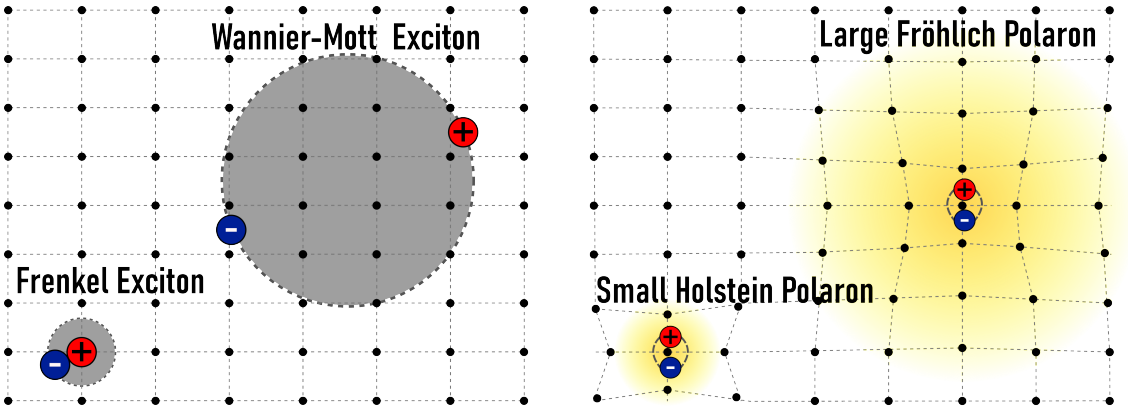

Figure 2.1): Graphical illustration of the different Exciton and polaronic Exciton concepts: The Wannier-Mott exciton is delocalized and can extend over several crystal unit cells. It can be imagined as a cloud of electron-hole pairs spread out across multiple units of the crystal lattice. In contrast, the Frenkel exciton is localized at a distinct atomic center, confined to a single lattice site or molecule, with the electron and hole closely bound. For polarons, we can imagine Frenkel or Wannier-Mott excitons coupled to phonons. The model description differentiates between the long-range coupling over several crystal units (Fröhlich) and short-range coupling (Holstein) with the exciton or excited charge carrier.

The electronic energy term contains the equilibrium interaction energy term with the periodic crystal lattice H^0_{el-ion}. This includes all ground state electrons as well as all excited states, as treated above, in the electronic gas in a dielectric surrounding. The excited states can be localized or delocalized. Additionally, as a perturbation, the interaction of electrons with phonons $H_{phonon-el}$ is added. This excited state coupled to a phonon is called a polaron, which is a pseudo-particle created by the second quantization of quantum mechanics. In general, this description can be extended to an exciton (polaronic exciton), or any other form of an excited state coupled to a phonon, generalizing the definition of a polaronic pseudo-particle. We can write down a general Hamiltonian:

$$\begin{aligned} H_{polaron} &= H_{exciton} + H_{phonon} + H_{phonon-el} \\ &= H = \sum_{\boldsymbol{k}} \epsilon_{\boldsymbol{k}} \hat{c}^\dagger_{\boldsymbol{k}} \hat{c}_{\boldsymbol{k}} + \hbar\omega_0 \sum_{\boldsymbol{q}} \hat{a}^\dagger_{\boldsymbol{q}} \hat{a}_{\boldsymbol{q}} + H_{phonon-el} \end{aligned} \tag{2.13}$$

For the excited state, an exciton and a phonon are created, which both couple together. All terms are expressed by the creation operators $\hat{c}^\dagger, \hat{a}^\dagger$ and the annihilation operators $\hat{c}, \hat{a}$ for the exciton and phonon, respectively. Here, the description is generalized, which means the exciton can be localized (Frenkel) or delocalized (Wannier). The same is valid for the excited phonon, which can be an optical or acoustic lattice vibration or a vibrational mode of a molecule built into the crystal structure. In general, there are many different types of polaron descriptions, but they can be broken down into two main types.

Holstein polaron The first one is the Holstein polaron[5, 9].

$$H_{phonon-el} = \frac{V}{\sqrt{N}} \sum_{\boldsymbol{k},\boldsymbol{q}} \hat{c}^\dagger_{\boldsymbol{k}+\boldsymbol{q}} \hat{c}_{\boldsymbol{k}+} \left(\hat{a}_{\boldsymbol{q}} + \hat{a}^\dagger_{\boldsymbol{q}} \right) \tag{2.14}$$

The coupling of excitons and polarons is localized to the atomic or molecular sides of the crystal structure. This type is not very mobile due to its localization within the lattice. A hopping transport mechanism is expected.

Fröhlich polaron The second is the Fröhlich polaron[5, 9].

$$H_{phonon-el} = \sum_{\boldsymbol{k},\boldsymbol{q}} V(\boldsymbol{q})\ \hat{c}^{\dagger}_{\boldsymbol{k}+\boldsymbol{q}} \hat{c}_{\boldsymbol{k}+} \left(\hat{a}_{\boldsymbol{q}} + \hat{a}^{\dagger}_{\boldsymbol{q}}\right) \tag{2.15}$$

Here, the coupling extends over several unit cells of the crystal. This makes these excited states more mobile, and a more coherent transport mechanism is expected. In general, polarons are expected to be less mobile, since their movement deforms their surroundings, which costs additional energy. Observations for the materials investigated here, especially for lead-free perovskites and COF materials, indicate that the polaron forms from a free, non-phonon-coupled excited state. After excitation, the temperature of the electrons is not the same as that of the phonon bath. This means that the coupling between them occurs after a certain time to reach equilibrium. However, this depends on the properties of each material and cannot be generalized for all excited polarons.

2.2 Molecule Model

Now let's briefly describe an excited single molecule[10, 11]. The total molecular many-electron wave function can also be approximated as a product of several single-electron wave functions, known as molecular orbitals. The molecular orbitals follow the symmetry of the underlying molecule. Here, a similar approximation is used: the atomic core, including the inner electrons, is seen as a rigid, slow-moving framework, while the valence electrons move more freely around, responsible for forming bonds between atoms. Different types of bonds are possible, such as covalent and ionic bonds. After absorbing a photon, as depicted in figure 2.2, the surrounding electron gas will have a different configuration. Since the atomic framework of the molecule is much heavier, it is assumed to be rigid, known as the Born-Oppenheimer approximation. The response of the electrons is almost instantaneous, on an attosecond timescale. The molecular transition probability scales with the overlap of their nuclear wave functions. This scaling factor is called the Franck-Condon factor. The overlap of the nuclear wave function between the lowest excited state and the ground state depends on the molecule and is generally low. Thus, the molecule goes into a higher-lying excited state after excitation (figure2.2). From here, the atoms change their spatial configuration and can return to the energetically lowest excited state through internal conversion. Internal conversion involves the excess energy being converted into thermal energy, heating up the molecule, which occurs on the femtosecond timescale. Other interaction or transfer mechanisms are also possible, such as intersystem crossing, charge transfer, or different energy transfer processes. Now, let us compare the description of an excited single molecule with an exciton in a semiconductor. An exciton is a mobile excited state. To conceptualize this, we imagine a single excited molecule within a film of unexcited molecules that form a surrounding structure. This excited state can induce structural reorganization of the surrounding molecules, depending on interactions with its neighbors, such as electromagnetic shielding effects. However, it differs from the exciton introduced earlier. In an excited molecule which is incorporated in a molecular structure, the electronic wave function differs compared to an exciton where one electron is moved from the valence to the conduction band, forming a bound state with a hole.

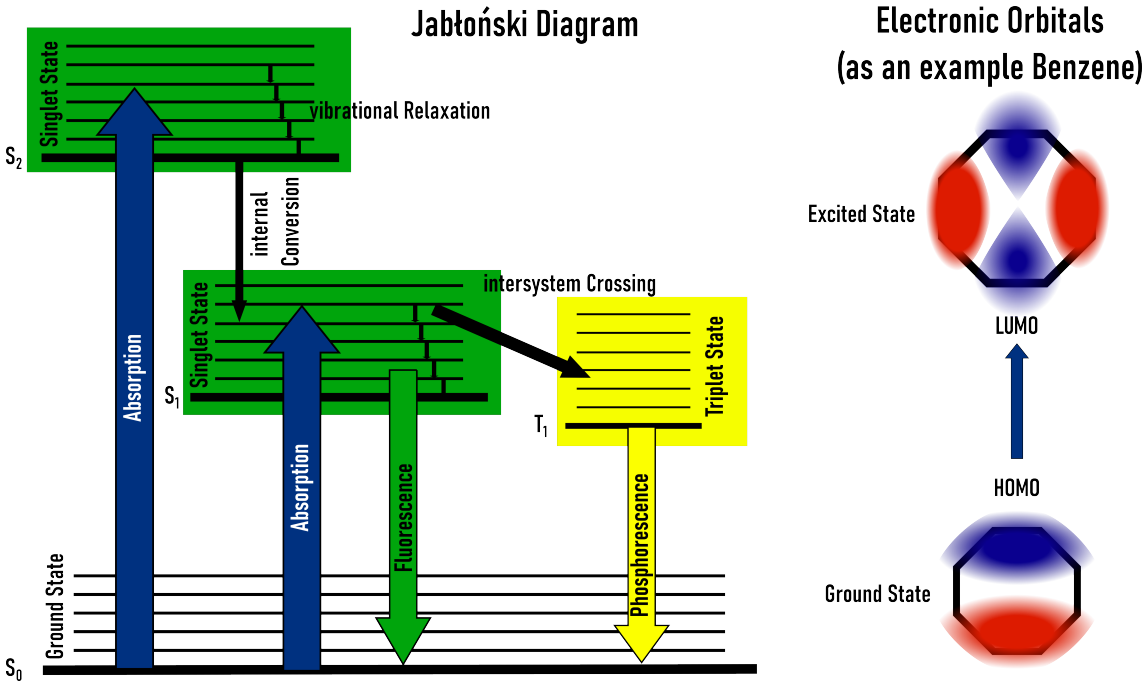

Figure 2.2): The scheme represents the dynamics and processes occurring in a molecule after excitation. In this representation, the excited states in molecules are related to changes in electron orbital densities, which in turn affect the symmetry and coordinates of atom positions. Using benzene as a simple example, the illustration depicts how excitation alters the electron distribution[12, 13].

Bringing several molecules next to each other in a periodic structure and overlapping their excited state wavefunctions leads to a very similar description as introduced in the previous chapter. This connection allows both models to be linked.

2.3 Fermi's Golden Rule

As a last step, we need to connect the excited state with the emitted photons that are measured. A photon will be emitted by an excited state transitioning to its ground state, if the symmetry and selection rules for radiative decay are fulfilled. Since the excited state results in a change of the charge distribution, this can be described by the transition dipole moment. The transition dipole moment $\boldsymbol{\mu}$ from the excited state Φ_2 compared to the ground state Φ_1 is as follows[14, 15, 16]:

$$\boldsymbol{\mu}_{12} = e \cdot \langle \Phi_1 | \, \boldsymbol{r} \, | \Phi_2 \rangle \tag{2.16}$$

The transition dipole moment is induced by a periodic perturbation, such as a photon. To estimate the transition rate P_{12}, we use the time-dependent perturbation of the Schrödinger equation to the first order, which accounts for the transition dipole moment for a specific energetic transition $E_2 - E_1 = \hbar\omega$. It shows that a small perturbation can initiate a transition from an initial state to a different state.

$$P_{21} \quad \sim \quad |\boldsymbol{E}_0|^2 \; | \langle \Phi_1 | \, \boldsymbol{r} \, | \Phi_2 \rangle \, |^2 \rho_f(\hbar\omega) \; \delta(E_2 - E_1 - \hbar\omega) \tag{2.17}$$

We also have to include all possible joint state density $\rho_f(\hbar\omega)$ that are available in the final state. In a semiconductor, we integrate over all states in the Brillouin zone, which represents the joint density of states. This is also referred to as Fermi's golden rule, which in this context is a specific form for semiconductor transitions[15]. In this description, all the information about the symmetry and quantum numbers of the system is included in the wavefunctions Φ. In case the wavefunctions are known, the possible transitions can be calculated and predicted. In reality, this is often not the case. However, by using simple symmetry arguments, some transitions can be excluded or predicted as radiative.

These sketched models describe the measured excited states and will help to understand the photophysics of them. Moreover, these descriptions also underlie the temporal, spectral, and temperature behavior observed in spectroscopic data. All these models are not complete, and there are many more details that can be theoretically explained, but it should be enough to understand all the investigations made on different materials illustrated in this work.

3 Diffusion

When running a catalytic process or a solar cell, photo-excited charge carriers need to be mobile, transferring their energy to contacts or reaction centers. In the absence of an external field, the transport is driven by the chemical potential of the excited states themselves, namely diffusion. The combination of photo physics and the diffusive transport of an excited state leads to an understanding of the energy conversion processes in the material as an intrinsic property. This chapter mainly answers the question of what we understand by diffusive transport. First, a general concept is shown, and later we apply this concept by combining it with excited states in semiconductor materials. Lastly, it is discussed how the equations can be used to analyze recorded data.

3.1 From thermodynamical description of a liquid to the classical differential equation of diffusion

The following chapter is mainly from the Landau and Lifschitz book of hydrodynamics[17]. Here we start with a hydro dynamical description of a diffusion process. At the first glance the excited states in the semiconductors can be described like a liquid or a gas. One of the main concepts of the description of diffusion is that it is described by statistical physics. The starting point is a small volume consisting of a two component liquid connected by the concentration c. If within the overall volume a gradient of the concentration exists, it will create a chemical potential μ leveling out the concentration with every time step until the thermodynamic equilibrium will be reached. Moreover it maximizes the entropy. This certain defined Volume is small but much bigger then the interparticle distance, which means it averages over many particles and it is very small compared to the overall system. In the picture of an electron system in a semi conductor, it is a mixture of excited state charges in a bath of ground state particles. In the first step we use the equation of continuity, where ρ is the local density of the liquid:

$$\frac{\partial \rho}{\partial t} + \operatorname{div}(\rho \boldsymbol{v}) = 0 \tag{3.1}$$

This equation describes that the local mass of a liquid inside a volume will change over time if some liquid flows in or out through the lateral faces of the volume with a velocity $\boldsymbol{v}$. It conserves the mass of the liquid. In a semiconductor, the system consists of a free electron gas captured in a periodic potential. In a simple approach, this free-moving electron gas can be depicted as a liquid or a gas in a hydrodynamic way. Here, the excited states, e.g., excitons, are a different species inside the ground state electron gas, creating a chemical potential and leading to possible diffusive transport of excited states. First, an ideal system is described which has no defect states capturing excited states, and the lifetime is much longer than needed to bring the system into equilibrium via diffusive transport.

Therefore, we need to introduce the term concentration c into the description of an ideal fluid. The parameter of the concentration $c(t, x, y, z)$ depends on local vector variables

$\boldsymbol{x}(t)$ and on the time t. As a consequence, the total derivation in time of c consists of two terms and is zero in a fully equilibrated system.

$$\frac{dc}{dt} = \frac{\partial c}{\partial t} + \boldsymbol{v}\nabla c = 0 \tag{3.2}$$

Now, with the additional term of c, we need to expand the description of the liquid. As a consequence of the concentration change over time, by comparing the equations, it is possible to extend the equation of continuity:

$$\frac{\partial(\rho c)}{\partial t} + \operatorname{div}(\rho c \boldsymbol{v}) = 0 \tag{3.3}$$

This equation is valid in a system that is completely in equilibrium. To see the consequence, it is necessary to rewrite it in an integral form. This mathematical trick leads to

$$\frac{\partial}{\partial t} \int \rho c \; dV = - \oint \rho c \boldsymbol{v} \; d\boldsymbol{f} \tag{3.4}$$

The change in time of the density and concentration in a defined volume, on the left side, is exactly the sum of the flow through the lateral faces of this volume, where the concentration is also conserved. If there is a change in concentration and the system is out of equilibrium within the full volume, a chemical potential is built. The concentration will no longer be conserved. As a result, we have a diffusion-driven flow bringing the entire system into equilibrium. For this, we need a current $\boldsymbol{i}$ to conserve the overall concentration:

$$\begin{aligned} \frac{\partial(\rho c)}{\partial t} &= -\operatorname{div}(\rho c \boldsymbol{v}) - \operatorname{div} \boldsymbol{i} \\ \rho \left(\frac{\partial c}{\partial t} + \boldsymbol{v}\nabla c \right) &= -\operatorname{div} \boldsymbol{i} \end{aligned} \tag{3.5}$$

We will leave this equation for now and come back to it later for further interpretation. It is a statistical process, which means it depends on thermodynamic parameters. Let us now move on to the energy of the system. The energy needs to be conserved and consists of two parts: the kinetic energy , which depends on the velocity $\boldsymbol{v}$, and the internal energy. The internal energy is the amount of energy stored in the liquid. Thus, the energy per unit volume of a liquid is:

$$\frac{\partial}{\partial t} \left(\frac{\rho v^2}{2} + \rho \epsilon \right) \tag{3.6}$$

Let us introduce some thermodynamic observables[18] for our system, like the temperature T, the entropy s, the pressure p, the density ρ, and, since the change in concentration is to be observed, the chemical potential μ. The thermodynamic internal energy ϵ for two substances is defined as:

$$d\epsilon = T \; ds - p \; dV + \mu_1 \; dn_1 + \mu_2 \; dn_2 \tag{3.7}$$

n_1 and n_2 are the particle numbers for 1g of a certain substance. Each particle species has its own mass m_1 and m_2. Therefore :

$$n_1 \cdot m_1 + n_2 \cdot m_2 = 1 \tag{3.8}$$

The concentration c is defined as $c = m_1 \cdot n_1$. Hence, the internal energy ϵ, the enthalpy w and the Gibbs free energy Φ have the following form:

$$\begin{aligned} d\epsilon &= T\ ds + \frac{p}{\rho^2}\ d\rho + \left(\frac{\mu_1}{m_1} - \frac{\mu_2}{m_2}\right)\ dc, \qquad \mu = \left(\frac{\mu_1}{m_1} - \frac{\mu_2}{m_2}\right) \\ d\epsilon &= T\ ds + \frac{p}{\rho^2}\ d\rho + \mu\ dc \quad \text{(internal energy)} \end{aligned} \tag{3.9}$$

$$\begin{aligned} dw &= T\ ds + \frac{1}{\rho}\ dp + \mu\ dc \quad \text{(enthalpy)} \\ \rightarrow\ & dp = \rho\ dw - \rho T\ ds - \rho\mu\ dc \\ & w = \epsilon + \frac{p}{\rho} \quad \text{(relation of enthalpy and internal energy)} \end{aligned} \tag{3.10}$$

$$d\Phi = -s\ dT + V\ dp + \mu\ dc \quad \text{(Gibbs free energy)} \tag{3.11}$$

All three of these equations characterize the general thermodynamic potential, varying with different parameters. Here, we will not delve further into the details of thermodynamics, but these equations are needed to complete the description[18].

Before we combine the thermodynamic potentials with the description of the liquid, let us rewrite equation 3.1:

$$\frac{\partial \rho}{\partial t} = -\operatorname{div}(\rho \boldsymbol{v}) \quad \text{(Equation of continuity)} \tag{3.12}$$

Furthermore, the equation of motion for a liquid is needed. The main force acting on a volume is the sum of the pressure over all face sides $\boldsymbol{f}$:

$$-\oint p\ d\boldsymbol{f} = -\int \nabla p\ dV \tag{3.13}$$

By reformulating the integral from one over the face sides to one over the volume V, the equation shows that the main force is $\operatorname{grad} p$, which acts on a volume element. In conclusion, the force is equal to the product of the mass per unit volume ρ and the acceleration $\frac{d\boldsymbol{v}}{dt}$:

$$\rho \frac{d\boldsymbol{v}}{dt} = -\nabla p \tag{3.14}$$

Since the velocity $\boldsymbol{v}(x, y, z, t)$ is a vector, each velocity component depends not only on time but also on the location in the liquid. This means the total time derivation consists

of two terms:

$$\frac{d\boldsymbol{v}}{dt} = \frac{\partial \boldsymbol{v}}{\partial t} + (\boldsymbol{v}\nabla)\boldsymbol{v} \tag{3.15}$$

Inserting this into the previous equation leads to the equation of motion of an ideal liquid:

$$\frac{\partial \boldsymbol{v}}{\partial t} = -(\boldsymbol{v}\nabla)\boldsymbol{v} - \frac{1}{\rho}\nabla p \tag{3.16}$$

This equation is not complete. Normally, a liquid or a gas has internal friction, which is characterized by the dynamic viscosity η. This adds a counterforce. However, the liquid here is incompressible, and its strain tensor has the form:

$$\sigma_{ik} = -p\ \delta_{ik} + \eta\left(\frac{\partial v_i}{\partial x_k} + \frac{\partial v_k}{\partial x_i}\right) \tag{3.17}$$

Also, for excitons, a possible viscosity is conceivable in the sense that a moving cloud of bound or unbound charges has internal resistance. For completeness, it should be mentioned, but for later derivations, it does not play a major role. As a result, completing the equation of motion, we end up with the Navier-Stokes equation:

$$\frac{\partial \boldsymbol{v}}{\partial t} = -(\boldsymbol{v}\nabla)\boldsymbol{v} - \frac{1}{\rho}\nabla p + \frac{\eta}{\rho}\Delta\boldsymbol{v} \quad \text{(Navier Stokes equation)} \tag{3.18}$$

As a final additional equation, we need the temporal change of the internal energy and insert the equation of continuity:

$$\begin{aligned} \frac{\partial \epsilon}{\partial t} &= T\frac{\partial s}{\partial t} + \frac{p}{\rho^2}\frac{\partial \rho}{\partial t} + \mu\frac{\partial c}{\partial t} \\ &= T\frac{\partial s}{\partial t} - \frac{p}{\rho^2}\operatorname{div}(\rho\boldsymbol{v}) + \mu\frac{\partial c}{\partial t} \end{aligned} \tag{3.19}$$

Now let us return to the relationship of energy and its time evolution. The different terms are replaced by the previously derived formulas, such as the Navier-Stokes equation, the equation of continuity, and the expressions for internal energy and enthalpy.

$$\begin{aligned} \frac{\partial}{\partial t}\left(\frac{1}{2}\rho v^2 + \rho\epsilon\right) &= \frac{v^2}{2}\frac{\partial \rho}{\partial t} + \rho\boldsymbol{v}\frac{\partial \boldsymbol{v}}{\partial t} + \rho\frac{\partial \epsilon}{\partial t} + \epsilon\frac{\partial \rho}{\partial t} \\ &= \frac{v^2}{2}\operatorname{div}(\rho\boldsymbol{v}) - \rho\boldsymbol{v}\nabla\frac{v^2}{2} - \boldsymbol{v}\nabla p + v_i\frac{\partial \sigma'_{ik}}{\partial x_k} + \cdots \\ &\quad \rho T\frac{\partial s}{\partial t} - \frac{p}{\rho}\operatorname{div}(\rho\boldsymbol{v}) + \mu\rho\frac{\partial c}{\partial t} - \epsilon\operatorname{div}(\rho\boldsymbol{v}) \\ &= -\left(\frac{v^2}{2} + w\right)\operatorname{div}(\rho\boldsymbol{v}) - \rho\boldsymbol{v}\nabla\frac{v^2}{2} - \boldsymbol{v}\nabla p + v_i\frac{\partial \sigma'_{ik}}{\partial x_k} + \rho T\frac{\partial s}{\partial t} + \mu\rho\frac{\partial c}{\partial t} \end{aligned} \tag{3.20}$$

The tensor of viscosity can be rewritten as follows:

$$v_i\frac{\partial \sigma'_{ik}}{\partial x_k} = \frac{\partial}{\partial x_k}\left(v_i\sigma'_{ik}\right) - \sigma'_{ik}\frac{\partial v_i}{\partial x_k} \equiv \operatorname{div}(\boldsymbol{v}\boldsymbol{\sigma'}) - \sigma'_{ik}\frac{\partial v_i}{\partial x_k}$$

Moreover, within a liquid, heat transport is possible. The density of the heat flow through a face, also known as heat flux, $\boldsymbol{q}$, will be expanded in terms of the temperature gradient up to the first order. An additional assumption is that the temperature gradients are

sufficiently small. The constant term cancels out because heat flow only occurs when there is a temperature gradient in the medium. The constant χ is called the thermal conductivity and is always positive, as heat flux is an irreversible process.

$$\boldsymbol{q} = -\chi \nabla T \tag{3.21}$$

This process is important because it occurs in parallel as an additional energy transport phenomenon alongside diffusion. Both influence each other. Since the heat flux contributes to the energy flux, we need to add its divergence to this equation. Here, the term is added to both sides, leading to addition and subtraction of these terms on the same side of the formula. Furthermore, the enthalpy w incorporates the tensor of viscosity into the energy relationship.

$$\begin{aligned}
\frac{\partial}{\partial t}\left(\frac{1}{2}\rho v^2 + \rho\epsilon\right) &= -\left(\frac{v^2}{2} + w\right)\operatorname{div}(\rho \boldsymbol{v}) - \rho \boldsymbol{v}\nabla\frac{v^2}{2} - \boldsymbol{v}\nabla p \cdots \\
&\quad + \operatorname{div}(\boldsymbol{v}\boldsymbol{\sigma'}) - \sigma'_{ik}\frac{\partial v_i}{\partial x_k} + \rho T\frac{\partial s}{\partial t} + \mu\rho\frac{\partial c}{\partial t} + \operatorname{div}(\boldsymbol{q}) - \operatorname{div}(\boldsymbol{q}) \\
&= -\operatorname{div}\left[\rho \boldsymbol{v}\left(\frac{v^2}{2} + w\right) + \boldsymbol{v}\boldsymbol{\sigma'} + \boldsymbol{q}\right] \cdots \\
&\quad -\sigma'_{ik}\frac{\partial v_i}{\partial x_k} + \rho T\left(\frac{\partial s}{\partial t} + \boldsymbol{v}\nabla s\right) + \mu\rho\left(\frac{\partial c}{\partial t} + \boldsymbol{v}\nabla c\right) + \operatorname{div}(\boldsymbol{q})
\end{aligned} \tag{3.22}$$

As an intermediate step, let us first examine this equation. If it is an ideal liquid without internal friction and with constant concentration, all terms except the first one will be zero. Additionally, the change in entropy is zero because there is no exchange of heat, indicating the liquid behaves adiabatically. Thus, the energy balance for an ideal liquid is:

$$\frac{\partial}{\partial t}\left(\frac{1}{2}\rho v^2 + \rho\epsilon\right) = -\operatorname{div}\left[\rho \boldsymbol{v}\left(\frac{v^2}{2} + w\right)\right] \tag{3.23}$$

This is the conservation of energy for an ideal liquid. When this equation is rewritten in integral form, the right-hand side represents the energy flux through the faces of a volume, equal to the temporal change of the overall energy inside. For an ideal liquid with heat flux and internal friction included, the energy flux $\boldsymbol{E}$ is reduced by viscosity and includes an additional heat flux term contributing to the energy balance:

$$\boldsymbol{E} = \rho \boldsymbol{v}\left(\frac{v^2}{2} + w\right) - \boldsymbol{v}\boldsymbol{\sigma'} + \boldsymbol{q} \tag{3.24}$$

The first part is the reversible flux of energy. If there is a flow in the liquid, the difference between internal friction and heat flux becomes irreversible. In the case of no macroscopic flow, both terms cancel out because the fluxes are equal, leading to the conservation of energy as follows:

$$\frac{\partial}{\partial t}\left(\frac{1}{2}\rho v^2 + \rho\epsilon\right) = -\operatorname{div}\left[\rho \boldsymbol{v}\left(\frac{v^2}{2} + w\right) + \boldsymbol{v}\boldsymbol{\sigma'} + \boldsymbol{q}\right] \tag{3.25}$$

Comparing this equation to the energy balance, the last four terms in equation 3.22 must cancel each other. Moreover, we incorporate the extended equation of continuity for a

mixture of two liquids (equation 3.5):

$$\begin{aligned} 0 &= -\sigma'_{ik}\frac{\partial v_i}{\partial x_k} + \rho T\left(\frac{\partial s}{\partial t} + \boldsymbol{v}\nabla s\right) + \mu\rho\left(\frac{\partial c}{\partial t} + \boldsymbol{v}\nabla c\right) + \operatorname{div}(\boldsymbol{q}) \\ &= -\sigma'_{ik}\frac{\partial v_i}{\partial x_k} + \rho T\left(\frac{\partial s}{\partial t} + \boldsymbol{v}\nabla s\right) - \mu \operatorname{div}\boldsymbol{i} + \operatorname{div}(\boldsymbol{q}) \\ \rightarrow \quad & \operatorname{div}(\boldsymbol{q}) - \mu\operatorname{div}(\boldsymbol{i}) = \operatorname{div}(\boldsymbol{q} - \mu\boldsymbol{i}) + \boldsymbol{i}\cdot\nabla\mu \end{aligned}$$

Let us rewrite the full equation as follows:

$$\rho T\left(\frac{\partial s}{\partial t} + \boldsymbol{v}\nabla s\right) = \sigma'_{ik}\frac{\partial v_i}{\partial x_k} - \operatorname{div}(\boldsymbol{q} - \mu\boldsymbol{i}) - \boldsymbol{i}\nabla\mu \tag{3.26}$$

This result provides the change in entropy for a liquid with two components. Furthermore, it completes its hydrodynamic description. In the next steps, we require a different expression for the heat flux and the diffusive flux as functions of concentration and temperature, giving this equation a physical understanding and meaning. An integral form can also be derived here. The terms contributing to viscosity are neglected because they are no longer needed for the next steps.

$$\frac{\partial}{\partial t}\int \rho s \; dV = -\int \frac{(\boldsymbol{q} - \mu\boldsymbol{i})\nabla T}{T^2}\; dV - \int \frac{\boldsymbol{i}\nabla\mu}{T}\; dV + \int (\text{Terms of Viscosity}) \tag{3.27}$$

Now we need to express the heat flux and the diffusion flux in terms of the temperature and concentration gradients. It is important to mention that both fluxes depend on both gradients. This assumption is made because changes in temperature cause changes in concentration and vice versa. If these two gradients are small enough, it will be possible to expand both equations in terms of the temperature and concentration gradients. Higher-order terms can be neglected because they are too small.

$$\boldsymbol{i} = -\alpha\;\nabla\mu - \beta\;\nabla T \tag{3.28}$$

$$\begin{aligned} \boldsymbol{q} &= -\delta\;\nabla\mu - \gamma\;\nabla T + \mu\;\boldsymbol{i} \\ \boldsymbol{q} - \mu\;\boldsymbol{i} &= -\delta\;\nabla\mu - \gamma\;\nabla T \end{aligned} \tag{3.29}$$

This set of equations describes the dynamics between temperature and concentration[19, 20]. The question arises: how are these two gradients coupled and related to each other? The heat flux arises due to a temperature gradient, while diffusion arises from a change in chemical potential. However, equations 3.29 show that a change in temperature also causes a change in chemical potential. The symmetry principle of kinetic coefficients connects β and δ. Let us consider a universal closed system to explain this symmetry principle. This closed system is characterized by parameters $x_1, x_2, \ldots, x_n$ and the total entropy $S(x_1, x_2, \ldots, x_n)$. In equilibrium, entropy is maximized, and therefore the change in entropy is zero. Slightly out of equilibrium, where the parameters x_i are small, it is

possible to expand the entropy in terms of x_i:

$$\begin{aligned} \left.\frac{\partial S}{\partial x_i}\right|_{x_i=0} &= 0, \quad \left.\frac{\partial^2 S}{\partial x_i^2}\right|_{x_i=0} < 0 \\ \Rightarrow S(x_1, x_2, ..., x_n) &= S(0) - \sum_{i,k} \frac{\beta_{ik}}{2} x_k x_i + \mathcal{O}(x^3) \end{aligned} \tag{3.30}$$

Here, β_{ik} is constant. Since the parameters x_i contribute equally and symmetrically to the entropy, the constant coefficient β_{ik} equals β_{ki}:

$$\beta_{ik} = -\frac{\partial^2 S}{\partial x_i \partial x_k} = -\frac{\partial^2 S}{\partial x_k \partial x_i} = \beta_{ki} \tag{3.31}$$

In total equilibrium, the entropy is maximized and the thermodynamic conjugates X_i are zero:

$$X_i = -\frac{\partial S}{\partial x_i} = \sum_k \beta_{ik} x_k \tag{3.32}$$

Since it is a dynamic system, it is necessary to introduce a velocity $\dot{x}_i$ of the parameters. The fluctuations around the mean value $\bar{x_i}$ are small. Therefore, it is sufficient to consider only the sum of linear terms.

$$\dot{x} = \sum_k -\lambda_{ik} x_k = -\sum_{k,l} \lambda_{il} \beta_{lk}^{-1} X_k = \sum_k -\gamma_{ik} X_k \tag{3.33}$$

The fluctuations among the parameters $x_1, x_2, \ldots, x_n$ are assumed to be symmetric. A value $x(t)$ at time t has a time correlation with a value at time t', indicating that both values have a certain probability of influencing each other. This correlation is symmetric in time, meaning that if we exchange both events and look backwards, the correlation remains the same. As the time difference between fluctuating events becomes very large, the correlation converges to zero. To facilitate comparison of the equations, let us rewrite them as a system of equations:

$$\begin{aligned} \dot{x}_1 &= -\gamma_{11} X_1 - \gamma_{12} X_2 - \cdots \\ \dot{x}_2 &= -\gamma_{21} X_1 - \gamma_{22} X_2 - \cdots \\ &\vdots \end{aligned} \tag{3.34}$$

Introducing entropy renders the entire process irreversible, despite the symmetric nature of fluctuations. Moreover, the Onsager symmetry principle states that these symmetric macroscopic fluctuations lead to reciprocal relations of the kinetic coefficients γ_{ik} for irreversible processes. This implies that the kinetic coefficients are symmetric:

$$\gamma_{ik} = \gamma_{ki} \tag{3.35}$$

Finalizing the description, the rate of change of entropy $\dot{S}$ is given by the following equa-

tions. Since x_i are local parameters, integration over the entire system volume is necessary.

$$\begin{aligned} \dot{S} &= -\sum_i X_i \dot{x}_i = \sum_{i,k} \gamma_{ik} X_i X_k \\ \text{(over the entire volume)} \quad \dot{S} &= -\int \sum_i X_i \dot{x}_i \, dV \end{aligned} \tag{3.36}$$

The term $\sum_{i,k} \gamma_{ik} X_i X_k$ is positive definite because entropy must be maximized, imposing specific constraints on the kinetic coefficients. These equations cannot fully describe an irreversible system, but the probability of the entire system reversing is almost zero. To better understand this, consider an example: a thermally isolated chamber filled with two different gases, each on one side separated by a gate. Upon opening the gate, both gases will mix until the concentration gradient is zero, as dictated by the system's partition sum favoring mixed events. However, there exists a minuscule chance that the system could return to its initial state—an extremely improbable event requiring an almost infinitely long time.

Furthermore, we assume that the direct and reversed energy are the same, ensuring the conservation of energy and the time reversibility of the steady-state system. The number of forward and reversed motions is identical.[19, 20]

Let us return to the diffusive system and compare equation 3.27 with equations 3.28 and 3.29, then rewrite everything:

$$\boldsymbol{i} = -\alpha T \left(\frac{\nabla \mu}{T} \right) - \beta T^2 \left(\frac{\nabla T}{T^2} \right) \tag{3.37}$$

$$\boldsymbol{q} - \mu \, \boldsymbol{i} = -\delta T \left(\frac{\nabla \mu}{T} \right) - \gamma T^2 \left(\frac{\nabla T}{T^2} \right) \tag{3.38}$$

From the reciprocal relation 3.35, we get the relation between δ and γ:

$$\delta = \beta T \tag{3.39}$$

$$\boldsymbol{i} = -\alpha \nabla \mu - \beta \nabla T, \qquad \nabla \mu = -\frac{1}{\alpha} \boldsymbol{i} + \frac{ß}{\alpha} \nabla T \tag{3.40}$$

$$\begin{aligned} \boldsymbol{q} &= -\beta T \nabla \mu - \gamma \nabla T + \mu \boldsymbol{i} \\ &= \left(\mu + \beta \frac{T}{\alpha} \right) \boldsymbol{i} - \left(\gamma - \beta^2 \frac{T}{\alpha^2} \right) \nabla T \\ &= \left(\mu + \beta \frac{T}{\alpha} \right) \boldsymbol{i} - \chi \nabla T \end{aligned} \tag{3.41}$$

In the last equation, it is evident that only the heat flux remains if there is no change in concentration and the chemical potential is zero. Importantly, the heat conductivity and the chemical potential also depend on the pressure p. Let us express the gradient in chemical potential in terms of concentration c, pressure p, and temperature T, as it is a

function of these thermodynamic parameters.

$$\nabla\mu = \left(\frac{\partial\mu}{\partial c}\right)_{p,T} \nabla c + \left(\frac{\partial\mu}{\partial T}\right)_{c,p} \nabla T + \left(\frac{\partial\mu}{\partial p}\right)_{c,T} \nabla p \tag{3.42}$$

Using the Gibbs free energy Φ from equation 3.11, we can rewrite as follows::

$$\left(\frac{\partial\mu}{\partial p}\right)_{c,T} = \frac{\partial\Phi^2}{\partial p\,\partial c} = \left(\frac{\partial V}{\partial c}\right)_{p,T} \tag{3.43}$$

Now, $\nabla\mu$ is incorporated into the set of equations 3.46 and 3.47. Furthermore, certain relations are utilized:

$$D = \frac{\alpha}{\rho}\left(\frac{\partial\mu}{\partial c}\right)_{p,T}, \quad \frac{\rho k_T D}{T} = \alpha\left(\frac{\partial\mu}{\partial T}\right)_{c,p} + \beta \tag{3.44}$$

$$k_p = p\left(\frac{\left(\frac{\partial V}{\partial c}\right)_{p,T}}{\left(\frac{\partial\mu}{\partial c}\right)_{p,T}}\right) \tag{3.45}$$

Here, D represents the diffusion coefficient. Since diffusive transport is an irreversible process, similar to heat flux, D is always greater than zero. Pressure or temperature gradients can influence diffusive transport, hence k_T and k_p are introduced as thermometric and barometric diffusion coefficients, respectively. Both coefficients vanish in extreme cases where the concentration c equals zero or one. We have:

$$\boldsymbol{i} = -\rho D\left[\nabla c + \frac{k_T}{T}\nabla T + \frac{k_p}{p}\nabla p\right] \tag{3.46}$$

$$\boldsymbol{q} = \left[k_T\left(\frac{\partial\mu}{\partial c}\right)_{p,T} - T\left(\frac{\partial\mu}{\partial T}\right)_{p,c} + \mu\right]\boldsymbol{i} - \chi\nabla T \tag{3.47}$$

Additionally, the pressure gradient remains in the description for completeness. It becomes significant when an external field is applied to the system or when particles interact strongly. In the context of excited states in a semiconductor, this could correspond to applying a strong magnetic or electrical field, or to strong interparticle coupling in a high-density regime. However, for further description, we assume the pressure gradient is very small and set to zero. Considering that the entropy of a closed system always increases, let us rewrite equation 3.27 with these new constraints:

$$\frac{\partial}{\partial t}\int \rho\, dV = \int \frac{\chi(\nabla T)^2}{T^2}\, dV + \int \frac{\boldsymbol{i}^2}{\alpha T}\, dV + \cdots \tag{3.48}$$

From this entropy constraint, it follows that α must be greater than zero. Up to this point, a generalized description of diffusive transport phenomena in a liquid has been provided. To connect this description to photophysical problems or simple diffusion in liquids, the velocity terms can be neglected because we assume there is no macroscopic velocity. Let us revisit equations 3.26 and 3.5:

$$\begin{aligned} \rho\left(\frac{\partial c}{\partial t} + \cancel{\boldsymbol{v}\nabla c}\right) &= -\operatorname{div}\boldsymbol{i} \\ \rho T\left(\frac{\partial s}{\partial t} + \cancel{\boldsymbol{v}\nabla s}\right) &= \cancel{\sigma'_{ik}\frac{\partial v_i}{\partial x_k}} - \operatorname{div}(\boldsymbol{q} - \mu\boldsymbol{i}) - \cancel{\boldsymbol{i}\nabla\mu} \end{aligned} \tag{3.49}$$

Here, $\boldsymbol{i}\nabla\mu$ is a second-order term and will be small compared to the first-order terms. We assume that all deviations from equilibrium are very small. Now, $\frac{\partial s(T,c)}{\partial t}$ is rewritten as follows:

$$\begin{aligned} \frac{\partial s}{\partial t} &= \left(\frac{\partial s}{\partial T}\right)_{c,p}\frac{\partial T}{\partial t} + \left(\frac{\partial s}{\partial c}\right)_{T,p}\frac{\partial c}{\partial t} \\ \text{(using Gibbs free energy)} \quad &\rightarrow \left(\frac{\partial s}{\partial c}\right)_{T,p} = -\frac{\partial^2\Phi}{\partial c\partial T} = -\left(\frac{\partial \mu}{\partial T}\right)_{p,c} \\ \Rightarrow \frac{\partial s}{\partial t} &= -\frac{c_p}{T}\frac{\partial T}{\partial t} - \left(\frac{\partial \mu}{\partial T}\right)_{p,c}\frac{\partial c}{\partial t} \end{aligned} \tag{3.50}$$

By utilizing equations 3.46 and 3.47 along with the relation mentioned above, everything is reformulated, leading to the final set of equations. The pressure terms are neglected.

$$\frac{\partial c}{\partial t} = D\left[\Delta c + \frac{k_T}{T}\Delta T\right] \tag{3.51}$$

$$\frac{\partial T}{\partial t} = \chi\Delta T + \frac{k_T}{c_p}\left(\frac{\partial \mu}{\partial c}\right)_{p,T}\frac{\partial c}{\partial t} \tag{3.52}$$

In the case where the temperature remains in equilibrium over time, meaning the terms involving temperature gradients approach zero, this leads to the well-known equation of diffusion:

$$\frac{\partial c}{\partial t} = D\Delta c \tag{3.53}$$

This equation also holds true for suspended particles in a liquid, known as Brownian motion. This analogy is applicable to excitons moving within a sea of delocalized electron gas, forming the band structure of a semiconductor. Here, the probability of finding a particle in a certain volume plays the role of concentration. This holds as long as the concentration is sufficiently low and the particles do not interact. Initially, we assume that the heating from the laser has no influence on the diffusive transport of excitons. Later, an example is considered where the temperature gradient has a significant influence, and equations 3.51 and 3.52 are discussed further.

3.2 Solving the diffusion problem for a 2 dimensional system

To analyze measured data, solving this differential equation is necessary. Since the measurements are on semiconductor thin films, only the diffusive transport in two dimensions is considered here. It's important to note that the Rayleigh length of the focused microscope objectives is greater than the sample thickness, which limits the analysis to a flat sheet in two dimensions. As excitons are particles, it is more convenient to use the density of states n instead of concentration c, which defines the number of excited states per unit volume.

$$\frac{\partial n(x,y,t)}{\partial t} = D\cdot\Delta n(x,y,t) \tag{3.54}$$

At the beginning, $n_0(x,y,t)$ represents the initial distribution of excited states at time $t = 0$. To solve the differential equation, we employ a technique using Fourier transforms[17].

The Fourier functions of n are well known as:

$$\begin{aligned} n(x,y,t) &= \frac{1}{(2\pi)^2}\int n_k(t)\cdot\exp(ikr)\,d^2k, \\ n_k(t) &= \int n(x',y',t)\cdot\exp(-ikr)\,d^2r \end{aligned} \tag{3.55}$$

To solve it, we use the following Fourier integral ansatz for $n(x,y,t)$:

$$\begin{aligned} 0 &= \frac{\partial n}{\partial t} - D\cdot\Delta n \\ 0 &= \int \frac{dn_k(t)}{dt}\cdot\exp(ikr)\,d^2k - Dk^2\int n_k(t)\cdot\exp(ikr)\,d^2k \\ 0 &= \int\left[\frac{dn_k(t)}{dt} - Dk^2 n_k(t)\right]\cdot\exp(ikr)\,d^2k \end{aligned} \tag{3.56}$$

For each Fourier component, we obtain this differential equation:

$$\frac{dn_k(t)}{dt} - Dk^2 n_k(t) = 0 \tag{3.57}$$

"From that, we obtain the solution for the time dependence of $n_k(t)$:

$$n_k(t) = n_{0k}\exp\left(-k^2 Dt\right) \tag{3.58}$$

It is evident that for $t = 0$, $n = n_0(x,y,t)$, therefore, $n0_k$ is its Fourier function. For simplicity, we denote $n(x,y,t)$ as $n(r,t)$ and $n(k,t)$ as $n(k_x,k_y,t)$:

$$n_{0k} = \int n_0(r)\exp(-ikr)d^2r \tag{3.59}$$

$$\begin{aligned} \Rightarrow n &= \frac{1}{(2\pi)^2}\int n_0(r')\exp(-k^2Dt)\ \exp(-ik(r-r'))\ d^2r'd^2k \\ &= \frac{1}{(2\pi)^2}\int n_0(r')\left[\int_{-\infty}^{\infty}\exp(-k_x^2Dt)\ \exp(-ik_x(x-x'))\ dk_x\right]\cdots \\ &\quad \left[\int_{-\infty}^{\infty}\exp(-k_y^2Dt)\ \exp(-ik_y(y-y'))\ dk_y\right]d^2r' \\ &= \frac{1}{(2\pi)^2}\int n_0(r')\left[\int_{-\infty}^{\infty}\exp(-k_x^2Dt)\ \cos(k_x(x-x'))\ dk_x\right]\cdots \\ &\quad \left[\int_{-\infty}^{\infty}\exp(-k_y^2Dt)\ \cos(k_y(y-y'))\ dk_y\right]d^2r' \\ &= \frac{1}{(2\pi)^2}\int n_0(r')\left[\sqrt{\frac{\pi}{Dt}}\exp\left(-\frac{(x-x')^2}{4Dt}\right)\right]\left[\sqrt{\frac{\pi}{Dt}}\exp\left(-\frac{(y-y')^2}{4Dt}\right)\right]d^2r' \\ n(x,y,t) &= \frac{1}{4\pi Dt}\int n_0(x',y',t)\exp\left(-\frac{(x-x')^2-(y-y')^2}{4Dt}\right)\ dx'dy' \end{aligned} \tag{3.60}$$

This equation is the solution of the differential equation describing diffusive transport and is valid only for $Dt > 0$, depending on the initial distribution at $t = 0$. In microscopy, a Gaussian distribution can be assumed at the focal point. In reality, this distribution is in an approximation to the Airy function[21] when focusing a laser with a Gaussian beam (transversal Mode $T_{0,0}$) using an overfilled objective, but a Gaussian curve is a very good approximation (see Figure 3.1). For a perfect beam, it is symmetric in x and y, so the width $\sigma_x = \sigma_y$. N_0 represents the total number of excited states.

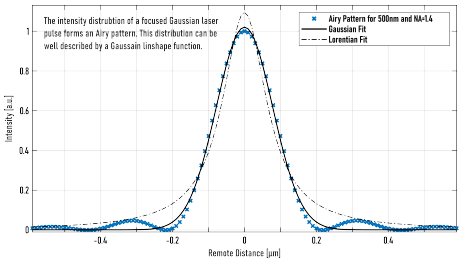

Figure 3.1): A Gaussian fit represents a very good approximation for the actual excitation- and emission point spread function (see also Figure 4.5).

$$n_0(x,y) = N_0 \exp\left(\frac{-x^2-y^2}{2\sigma^2}\right), \quad \text{at } t = 0 \tag{3.61}$$

To provide a complete solution, the integral including the initial condition needs to be solved. It is evident that the integral separates into two independent integrals because x and y are orthogonal and therefore independent of each other. Firstly, the integral is solved for one dimension, and later the solutions will be combined for two dimensions.

$$\begin{aligned} n(x,t) &= \frac{1}{2\sqrt{\pi Dt}} \int N_0 \exp\left(\frac{-x'^2}{2\sigma^2}\right) \exp\left(\frac{(x-x')^2}{4Dt}\right) dx' \\ &= \frac{1}{2\sqrt{\pi Dt}} \int_{-\infty}^{\infty} N_0 \exp\left[-\left(\frac{2\sigma^2+4Dt}{8Dt\sigma^2}\right)x'^2 + \left(\frac{2x}{4Dt}\right)x' - \frac{x^2}{4Dt}\right] dx' \\ &= \frac{N_0}{2\sqrt{\pi Dt}} \sqrt{\frac{8\pi Dt\sigma^2}{2\sigma^2+4Dt}} \exp\left(-\frac{x^2}{2\sigma^2+4Dt}\right) \end{aligned} \tag{3.62}$$

Since the integration extends from $-\infty$ to ∞, mathematically it represents nothing else than a convolution of two Gaussians. From the one-dimensional solution, it leads to the following result:

$$n(x,y,t) = \frac{N_0\ 2\sigma^2}{2\sigma^2+4Dt} \exp\left(\frac{-x^2-y^2}{2\sigma^2+4Dt}\right) \tag{3.63}$$

Since the created species have a finite lifetime, it is important to extend the description with an additional decay term. An analytic solution is possible as long as this term is proportional to n. This holds true for the decay of an exciton or a monomolecular recombination process.

$$\frac{\partial n(x,y,t)}{\partial t} = D \cdot \Delta n(x,y,t) - k \cdot n(x,y,t) \tag{3.64}$$

The solution of this differential equation is given by the equation 3.63 multiplied by an exponential decay function:

$$n(x,y,t) = \frac{N_0\ 2\sigma^2}{2\sigma^2+4Dt} \exp\left(\frac{-x^2-y^2}{2\sigma^2+4Dt}\right) \cdot \exp\left(-kt\right) \tag{3.65}$$

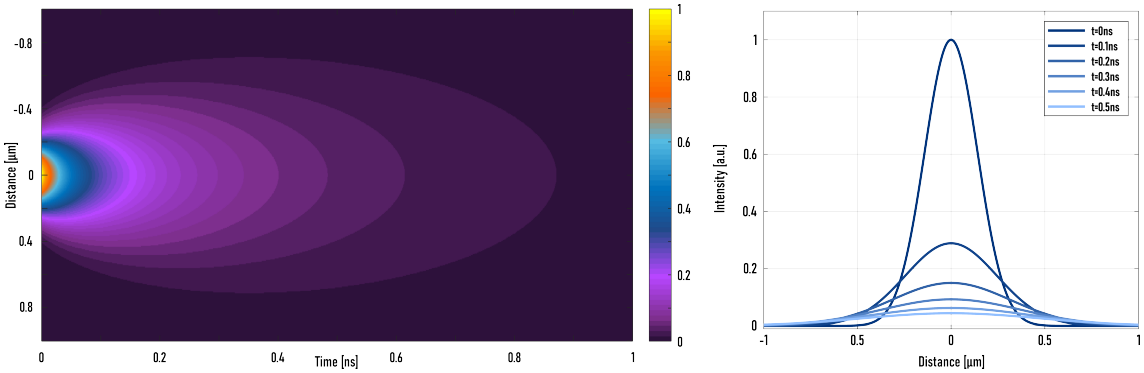

Figure 3.2): Illustration of the density of excited states for 2D diffusive transport after diffraction-limited excitation, where the state density equals to the density of excited states (with $D = 0.1\mu m/ns$) incorporating a final lifetime of $\tau = 0.7ns$. The analytical solution presented above is utilized for the calculation.

This formula represents the solution for diffusive transport in two dimensions. It is important to note that this solution may vary depending on the initial distribution. Furthermore, the width of the distribution changes linearly with time, given by:

$$\sigma(t)^2 \sim 2Dt \tag{3.66}$$

This simple equation allows for extracting the diffusion coefficient D from the change in width of a Gaussian curve at each time step. This applies to a simple mono-exponential decay or monomolecular process where the excited state has only one channel to return to the original state. If higher-order terms need to be included, such as in a bimolecular decay process where the excited states have several parallel decay channels, the differential equation becomes nonlinear.

$$\frac{dn}{dt} = -D\frac{\partial^2 n}{\partial t^2} - k_1 n(t) - k_2 n(t)^2 \tag{3.67}$$

These higher-order decay terms become significant with high-power excitation. The intensity response to excitation power can be characterized by a power series, where most measurements are conducted in the linear regime to avoid nonlinear effects. For this differential equation, no analytical solution can be found, and computation becomes more challenging. It is important to note that k_2 can also be time-dependent, and the system remains in thermal equilibrium, neglecting a thermal gradient. However, if the temperature gradient increases, this term cannot longer be neglected, diffusive transport will depend on the heat flux.

3.3 Diffusion in the Limit of out-of thermal Equilibrium

Let us consider the scenario where excited states are out of thermal equilibrium and internal heat affects diffusive transport. As discussed earlier, these two equations connect

the change in chemical potential with the heat flux[17]:

$$\begin{aligned} \frac{\partial c}{\partial t} &= D\left[\Delta c + \frac{k_T}{T}\Delta T\right] \\ \frac{\partial T}{\partial t} &= \chi \Delta T + \frac{k_T}{c_p}\left(\frac{\partial \mu}{\partial c}\right)_{p,T}\frac{\partial c}{\partial t} \end{aligned}$$

Due to the strong focusing of laser light, high energy densities are expected at the excitation spot, leading to localized heating. This heat can be distributed to the phonon bath of the crystal or to the excited states themselves. Both reservoirs may reach different temperatures after high laser excitation, a scenario known as the two-temperature model. If the excited states attain a significantly higher temperature, internal heat flux can influence diffusive transport. Another possibility is a heated phonon bath, which efficiently transfers heat to the excited states, often observed shortly after excitation on a femtosecond timescale. If the heat persists much longer in the system compared to the lifetime of excited states, these effects become apparent.

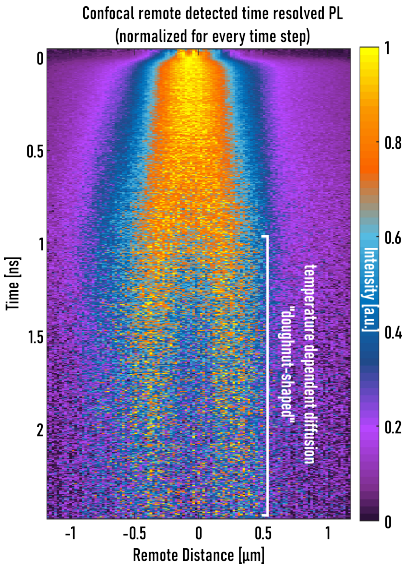

Figure 3.3): At high excitation densities, remote detected time resolved PL data of $MoSe_2$ reveals the halo effect.

Interpreting these two equations, the dynamics of heat dissipation and diffusive transport show similarities. Heat dissipation is governed by the heat conductivity χ , while transport is governed by the diffusion coefficient D. Additionally, two additional terms emerge that connect both dynamics, indicating their interaction. Initially, with two Gaussian distributions at time zero, excited states later form a halo shape around the Gaussian heat distribution. We observed such an effect in a monolayer of $MoSe_2$. This effect has been documented in literature for transition metal dichalcogenides (TMDCs)[22, 23]. It is noted that TMDCs exhibit a halo effect in diffusion due to coupling with a hot optical phonon bath. None of the other semiconductors investigated in this work showed this effect.

3.4 Numerical Implementation of Diffusion

Another approach to model a diffusive process via numerical methods is needed when the initial distribution is not a Gaussian function but another type of function. In such cases, the integral from equation 3.59 may not yield an analytical solution. The idea is to compute the differential equation 3.64 by solving the change in excited states for each time step. This requires calculating the first derivation in time and the second derivation in space of the discrete density function $\boldsymbol{u}(t_i, x_i)$. Since numerical data is discrete, the derivation assumes linearity between pixels, with the spacing of data points small compared to changes in slope. Inserting the mathematical definition of a slope for a finite distance between two points.

$$\frac{\partial u(t_n, x_i)}{\partial t} = \frac{u_i^{n+1} - u_i^n}{\Delta t} \tag{3.68}$$

Here the indices's $i, n \in \mathbb{N}$ denote the enumeration for each entry in the digital array in time t_n and space x_i. The difference between two time steps is Δt. Furthermore, the second derivation in space can be written as:

$$\begin{aligned} \frac{\partial^2 u(t_n, x_i)}{\partial x^2} &= \frac{\frac{u_{i-1}^n - u_i^n}{\Delta x} - \frac{u_i^n - u_{i+1}^n}{\Delta x}}{\Delta x} \\ &= \frac{u_{i-1}^n - 2u_i^n + u_{i+1}^n}{\Delta x^2} \end{aligned} \tag{3.69}$$

Δx represents the difference between two array points along the space coordinate.

1D Diffusion Now, let us introduce diffusion in one dimension using the Crank-Nicolson method[24, 25]. This algorithm is known for its stability and accurate convergence to the solution. It calculates the solution backward in time and averages the second derivation in space over both time steps, making it particularly robust with respect to point distances. Additionally, a secondary decay term is subtracted, involving the excited state's lifetime τ. Instead of using τ, a rate k, which is the inverse of the lifetime, is employed. The time average is also utilized here. In general, averaging over both time steps enhances the stability and convergence of the algorithm.

$$\frac{u_i^{n+1} - u_i^n}{\Delta t} = D\frac{(u_{i+1}^{n+1} - 2u_i^{n+1} + u_{i-1}^{n+1}) + (u_{i+1}^n - 2u_i^n + u_{i-1}^n)}{2\Delta x^2} - k \cdot \frac{u_i^{n+1} + u_i^n}{2} \tag{3.70}$$

This formula represents the known differential equation for diffusion. After separating the terms of the time step $n+1$ and n:

$$\begin{aligned} (1 + 2\alpha + \frac{k\Delta t}{2})u_i^{n+1} - \alpha u_{i+1}^{n+1} - \alpha u_{i-1}^{n+1} &= (1 - 2\alpha - \frac{k\Delta t}{2})u_i^n + \alpha u_{i+1}^n + \alpha u_{i-1}^n, \\ \text{with the term } \alpha &= \frac{D\Delta t}{2\Delta x^2} \end{aligned} \tag{3.71}$$

This is a linear equation system, which can be rewritten into matrix form.

$$A\boldsymbol{u^{n+1}} = B\boldsymbol{u^n} \tag{3.72}$$

Here, as an example, the matrix looks like this for one side with the corresponding vector:

$$A\boldsymbol{u^{n+1}} = \begin{pmatrix} 1 + 2\alpha + \frac{k\Delta t}{2} & \alpha & 0 & \cdots & 0 & 0 & 0 \\ \alpha & 1 + 2\alpha + \frac{k\Delta t}{2} & \alpha & \cdots & 0 & 0 & 0 \\ \vdots & \vdots & \vdots & \ddots & \vdots & \vdots & \vdots \\ 0 & 0 & 0 & \cdots & \alpha & 1 + 2\alpha + \frac{k\Delta t}{2} & \alpha \\ 0 & 0 & 0 & \cdots & 0 & \alpha & 1 + 2\alpha + \frac{k\Delta t}{2} \end{pmatrix} \begin{pmatrix} u_1^{n+1} \\ u_2^{n+1} \\ \vdots \\ u_i - 1^{n+1} \\ u_i^{n+1} \end{pmatrix}$$

The unknown vector $\boldsymbol{u^{n+1}}$ can be calculated by reforming equation 3.72. It corresponds to a trivial solving of a linear equation system, which is straightforward for most programming languages.

$$\boldsymbol{u^{n+1}} = B\boldsymbol{u^n}/A \tag{3.73}$$

Finally, the resulting vector u^{n+1} provides the solution for the next time step. For every new time step, the method needs to be repeated. This is the implementation for the 1D

diffusion problem.

2D Diffusion Since the solution for a 1D diffusion transport is different from the 2-dimensional process, the numerical differential equation has to be extended in x and y direction[26, 27].

$$\begin{aligned}\frac{u_{i,j}^{n+1}-u_{i,j}^{n}}{\Delta t} &= -D\frac{(u_{i+1,j}^{n+1}-2u_{i,j}^{n+1}+u_{i-1,j}^{n+1})+(u_{i+1,j}^{n}-2u_{i,j}^{n}+u_{i-1,j}^{n})}{2\Delta x^2}\cdots \\ &\quad -D\frac{(u_{i,j+1}^{n+1}-2u_{i,j}^{n+1}+u_{i,j-1}^{n+1})+(u_{i,j+1}^{n}-2u_{i,j}^{n}+u_{i,j-1}^{n})}{2\Delta y^2}\cdots \\ &\quad -k\cdot\frac{u_{i,j}^{n+1}+u_{i,j}^{n}}{2} \end{aligned} \tag{3.74}$$

Here we make now the assumption that both derivations directions (x, y) are independent of each other. The change in x-direction has no effect on the y-direction, which stays constant. Therefore, it is possible to solve the matrices for the two dircetions independently. The trick is to have an intermediate time step at 1/2:

$$\begin{aligned}\boldsymbol{u^{n+1/2}}A\Big|_{y=const} &= B\boldsymbol{u^{n}}|_{x=const} \\ \boldsymbol{u^{n+1}}A\big|_{x=const} &= B\boldsymbol{u^{n+1/2}}\Big|_{y=const}\end{aligned} \tag{3.75}$$

This alternating system results in the following linear system of equations:

$$\begin{aligned}(1+2\alpha)u_{i,j}^{n+1/2}-\alpha u_{i+1,j}^{n+1/2}-\alpha u_{i-1,j}^{n+1/2} &= (1-2\beta)u_{i,j}^{n}+\beta u_{i,j+1}^{n}+\beta u_{i,j-1}^{n}, \\ (1+2\alpha+\frac{k\Delta t}{2})u_{i,j}^{n+1}-\alpha u_{i,j+1}^{n+1}-\alpha u_{i,j-1}^{n+1} &= (1-2\beta-\frac{k\Delta t}{2})u_{i,j}^{n}+\beta u_{i+1,j}^{n}+\beta u_{i-1,j}^{n}, \\ \text{with the terms} \qquad \alpha=\frac{D\Delta t}{2\Delta x^2}, &\quad \beta=\frac{D\Delta t}{2\Delta y^2}\end{aligned} \tag{3.76}$$

Here, the decay term appears only once, since it represents a change in time that is independent of the x-y direction. With this numerical approach, it is now possible to compute a 2D diffusion problem for any initial distribution of excited states.

3.5 Diffusion within the confocal spot- Annihilation of Excited States

In some cases, the diffusion of excited states is limited to their immediate surroundings, resulting in no observable spatial broadening of the confocal spot. However, in these systems, higher-order processes can appear under high fluence laser excitation. These are quadratic terms in the decay, defined as bimolecular decays. In a monomolecular process[2, 3, 4] with linear decay terms $\sim k_1 n$, the excited states recombine to the same ground state from which they were excited. There is only one possible channel for recombination. In bimolecular decay $\sim k_2 n^2$, a higher density of states and mobility of states are needed. Here, the excited states have many possible states with which they can recombine. This means that recombination is no longer localized. All the excited states are mobile and can interact with each other. This can result in either the annihilation

of excited states or a moving state recombining at a different local point. This mobility can also be described by diffusive transport. Since it is strongly dependent on the density of states, the diffusion constant is expected to be time and geometry dependent. If this process stays within the focal point, no broadening is expected either. Let us consider the rate equation:

$$\frac{dn}{dt} = -k_1 n(t) - k_2 n(t)^2 \tag{3.77}$$

Since k_2 is assumed to be time-independent for simplicity and to enable an analytical solution, we start by substituting it into the rate equation:

$$v = \frac{1}{n}, \qquad \frac{\partial v}{\partial t} = \frac{\partial v}{\partial n}\frac{\partial n}{\partial t} = -n^{-2}\frac{\partial n}{\partial t}$$

Now the formulas are rearranged, and the substitution is set in:

$$\begin{aligned} \frac{\partial n}{\partial t} n^{-2} + k_1 n^{-1} &= -k_2 \\ \Rightarrow -\frac{\partial v}{\partial t} + k_1 n^{-1} &= -k_2 \end{aligned}$$

Now let us use the following ansatz:

$$\begin{aligned} \exp\left(\int_0^t -k_1 dt'\right) &= \exp\left(\left[-k_1 t'\right]_0^t\right) \\ &= \exp\left(-k_1 t\right) \end{aligned}$$

This function is now multiplied to every term, and afterward the whole equation is integrated over time

$$\begin{aligned} \frac{\partial v}{\partial t}\exp\left(-k_1 t\right) - k_1 v \exp\left(-k_1 t\right) &= k_2 \exp\left(-k_1 t\right) \\ \frac{\partial}{\partial t}\left(\exp\left(-k_1 t\right)\cdot v\right) &= k_2 \exp\left(-k_1 t\right) \\ \exp\left(-k_1 t\right)\cdot v &= \int_0^t k_2 \exp\left(-k_1 t^*\right) dt^* \\ \exp\left(-k_1 t\right)\cdot v &= k_2\left(-\frac{1}{k_1}\exp\left(-k_1 t\right) + C\right) \end{aligned}$$

$$\begin{aligned} v &= -\frac{k_2}{k_1} + \frac{k_2}{k_1}\cdot C \cdot \exp\left(k_1 t\right) \\ \text{Resubstitution } \Rightarrow n(t) &= \frac{1}{-\frac{k_2}{k_1} + k_2 \cdot C \cdot \exp\left(-k_1 t\right)} \end{aligned} \tag{3.78}$$

The last step from C is a constant that arises from the integration and can be determined by the initial number of excited states at time zero, $n(t=0) = n_0$

$$\begin{aligned} C &= \frac{1}{k_2 n_0} + \frac{1}{k_1} \\ \Rightarrow n(t) &= \frac{1}{-\frac{k_2}{k_1} + \frac{1}{n_0}\left(1 + \frac{k_2}{k_1}\cdot n_0\right)\exp(k_1 t)} \end{aligned} \tag{3.79}$$

This is the analytical solution for the decay processes up to second-order terms. The solution shows that higher-order recombinations appear in the earlier times. For later times $t \to \infty$, the exponential terms dominate, and therefore the function converges to a simple exponential decay $n(t) \sim \exp(-k_1 t)$. Consequently, the rate k_1 can be determined from later times in the transients. Afterwards, it is possible to fit the whole dataset, setting k_1 constant to obtain n_0 and k_2. Since this function is not continuous at zero, a numerical convolution with an instrument response function makes the fit very unstable.

3.6 Connection of Mobility and Diffusion

In general, excited charges in a semiconductor can also move due to an applied electrical field. This is also valid for ions or other charges moving in a lattice. As long as the forces of internal friction balance the external force, the charge will accelerate to a constant drift velocity,$\boldsymbol{v}$. This results in a linear relationship between the electrical field $\boldsymbol{E}$ and drift speed, connected by the mobility b[28].

$$\boldsymbol{v} = b \cdot \boldsymbol{E} \tag{3.80}$$

$$= \frac{b}{q} \cdot \boldsymbol{F_{el}} \tag{3.81}$$

We can replace the electrical field with the electrical force $\boldsymbol{F_{el}} = q\boldsymbol{E}$, which acts on charged particles with charge q. This can also include shielding effects, resulting in an effective charge. Now, we want to connect the diffusion coefficient D with the mobility b. Let us recall the flux of diffusion, adding an additional term representing the force on charged particles[17, 28]:

$$\boldsymbol{i} = -\rho D \nabla c + \rho c \frac{b}{Ze} \boldsymbol{F_{el}} \tag{3.82}$$

In thermodynamic equilibrium, the flux $\boldsymbol{i} = 0$ vanishes. Moreover, the concentration in an external field $\boldsymbol{F}_{ext} = -\nabla U$ is given according to Boltzmann's distribution:

$$c = C_{const} \cdot \exp\left(\frac{U}{k_B T}\right) \tag{3.83}$$

$$\Rightarrow \quad \nabla c = \frac{\boldsymbol{F}_{ext}}{k_B T} c \tag{3.84}$$

U is the potential energy caused by the applied external field, which is the electrical field ($\boldsymbol{F}_{ext} = \boldsymbol{F_{el}}$). Substituting everything, we end up with the Einstein-Smoluchowski relation:

$$D = \frac{b \cdot k_B T}{q} \tag{3.85}$$

This relation connects the diffusion coefficient with mobility. Since shielding effects of the excitations in the crystal lattice are unknown and it is unclear how many of them contribute to the mobility, calculating the mobility b from the measured diffusion coefficient D is only a rough estimation. However, assuming these additional shielding effects are thermally independent, this relation can help determine a thermal trend of the mobility. For precise absolute numbers, different experiments involving the application of external forces to the sample would be necessary, but this is not further discussed in this work.

4 Confocal Microscopy

In our world, the nanoscale plays a crucial role because many physical phenomena occur at these length scales, especially in addressing challenges related to generating energy from renewable and sustainable sources. At the forefront of these efforts are new photoactive materials that interact with light to convert energy. How can we describe this interaction? What mechanisms are at play? To answer these questions, we utilize optical microscopes in various configurations. While they do not provide the full resolution of the entire nanoworld, they offer sufficient capabilities to study several phenomena. With the combination of time resolution and cryogenic temperatures, microscopic investigations reveal the beauty of the nanoscale. To distinguish the measured signals reflecting the properties of the investigated materials, it is essential to understand the signal generation and technical details of the measuring apparatus. The following chapter will provide a brief introduction to confocal microscopy.

4.1 Setup

All presented measurements are based on microscopic techniques combined with a laser. Depending on the specific question, different lasers are implemented. Before delving into the details of the different measurement techniques, let's introduce the setup. Two different microscopes sharing the same detection arm are used. One is combined with a closed-cycle helium-4 cryostat, allowing the sample to be cooled to around 4.5 to $4.7K$, depending on the season and laboratory conditions. A cold plate in ultra-high vacuum cools down to $3.8K$. The sample holder sits on a stack of stick-slip positioners and scanners based on piezoceramics. The scanning range is $30\mu m$ at $5K$ and $50\mu m$ at room temperature, with positioners reaching several millimeters in all three directions. Additionally, it is connected via a gold-coated metal contact. Inside the sample holder, a temperature sensor and heater are integrated to control the temperature range from 4.7 to $300K$. This setup is a commercial product from Attocube (AttoDry 800), with all optics built by ourselves. We use a Nikon objective with a numerical aperture (NA) of 0.75 and an ultra-long working distance of 4 mm to accommodate the distance between two windows in the cryogenic system: one from the vacuum chamber and the other from an additional heat shield that prevents thermal radiation from entering. Maintaining approximately equal distances between the sample and window, and the objective and window, is crucial to ensuring both windows are in the middle. Otherwise, the focus may be disrupted or the image blurred due to the higher refractive index of the glass windows in the confocal setup. These two windows also prevent clear wide-field imaging of the sample due to reflections on the glass surfaces. One approach is to use a highly reflective surface on the sample and replace the objective with a low-NA objective with a large back aperture (e.g., NA=0.2), combined with white light coupled into the system. This provides an image that outlines the area of interest. Subsequently, detailed scans using the positioners are necessary to relocate the exact position with the original objective. A map of the sample recorded by another light microscope is essential. This approach was used with a sample of exfoliated hexagonal boron nitride (hBN) on a silicon substrate. It's also important to note that the

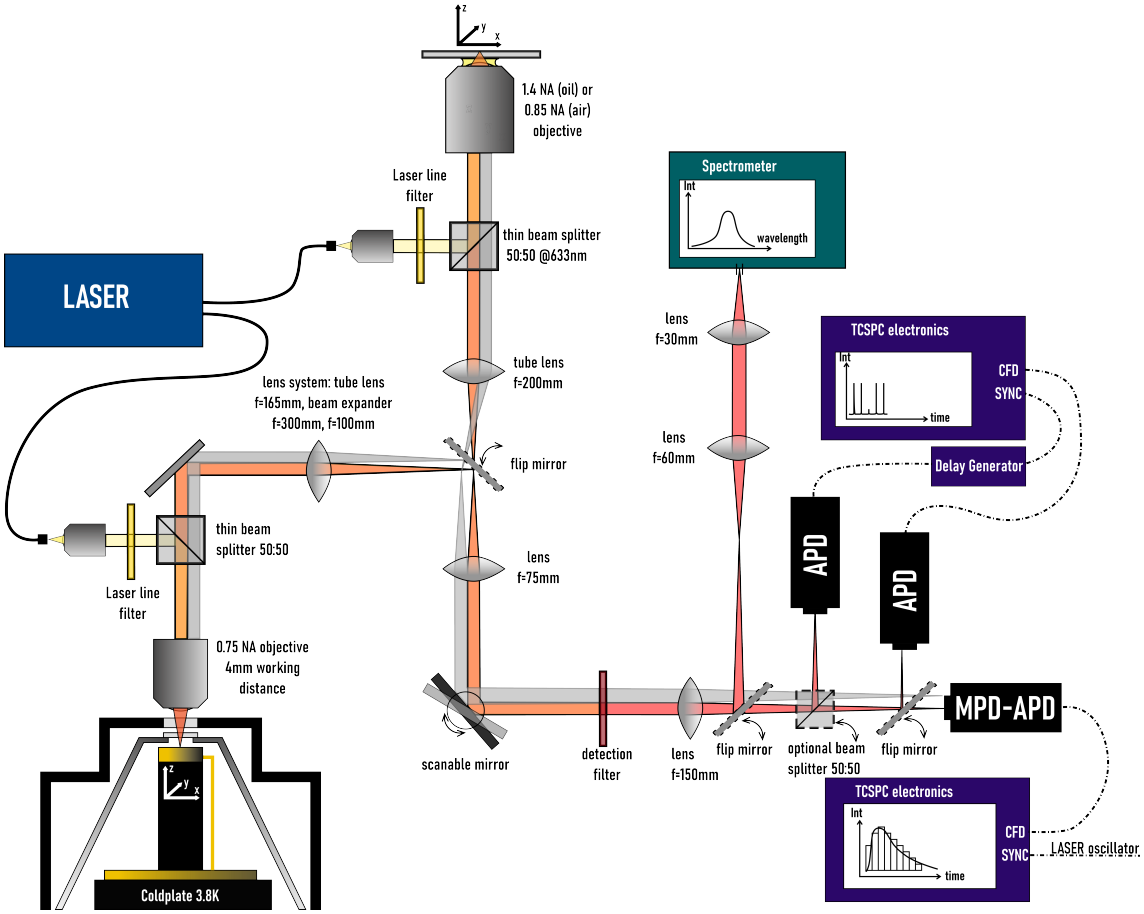

Figure 4.1): The sketch shows all components implemented in the microscopic system used for the measurements.

sample requires vacuum grease at low temperatures to ensure better thermal contact with the cooled sample holder. The second microscope operates only at room temperature. An advantage here is the use of oil immersion objectives, which have a larger numerical aperture (NA), resulting in higher resolution and detection efficiency. Various objectives are employed, ranging from NA 1.4 to 0.85, each suited for different purposes. Both types of microscopes collect signals in the epi-direction, where light generated from the sample is collected using the same microscope objective. In the detection beam path, the collected light undergoes filtering to eliminate reflected laser light. The microscope setup is based on a Nikon microscope body combined with a closed-loop piezo stage. This stage allows for a range of $100\mu m$ in both the x and y directions, and $20\mu m$ in the z-direction. Obtaining wide-field images from the sample is easier here, as the sample can be illuminated from above or via laser line input for non-transparent samples. The entire setup can be observed through an eyepiece. In both microscopes, a beam splitter is installed behind the objective. Several options are available. Cube beam splitters are often polarization-independent for both s- and p-polarized light. This is important for maintaining laser polarization during excitation and for observing the polarized emission from the sample. However, cube beam splitters have disadvantages: they may introduce additional reflections due to their cube surfaces, leading to distortion in wide-field images. Alternatively, thin glass beam splitters can be used where polarization components are reflected and transmitted differently. In both setups, thin beam splitters offer better

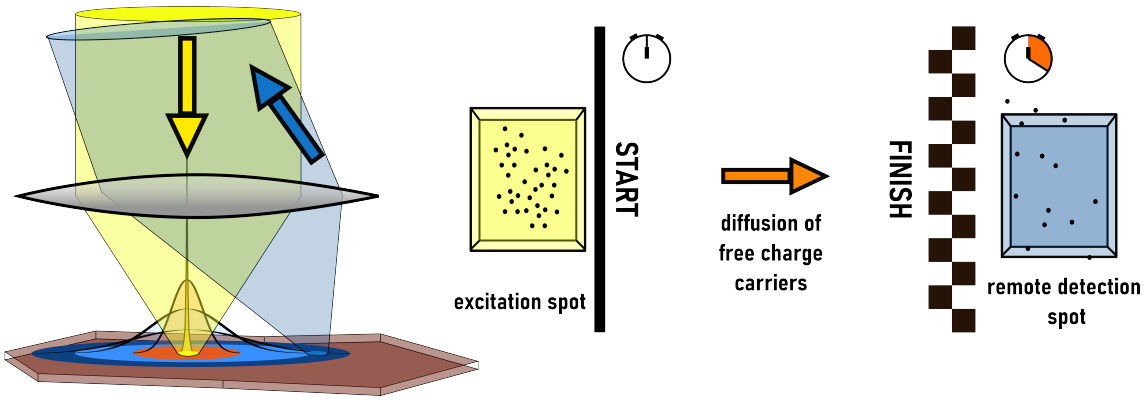

Figure 4.2): The idea of the remote detected time resolved PL measurements is to fix the laser excitation spot while detecting the PL light from a remote position using a tiltable mirror in the detection line. This setup, combined with TCSPC electronics, allows for the observation of diffusing excited states.

imaging properties. A classical confocal microscope typically includes a pinhole in the image plane to filter out additional signals outside the confocal spot. However, when measuring single molecules in solution, enhancing contrast is necessary. For solid thin film samples, the focus is directly on the sample ensuring emitters are generated within the confocal spot and not around it. Therefore, using an aperture would block signals from diffuse emitters surrounding the excitation spot.

4.1.1 Using Scanning Mirror

The key feature of the detection beam line is the scan mirror, mounted on a piezo stage that tilts the mirror. Positioned in a plane conjugate to the back focal plane after the tube lens and an additional lens, all rays from the same angular direction are focused onto a single point. Consequently, the scanned image remains undisturbed while tilting. However, the 90° angle between the incoming and reflected beams causes distortion in the remotely detected image. By scanning a periodic structure, corrections for rotation and squeezing can be applied. Both microscopes have slightly different correction mechanisms. The microscope's focal point is imaged onto an avalanche photodiode (APD) with an active pixel area of $50x50\mu m^2$. The lenses are configured such that the chip is overfilled by the light spot, with the silicon chip acting as an aperture. This configuration sacrifices some detection efficiency compared to one where the imaged focus is much smaller than the active pixel area, but it ensures reasonable resolution in the remotely detected image. The APD is integrated with time-correlated single photon counting (TCSPC) electronics.

4.1.2 Spectral measurements

In the detection path, a flip mirror directs the signal to a spectrometer for analysis. The spectrometer is equipped with different reflecting blazed gratings: 150 lines/mm, 600 lines/mm, and 1200 lines/mm.

$$\frac{\lambda}{\Delta\lambda} = n \cdot N \tag{4.1}$$

This formula describes the resolution of dispersed light at a grating[29]. λ represents the incoming wavelength, n denotes the distance between the lines on the grating, and N indi-

cates the number of illuminated lines. This formula illustrates that wavelength dispersion is linear, and higher line density (more lines per millimeter) enhances resolution. However, a drawback is the loss of some signal due to light being reflected in different directions from various reflection orders. The incident angle of the incoming beam needs to be greater than 0° , resulting in a dispersion of light into higher reflective orders as well as a strong non-dispersed zeroth-order reflection ray. To reduce signal loss, we use blazed gratings, which have a reduced reflection intensity for the zeroth order and more optical power for the first reflection order. These gratings have an asymmetric triangular sawtooth-like shape in cross section[30]. The distance between the triangles is equal to the line distance n. The internal angle of the triangle, known as the blaze angle, can be chosen so that the incoming ray and the zeroth-order reflected one overlap, depending on the incoming wavelength. All blazed gratings are optimized for a specific wavelength, where they have a reflection intensity maximum, but they also work very efficiently in a surrounding range. This reflection efficiency for different wavelengths needs to be corrected in the measured data. Additionally, the use of blazed gratings simplifies the separation of zeroth- and first-order reflected rays. The dispersed light is projected onto an open electrode Charged Coupled Device (CCD) camera. "Open electrode" refers to front electrodes with larger holes to efficiently absorb incoming light through the depleted silicon layer, enhancing the CCD camera's light detection efficiency. In our specific device, 2-3 absorbed photons are needed to generate one charge. Since it's a CCD, all charges are accumulated and subsequently amplified per pixel. This results in a highly sensitive readout with a maximum of 1 MHz. All recorded spectra are steady-state measurements, meaning they do not provide time-resolved information. To ensure accurate measurements, corrections are made for the reflecting and transmission properties of each optical component between the sample and the CCD camera. Some optical components undergo white light absorption measurements for calibration. The CCD chip is calibrated using a thermal light source with a known spectrum. For the objectives used, all properties are based on data provided by the manufacturer. These calibrated spectra enable correction of the measured Photoluminescence (PL) spectrum in terms of relative intensities, although they do not directly provide the absolute spectral quantum yield of the sample.

4.1.3 Time Correlated Single Photon Counting -TCSPC

Switching to time-resolved measurements, all such measurements employ Avalanche Photodiodes (APDs) combined with Time Correlated Single Photon Counting (TCSPC) electronics. APDs generate an avalanche of charges from a single electron excited by a photon under high voltage. This avalanche is electronically transformed into a digital pulse (e.g., TTL, or NIM in case of the MPDs) for each absorbed photon. However, the signal also includes Poisson noise, known as dark counts, originating from the electronics. Additionally, after measuring one photon, these devices have a dead time of several nanoseconds. A maximum count rate of up to $1MHz$ can be achieved before the APDs' response becomes nonlinear, making detection highly sensitive and capable of measuring single photons. When connected to very fast electronics, each photon receives a time stamp upon arrival. Let us discuss the measurement of time-resolved PL signals first. A TCSPC[31] card has two inputs: a Constant Fraction Discriminator (CFD) channel and a synchronization channel. The laser's oscillator serves as the clock. The CFD channel connects to the APD. To limit the starting rate of the TAC channel and avoid dead time losses due to high laser repetition rates (up to $40MHz$), the operating clock is reversed. This means the incoming photon starts the clock, and the laser oscillator pulse stops it. The measurement principle involves the electronics generating a voltage ramp after the start photon arrives

and stopping it with the TTL pulse from the laser oscillator. The slope of this voltage ramp is proportional to the observed time window. Adjusting the voltage offset allows shifting the time window to correct for different cable lengths between the CFD and sync channel. Further adjustment is possible by elongating the signal cables or adjusting the delay of TTL pulses, taking into account the finite speed at which pulses travel through copper cables. The entire time window is divided into bins, and the measured time of a photon event is sorted into the corresponding bin. All events are summed to create the final transient. It is crucial that the probability of having two photons after a laser pulse is very low due to the detector's dead time, allowing only one photon to be measured per period. Consequently, if the photon count rate is too high, the recorded transients may exhibit nonlinear and disturbed characteristics. In practice, the photon count rate should not exceed 10% of the laser repetition rate. A specially designed timing-stable APD is used to measure these transients. Often, the Instrument Response Function (IRF) of the APD depends on the measured intensity and varies by several picoseconds. Using a timing-stable APD (such as MPD), a robust and reproducible IRF of approximately 25 to 28ps can be achieved, even with much faster laser pulses compared to the intrinsic electronic response. It's important to note that the IRF width can vary with incident wavelength. The most reliable method to evaluate the IRF is to tune the laser to the emission wavelength and record the temporal response. If a laser or light signal isn't available to represent the actual IRF, scattered laser light is recorded and used as an IRF, which is a practical compromise.

4.1.4 Hanbury Brown Twiss Configuration

In a Hanbury Brown Twiss (HBT)[31, 32] configuration, originally devised for enhancing resolution in astronomy, particularly for measuring star distances using radio telescopes, this concept is also highly valuable for studying the quantum mechanical behavior of light. In this setup, an additional beam splitter is introduced along with two Avalanche Photodiodes (APDs). One APD is positioned in the transmitted beam path, while the other is placed in the reflected beam path. The primary objective is to measure the second-order time correlation function $g_2(t)$:

$$g_2(t) = \frac{I(t)I(t+\tau)}{I(t)^2} \tag{4.2}$$

This measurement can distinguish between single photon emitters and emitters that emit photons in bunches. To illustrate this concept, imagine a single molecule situated at the excitation focus. This molecule is restricted to emitting only one photon per absorbed photon. After emitting a photon, it travels through the beam splitter before reaching the Avalanche Photodiodes (APDs). Depending on its path, whether it is reflected or transmitted by the beam splitter, only one APD detects an event due to the presence of a single photon. Consequently, the probability of both APDs registering an event simultaneously at time zero tends toward zero. Conversely, if multiple photons are emitted coincidentally during the decay process, the probability of both detectors clicking simultaneously increases. For events occurring at later or earlier times, the probability of both APDs registering an event is one, because these photons are not correlated. Additionally, when several emitters are present in the focus, depending on photon statistics, this can lead to non-correlated photons and thus distort the g_2 function. Here, two APDs are connected to the sync and CFD channels of the TCSPC electronics. To achieve negative time delays for electronic pulses, a delay generator or longer signal cable can be used on

the sync side. Furthermore, two different APDs with larger active pixel areas and higher sensitivity, rather than focusing solely on timing stability, are used. This approach allows for recording g_2 functions for various possible photon statistics. However, electronic distortions may arise due to cross-connections to counters or other devices, stemming from differences in device impedances.

4.2 Signal Generation

After presenting the setup, this part explains the signal generation of a confocal microscope. First, it discusses the incoming electrical field that excites the emitting dipoles. These dipoles subsequently emit light, which can be collected by the detectors described earlier. This overview aims to clarify the information obtained and its physical significance.

4.2.1 Focus of Laser Beams

Let us take a quick look at the laser focus that excites the sample in the microscope. Depending on the polarization, incoming laser mode, and used numerical aperture (NA), different dipole orientations are excited. The objective can be regarded as a single lens. The beam is focused according to the principles of geometrical optics as follows[21]:

$$h = f sin(\theta) \tag{4.3}$$

In this context, h represents the distance to the optical axis of the incoming rays, θ denotes their divergence angles, and f stands for the focal length of the lens. Before entering the objective, a Gaussian mode is employed as the incoming laser mode, which overfills the back aperture. The incident electrical field E_{inc} can be expressed as:

$$E_{inc} = E_0 \exp\left(-\frac{\left(x_\infty^2 + y_\infty^2\right)}{\omega_0^2}\right) = E_0 \exp\left(-\frac{f^2 sin(\theta)^2}{\omega_0^2}\right) \tag{4.4}$$

Getting to the focal point, the electrical far field E_∞ propagates through the lens system.

$$\boldsymbol{E}_\infty \quad = \quad \left[t^S \left[\boldsymbol{E}_{inc} \cdot \boldsymbol{n}_\phi\right] \boldsymbol{n}_\phi + t^P \left[\boldsymbol{E}_{inc} \cdot \boldsymbol{n}_\rho\right] \boldsymbol{n}_\theta\right] \sqrt{\frac{n_1}{n_2}} (cos\theta)^{\frac{1}{2}} \tag{4.5}$$

Here, t^P, t^S represent the Fresnel coefficients for the transmission of s and p polarized light, respectively[30]. The vectors $\boldsymbol{n}$ denote unit vectors in spherical or cylindrical coordinates. At the focal point, the electrical field is expressed before the lens in cylindrical coordinates (ρ, ϕ, z) and for the focus in spherical coordinates (r, ϕ, θ) for a spherical and aberration-corrected lens. Along the direction of the beam, the energy remains constant. To solve for the electrical field in angular representation at every point, the Fourier transform of E_∞ in x and y, multiplied by a field propagator along z, is calculated. Since this involves integration over k_x andk_y, and considering the spherical symmetry, the coordinates are transformed to ϕ and θ. In the Fourier plane, the directions of the individual rays become visible.

$$\boldsymbol{E}(\rho, \phi, z) = \frac{ikfe^{-ikf}}{2\pi} \int_0^{\Theta_{max}} \int_0^{2\pi} \boldsymbol{E}_\infty(\Theta, \Phi) e^{ikz \ \cos\theta} e^{ik\rho \ \sin\Theta \ \cos(\Phi - \phi)} \ \sin(\Theta) d\Phi d\Theta \tag{4.6}$$

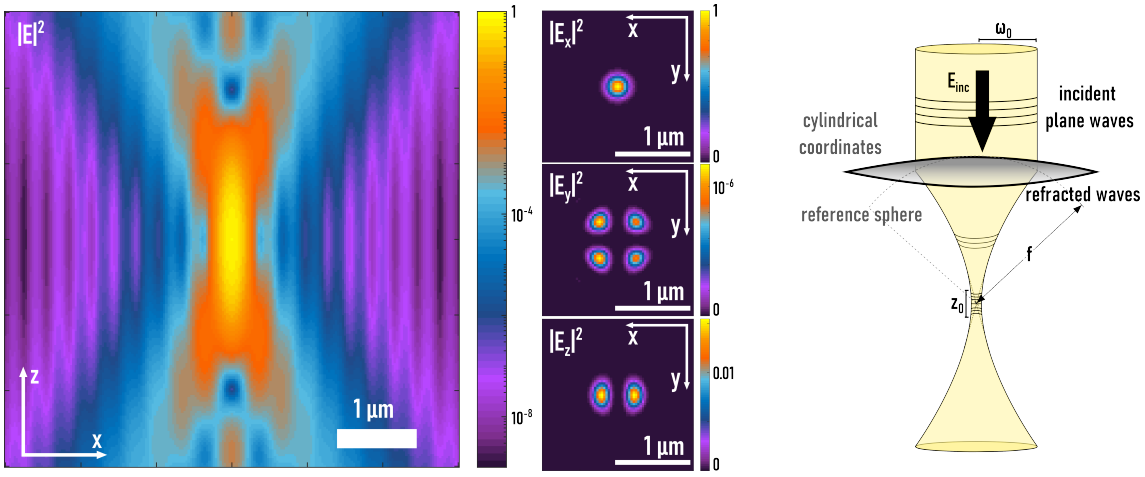

Figure 4.3): Calculated Intensity of a focused laser beam: the electric field is calculated for an objective with a numerical aperture (NA) of 1.4 in a medium with a refractive index n=1.52. The polarization of the incoming light is along the x-axis. The different field components are shown in the focal plane. As expected, the field component in the x-direction is the strongest, but due to strong focusing, field components in the y and z directions also exist. The sketch on the right shows the Rayleigh length and the transition from cylindrical to spherical coordinates used in the calculations.

Using $\boldsymbol{E}_\infty$ with both Fresnel coefficients equal to one, and an electric field polarized solely along the x-axis, results in:

$$\boldsymbol{E}_\infty = E_{inc}(\Theta,\Phi)\frac{1}{2}\begin{bmatrix} (1+\cos\Theta)-(1-\cos\Theta)\cos 2\Phi \\ -(1-\cos\Theta)\sin 2\Phi \\ -2\cos\Phi\sin\Theta \end{bmatrix}\sqrt{\frac{n_1}{n_2}}(\cos\Theta)^{1/2} \tag{4.7}$$

This leads to the following excitation field for a Gaussian mode as incoming field $\boldsymbol{E}_{inc}$:

$$\boldsymbol{E}(\rho,\phi,z) = \frac{ikf}{2}\sqrt{\frac{n_1}{n_2}}E_0\exp(-ikf)\begin{bmatrix} I_{00}+I_{02}\cos(2\phi) \\ I_{02}\sin(2\phi) \\ -2iI_{01}\cos(\phi) \end{bmatrix} \tag{4.8}$$

Here, the Is represent integrals, which can be found in the book 'Principles of Nanooptics' (Novotny et al.)[21]. These integrals involve Bessel functions, and since no analytical functions describe a focused electrical field, these integrals must be computed for every point in space. The resulting electrical field is depicted in Figure 4.3. Here, the focus is illustrated in a homogeneous medium with a single refractive index. The calculation can be extended to include changes in refractive index at different interfaces. This would yield focal patterns of scattered laser light at surfaces. Furthermore, incorporating the detailed interference of transmitted and reflected electrical fields becomes crucial in understanding the signal formation in scattering measurements. Since all the measured light here originates from photoluminescence (PL) emission, observing the field distribution from the focusing medium is sufficient to understand how it excites the emitting dipoles after excitation. The distribution and orientation of emitting dipoles are determined by the sample's symmetry and the polarization of the incoming light. As seen in Figure 4.3, the electrical field extends in the z-direction with little change over a distance known as the

Rayleigh length z_0. ω_0 represents the beam radius:

$$z_0 = \frac{k\omega_0^2}{2} \tag{4.9}$$

Within this length, the excitation can be assumed to remain uniform. For strongly focusing microscope objectives, the Rayleigh length is typically on the order of a few micrometers.

4.2.2 Dipole emission

Let us discuss the signal generation of a confocal microscope. Imagine we have an emitting dipole located on a surface with a higher refractive index than air, such as glass. The substrate is thin, transparent, and used in conjunction with an oil immersion objective. Because the oil, substrate, and the final lens of the objective share the same refractive index, this sets up a classical electrodynamical scenario of a dipole emitting light at the interface between two different dielectric media. The fundamental concept here is that the emission originates from a dipole, which radiates light. This holds true whether we are considering a single molecule, a quantum dot, or an array of dipoles in the case of 2-dimensional materials or thin crystalline films. For coherent signals like scattering or second harmonic generation, the electric fields interfere. However, for fluorescent or photoluminescent dipoles, the intensities add up in the observed signal because the emissions from each dipole are not coherent with each other. The electric field generated by radiative dipoles can be theoretically calculated using the Green's function approach. However, specific electrodynamical details are not elaborated here.

$$\boldsymbol{E}(\boldsymbol{r}) = \omega^2 \mu_1 \mu_2 \overleftrightarrow{\boldsymbol{G}}(\boldsymbol{r}, \boldsymbol{r_0}) \boldsymbol{\mu} \tag{4.10}$$

In the literature[21, 33, 34, 35], a solution in spherical coordinates describes the propagation of the electric field into the dielectric medium from a radiating dipole positioned on its surface. To comprehend the measured signal, visualizing the intensity and its direction is crucial. This visualization is akin to observing the back focal plane of a radiative dipole. The direction of electromagnetic energy in an electromagnetic field is defined by the Pointing Vector:

$$\langle \boldsymbol{S} \rangle = \frac{1}{2}\, Re\left[\boldsymbol{E} \times \boldsymbol{H}^*\right] = \frac{1}{2}\sqrt{\frac{\epsilon_1 \epsilon_2}{\mu_1 \mu_2}} \boldsymbol{E}\boldsymbol{E}^* \hat{\boldsymbol{n}}_r \tag{4.11}$$

Therefore, the measured intensity for the radiation pattern is given by:

$$I(r, \phi, \theta, \boldsymbol{\Phi}, \boldsymbol{\Theta}) \sim \frac{1}{cos(\theta)} \left[\boldsymbol{E_p}\boldsymbol{E_p^*} + \boldsymbol{E_s}\boldsymbol{E_s^*}\right] \tag{4.12}$$

The parameters r, ϕ, θ represent the spherical coordinates: radius, polar angle, and azimuthal angle, respectively. $\boldsymbol{\Phi}, \boldsymbol{\Theta}$ denote the angles of the dipole orientation on the surface as illustrated in figure4.4 . The azimuthal angles θ_1 and θ_2 are related through Snell's law for refraction.

$$\frac{\sin(\theta_1)}{\sin(\theta_2)} = \frac{n_2}{n_1} \tag{4.13}$$

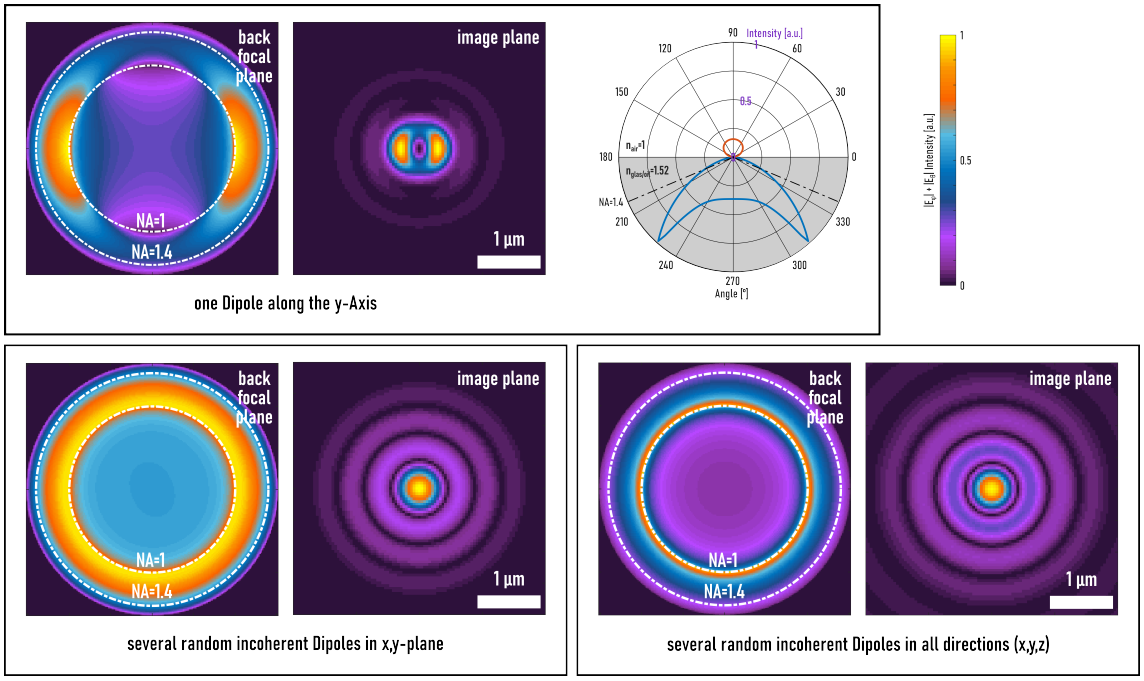

Figure 4.4): Different radiation patterns for several scenarios are calculated. For a single dipole emission, its orientation is clearly seen. When there are several incoherent randomly oriented in-plane or in-and-out-of-plane dipoles, the orientation is not visible. However, due to the refractive index differences, from air (n=1) to glass (n=1.52), the main energy is radiated towards the substrate in represented angles higher than NA = 1. This explains that using high NA objectives in the epi-direction is an optimal setting for our microscopic system regarding photon collection efficiency and resolution.

For calculating the electrical field, the solution in spherical coordinates is required. The exact derivative can be found in the literature[21]:

$$
\begin{aligned}
\boldsymbol{E} = \begin{bmatrix} E_p \\ E_s \end{bmatrix} &= \frac{\pi n_1^2}{\lambda^2 \epsilon_0 \epsilon_1} \frac{|\mu| \exp\left(i \frac{2\pi n_2}{\lambda} r\right)}{r} \begin{bmatrix} c_1 \cos(\boldsymbol{\Theta}) \sin(\theta_2) + c2 \sin(\boldsymbol{\Theta}) \cos(\theta_2) \cos(\phi - \boldsymbol{\Phi}) \\ c_3 \sin(\theta_2) \sin(\phi - \boldsymbol{\Phi}) \end{bmatrix} \\
c_1 &= \left(\frac{n_2}{n_1}\right)^2 \cdot \frac{\cos(\theta_2)}{\cos(\theta_1)} \cdot \hat{t}_p \cdot \boldsymbol{\Pi} \\
c_2 &= \frac{n2}{n_1} \cdot \hat{t}_p \cdot \boldsymbol{\Pi} \\
c_3 &= -\frac{n2}{n_1} \cdot \frac{\cos(\theta_2)}{\cos(\theta_1)} \cdot \hat{t}_s \cdot \boldsymbol{\Pi}
\end{aligned} \tag{4.14}
$$

This electrical field can be used to calculate the radiation pattern that can be observed in the back focal plane. Here, $\hat{t}_s$ and $\hat{t}_p$ are the Fresnel coefficients for transmission in a dielectric medium.

$$
\begin{aligned}
\hat{t}_p &= \frac{2 n_1 \cos(\theta_1)}{n_1 \cos(\theta_2) + n_2 \cos(\theta_1)} \\
\hat{t}_s &= \frac{2 n_1 \cos(\theta_1)}{n_1 \cos(\theta_1) + n_2 \cos(\theta_2)}
\end{aligned} \tag{4.15}
$$

Additionally, a propagating phase is needed if the emitting dipole is not exactly at the origin of the coordinate system. This phase is valid if the spatial extent of the emitter is small enough compared to the distance r.

$$\mathbf{\Pi} = \exp\left(i\frac{2\pi n_1}{\lambda}\left(x_0\sin(\theta_1)\cos(\phi) + y_0\sin(\theta_1)\sin(\phi) + z_0\cos(\theta_1)\right)\right) \tag{4.16}$$

With all these formulas[21, 33], it is possible to calculate different radiation patterns depending on the sample's emission characteristics. The most important result is that dipole emission mainly occurs into the optically denser medium. Furthermore, a significant portion of the emission is directed towards critical angles. This explains why the epi-direction is much more efficient and high NA objectives are needed. They enhance resolution and also increase detection efficiency. Since samples often have a low quantum yield and fewer emitting centers, this setup provides a means to observe these emitters. When combined with an APD, single photons can be measured and observed.

4.2.3 Resolution

From the paragraphs above, it is necessary to first calculate the excitation laser field $\boldsymbol{E}_{exc}$. This excitation field induces emitting dipoles $\boldsymbol{\mu}$, with orientations corresponding to the polarizability tensor $\overleftrightarrow{\alpha}$. This tensor depends on the symmetry of the crystal or molecular structure and the absorption properties[21].

$$\boldsymbol{\mu}_n(\omega) = \overleftrightarrow{\alpha}\boldsymbol{E}_{exc}(\boldsymbol{r}_n, \omega) \tag{4.17}$$

This emitted field generates a new electrical field, which can be measured as an intensity.

$$\boldsymbol{E}(\boldsymbol{r}) = \frac{\omega^2}{\epsilon_0 c^2}\overleftrightarrow{G}_{PSF}\boldsymbol{\mu}_n \tag{4.18}$$

In confocal microscopy, the emission from a dipole appears to originate from a single point where the incident laser light is focused. The tightly focused or localized electrical field extends spatially due to wave nature limitations in focusing. The intensity $I \sim |\boldsymbol{E}|^2$ is measurable and proportional to the power density. This characteristic is known as the point spread function (PSF), which determines the resolution capability. The signal PSF depends on both the excitation and the response and is the convolution of both:

$$I_{Total} \sim I_{excitation\ PSF} \times I_{emission\ PSF} \tag{4.19}$$

Here, assuming a perfect setup, any limitations in the setup will affect the PSF accordingly. For an emitting dipole aligned along the x-axis, the intensity profile along x is as follows:

$$\lim_{\theta_{max}\ll\pi/2} |\boldsymbol{E}(x, y, z = 0)|^2 \sim \left[2 \cdot \frac{J_1\left(\frac{2\pi\ \mathrm{NA}\rho}{M\lambda}\right)}{\left(\frac{2\pi\ \mathrm{NA}\rho}{M\lambda}\right)}\right]^2 \tag{4.20}$$

This formula is derived from the integral $\tilde{I}_{00}$. Other terms in this approximation can be neglected due to the small angles involved. The result remains accurate for calculating the PSF even with high NA objectives. The resulting function is known as the Airy function.

Its radius is:

$$\Delta x = 0.6098 \frac{M\lambda}{\mathrm{NA}} \tag{4.21}$$

It represents the first zero-crossing of the function. With a magnification $M = 1$, it precisely defines the resolution limit as given by Rayleigh. In this scenario, for instance, when an effective in-plane dipole emits incoherently and independently from the excitation light, this criterion overlaps two Airy functions in space. If one function reaches its maximum precisely at the zero-crossing of the other, this marks the closest possible position to distinguish both points. This criterion is one of many definitions of resolution. It is evident that changing the excitation mode and the response PSF can lead to completely different intensity patterns, necessitating a separate discussion. Additionally, in the case of a scattering signal, where incoming and outgoing rays interfere, it introduces a different aspect to consider.

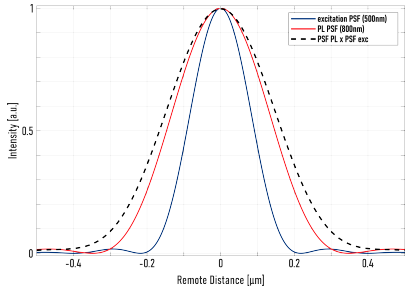

Figure 4.5): The point spread functions (PSFs) are shown for a PL emission at 800 nm, the excitation laser at 500 nm, and the resulting resolution of both (PSF excitation convoluted with PSF PL).

4.3 Data Analysis - Fitting

As a final chapter, let's briefly explain the principle of fitting the measured PL data.

4.3.1 Time-Resolved Data

We will begin with fitting time-resolved transients. Generally, the time resolution of the measured TCSPC PL signal depends on the Instrument Response Function (IRF), as discussed earlier. The IRF is obtained by measuring TCSPC of the reflected pulsed laser before or after recording series in different measurement configurations. This includes various setup settings, as well as different timing and binning settings of the TCSPC electronics. For this, a position on the sample without any sample material is used, if possible. In the case of a tunable laser source, the wavelength is set to be the closest to the PL wavelength. In all other cases, the used laser setting is recorded. To clean the laser from sidebands, which can influence the IRF, a spectral clean-up filter is always used. Since the IRF is asymmetric, in our case and signals cannot be analytically deconvoluted, the signal must be fitted using a convolution of a decay function $F_{decay}(t)$ and the IRF.

$$\begin{aligned} I_{signal}(t) &= IRF(t) * F_{decay}(t) \\ &= \int_{t_{min}}^{t_{max}} IRF(\tau) \cdot F_{decay}(t-\tau)\, d\tau \end{aligned} \tag{4.22}$$

In cases where the decay is much longer compared to the width of the IRF, the IRF approximates a delta function. Consequently, the convolution function becomes equal to the decay function $F_{decay}(t)$. Convolution functions for the analysis are essential for evaluating lifetimes ranging from picoseconds (ps) to lower nanoseconds (ns). The decay function varies depending on the specific decay processes. Below are examples illustrating

the solutions for monomolecular and bimolecular decays:

$$\begin{aligned} \frac{dn}{dt} = -k_1 n \quad &\rightarrow \quad F_{decay}(t) = n_0 \exp(-k_1 t) \quad \text{monomolecular} \\ \frac{dn}{dt} = -k_2 n^2 \quad &\rightarrow \quad F_{decay}(t) = \frac{1}{1/n_0 + k_2 t} \quad \text{bimolecular} \end{aligned} \tag{4.23}$$

These decay functions represent solutions to the corresponding differential equations describing the decay process for times $t > 0$. The initial rise of the signal is not of interest in these fits, as it is primarily determined by the electronics and the temporal shape of the laser pulse. n_0 represents the number of excited states at time zero, and $k_1 = 1/\tau_1$ and $k_2 = 1/\tau_2$ are the decay rates associated with the processes. Often, multiple decay channels are present in the systems under investigation, necessitating the use of a sum of several decay functions. The detailed understanding of the underlying decay processes is often lacking, which complicates the analysis. For systems exhibiting several monoexponential decays, plotting the intensity on a logarithmic scale can aid in identifying individual decay times, as each decay process appears as a line with a distinct slope when the lifetimes differ significantly. When the individual lifetimes are closely spaced or exhibit a statistical distribution, or when dynamics such as diffusion are involved, a sum of many exponential functions might provide a good fit. However, the resulting lifetimes may lack physical meaning when the fitting function includes too many variables. With more than five variables, almost any decay curve can be fitted well. In time-resolved photoluminescence (PL) measurements of crystalline films, decay curves often exhibit a banana shape when plotted on a logarithmic scale. To simplify the analysis of decay lifetimes without overly complicating the fit with too many variables, a stretched exponential fit function is employed[36, 37]:

$$F(t) = n_0 \cdot \exp\left(-\frac{t}{\tau}\right)^{\beta}, \text{ average lifetime: } \langle\tau\rangle = \frac{\tau}{\beta}\,\mathbf{\Gamma}\left(\frac{1}{\beta}\right) \tag{4.24}$$

It is an exponential function extended by an exponent β, which represents a statistical distribution of the lifetime τ around an average value $\langle\tau\rangle$. The average lifetime can be calculated using the Gamma function $\mathbf{\Gamma}$. The parameter β must lie between 0 and 1, or it can be a special case of 2 representing Gaussian statistics. However, the statistical nature cannot be fully determined solely from the exponent β without additional information. As an analytical tool for determining lifetimes in a comparable manner, this stretched exponential function is reproducible and provides a basis for comparison, particularly in cases involving unknown excited state dynamics. In crystalline films, which are typically imperfect and may exhibit surface states with dangling bonds, decay lifetimes can vary for different excited states. Moreover, this fitting function utilizes only 3 fitting variables, which typically yields a reasonable fit[36, 37].

4.3.2 Energy Resolved Data

Now, let us consider spectral measurements. Typically, for radiative transitions, a Lorentzian lineshape is expected in first order, while a Gaussian-shaped photoluminescence (PL) spectrum is expected for Gaussian distributions of different transitions. In these cases, simple Gaussian or Lorentzian curves can be fitted to the spectra. The measured spectra are recorded using a grating spectrometer that disperses light linearly in wavelength, and the spectra are plotted on a wavelength scale. It is important to note that symmetric lineshapes, such as a Lorentzian curve, appear asymmetric on a wavelength scale but sym-

metric on an energy scale, given that $E \sim \frac{1}{\lambda}$. Therefore, the data needs to be rescaled to an energy scale. Additionally, the intensity values must be corrected by dividing by λ^2, as the effective detecting area $dI(\lambda) = \frac{dI(E)}{\lambda^2}$ changes upon rescaling. However, in reality, spectra often appear asymmetric due to the involvement of numerous defect states in crystalline films, as discussed earlier. To determine a central wavelength x_0 asymmetric peak function is used. This function is a sum of a Lorentzian $L(x)$ and a Gaussian peak $G(x)$, known as a pseudo-Voigt peak, and includes a non-constant width function $\sigma(x)$[38].

$$
\begin{aligned}
G(x) =& \frac{A}{\sigma(x)}\sqrt{\frac{4ln2}{\pi}}\ \exp\left(-4ln2\left(\frac{x-x_0}{\sigma(x)}\right)^2\right) && \text{(Gaussian)}\\
L(x) =& \frac{2A}{\pi\sigma(x)\left(1+\frac{4(x-x_0)}{\sigma(x)}\right)^2} && \text{(Lorentzian)}\\
\sigma(x) =& \frac{2\sigma_0}{1+\exp(\alpha(x-x_0))} && \text{(varying width)}\\
\\
V(x) =& p\ L(x) + (1-p)\ G(x) && \text{(pseudo-Voigt)} \qquad (4.25)
\end{aligned}
$$

The width function $\sigma(x)$ is a sigmoidal function that varies with a factor α , controlling its asymmetry. Typically, α ranges between -1 and 1, as higher values can lead to fits with multiple maxima, making the fit less stable and reliable. In the pseudo-Voigt function $V(x)$, the parameter$p$ weights the ratio of the Lorentzian and Gaussian distributions. While originally defined as the convolution of these two distributions, the pseudo-Voigt function uses a weighted sum approach, which is simpler to fit and often yields satisfactory results. This asymmetric peak function is highly effective for fitting spectra commonly found in crystalline solid-state materials.

A nonlinear least squares approach is utilized to fit a function to the measured data, yielding a set of parameters.

$$F_{opt}(\boldsymbol{a}) = min\left[\sum_{i=1}^{n}\left(F_i^{fit}(\boldsymbol{a},x) - Data(x)_i\right)^2\right] \qquad (4.26)$$

It is clear that the sum of the squared differences between the fit function and the measured data must approach zero, ensuring that the optimization function F_{opt} reaches an extremum. The second-order term, the sum of squared differences, aims to minimize and converge to the best possible solution. This sum encompasses individual data points i, where n represents the data length. The fit function is computed at each point x corresponding to the x-scale of the recorded data. It is important to note that the initial starting point can influence the final solution. Optimization algorithms are designed to find a minimum, and while many local minima may exist, they may not represent the best solution. Starting with values close to the expected solution and constraining the variable space boundaries is advisable. Iterative processes often help in finding the optimal solution, and weighting the fit with a logarithm can further refine this process.

$$F_{opt}(\boldsymbol{a}) = min\left[\sum_{i=1}^{n}\left(\log\left(F_i^{fit}(\boldsymbol{a},x)\right) - \log\left(Data(x)_i\right)\right)^2\right] \qquad (4.27)$$

The advantage lies in weighting low intensity values more heavily compared to higher intensity values, often leading to optimal physical solutions and stabilizing the fit. This

approach is particularly beneficial for TCSPC data, where long-lived states may have very low photon counts towards the end of the measurement interval. Looking ahead, I envision that fitting analyses could be optimized using artificial intelligence (AI) in the future. AI could potentially accelerate the subtraction of physical models by directly inputting measured transients. Moreover, AI could aid in finding optimized parameters without depending heavily on initial conditions, thereby speeding up and enhancing the efficiency of analysis. This advancement could provide researchers with more time in the laboratory, leading to the discovery of more intriguing new results.

5 Perovskite and Coordinated Polymer Frameworks - Photoactive semiconductors

This chapter summarizes the work of my doctoral thesis. Often, these studies are collaborative efforts involving many people, especially for the synthesis. Nonetheless, this provides you, the reader, with a brief introduction to the main publications, which are attached to show the detailed story. Given the world's high energy consumption and reliance on oil and gas, new renewable energy sources are essential. Solar energy is a significant renewable source, with photons freely available to everyone. The possible power density on Earth ranges between 300 and 800 W/m^2 having no clouds[39], representing a vast amount of energy that we can potentially harvest. Cost-effective production of solar cell devices remains a challenge. Here, we present materials that can be produced by spin-coating or solvothermal reactions of reagents, making them interesting candidates for potential devices due to their low production costs. Additionally, we need more efficient solar cell devices because of limited space for installation on fields or rooftops. However, these photoactive materials might also have other applications. The different projects in this work focus on novel materials and their intrinsic properties, aiming to explain the photophysics of these materials, which could be useful for various applications.

5.1 Methylammonium Lead Iodide - a Lead Perovskite

For one generation of PhD students, this material was a very hot topic. A new solar material that achieves almost the same efficiencies as silicon solar cells with much less energetic effort. It is generally printable and based on two solutions (Methylammonium and Lead iodide precursor) that crystallize on the surface to form Methylammonium lead iodide ($MAPbI_3$). By tuning the fabrication process, it is possible to achieve highly crystalline films that show high power conversion efficiencies. This material has high potential for commercialization as a solar cell material, especially as a tandem cell material. A tandem solar cell combines several materials to overcome the Shockley limit and utilize the solar spectrum more efficiently. The combination of silicon and $MAPbI_3$ is the most prominent one. In our investigations, we focus on the excited state dynamics of the intrinsic material. The sample is a film on glass with a thickness of $400nm$ and large crystals ranging from 30 to 50 μm in diameter. The sample is excited by a $635nm$ diode laser with a tunable repetition rate. This laser wavelength excites the material above the exciton absorption, targeting the free charge carrier absorption. In general, the excitons at room temperature are not stable since the binding energy can be easily overcome by thermal energy. They dissociate, and after excitation, only ambipolar free charge carriers remain in the system. The charge carriers must move together; otherwise, the electrical field would become too high, making them ambipolar. Furthermore, it is assumed that the number of electrons equals the number of holes ($n_e = n_h$). We also know from previous studies that the

mobility of holes and electrons in these materials is almost equal ($\mu_e \sim \mu_h$).

$$\frac{\partial n(x,y,t)}{\partial t} = \underbrace{D\Delta n}_{\text{Diffusion}} - \overbrace{\underbrace{k_1 n}}^{\text{nonradiative}}_{\text{monomolecular}} - \overbrace{\underbrace{k_2 n^2}}^{\text{radiative}}_{\text{bimolecular}} - \overbrace{\underbrace{k_3 n^3}}^{\text{nonradiative}}_{\text{Auger-recombination}} \tag{5.1}$$

It was shown that the recombination of the ambipolar charge carriers is a bimolecular process ($\sim k_2 n^2$). This means that the measured intensity $I_{measured}$ is proportional to n^2. The Auger process ($\sim n^3$) , which is the annihilation of excited charge carriers, is a non-radiative process. The recombination on defects or localized states, the monomolecular recombination ($\sim n$), is also non-radiative. Nevertheless, by keeping the excitation power low, the quadratic and third-order terms are negligible.

$$\frac{\partial n(x,y,t)}{\partial t} \simeq D\Delta n - k_1 n - \cancel{k_2 n^2} - \cancel{k_3 n^3}, \quad \text{where} \quad I_{measured} \sim n^2 \tag{5.2}$$

The excited states have a lifetime of around $1\mu s$ and are highly mobile. To measure the diffusion coefficient without introducing additional contacts, a remote detection scheme is used. In a solar cell configuration, the contacts are on the top and bottom, meaning the charge carrier separation would happen within the $400nm$ film, where it is monocrystalline. Additionally, the excited states cannot overcome the grain boundaries of neighboring crystal grains, so observing mobile excited states in large crystallites of several μm is necessary. Given the long-lived and mobile states, it is possible to measure the diffusion coefficient from them. To determine the limitation of diffusive transport, we measured the temperature dependence of the diffusion coefficient of $MAPbI_3$, ranging from $300K$ down to $5K$. The diffusion coefficients are recalculated to a mobility using the Einstein-Smoluchowski relation[28]. It is assumed that the free charge carriers are not shielded and all participate equally in the mobility. Although the absolute calculated value may not be correct, the shielding effects can be assumed to be temperature-independent. Therefore, the trend of mobility along the measured temperatures remains valid. The temperature-dependent diffusion measurements show that the mobility trend is limited by scattering on lattice fluctuations and optical phonons, as indicated by comparing datasets to theoretical calculations in the literature[40, 41]. Interestingly, the diffusive transport stops between 140 to $180K$. This is because the tetragonal phase present at room temperature transitions to the orthorhombic phase in this temperature range. In the PL spectra, a certain jump of a few nanometers in the PL maximum ($\sim 780nm$)is observed and additionally a second peak on the blue side ($\sim 740nm$) is rising with further lowering temperature. After the red-sided peak smears out, only one PL peak is left around $90K$, which corresponds to the pure orthorhombic phase. The red-shifted peak above the phase transition belongs to the tetragonal phase, while the region with two peaks indicates a mixture of both phases. The phase transition temperature can differ for each thin crystal, typically occurring between 159 and $160K$ when coming from high temperatures. This shifts to around $169K$ when increasing temperatures from lower values. The material shows a hysteresis in its phase transition, and the absolute values of the phase transition points differ slightly from sample to sample but consistently reproduce the same trend. During the phase transition, both phases appear simultaneously. This is observed in confocal scans as well, where large homogeneous light-emitting crystals change to small inhomogeneous PL spots, indicating local disorder in the system. This is why diffusive transport stops: the excited states become localized, and phase mixing creates an energetic barrier they cannot overcome. This demonstrates that disorder can significantly influence diffusive transport, highlighting the importance of grain crystallinity on charge transport in $MAPbI_3$.

This section is a summary of these two published papers, which are attached:

Local Disorder at the Phase Transition Interrupts Ambipolar Charge Carrier Transport in Large Crystal Methylammonium Lead Iodide Thin Films[42]

Temperature-Dependent Ambipolar Charge Carrier Mobility in Large-Crystal Hybrid Halide Perovskite Thin Films[43]

5.1.1 $CsFAPbI_3$ Nanocrystals

Another lead perovskite system of interest is the caesium formamidinium lead triiodide $CsFAPbI_3$ quantum dots. A significant challenge with lead perovskites is their rapid degradation over time. However, synthesizing nanocrystals with ligands around them helps to passivate the surface, keeping oxygen and moisture away from the material. Additionally, the quantum dots are in solution, making it convenient to print solar cells. In this study, the nanocrystals are slot-die coated to print solar cell devices. Various post-print treatments are compared to evaluate their influence on performance. The photophysical properties are measured on films coated only on glass. The post-print treatments involve multiple steps. Initially, the long-chain oleic acids and oleylamines surrounding the nanocrystals are exchanged with $Pb(NO_3)_2$. Subsequently, the surface layers are passivated with formamidinium iodide (FAI). These treatments enhance the solar cell performance from approximately ~ 0.5 to 6.4% photo conversion efficiency (PCE). It has been shown that the average lifetime of the excited charge carriers increases from 5 to $40ns$, and there is a redshift in PL emission from 1.71 to $1.65eV$ when comparing pristine and treated materials, respectively. The excited state dynamics are assumed to be similar to those in $MAPbI_3$, excluding the diffusion out of the confocal spot, as no temporal broadening is observed. However, the density of states is not negligibly small, which includes the bimolecular decay channel.

$$\frac{\partial n(t)}{\partial t} \simeq -k_1 n - k_2 n^2, \quad \text{where} \quad I_{measured} \sim n^2 \tag{5.3}$$

This solution of the differential equation is used to fit the observed transients. Moreover, the structure in these films changes from pure cubic to a mixture α- and β-phase. These reorganizations, including the change in photophysical properties, seem to be the reason for the improved performance in this example.

In general, lead-based perovskites perform very well in solar cell applications. It is promising that these types of materials will play a significant role in future energy conversion concepts. However, these materials are very unstable under ambient conditions, which needs to be improved. So far, devices made from lead perovskite require a very robust and stable encapsulation to shield them from water and oxygen. Moreover, this encapsulation needs to be robust enough to prevent any contamination of lead into the environment. Additionally, after degradation, it is not easy to recycle the material because of the lead toxicity. One future direction could be improving the inertness of lead perovskites or finding ways to replace the lead with a different, less toxic material. Nevertheless, a lot of screening work still needs to be done to find other possible candidates that can improve the harvesting of sunlight.

This section is a summary of the scientific contribution to this published paper:

> Layer-By-Layer Printed Metal Hybrid $(Cs:FA)PbI_3$ Perovskite Nanocrystal Solar Cells[44]

5.2 Lead Free Perovskites

Lead-based perovskites are very efficient solar cell materials, as discussed in the previous chapter. Unfortunately, without encapsulation, these materials degrade within weeks to months. Moreover, these materials contain lead salts, which are very harmful to the environment. Organisms can absorb lead salts more easily than elemental lead, and these salts are water-soluble. Deploying these types of solar cells on a large scale in fields poses a risk of environmental contamination, comparable to the lead intoxication from leaded gasoline used until the late 1980s. The consequences of such contamination were only identified in hindsight because these effects do not appear immediately. It has already been shown that plants can efficiently absorb lead when grown in lead-perovskite-contaminated soil[45, 46]. Thus, more research is necessary. One approach is to use the perovskite crystal structure but replace the lead, exploring combinations of many elements to find a new, less toxic material. Hypothetically, there are over $> 10^6$ possible perovskite structures without lead. However, screening every material and achieving chemical realization through synthesis is almost impossible. By using computational methods, many structures can be excluded[47, 48, 49], but experimental validation is still necessary. The more we understand how the photophysical properties are connected to their structure, the better we can predict novel materials. There is still much work to do to improve energy conversion materials in the energy transition. In this chapter, we focus on the investigation of 2D lead-free perovskite thin films. The benefits of 2D materials include their stability due to the surrounding ligands that isolate the material from oxygen and water in the ambient environment. Additionally, incorporating organic spacer molecules into the crystal structure allows for the tuning of physical properties. This tuning can affect the density of states, contributing to the valence and conduction bands in a way that influences the excited state decay. We have contributed microscopic time- and spectral-resolved photoluminescence (PL) measurements to support the photophysical understanding. Three different studies are highlighted: one where in a Ruddelsen-Popper perovskite the halides were changed ($(4FPEA)4AgBiX_8$, where $X = Cl, I, Br$), one where the cations of a Ruddolfite perovskite are changed ($Cu1 - xAg_xSbI$), and one where the interlayer organic ligands are exchanged on AgBiI and CuBiI. All these materials are 2D perovskite thin films. We will not delve into the chemical details of realization, synthesis, and structure, as these are outside my expertise and can be found in the respective publications. Our contributions are primarily focused on the photoluminescence measurements. From a photophysical point of view, the processes observed in these materials are comparable and can be summed up in a single model representing the observed material class. After excitation, free excited charge carriers exist and form a polaronic state within approximately a picosecond. This polaronic excited state, due to phonon coupling and the resulting local lattice deformation, does not travel far. Additionally, these materials have numerous defects and trap states. Consequently, the excited polaronic state falls into these trap states and ceases to move further. These trap states have a lifetime of several nanoseconds, meaning the lifetime of the excited states is much shorter compared to $MAPbI_3$. The excited states also exhibit much

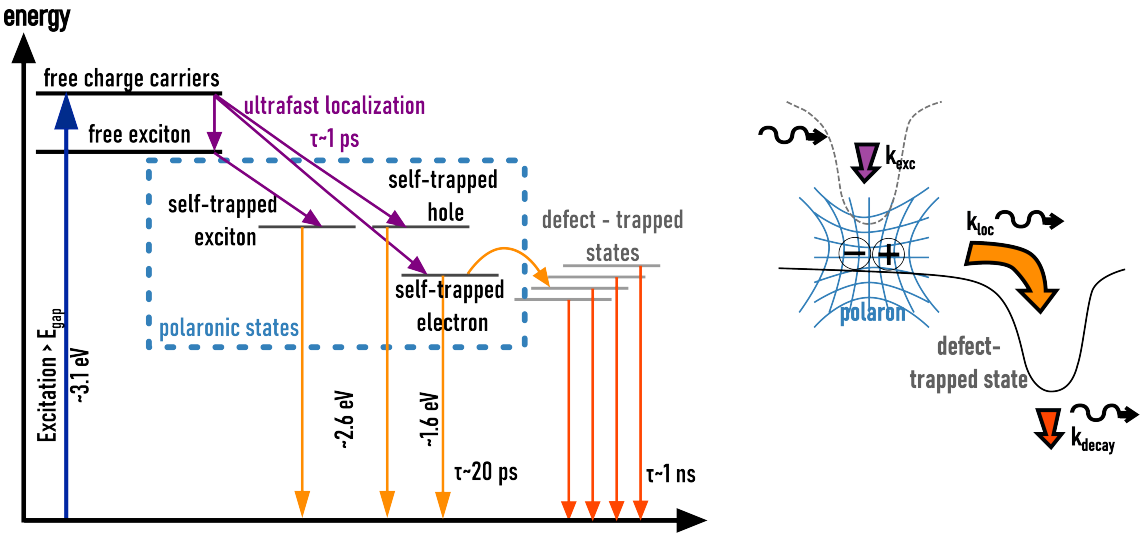

Figure 5.1): Scheme of charge carrier dynamics, emission, and energy levels of Ag-Bi based 2D double perovskites This model was developed specifically for the silver-bismuth based 2D double perovskite ($(4FPEA)_4AgBiX_8$, X = Cl, Br, I) system[50], but it represents the entire class of lead-free perovskites. In PL measurements, the formation and localization of the polaron, followed by its decay, is observed. The ultrafast localization is detected through THz pump-probe measurements.

stronger coupling to phonons, and these materials appear to have significantly more defect states, as evidenced by the broader PL spectrum at low temperatures. While the specific numbers for the different combinations of materials vary slightly, they remain within the same order of magnitude, resulting in similar behavior. The efficiency ranges from 0.7 to 1.1%, which is much lower than that of the lead-based types. Hopefully, by exchanging molecules within the structure and reducing the defect states, the strong phonon coupling and localization of the excited state can be reduced.

This section is a summary of the scientific contributions to these published papers:

> Silver-Bismuth Based 2D Double Perovskites $(4FPEA)_4AgBiX_8$ (X=Cl,Br,I): Highly Oriented Thin Films with Large Domain Sizes and Ultrafast Charge-Carrier Localization[50]
>
> Cu/Ag-Sb-I Rudorffite Thin Films for Photovoltaic Applications[51]
>
> *Overcoming Intrinsic Quantum Confinement and Ultrafast Self-Trapping in Ag-Bi-I and Cu-Bi-I Based 2D Double Perovskites through Electroactive Cations*[52] (under revision)

5.3 Covalent Organic Frameworks

A novel approach involves using highly oriented crystalline structures made of organic molecules connected by covalent bonds. These ordered polymer-like structures are called covalent organic frameworks (COF). The advantage of this material class lies in its tunability and design flexibility by choosing different linker and node molecules. Investigating the excited state dynamics can provide more insights into the connection between the crystal

structure and its properties. This study explores a photoactive material beyond perovskite materials, focusing on fundamental material characteristics to evaluate the performance and limitations of this specific COF as an example of the entire material class. Here, a highly crystalline WBDT COF is spectroscopically investigated. It is a 2-dimensional system with planar sheets oriented parallel to the substrate surface. The crystal grains are about $200\mu m$ in size. Although individual crystals have different orientations, the 2D sheets appear to connect across different grains, forming grain boundaries. Interestingly, these films show the diffusion of excited states across several grains, which is entirely different from MAPI thin films where excited ambipolar charge carriers do not pass grain boundaries. Additionally, the excited state dynamics are very similar to lead-free perovskite systems. In the early picoseconds, free ambipolar charges are very mobile before they get localized into a polaronic exciton state. This exciton diffuses as well, reaching diffusion coefficients up to $4cm^2/s$, which is very high compared to reported values in the literature for COF systems. As mentioned before, this system is made entirely of organic molecules, achieving values expected for semiconductor materials. To model the transport of the excited states, temperature-dependent remote-detected time-resolved PL measurements are conducted. The PL spectrum has a spectral width of around $0.3eV$, which remains constant at low temperatures. Additionally, when measuring only the red side of the spectrum, no significant broadening is observed in the remote-detected time-resolved PL measurements This provides evidence for a localized species trapped in defect states and possible localized states belonging to individual organic molecules. Immediately after excitation, an unbound excited state consisting of ambipolar free charge carriers is observed. It is challenging to distinguish if freely moving excitons are also involved. These unbound states are detected in time-resolved PL measurements and additional transient THz measurements, specifically performed at room temperature. In the room temperature THz pump-probe measurements, only a signature of the free ambipolar charge carriers is observed due to the limited probing THz spectrum. This unresonant signal from the excited charge carriers decays within $1.4ps$, which represents the lifetime of this unbound species. In PL measurements, these unbound excited charges manifest as initial broadening within the first $10ps$ in the signal rise observed in the remote-detected TCSPC signal. These rapidly moving free unbound excited states reach an average diffusion coefficient of about $10cm^2/s$. No temperature dependence is observed for these states due to the excess energy from excitation over the bandgap. Additionally, during excitation, the excited states and the phonon bath are not in equilibrium and not coupled, contributing to the high mobility of these charge carriers. Subsequently, these fast-moving excited charges localize into excitons, which appear to couple with crystal lattice phonon modes, slowing their mobility by an order of magnitude. Calculations of the excited state at room temperature yield similar diffusion coefficients of approximately $0.2cm^2/s$, comparable to the measured values ranging from 0.1 to $0.4cm^2/s$ at room temperature. Simulations assume a phonon-assisted hopping process, revealing a temperature-dependent diffusion coefficient $D(T)$ that indicates two competing transport processes: coherent band transport and incoherent hopping transport. At room temperature, the degree of disorder in these organic molecular systems favors dominant phonon-assisted hopping transport. Coherent band movement is slower due to phonon scattering. Lower temperatures increase coherent transport values by reducing phonon scattering effects. Phonon-assisted hopping slows as phonons freeze out, resulting in a peak diffusion coefficient of $4cm^2/s$ at $200K$. At very low temperatures, coherent transport dominates, while incoherent transport diminishes, explaining the decreasing trend in diffusion coefficient below $200K$ to $100K$ and stays then constant at around $2cm^2/s$ until $5K$. This temperature dependence reflects the dis-

order of the system, particularly evident in this WBDT COF. It remains unclear whether this disorder is intrinsic to the material or arises from imperfections in crystallization during synthesis. Future synthesis efforts may explore methods to reduce disorder, but current limitations persist with crystalline films that lack ordered structure accessibility. Alternatively, synthesizing unoriented thin films where single crystallites are randomly oriented shows comparable diffusion coefficients for the longer-lived state at room temperature, albeit decreasing with lower temperatures. Higher disorder in these films results in predominantly incoherent hopping transport of excited states. Nevertheless, the efficient transport observed in highly oriented crystalline films makes them intriguing for further energy conversion applications, such as catalytic reactions where they can serve as photon absorbers transporting charges to catalytic centers positioned within the COF-films' pores. The direct access to the molecular structure in this architecture will enable more detailed insights linking photophysical properties with the semiconductor crystal structure in future studies. Using crystalline COF films with different linker isomers, which exhibit varying absorption and emission spectra[53], will allow investigation into how these differences influence the dynamics of excited states. Moreover, exploring combinations of different molecules may reveal variations in disorder within crystalline films, potentially enhancing our understanding of how to tailor crystal structures to optimize the efficiency of energy conversion processes driven by light absorption.

This section is a summary of this preliminary manuscript, which is attached:

> **Spatiotemporal Spectroscopy of Fast Excited-State Diffusion in 2D Covalent Organic Framework Thin Films[54]**

5.4 Metall-Organic Frameworks

Another class of controllable crystal structures on a molecular basis are Metal-Organic Frameworks (MOFs). These crystalline structures combine organic frameworks with metal centers, offering porous properties and high conductivity within the organic electronic material class. In this study, we investigate a MOF crystal incorporating rare earth ions (REIs), resulting in single crystals on the order of several hundred micrometers. These large crystals are unusual in this material class and present an intriguing candidate for further research. Notably, the crystal structure could be determined crystallographically due to their large size, using a novel synthesis approach. Furthermore, these crystals exhibit remarkable stability in water and under ambient conditions, maintaining their properties over a year. Interestingly, these MOF crystals exhibit emission lines from the REIs incorporated into the framework. This prompts an exploration of the photophysical relationship between the MOF framework and the REIs. In general, transitions in lanthanides from the excited state to the ground state are forbidden in the elementary state, thus they do not emit photons naturally. However, when the atomic states couple with a crystal matrix, this symmetry is broken, allowing for radiative transitions. The 4f-electrons in lanthanides exhibit many energy levels due to Coulomb interactions and spin-orbit coupling, leading to energy level degeneracies. Fine splitting of these atomic states occurs when they couple with the surrounding crystal lattice, enabling radiative transitions. In the case of MOF matrices, these serve as light-absorbing materials capable of transferring energy to REI metal centers. Various combinations of REIs are possible, including ytterbium, neodymium, europium, samarium, and erbium, with current focus on

ytterbium and neodymium for further investigations. The absorption onset of MOF crystals typically occurs around $650nm$. These crystals exhibit a broad-band emission with Stokes shift (500 to $700nm$) originating from the framework, along with smaller significant emission lines attributed to the REIs. Due to their wide absorption spectrum, it is feasible to excite these materials at $405nm$ and observe emission lines in the near-infrared range ($800-1024nm$). Two distinct timescales are observed in the photoluminescence (PL) emission. The broadband emission exhibits an average lifetime below $10ps$, interpreted as the average time for the energy transfer process within the MOF framework. The PL emission lines from the rare earth ion (REI) have lifetimes ranging from 130 to $150ns$ for ytterbium and 30 to $50ns$ for neodymium. These lifetimes are surprisingly short for REIs compared to reported values for neodymium and ytterbium crystals in the literature. This is likely due to the high density of REI metal centers causing quenching among them, exacerbated by the presence of embedded water molecules that further quench the excited states of the REIs. For REIs, a reported process involves one photon generating two photons with half the energy, emitted in parallel within the excited state's lifetime-a non-parametric, incoherent process. This is evidenced in many materials through the measured quantum yield of emitters, where more photons are emitted than absorbed. In the DHBQ framework, the matrix may emit photons in addition to the excited REIs. However, the efficiency of energy transport from the framework to the REIs remains unknown, and potential dark transitions further complicate interpretations of quantum yield measurements. To address this, we employ a different approach: measuring the second-order time correlation function of emitted photons via a Hanbury-Brown-Twiss configuration. This method relies on the emission of two photons within the lifetime of the excited REI. We observe a $\sim 1\%$ bunching for ytterbium DHBQ systems, while neodymium crystals do not exhibit bunching. This difference may be explained by neodymium's multiple energy transitions due to its atomic properties. In ytterbium-DHBQ crystals, we confirm that after absorbing one photon, energy is transferred to two independent ytterbium metal centers, which become excited and decay in parallel within their lifetimes-confirming the non-parametric downconversion process. The second-order time correlation function depends approximately on $\sim 1 + \frac{1}{n}$, where n is the number of excited states. Given many independent emitters, the observed bunching is only around 1%. These results highlight the potential of the materials for imaging applications, due to their large Stokes shift, efficient photon emission, short lifetimes, and the downconversion process. Moreover, their stability in air and water is noteworthy.

This section is a summary of this preliminary manuscript, which is attached:

> **Giant rare-earth metal catecholate crystals - morphology control and rapid NIR luminescence response** [55]

5.5 Conclusion

In summary, several intriguing phenomena were observed across different projects using advanced time-resolved photoluminescence microscopy and spectroscopy techniques. In $MAPbI_3$, the diffusive transport of excited ambipolar charge carriers is hindered by optical phonons and lattice fluctuations. Additionally, the disorder induced by phase transitions in thin films was found to halt this transport. In $CsFAPbI_3$ quantum dot films, restructuring of the clustering improved photophysical properties and consequently enhanced power

conversion efficiency. For lead-free perovskite systems, the inferior solar cell performance was attributed to strong localization of excited states on lattice phonons and immobile defect states. The novel approach using WBDT COF, a tunable material composed solely of organic molecules, exhibited semiconductor-like behavior, with disorder identified as a critical factor influencing excited state diffusive transport. Finally, measurements on REI MOFs revealed a non-parametric downconversion process in ytterbium DHBQ MOFs, demonstrated through second-order time correlation function analysis of emitted photons.

Bibliography

[1] Goddéris, Yves ; Donnadieu, Yannick ; Le Hir, Guillaume ; Lefebvre, Vincent ; Nardin, Elise: The role of palaeogeography in the Phanerozoic history of atmospheric CO2 and climate. In: Earth-Science Reviews 128 (2014), Januar, S. 122–138. http://dx.doi.org/10.1016/j.earscirev.2013.11.004. – DOI 10.1016/j.earscirev.2013.11.004. – ISSN 0012–8252

[2] Madelung, O.: Festkörpertheorie I. Springer, 1988

[3] Madelung, O.: Festkörpertheorie II. Springer, 1972

[4] O.Madelung: Festkörpertheorie III. Springer, 1973

[5] C.G.Kuper, G.D.Whitefield (Hrsg.): Polarons and Excitons - Scottish Universities' Summer School. Plenum Press, 1963

[6] T.P.Das, W. Low A.A. Maradudin E.W. Montroll G.H. Weiss A.C. Beer R.S. Knox S. A. E.L. Hahn H. E.L. Hahn: Solid State Physics - Advances in Resaerch and Applications. Academic Press, 1963

[7] Dresselhaus, G.: Effective mass approximation for excitons. In: Journal of Physics and Chemistry of Solids 1 (1956), September, Nr. 1–2, S. 14–22. http://dx.doi.org/10.1016/0022-3697(56)90004-x. – DOI 10.1016/0022–3697(56)90004–x. – ISSN 0022–3697

[8] Li, J ; Zhong, Y L. ; Zhang, Dong: Excitons in monolayer transition metal dichalcogenides. In: Journal of Physics: Condensed Matter 27 (2015), Juli, Nr. 31, S. 315301. http://dx.doi.org/10.1088/0953-8984/27/31/315301. – DOI 10.1088/0953–8984/27/31/315301. – ISSN 1361–648X

[9] Franchini, Cesare ; Reticcioli, Michele ; Setvin, Martin ; Diebold, Ulrike: Polarons in materials. In: Nature Reviews Materials 6 (2021), März, Nr. 7, S. 560–586. http://dx.doi.org/10.1038/s41578-021-00289-w. – DOI 10.1038/s41578–021–00289–w. – ISSN 2058–8437

[10] H.Haken, H.C.Wolf: Molekülphysik und Quantenchemie - Einführung in die experimentellen und theoretischen Grundlagen. Springer, 2006

[11] Demtröder, W.: Molekülphysik. Oldenbourg Verlag München, 2013

[12] Slanina, Tomáš ; Ayub, Rabia ; Toldo, Josene ; Sundell, Johan ; Rabten, Wangchuk ; Nicaso, Marco ; Alabugin, Igor ; Fdez. Galván, Ignacio ; Gupta, Arvind K. ; Lindh, Roland ; Orthaber, Andreas ; Lewis, Richard J. ; Grönberg, Gunnar ; Bergman, Joakim ; Ottosson, Henrik: Impact of Excited-State Antiaromaticity Relief in a Fundamental Benzene Photoreaction Leading to Substituted Bicyclo[3.1.0]hexenes. In: Journal of the American Chemical Society 142 (2020), Mai, Nr. 25, S. 10942–10954. http://dx.doi.org/10.1021/jacs.9b13769. – DOI 10.1021/jacs.9b13769. – ISSN 1520–5126

[13] Kim, Heechan ; Park, Woojin ; Kim, Younghun ; Filatov, Michael ; Choi, Cheol H. ; Lee, Dongwhan: Relief of excited-state antiaromaticity enables the smallest red emitter. In: Nature Communications 12 (2021), September, Nr. 1. http://dx.doi.org/10.1038/s41467-021-25677-2. – DOI 10.1038/s41467–021–25677–2. – ISSN 2041–1723

[14] Dirac, P.M.A: The quantum theory of the emission and absorption of radiation. In: Proceedings of the Royal Society of London. Series A, Containing Papers of a Mathematical and Physical Character 114 (1927), März, Nr. 767, S. 243–265. http://dx.doi.org/10.1098/rspa.1927.0039. – DOI 10.1098/rspa.1927.0039. – ISSN 2053–9150

[15] Edvinsson, T.: Optical quantum confinement and photocatalytic properties in two-, one- and zero-dimensional nanostructures. In: Royal Society Open Science 5 (2018), September, Nr. 9, S. 180387. http://dx.doi.org/10.1098/rsos.180387. – DOI 10.1098/rsos.180387. – ISSN 2054–5703

[16] L.D.Landau, E.M. L.: Quantenmecahnik. Akademie-Verlag, 1985

[17] L.D. Landau, E.M L.: Hydrodynamik. Akademie Verlag Berlin, 1978

[18] L.D. Landau, L.P.Pitajewski E.M L. E.M Lifschitz: statistische Physik Teil 1. Akademie Verlag Berlin, 1984

[19] Onsager, L.: Reciprocal Relations in irreversible Processes. In: Physical Review 37 (1931)

[20] Onsager, L.: Reciprocal Relations in irreversible Processes II. In: Physical Review 38 (1931)

[21] L. Novotny, B. H.: Principles of Nano-Optics. Cambridge University Press, 2006

[22] Perea-Causín, Raül ; Brem, Samuel ; Rosati, Roberto ; Jago, Roland ; Kulig, Marvin ; Ziegler, Jonas D. ; Zipfel, Jonas ; Chernikov, Alexey ; Malic, Ermin: Exciton Propagation and Halo Formation in Two-Dimensional Materials. In: Nano Letters 19 (2019), September, Nr. 10, S. 7317–7323. http://dx.doi.org/10.1021/acs.nanolett.9b02948. – DOI 10.1021/acs.nanolett.9b02948. – ISSN 1530–6992

[23] Kulig, Marvin ; Zipfel, Jonas ; Nagler, Philipp ; Blanter, Sofia ; Schüller, Christian ; Korn, Tobias ; Paradiso, Nicola ; Glazov, Mikhail M. ; Chernikov, Alexey: Exciton Diffusion and Halo Effects in Monolayer Semiconductors. In: Physical Review Letters 120 (2018), Mai, Nr. 20, S. 207401. http://dx.doi.org/10.1103/physrevlett.120.207401. – DOI 10.1103/physrevlett.120.207401. – ISSN 1079–7114

[24] Crank, J. ; Nicolson, P.: A practical method for numerical evaluation of solutions of partial differential equations of the heat-conduction type. In: Mathematical Proceedings of the Cambridge Philosophical Society 43 (1947), Januar, Nr. 1, S. 50–67. http://dx.doi.org/10.1017/s0305004100023197. – DOI 10.1017/s0305004100023197. – ISSN 1469–8064

[25] Tuncer Cebeci, Peter B.: Physical and Computational Aspects of Convective Heat Transfer. Springer, 1984

[26] Sun, C. ; Trueman, C.W.: Unconditionally stable Crank-Nicolson scheme for solving two-dimensional Maxwell's equations. In: Electronics Letters 39 (2003), Nr. 7, S. 595. http://dx.doi.org/10.1049/el:20030416. – DOI 10.1049/el:20030416. – ISSN 0013–5194

[27] R.Pletcher, D. A. J. Tannehill T. J. Tannehill: Computational fluid mechanics and heat transfer. Taylor and Francis, 1997

[28] P.W.Atkins: Physical Chemistry. Oxford University Press, 1982

[29] W. Zinth, U. Z.: Optik Lichtstrahlen-Wellen-Photonen. Oldenbourg Verlag München, 2009

[30] Hecht, E.: Optics. Pearson, 2017

[31] W.Becker: Advanced Time-Correlated Single Photon Counting Techniques. Springer, 2005

[32] Brown, R. H. ; Twiss, R.Q.: LXXIV. A new type of interferometer for use in radio astronomy. In: The London, Edinburgh, and Dublin Philosophical Magazine and Journal of Science 45 (1954), Juli, Nr. 366, S. 663–682. http://dx.doi.org/10.1080/14786440708520475. – DOI 10.1080/14786440708520475. – ISSN 1941–5990

[33] Lieb, M. A. ; Zavislan, James M. ; Novotny, Lukas: Single-molecule orientations determined by direct emission pattern imaging. In: Journal of the Optical Society of America B 21 (2004), Juni, Nr. 6, S. 1210. http://dx.doi.org/10.1364/josab.21.001210. – DOI 10.1364/josab.21.001210. – ISSN 1520–8540

[34] Agrawal, Anurag ; Quirin, Sean ; Grover, Ginni ; Piestun, Rafael: Limits of 3D dipole localization and orientation estimation for single-molecule imaging: towards Green's tensor engineering. In: Optics Express 20 (2012), November, Nr. 24, S. 26667. http://dx.doi.org/10.1364/oe.20.026667. – DOI 10.1364/oe.20.026667. – ISSN 1094–4087

[35] Backer, Adam S. ; Moerner, W. E.: Extending Single-Molecule Microscopy Using Optical Fourier Processing. In: The Journal of Physical Chemistry B 118 (2014), Mai, Nr. 28, S. 8313–8329. http://dx.doi.org/10.1021/jp501778z. – DOI 10.1021/jp501778z. – ISSN 1520–5207

[36] Zatryb, G ; Podhorodecki, A ; Misiewicz, J ; Cardin, J ; Gourbilleau, F: On the nature of the stretched exponential photoluminescence decay for silicon nanocrystals. In: Nanoscale Research Letters 6 (2011), Januar, Nr. 1, S. 106(1–8). http://dx.doi.org/10.1186/1556-276x-6-106. – DOI 10.1186/1556–276x–6–106. – ISSN 1556–276X

[37] Chen, Reuven: Apparent stretched-exponential luminescence decay in crystalline solids. In: Journal of Luminescence 102–103 (2003), Mai, S. 510–518. http://dx.doi.org/10.1016/s0022-2313(02)00601-4. – DOI 10.1016/s0022–2313(02)00601–4. – ISSN 0022–2313

[38] Stancik, Aaron L. ; Brauns, Eric B.: A simple asymmetric lineshape for fitting infrared absorption spectra. In: Vibrational Spectroscopy 47 (2008), Mai, Nr. 1, S. 66–69. http://dx.doi.org/10.1016/j.vibspec.2008.02.009. – DOI 10.1016/j.vibspec.2008.02.009. – ISSN 0924–2031

[39] Wald, Lucien: BASICS IN SOLAR RADIATION AT EARTH SURFACE / HAL open science. 2018. – Forschungsbericht

[40] Poncé, Samuel ; Schlipf, Martin ; Giustino, Feliciano: Origin of Low Carrier Mobilities in Halide Perovskites. In: ACS Energy Letters 4 (2019), Januar, Nr. 2, S. 456–463. http://dx.doi.org/10.1021/acsenergylett.8b02346. – DOI 10.1021/acsenergylett.8b02346. – ISSN 2380–8195

[41] Mayers, Matthew Z. ; Tan, Liang Z. ; Egger, David A. ; Rappe, Andrew M. ; Reichman, David R.: How Lattice and Charge Fluctuations Control Carrier Dynamics in Halide Perovskites. In: Nano Letters 18 (2018), November, Nr. 12, S. 8041–8046. http://dx.doi.org/10.1021/acs.nanolett.8b04276. – DOI 10.1021/acs.nanolett.8b04276. – ISSN 1530–6992

[42] Biewald, Alexander ; Giesbrecht, Nadja ; Bein, Thomas ; Docampo, Pablo ; Hartschuh, Achim ; Ciesielski, Richard: Temperature-Dependent Ambipolar Charge Carrier Mobility in Large-Crystal Hybrid Halide Perovskite Thin Films. In: ACS Applied Materials and Interfaces 11 (2019), Mai, Nr. 23, S. 20838–20844. http://dx.doi.org/10.1021/acsami.9b04592. – DOI 10.1021/acsami.9b04592. – ISSN 1944–8252

[43] Biewald, Alexander ; Giesbrecht, Nadja ; Bein, Thomas ; Docampo, Pablo ; Hartschuh, Achim ; Ciesielski, Richard: Local Disorder at the Phase Transition Interrupts Ambipolar Charge Carrier Transport in Large Crystal Methylammonium Lead Iodide Thin Films. In: The Journal of Physical Chemistry C 124 (2020), August, Nr. 38, S. 20757–20764. http://dx.doi.org/10.1021/acs.jpcc.0c06240. – DOI 10.1021/acs.jpcc.0c06240. – ISSN 1932–7455

[44] Reus, Manuel A. ; Krifa, Ahmed ; Akkerman, Quinten A. ; Biewald, Alexander ; Xu, Zehua ; Kosbahn, David P. ; Weindl, Christian L. ; Feldmann, Jochen ; Hartschuh, Achim ; Mueller Buschbaum, Peter: Layer-By-Layer Printed Metal Hybrid (CsFA)PbI3 Perovskite Nanocrystal Solar Cells. In: Advanced Optical Materials 12 (2023), September, Nr. 8, S. 2301008(1–9). http://dx.doi.org/10.1002/adom.202301008. – DOI 10.1002/adom.202301008. – ISSN 2195–1071

[45] Li, Junming ; Cao, Hai L. ; Jiao, Wen B. ; Wang, Qiong ; Wei, Mingdeng ; Cantone, Irene ; Lü, Jian ; Abate, Antonio: Biological impact of lead from halide perovskites reveals the risk of introducing a safe threshold. In: Nature Communications 11 (2020), Januar, Nr. 1, S. 1–5. http://dx.doi.org/10.1038/s41467-019-13910-y. – DOI 10.1038/s41467–019–13910–y. – ISSN 2041–1723

[46] Zahran, Sammy ; Keyes, Christopher ; Lanphear, Bruce: Leaded aviation gasoline exposure risk and child blood lead levels. In: PNAS Nexus 2 (2023), Januar, Nr. 1, S. 1–11. http://dx.doi.org/10.1093/pnasnexus/pgac285. – DOI 10.1093/pnasnexus/pgac285. – ISSN 2752–6542

[47] Giustino, Feliciano ; Snaith, Henry J.: Toward Lead-Free Perovskite Solar Cells. In: ACS Energy Letters 1 (2016), November, Nr. 6, S. 1233–1240. http://dx.doi.org/10.1021/acsenergylett.6b00499. – DOI 10.1021/acsenergylett.6b00499. – ISSN 2380–8195

[48] Afroz, Mohammad A. ; Singh, Anupriya ; Gupta, Ritesh K. ; Garai, Rabindranath ; Tailor, Naveen K. ; Yukta ; Choudhary, Shivani ; Sharma,

Bhavna ; Mahajan, Prerna ; Padha, Bhavya ; Verma, Sonali ; Arya, Sandeep ; Gupta, Vinay ; Akin, Seckin ; Prochowicz, Daniel ; Tavakoli, Mohammad M. ; Singh, S. P. ; Iyer, Parameswar K. ; Yadav, Pankaj ; Hu, Hanlin ; De, Goutam ; Satapathi, Soumitra: Design potential and future prospects of lead-free halide perovskites in photovoltaic devices. In: Journal of Materials Chemistry A 11 (2023), Nr. 25, S. 13133–13173. http://dx.doi.org/10.1039/d2ta07687j. – DOI 10.1039/d2ta07687j. – ISSN 2050–7496

[49] Chakraborty, Sudip ; Xie, Wei ; Mathews, Nripan ; Sherburne, Matthew ; Ahuja, Rajeev ; Asta, Mark ; Mhaisalkar, Subodh G.: Rational Design: A High-Throughput Computational Screening and Experimental Validation Methodology for Lead-Free and Emergent Hybrid Perovskites. In: ACS Energy Letters 2 (2017), März, Nr. 4, S. 837–845. http://dx.doi.org/10.1021/acsenergylett.7b00035. – DOI 10.1021/acsenergylett.7b00035. – ISSN 2380–8195

[50] Hooijer, Rik ; Weis, Andreas ; Biewald, Alexander ; Sirtl, Maximilian T. ; Malburg, Julian ; Holfeuer, Rico ; Thamm, Simon ; Amin, Amir Abbas Y. ; Righetto, Marcello ; Hartschuh, Achim ; Herz, Laura M. ; Bein, Thomas: Silver-Bismuth Based 2D Double Perovskite (4FPEA)4AgBiX8 (X=Cl,Br,I): Highly Oriented Thin Films with Large Domain Sizes and Ultrafast Charge-Carrier Location. In: Advanced Optical Materials 10 (2022), Juli, Nr. 14, S. 2200354–2200354. http://dx.doi.org/10.1002/adom.202200354. – DOI 10.1002/adom.202200354. – ISSN 2195–1071

[51] Hooijer, Rik ; Weis, Andreas ; Kaiser, Waldemar ; Biewald, Alexander ; Dörflinger, Patrick ; Maheu, Clément ; Arsatiants, Oleksandr ; Helminger, David ; Dyakonov, Vladimir ; Hartschuh, Achim ; Mosconi, Edoardo ; De Angelis, Filippo ; Bein, Thomas: Cu/Ag-Sb-I Rudorffite Thin Films for Photovoltaic Applications. In: Chemistry of Materials 35 (2023), November, Nr. 23, S. 9988–10000. http://dx.doi.org/10.1021/acs.chemmater.3c01837. – DOI 10.1021/acs.chemmater.3c01837. – ISSN 1520–5002

[52] Hooijer, Rik ; Wang, Shizhe ; Biewald, Alexander ; Eckel, Christian ; Righetto, Marcello ; Chen, Meizhu ; Xu, Zehua ; Blaette, Dominic ; Hubert Ebert, Dan H. ; Herz, Laura M. ; Weitz, R. T. ; Hartschuh, Achim ; Bein, Thomas: Overcoming Intrinsic Quantum Confinement and Ultrafast Self-Trapping in Ag-Bi-I and Cu-Bi-I Based 2D Double Perovskites through Electroactive Cations. In: Journal of the American Chemical Society (under revision) (2024)

[53] Guntermann, Roman ; Frey, Laura ; Biewald, Alexander ; Hartschuh, Achim ; Clark, Timothy ; Bein, Thomas ; Medina, Dana D.: Regioisomerism in Thienothiophene-Based Covalent Organic Frameworks-A Tool for Band-Gap Engineering. In: Journal of the American Chemical Society 146 (2024), Juni, Nr. 23, S. 15869–15878. http://dx.doi.org/10.1021/jacs.4c02365. – DOI 10.1021/jacs.4c02365. – ISSN 1520–5126

[54] Spies, Laura ; Biewald, Alexander ; Fuchs, Laura ; Merkel, Konrad ; Righetto, Marcello ; Xu, Zehua ; Guntermann, Roman ; Hooijer, Rik ; Herz, Laura M. ; Ortmann, Frank ; Schneider, Jenny ; Bein, Thomas ; Hartschuh, Achim: Spatiotemporal Spectroscopy of Fast Excited-State Diffusion in 2D Covalent Organic Framework Thin Films. In: preliminary Manuskript (2024)

[55] Schoenherr, Marina ; Biewald, Alexander ; Maaehringer, Andre ; Mayer, Peter ; Doeblinger, Markus ; Scheurle, Patricia I. ; Hartschuh, Achim ; Medina, Dana D.: Giant rare-earth metal catecholate crystals - morphology control and rapid NIR luminescence response. In: preliminary Manuscript (2024)

6 Appendix

List of all scientific contributions

Temperature-dependent ambipolar charge carrier mobility in large-crystal hybrid halide perovskite thin films
A Biewald, et al. ACS applied materials & interfaces 11 (23), 20838-20844, 2019

Local disorder at the phase transition interrupts ambipolar charge carrier transport in large crystal methylammonium lead iodide thin films
A Biewald, et al. The Journal of Physical Chemistry C 124 (38), 20757-20764, 2020

Silver-Bismuth Based 2D Double Perovskites (4FPEA)4AgBiX8 (X = Cl, Br, I): Highly Oriented Thin Films with Large Domain Sizes and Ultrafast Charge-Carrier Localization
R Hooijer, et al. Advanced Optical Materials 10 (14), 2200354, 2022

MOF-74 (M) films obtained through vapor-assisted conversion—impact on crystal orientation and optical properties
PI Scheurle, et al. Chemistry of Materials 33 (15), 5896-5904, 2021

A Novel Electrically Conductive Perylene Diimide-Based MOF-74 Series Featuring Luminescence and Redox Activity
PI Scheurle, et al. Small Structures 3 (5), 2100195, 2022

Room-temperature synthesis of lead-free copper (I)-antimony (III)-based double perovskite nanocrystals
S Wang, et al. APL Materials 11 (4), 041110, 2023

Controlling photon antibunching from 1D emitters using optical antennas
L Lange, et al. Nanoscale 11 (31), 14907-14911, 2019

Helical anthracene–ethyne-based MOF-74 analogue
PI Scheurle, et al. Crystal Growth & Design 22 (5), 2849-2853 Small Structures 3 (5), 2100195, 2022

Cu/Ag–Sb–I Rudorffite Thin Films for Photovoltaic Applications
R Hooijer, et al. Chemistry of Materials 35 (23), 9988-10000, 2023

Photoexcitation Control of Excitation Relaxation in Mixed-Phase Ruddlesden-Popper Hybrid Organic-Inorganic Lead-Iodide Perovskites
A Stadlbauer, et al., Advanced Optical Materials 12 (8), 2301331, 2024

Layer-By-Layer Printed Metal Hybrid (Cs:FA)PbI3 Perovskite Nanocrystal Solar Cells
MA Reus, et al. Advanced Optical Materials, 12(8), 2301008, 2024

Regioisomerism in Thienothiophene-Based Covalent Organic Frameworks - A Tool for Band-Gap Engineering
R. Guntermann, et al. Journal of the American Chemical Society, 146 (23), 15869-15878, 2024

Interpenetrated Donor-Acceptor Heterojunctions in 2D Conjugated Dibenzo[g,p]chrysene-Based Kagome Covalent Organic Frameworks
T. Xue, et al. ACS applied materials & interfaces (accepted), 2024

Overcoming Intrinsic Quantum Confinement and Ultrafast Self-Trapping in Ag-Bi-I and Cu-Bi-I Based 2D Double Perovskites through Electroactive Cations
R. Hooijer, et al. Journal of the American Chemical Society (under revision), 2024

Spatiotemporal Spectroscopy of Fast Excited-State Diffusion in 2D Covalent Organic Framework Thin Films
L. Spies, A. Biewald, et al. preliminary manuscript, 2024

Giant rare-earth metal catecholate crystals - morphology control and rapid NIR luminescence response
M. Schoenherr, A. Biewald, et al. preliminary manuscript, 2024

The next few pages contain all the main scientific publications, which have been summarized previously.

ACS APPLIED MATERIALS & INTERFACES

Research Article

Cite This: ACS Appl. Mater. Interfaces 2019, 11, 20838−20844

www.acsami.org

Temperature-Dependent Ambipolar Charge Carrier Mobility in Large-Crystal Hybrid Halide Perovskite Thin Films

Alexander Biewald,[†,‡] Nadja Giesbrecht,[†,‡] Thomas Bein,[†,‡] Pablo Docampo,[§] Achim Hartschuh,[†,‡] and Richard Ciesielski*[,†,‡]

[†]Department of Chemistry and Center for NanoScience (CeNS), LMU Munich, Butenandtstr. 5-13, 81377 Munich, Germany

[‡]Nanosystems Initiative Munich (NIM), LMU Munich, Schellingstr. 4, 80799 Munich, Germany

[§]School of Electrical and Electronic Engineering, Newcastle University, Merz Court, NE1 7RU Newcastle upon Tyne, United Kingdom

Supporting Information

ABSTRACT: Perovskite-based thin-film solar cells today reach power conversion efficiencies of more than 22%. Methylammonium lead iodide (MAPI) is prototypical for this material class of hybrid halide perovskite semiconductors and at the focal point of interest for a growing community in research and engineering. Here, a detailed understanding of the charge carrier transport and its limitations by underlying scattering mechanisms is of great interest to the material's optimization and development. In this article, we present an all-optical study of the charge carrier diffusion properties in large-crystal MAPI thin films in the tetragonal crystal phase from 170 K to room temperature. We probe the local material properties of individual crystal grains within a MAPI thin film and find a steady decrease of the charge carrier diffusion constant with increasing temperature. From the resulting charge carrier mobility, we find a power law dependence of $\mu \propto T^m$ with $m = -(1.8 \pm 0.1)$. We further study the temperature-dependent mobility of the orthorhombic crystal phase from 50 to 140 K and observe a distinctly different exponent of $m = -(1.2 \pm 0.1)$.

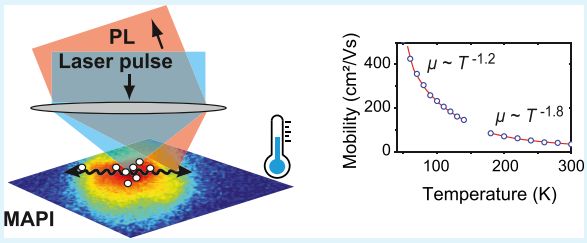

KEYWORDS: *hybrid halide perovskite, MAPI, solar cell material, ambipolar charge carrier mobility, temperature dependence, photoluminescence, remote detection*

INTRODUCTION

In the context of global climate change, the development and optimization of photovoltaics play a major role. It is desirable to establish alternatives to silicon-based technologies that can fill gaps in productivity in a flexible and fast way.[1,2] With a solar cell efficiency of more than 22%,[3] hybrid organic−inorganic perovskites proved to be a very promising class of materials for this purpose. In addition to the outstanding device performance, the low-cost solution-based processing techniques and the abundance of the raw materials are the most important factors in favor of hybrid perovskites.[4−6] Apart from photovoltaics, perovskite-based photodetectors,[7,8] light-emitting diodes,[9] and lasers[10] were successfully developed. For all of these applications, a precise and detailed knowledge and understanding of the charge carrier dynamics are key for further progress in optimization and engineering. Despite the good device performance in photovoltaics, the drift mobility of $\mu = 10...100$ cm^2/Vs in methylammonium lead iodide (MAPI) is not particularly high when compared with that of conventional semiconductors, such as silicon, gallium arsenide, or cadmium selenide[11,12] with $\mu > 1000$ cm^2/Vs. On the other hand, they show quite high typical diffusion lengths of up to several microns, which means that diffusing charge carriers will very likely reach the contact electrodes within their lifetime.

In thin films, the physical transport properties can differ from those of macroscopic samples because of the influence of interfaces and the local grain structure. In this context, a microscopic measurement approach for the charge carrier mobility has the advantage that it suits the situation of thin-film devices and that it can help identify local variations or the influence of grain boundaries. The charge carrier mobility μ of single-crystalline semiconductors is typically limited by scattering off impurities and phonons.[13] Since these mechanisms result in different temperature dependencies, low-temperature measurements help differentiate them.[13] Elastic scattering off of acoustic phonons leads to a power law of $\mu \propto T^{-3/2}$, inelastic scattering off of optical phonons leads to a power law of $\mu \propto T^{-1/2}$, and scattering off impurities or ions results in a power law of $\mu \propto T^{+3/2}$. If a mixture of those effects is present at the same time, the reciprocal mobilities add up, and the resulting exponent can take different values. Based on

Received: March 14, 2019
Accepted: May 17, 2019
Published: May 17, 2019

DOI: 10.1021/acsami.9b04592
ACS Appl. Mater. Interfaces 2019, 11, 20838−20844

the exponent only, experimental studies on MAPI would very consistently suggest that acoustic phonon scattering ($T^{-3/2}$) should be the dominant scattering mechanism,[14−16] but its polar crystal structure makes it very unlikely to be the correct description.[17,18] A recent theoretical study on MAPI found a power law of $\mu \propto T^{-2.11}$ and assigned this to a more complex interplay between optical phonon scattering and lattice fluctuations,[19] whereas an analysis of the temperature-dependent photoluminescence (PL) line widths indicated that optical phonons play a major role in mobility.[17]

In this paper, we study the temperature-dependent diffusion properties of highly crystalline MAPI thin films in an all-optical, that is, contactless, fashion. We show that transport of photoexcited charge carriers is driven by diffusion and can be visualized through photoluminescence in a very direct way in time and space. The direct measurement of the diffusion properties via time-resolved PL microscopy is complementary to the various existing measurements of drift mobility.[14−16,18,20,21] With our contactless and voltage-free experimental approach we contribute to the long-standing question of charge carrier mobility limitations.

EXPERIMENTAL APPROACH

We use highly crystalline MAPI thin films of 400 nm thickness on a glass substrate covered with a 500 nm-thick layer of poly(methyl methacrylate) to prevent degradation. The individual crystal grains reach lateral sizes of up to 10 μm, as is shown in a scanning electron micrograph in Figure 1a. In the vertical direction, these MAPI films

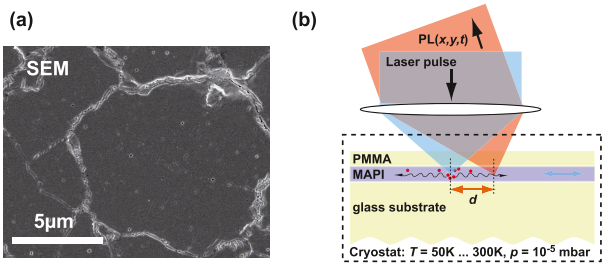

Figure 1. (a) Scanning electron micrograph of a MAPI thin-film sample in top view. The monocrystalline grains reach sizes of several microns. (b) Schematic of the experimental approach: confocal images are recorded by raster-scanning the sample with overlapping excitation and detection position. Detection beam scans are obtained after local excitation at a fixed position while scanning the detection point d. PL from mobile charge carriers is detected as a function of position x, y (distance d), time delay t, and temperature T.

are continuous and monocrystalline, as has been reported elsewhere.[22,23] When used in solar cells with state-of-the-art materials in a planar device configuration, these MAPI thin films can achieve a power conversion efficiency of 18% (see the Supporting Information, Section S2).

The sample is situated within a closed-cycle liquid helium cryostat on an *xyz*-piezo positioning stage. An additional heater within the vacuum chamber allows us to adjust the sample temperature from 5 to 350 K; here, we use the range of 170−300 K for the tetragonal crystal phase and 50−150 K for the orthorhombic crystal phase. Below a temperature of about 50 K, the model is not able to provide a reliable fit to the transients anymore, which is why we chose this as the lower limit. A picosecond pulsed diode laser (635 nm/1.95 eV, 250 kHz repetition rate) is focused at the sample by an air objective (NA 0.75) to create a localized charge carrier distribution, illustrated in Figure 1b and the Supporting Information Section S1. The laser fluence was adjusted such that the peak charge carrier density n would not exceed 5×10^{18} cm^{-3} to prevent a substantial nonlinear contribution to the charge carrier decay dynamics.[24] The photocreated electrons and holes undergo diffusion and eventually recombine, emitting photoluminescence (PL) light centered at a temperature-dependent wavelength between 768 nm (1.61 eV) and 781 nm (1.59 eV). PL of the film is detected as a function of distance d between excitation and detection, time t, and temperature T. This is achieved by an additional scanning mirror in the detection beam path, an avalanche photodiode, and fast electronics (time-correlated single-photon counting). The spatial resolution of the setup is about 600 nm, the temporal resolution is 2 ns, and the temperature can be adjusted to below 100 mK accuracy. The diffusion length in MAPI thin films is typically about 10 μm or larger,[4] so the diffusion dynamics is mapped with little spatial averaging.

Through absorption of a photon of sufficient energy, an electron−hole pair is created in the MAPI thin film. The reverse process can occur if an electron and a hole come into proximity, emitting PL light.[25] This emission directly reflects the charge carrier density inside the materials and can thus be used to monitor the local density of mobile charges. Our approach, combining pulsed optical excitation with a remote, time- and space-resolved detection scheme, allows us to selectively excite individual grains within a thin film and then to monitor the lateral movement and decay of the charge carriers. By analyzing the data in terms of charge carrier diffusion, we can extract the diffusion constant D of the material in a contactless fashion.[26,27]

RESULTS

Figure 2a presents a confocal PL scan of a MAPI thin film at a temperature of 240 K. Individual crystallites are clearly separated by grain boundaries, visible as dark lines. In Figure 2b, PL spectra at different temperatures for the two crystal phases are presented. Similar to earlier reports,[15,17] we observe a blue shift of the PL emission with increasing temperature for each phase. At 150 K, there is a coexistence of the two phases,

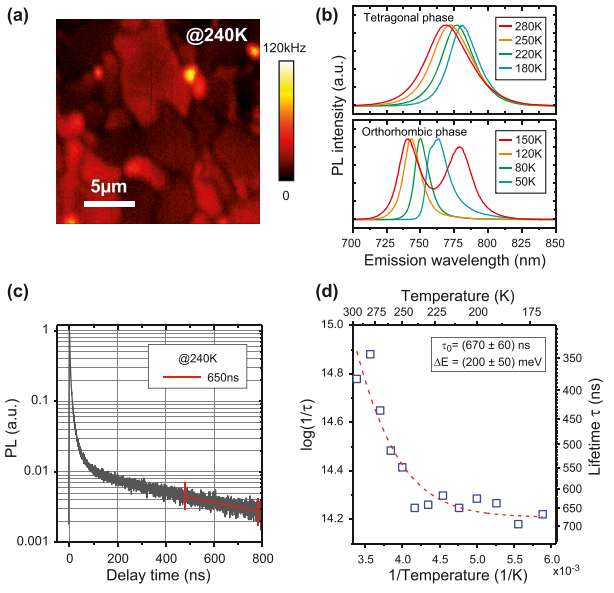

Figure 2. (a) Confocal image of a MAPI thin-film sample at 240 K temperature. Grain boundaries are visible as dark lines, separating the individual crystallites. (b) PL spectra at different temperatures show a blue shift and a broadening of the emission with increasing temperature. (c) PL transient including a lifetime fit at 240 K. (d) Temperature-dependent lifetimes τ in an Arrhenius plot. The dashed line is a fit to the data including a thermally activated decay channel with an energy barrier of ΔE = 200 meV and a constant low-temperature lifetime of τ_0 = 670 ns.

DOI: 10.1021/acsami.9b04592
ACS Appl. Mater. Interfaces 2019, 11, 20838−20844

visible through the two distinctly different bands in the PL spectrum. From recorded PL transients in the confocal spot, we determine the monoexponential PL lifetime, which is equal to the carrier lifetime,[15,25] shown in Figure 2c,d. It is important to note that in a localized measurement, the PL lifetime cannot be determined from the initial decrease because this reflects both fast charge carrier diffusion[26] and bimolecular recombination[25] rather than the monoexponential decay. Rather than this, one has to use the later parts when the relatively fast diffusion has already spread the charges throughout the crystal evenly. In the present case, we use the data from 500 ns onward to determine the monoexponential lifetime, which is found to be roughly constant at 670 ns from 170 to 240 K and to then rapidly decrease to 350 ns at room temperature. The Arrhenius plot in Figure 2d suggests a thermally activated process for the rapid change in lifetime. A fit to the data provides an activation energy of 200 meV and a low-temperature lifetime value of 670 ns for the present temperature range. Local, subwavelength energy fluctuations are known to exist in hybrid perovskite thin films in an energy range of tens of meV to hundreds of meV as a result of distortions of the lattice, surface defects, or ion migration.[28] The observed energy barrier of 200 meV can be explained by such fluctuations, taking into account the fact that the surface quality of large-crystal MAPI thin films is the main source for defects with an impact on the lifetime. Since some variation is observed in the lifetime throughout different samples of the same kind, the lifetime values can serve as a measure of the local surface quality rather than being a universal constant for the material.

In an earlier study, we investigated the charge carrier diffusion dynamics of MAPI on highly crystalline thin films at room temperature.[26] We here repeat and extend these measurements in a series of low-temperature scans on a representative part of a MAPI thin film. We first use the temperature range between 170 K and room temperature to remain within the tetragonal crystal phase of MAPI,[29] which is the most relevant for device applications, and then apply the method to the orthorhombic crystal phase in the temperature range of 50−150 K. Figure 3a shows three confocal PL images of the tetragonal series at increasing temperature. Except for a slightly reduced general image contrast at lower temperatures, the confocal images show no apparent differences. Figure 3b presents intensity-normalized detection beam scans at the same sample area as in Figure 3a, with the position of excitation marked by a cross-hair. The width of the scans differs significantly: at low temperatures it is much less confined than at high temperatures, indicating a faster and more efficient transport at low temperatures as compared with that at high temperatures. This trend can readily explain the changing contrast in the confocal images of Figure 3a: a broader (narrower) detection volume results in lower (higher) optical contrast. The physical reason for the temperature-dependent contrast lies in varying diffusion properties, as will be discussed in the following.

PL transients recorded at increasing distance from the excitation point can directly map the square of the charge carrier population $n(\vec{r}, t)^2$ in time and space.[26,27,30] In Figure 4, we present such transients for the crystal position marked in Figure 3 at four representative temperatures and three representative distances. At the laser position (0 μm), a rapid decay is visible for all four temperatures. At 2 μm distance from the point of excitation, a shoulder in the PL

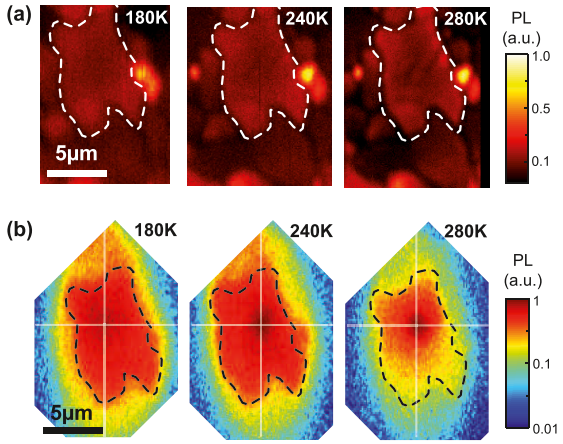

Figure 3. (a) Confocal PL scans of a representative grain (white dashed line) within a MAPI thin film at 180, 240, and 280 K temperatures. The image contrast appears slightly reduced for lower temperatures. (b) PL detection beam scans (log scale) at the same sample position and temperatures, recorded upon focused excitation in the center of the crystallite marked by the white cross-hair. The emission becomes more uniform at lower temperatures, indicating increasingly efficient charge carrier transport.

transient appears, which transforms to a clearly visible delayed peak at a distance of 4 μm below 250 K. The origin of this shoulder/peak lies in the finite velocity of charge carrier diffusion, which leads to the following spatiotemporal distribution of charge carriers after pulsed excitation[26]

$$n(\vec{r}, t) = \frac{N_0}{4\pi Dth} \exp\left(\frac{-r^2}{4Dt}\right) \quad (1)$$

D is the temperature-dependent diffusion constant, N_0 is the initial number of charge carriers, h is the height of the film, $\vec{r}$ is the position relative to the excitation point, and $r = |\vec{r}|$ is the corresponding distance. The detected PL signal is proportional to the square of the charge carrier density $I_{PL}(\vec{r}, t) \propto n(\vec{r}, t)^2$ since an electron and a hole are required to produce a photon. To give a quantitative description of the experimental data, various effects have to be considered. First, eq 1 has to be spatially convoluted with a function $f(\vec{r}) \propto \exp(-r/\sigma)/r$ to account for wave-guiding modes within the thin film,[26,31] where σ is the extinction length for PL light, corresponding to an average penetration depth in the range of the PL emission. Losses in the film are due to scattering and reabsorption. Second, the influence of the finite size of the crystal grains has to be included in the model. In a restricted geometry as shown in Figure 3, the charge carriers cannot travel freely but will be confined to the finite space of the very crystal that was initially excited.[26] We include this effect heuristically through an additional offset term of the PL whose magnitude is adjusted to the signal at later times. Third, the spatial and temporal resolutions of the setup have to be taken into account by a convolution of the theoretical data with the point-spread function (full width at half maximum (FWHM) of 600 nm) and the instrument response function (FWHM of 2 ns). The calculated curves are shown in Figure 4 as solid lines and provide a good fit to the experimental data. The clearly visible initial, fast decay in all transients of Figure 4 can now be understood based on the wave-guiding effect: it predominantly reflects the PL dynamics in the bright spot at the laser position.

DOI: 10.1021/acsami.9b04592
ACS Appl. Mater. Interfaces 2019, 11, 20838−20844

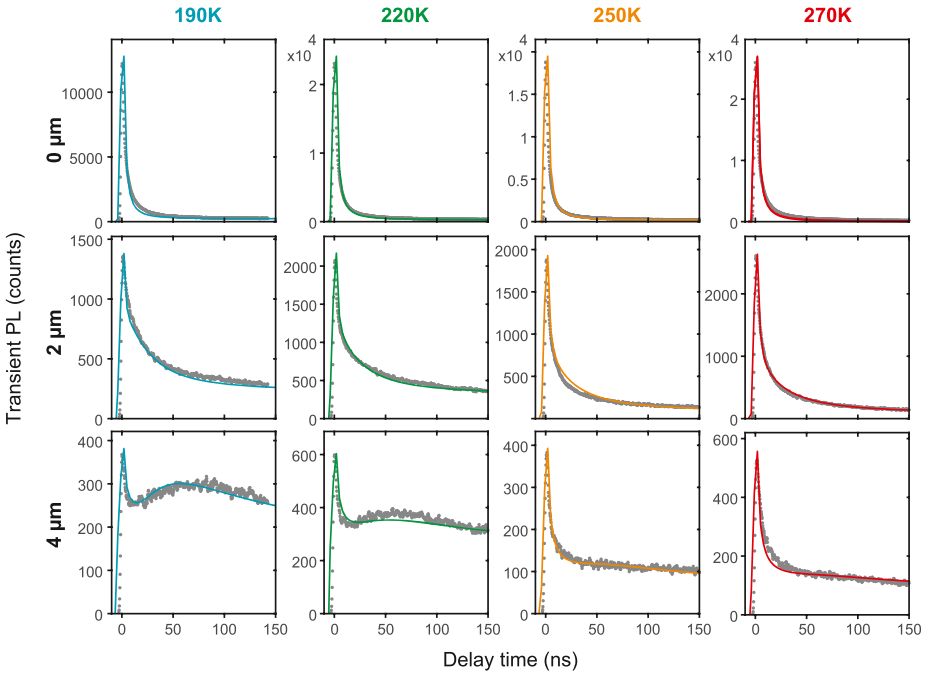

Figure 4. Transient PL signal (points) and a model calculation (lines) for temperatures of 190−270 K (left to right) and distances of 0−4 μm from the laser excitation spot (top to bottom). The theoretical description of the data set is based on charge carrier diffusion and waveguided PL (see main text).

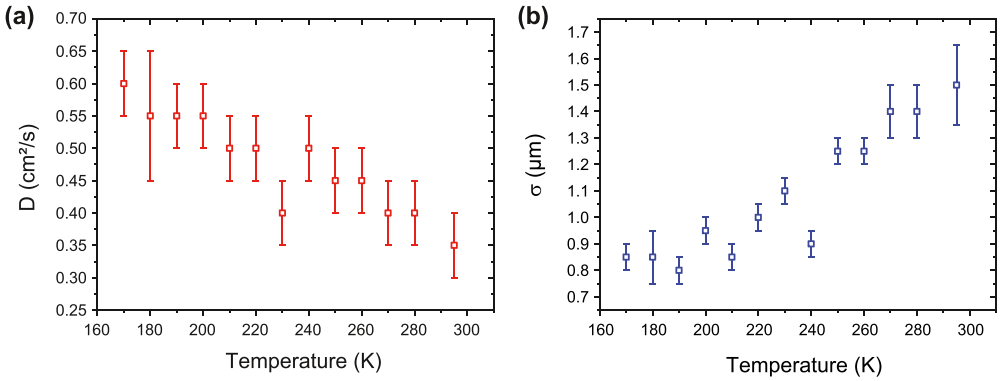

Figure 5. Diffusion constant D and extinction length σ of the PL emission from fits in Figure 4. (a) Diffusion constant decreases from 0.6 cm^2/s at 170 K to 0.35 cm^2/s at 295 K, indicating more frequent charge carrier scattering events. (b) Extinction length of the PL emission smoothly increases from 0.85 μm at 170 K to 1.5 μm at 295 K, which is caused by an increasing Stokes shift.

The second peak/shoulder originates from eq 1, which produces a delayed rise of the PL in time, depending on the distance r from the point of excitation. The exact shape of all of the transients depends on the charge carrier diffusion constant D and the lateral extinction coefficient σ. For each temperature, a set of three parameters (D, σ, and an offset) is sufficient to describe the shape of the transients at all remote distances.

Fitting this model to our PL data allows us to directly determine the charge carrier diffusion constant D and the lateral extinction length σ in the MAPI thin film as a function of temperature. We find clear trends in D and σ with temperature, presented in Figure 5 for the tetragonal crystal phase (additional data on a larger temperature range is presented in the Supporting Information, Section S3). In the given sample, the diffusion constant decreases from 0.60 ± 0.05 cm^2/s at 170 K down to 0.35 ± 0.05 cm^2/s at room temperature, and at the same time, the extinction length increases from 0.85 ± 0.05 to 1.5 ± 0.15 μm. We observe that these numbers vary in amplitude for different samples but show a consistent temperature dependence (cf. the Supporting Information Figures S4−S6). The error bars were estimated from the quality of the model fit.

The morphology of the sample, and with this scattering at surface roughnesses, is not expected to vary with temperature. Changes in σ are thus connected to variations in reabsorption. We know that at room temperature, the PL spectrum is blue-shifted with respect to 170 K;[24] see Figure 2b. The observed increasing extinction length for rising temperature is thus due to an increasing Stokes shift and reduced reabsorption of emitted PL light. As the Stokes shift in MAPI is found to correlate with the degree of disorder,[32] we can interpret this result in terms of a reduced structural disorder in the material at lower temperatures. This is also in good agreement with the

DOI: 10.1021/acsami.9b04592
ACS Appl. Mater. Interfaces 2019, 11, 20838−20844

temperature trend of the diffusion constant in Figure 5a because structural disorder is expected to interfere with charge carrier transport through scattering, in general.[13]

DISCUSSION

We first discuss the relevance and possible benefits of the applied PL-based approach for studying charge carrier transport in perovskite thin films. We then review the possible transport-limiting scattering mechanisms put forward in the literature and compare the theoretical predictions to the observed temperature dependence.

In case that charge carriers can travel distances much longer than the typical film's thickness, they will encounter the film's surface multiple times within their lifetime. For that reason, the interfaces between the layers play a major role in the overall device performance in thin-film photovoltaics.[33−35] It is thus preferable to determine the absorber's properties in a thin-film configuration that is also used in actual devices. The microscopic approach of spatially resolved PL dynamics, on the other hand, still enables us to perform the measurements on a single-crystal level because individual grains can be addressed. This yields insight into the homogeneity of the thin films, which in our case appear to be very uniform, and allows for a direct mapping of the charge carrier movement via the emitted PL. Importantly, no additional metal contacts are required, whose impact on the measurement in terms of doping, internal fields, or the deposition process is nontrivial. Another important advantage of the present approach is the absence of external electric fields and the resulting effects of ion migration. The contactless and voltage-free method provides information on the charge carrier mobility without the influence of ion mobility.

We now discuss our data on charge carrier diffusion in terms of the associated ambipolar charge carrier mobility of the films, which can be directly linked to the impact of different scattering processes. We note that our PL measurements rely on the product of the local electron and hole densities rather than that of a single species; the determined transport properties are thus charge neutral. In other words, we observe ambipolar electron−hole diffusion rather than transport of positive and negative charges. Complementary time-of-flight measurements on the same type of large-crystal MAPI samples at room temperature had shown that electron and hole mobilities are almost identical.[23] This allows us to use the Einstein−Smoluchowski relation to calculate the charge carrier mobility from the diffusion constant, the result of which is presented in Figure 6. In total, we measured the temperature-dependent mobility of four individual crystal grains on two independently synthesized MAPI thin-film samples; the additional data sets can be found in the Supporting Information, Section S3. We find that our data from the tetragonal crystal phase consistently follows a power law of $\mu \propto T^{-(1.8\pm0.1)}$ and a power law of $\mu \propto T^{-(1.2\pm0.1)}$ in the orthorhombic crystal phase. The value of the exponent m in the tetragonal phase is lower than other reported thin-film values, which, measured with various techniques, are mostly centered around $m \approx -1.5$.[14−16] From this, it was concluded that the charge carrier transport is bandlike, and Karakus et al. identified acoustic phonon scattering as the limiting factor for MAPI.[14] The present data, however, does not confirm the notion of acoustic phonon scattering. Within the error margin, the derived exponent is clearly below $m = -1.5$. On the other hand, a more recent study by Shrestha et al. found $m_h = -2.0$ in the tetragonal phase and $m_h = -0.6$ in the orthorhombic phase for holes using time-of-flight measurements on a macroscopic single-crystal sample[18] and attributed this to charge carrier scattering off polar optical phonons. While this number compares well to our results, we note that a time-of-flight experiment also relies on localized photoexcitation with transient detection and is thus conceptually similar to our time-resolved PL studies. In a theoretical study, Mayers et al. suggested carrier scattering off optical phonons and lattice fluctuations to limit charge transport,[19] predicting a value of $m_h = -2.08$ for holes. This theoretical value is in good agreement with ours and offers an explanation for the observed trend. Another approach by Poncé et al.[36] included a larger number of optical phonons while omitting other concepts such as lattice fluctuation, which leads to a power law of $T^{-1.37}$ in the tetragonal and $T^{-2.26}$ in the orthorhombic crystal phase. Their curves are to be understood as upper boundaries for the transport properties of MAPI, limited by phonon scattering only. While the predicted absolute value of 30−80 cm^2/Vs at room temperature[36] agrees well with our results, the exponents differ, indicating that the mobility in our films is limited not only by phonon scattering.

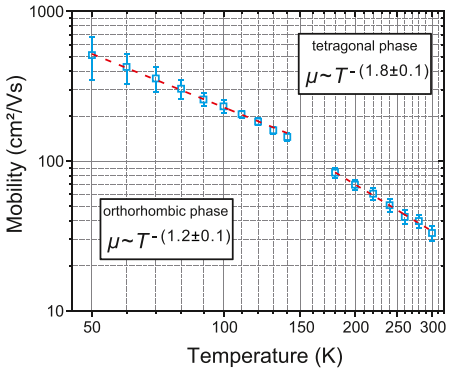

Figure 6. Charge carrier mobility μ, extracted from the diffusion constant D using the Einstein−Smoluchowski relation. The temperature-dependent mobility can be described by a power law $\mu \propto T^m$ with exponent $m = -(1.8 \pm 0.1)$ in the tetragonal crystal phase and $m = -(1.2 \pm 0.1)$ in the orthorhombic crystal phase.

CONCLUSIONS

We demonstrated an all-optical, microscopic approach to map and quantitatively determine the temperature-dependent charge carrier diffusion properties of highly crystalline MAPI thin films. For the tetragonal crystal phase in the temperature range of 170−295 K, the dynamics of the laser-excited charge carriers is quantitatively explained by a classical diffusion model and several decay channels, resulting in the temperature-dependent diffusion constant D. This model can further be applied to the orthorhombic crystal phase. From time-resolved PL data, we identified a thermally activated decay channel with an activation energy of 200 meV that is probably caused by surface defects. Moreover, in the tetragonal phase, we observed a temperature-dependent change of the optical extinction length σ in the film that relates to the Stokes shift between absorption and emission and is a sign of increasing lattice disorder at rising temperatures. From the diffusion constant, the charge carrier mobility μ can be calculated, which is found to follow a power law of $\mu \propto T^{-(1.8\pm0.1)}$ in the tetragonal phase. Our interpretation is that this supports the

DOI: 10.1021/acsami.9b04592
ACS Appl. Mater. Interfaces 2019, 11, 20838−20844

theoretical model of lattice fluctuations and optical phonons as dominant scattering mechanisms and transport limitations for charge carriers in large-crystal MAPI thin films,[19] whereas pure phonon scattering constitutes an upper limit to the mobility.[36] Within the orthorhombic phase, the observed mobility changes are less steep and are described by a power law of $\mu \propto T^{-(1.2\pm0.1)}$. Further studies could focus on the temperature-dependent charge carrier mobility of different material compositions and morphologies as well as the influence of other layers such as electron and hole transporters.

■ ASSOCIATED CONTENT

Supporting Information

The Supporting Information is available free of charge on the ACS Publications website at DOI: 10.1021/acsami.9b04592.

Experimental setup (S1), sample preparation and characterization (S2), additional data sets (S3) (PDF)

■ AUTHOR INFORMATION

Corresponding Author

*E-mail: richard.ciesielski@cup.uni-muenchen.de.

ORCID

Pablo Docampo: 0000-0001-6164-4748
Achim Hartschuh: 0000-0002-0518-6559
Richard Ciesielski: 0000-0002-7780-2904

Notes

The authors declare no competing financial interest.

■ ACKNOWLEDGMENTS

All authors acknowledge financial support from the German Federal Ministry of Education and Research (BMBF) via CISOVSKIT (03SF0516B), the Deutsche Forschungsgemeinschaft through the Nanosystems Initiative Munich (NIM) and e-conversion (EXC 2089/1 - 390776260), and the Bavarian research network SolTech.

■ REFERENCES

(1) Gong, J.; Darling, S. B.; You, F. Perovskite Photovoltaics: Life-Cycle Assessment of Energy and Environmental Impacts. *Energy Environ. Sci.* **2015**, *8*, 1953−1968.

(2) Darling, S. B.; You, F. The Case for Organic Photovoltaics. *RSC Adv.* **2013**, *3*, 17633−17648.

(3) Green, M. A.; Hishikawa, Y.; Dunlop, E. D.; Levi, D. H.; Hohl-Ebinger, J.; Ho-Baillie, A. W. Solar Cell Efficiency Tables (Version 52). *Prog. Photovolt: Res. Appl.* **2018**, *26*, 427−436.

(4) Petrus, M. L.; Schlipf, J.; Li, C.; Gujar, T. P.; Giesbrecht, N.; Müller-Buschbaum, P.; Thelakkat, M.; Bein, T.; Hüttner, S.; Docampo, P. Capturing the Sun: A Review of the Challenges and Perspectives of Perovskite Solar Cells. *Adv. Energy Mater.* **2017**, *7*, No. 1700264.

(5) Polman, A.; Knight, M.; Garnett, E. C.; Ehrler, B.; Sinke, W. C. Photovoltaic Materials: Present Efficiencies and Future Challenges. *Science* **2016**, *352*, No. aad4424.

(6) Green, M. A.; Ho-Baillie, A.; Snaith, H. J. The Emergence of Perovskite Solar Cells. *Nat. Photonics* **2014**, *8*, 506−514.

(7) Shen, L.; Fang, Y.; Wang, D.; Bai, Y.; Deng, Y.; Wang, M.; Lu, Y.; Huang, J. A Self-Powered, Sub-Nanosecond-Response Solution-Processed Hybrid Perovskite Photodetector for Time-Resolved Photoluminescence-Lifetime Detection. *Adv. Mater.* **2016**, *28*, 10794−10800.

(8) Dou, L.; Yang, Y. M.; You, J.; Hong, Z.; Chang, W.-H.; Li, G.; Yang, Y. Solution-Processed Hybrid Perovskite Photodetectors with High Detectivity. *Nat. Commun.* **2014**, *5*, No. 5404.

(9) Tan, Z.-K.; Moghaddam, R. S.; Lai, M. L.; Docampo, P.; Higler, R.; Deschler, F.; Price, M.; Sadhanala, A.; Pazos, L. M.; Credgington, D.; Hanusch, F.; Bein, T.; Snaith, H. J.; Friend, R. H. Bright Light-Emitting Diodes Based on Organometal Halide Perovskite. *Nat. Nanotechnol.* **2014**, *9*, 687−692.

(10) Sutherland, B. R.; Sargent, E. H. Perovskite Photonic Sources. *Nat. Photonics* **2016**, *10*, 295−302.

(11) Herz, L. M. Charge-Carrier Mobilities in Metal Halide Perovskites: Fundamental Mechanisms and Limits. *ACS Energy Lett.* **2017**, *2*, 1539−1548.

(12) Brenner, T. M.; Egger, D. A.; Rappe, A. M.; Kronik, L.; Hodes, G.; Cahen, D. Are Mobilities in Hybrid Organic-Inorganic Halide Perovskites Actually "High"? *J. Phys. Chem. Lett.* **2015**, *6*, 4754−4757.

(13) Yu, P. Y.; Cardona, M. *Fundamentals of Semiconductors: Physics and Materials Properties*, 4th ed.; Springer: Berlin, 2010; Chapter 5.2.

(14) Karakus, M.; Jensen, S. A.; D'Angelo, F.; Turchinovich, D.; Bonn, M.; Cánovas, E. Phonon-Electron Scattering Limits Free Charge Mobility in Methylammonium Lead Iodide Perovskites. *J. Phys. Chem. Lett.* **2015**, *6*, 4991−4996.

(15) Milot, R. L.; Eperon, G. E.; Snaith, H. J.; Johnston, M. B.; Herz, L. M. Temperature-Dependent Charge-Carrier Dynamics in CH3NH3PbI3 Perovskite Thin Films. *Adv. Funct. Mater.* **2015**, *25*, 6218−6227.

(16) Oga, H.; Saeki, A.; Ogomi, Y.; Hayase, S.; Seki, S. Improved Understanding of the Electronic and Energetic Landscapes of Perovskite Solar Cells: High Local Charge Carrier Mobility, Reduced Recombination, and Extremely Shallow Traps. *J. Am. Chem. Soc.* **2014**, *136*, 13818−13825.

(17) Wright, A. D.; Verdi, C.; Milot, R. L.; Eperon, G. E.; Pérez-Osorio, M. A.; Snaith, H. J.; Giustino, F.; Johnston, M. B.; Herz, L. M. Electron-Phonon Coupling in Hybrid Lead Halide Perovskites. *Nat. Commun.* **2016**, *7*, No. 11755.

(18) Shrestha, S.; Matt, G. J.; Osvet, A.; Niesner, D.; Hock, R.; Brabec, C. J. Assessing Temperature Dependence of Drift Mobility in Methylammonium Lead Iodide Perovskite Single Crystals. *J. Phys. Chem. C* **2018**, *122*, 5935−5939.

(19) Mayers, M. Z.; Tan, L. Z.; Egger, D. A.; Rappe, A. M.; Reichman, D. R. How Lattice and Charge Fluctuations Control Carrier Dynamics in Halide Perovskites. *Nano Lett.* **2018**, *18*, 8041−8046.

(20) Zhu, X.-Y.; Podzorov, V. Charge Carriers in Hybrid Organic-Inorganic Lead Halide Perovskites Might Be Protected as Large Polarons. *J. Phys. Chem. Lett.* **2015**, *6*, 4758−4761.

(21) Huang, J.; Yuan, Y.; Shao, Y.; Yan, Y. Understanding the Physical Properties of Hybrid Perovskites for Photovoltaic Applications. *Nat. Rev. Mater.* **2017**, *2*, No. 17042.

(22) Giesbrecht, N.; Schlipf, J.; Oesinghaus, L.; Binek, A.; Bein, T.; Müller-Buschbaum, P.; Docampo, P. Synthesis of Perfectly Oriented and Micrometer-Sized MAPbBr3 Perovskite Crystals for Thin-Film Photovoltaic Applications. *ACS Energy Lett.* **2016**, *1*, 150−154.

(23) Giesbrecht, N.; Schlipf, J.; Grill, I.; Rieder, P.; Dyakonov, V.; Bein, T.; Hartschuh, A.; Müller-Buschbaum, P.; Docampo, P. Single-Crystal-Like Optoelectronic-Properties of MAPbI3 Perovskite Polycrystalline Thin Films. *J. Mater. Chem. A* **2018**, *6*, 4822−4828.

(24) Crothers, T. W.; Milot, R. L.; Patel, J. B.; Parrott, E. S.; Schlipf, J.; Müller-Buschbaum, P.; Johnston, M. B.; Herz, L. M. Photon Reabsorption Masks Intrinsic Bimolecular Charge-Carrier Recombination in CH3NH3PbI3 Perovskite. *Nano Lett.* **2017**, *17*, 5782−5789.

(25) Davies, C. L.; Filip, M. R.; Patel, J. B.; Crothers, T. W.; Verdi, C.; Wright, A. D.; Milot, R. L.; Giustino, F.; Johnston, M. B.; Herz, L. M. Bimolecular Recombination in Methylammonium Lead Triiodide Perovskite is an Inverse Absorption Process. *Nat. Commun.* **2018**, *9*, No. 293.

(26) Ciesielski, R.; Schäfer, F.; Hartmann, N. F.; Giesbrecht, N.; Bein, T.; Docampo, P.; Hartschuh, A. Grain Boundaries Act as Solid Walls for Charge Carrier Diffusion in Large Crystal MAPI Thin Films. *ACS Appl. Mater. Interfaces* **2018**, *10*, 7974−7981.

(27) Handloser, K.; Giesbrecht, N.; Bein, T.; Docampo, P.; Handloser, M.; Hartschuh, A. Contactless Visualization of Fast

DOI: 10.1021/acsami.9b04592
ACS Appl. Mater. Interfaces 2019, 11, 20838−20844

Charge Carrier Diffusion in Hybrid Halide Perovskite Thin Films. *ACS Photonics* **2016**, *3*, 255−261.
(28) Baumann, A.; Väth, S.; Rieder, P.; Heiber, M. C.; Tvingstedt, K.; Dyakonov, V. Identification of Trap States in Perovskite Solar Cells. *J. Phys. Chem. Lett.* **2015**, *6*, 2350−2354.
(29) Onoda-Yamamuro, N.; Matsuo, T.; Suga, H. Calorimetric and IR Spectroscopic Studies of Phase Transitions in Methylammonium Trihalogenoplumbates (II). *J. Phys. Chem. Solids* **1990**, *51*, 1383−1395.
(30) Tian, W.; Zhao, C.; Leng, J.; Cui, R.; Jin, S. Visualizing Carrier Diffusion in Individual Single-Crystal Organolead Halide Perovskite Nanowires and Nanoplates. *J. Am. Chem. Soc.* **2015**, *137*, 12458−12461.
(31) Pazos-Outón, L. M.; Szumilo, M.; Lamboll, R.; Richter, J. M.; Crespo-Quesada, M.; Abdi-Jalebi, M.; Beeson, H. J.; Vrućinić, M.; Alsari, M.; Snaith, H. J.; Ehrler, B.; Friend, R. H.; Deschler, F. Photon Recycling in Lead Iodide Perovskite Solar Cells. *Science* **2016**, *351*, 1430−1433.
(32) Singh, S.; Li, C.; Panzer, F.; Narasimhan, K. L.; Graeser, A.; Gujar, T. P.; Köhler, A.; Thelakkat, M.; Huettner, S.; Kabra, D. Effect of Thermal and Structural Disorder on the Electronic Structure of Hybrid Perovskite Semiconductor CH3NH3PbI3. *J. Phys. Chem. Lett.* **2016**, *7*, 3014−3021.
(33) Tan, H.; et al. Efficient and Stable Solution-Processed Planar Perovskite Solar Cells via Contact Passivation. *Science* **2017**, *355*, 722−726.
(34) Chen, Q.; Zhou, H.; Song, T.-B.; Luo, S.; Hong, Z.; Duan, H.-S.; Dou, L.; Liu, Y.; Yang, Y. Controllable Self-Induced Passivation of Hybrid Lead Iodide Perovskites toward High Performance Solar Cells. *Nano Lett.* **2014**, *14*, 4158−4163.
(35) Zhou, H.; Chen, Q.; Li, G.; Luo, S.; Song, T.-b.; Duan, H.-S.; Hong, Z.; You, J.; Liu, Y.; Yang, Y. Interface Engineering of Highly Efficient Perovskite Solar Cells. *Science* **2014**, *345*, 542−546.
(36) Poncé, S.; Schlipf, M.; Giustino, F. Origin of Low Carrier Mobilities in Halide Perovskites. *ACS Energy Lett.* **2019**, *4*, 456−463.

DOI: 10.1021/acsami.9b04592
ACS Appl. Mater. Interfaces 2019, 11, 20838−20844

Supporting Information: Temperature dependent ambipolar charge carrier mobility in large crystal hybrid halide perovskite thin films

Alexander Biewald,[†] Nadja Giesbrecht,[†] Thomas Bein,[†] Pablo Docampo,[‡] Achim Hartschuh,[†] and Richard Ciesielski[*,†]

[†]*Department of Chemistry and Center for NanoScience (CeNS), LMU Munich, Butenandtstr. 5-13, 81377 Munich, Germany, Nanosystems Initiative Munich (NIM), LMU Munich, Schellingstr. 4, 80799 Munich, Germany*

[‡]*School of Electrical and Electronic Engineering, Newcastle University, Merz Court, NE1 7RU, Newcastle upon Tyne, United Kingdom*

E-mail: achim.hartschuh@lmu.de,richard.ciesielski@cup.uni-muenchen.de

S1 Experimental setup

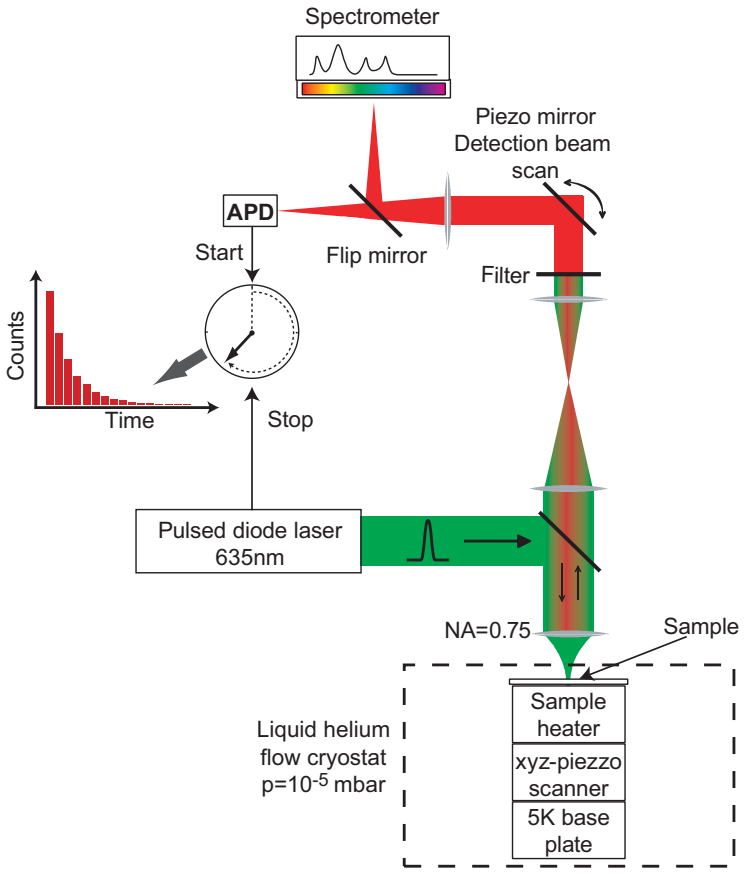

Figure S1: Schematic of the optical low temperature setup. The sample is placed inside a vacuum chamber that can be cooled down to about 5 K through a closed-cycle liquid helium flow cryostat (attocube AttoDRY 800). A heater below the sample allows to access the full temperature regime from 5 K to 300 K. The sample is optically excited by a pulsed diode laser at 635 nm wavelength. Confocal scans are performed using the piezo scanner within the cryostat. Detection beam scans are obtained after local excitation at a fixed position while scanning the detection beam over the detector (fast APD or spectrometer). Time correlated single photon counting (TCSPC) electronics allow to record transients of the signal. PL from diffusing charge carriers is then detected as a function of position, time delay, and temperature.

S2 Sample preparation and characterization

The sample preparation follows the route of Giesbrecht et al.[1] with modifications for methylammonium lead iodide[2] and was carried out in a glove box under nitrogen atmosphere. We used 160 μm thick borosilicate microscope cover slips as substrates which we covered for better wetting with 0.2 wt% solution of Al_2O_3 nanoparticles (Sigma Aldrich <50 nm particle size, 20 wt%) in isopropanol at 2000 rpm for 30 s. This resulted in about 10 % coverage of the substrate. A 62 wt% perovskite precursor solution with lead acetate ($PbAc_2 \times 3H_2O$, Sigma Aldrich 99.999 %) and methylammonium iodide (MAI, Dyesol) in a 1:3 ratio was prepared in a solvent mixture tetrahydrothiophene 1-oxide (THTO, Alpha Aesar, 97 %) / dimethylformamide (DMF, Sigma Aldrich anhydrous) with 13 vol% THTO and spin-coated for 3 min at 5000 rpm. After spin-coating, the film appears yellow and transparent and after 5 min turns orange-brown when pre-crystallizes at room temperature to the perovskite. After pre-crystallization, the substrate was transferred to the hotplate and annealed at 130 °C for 5 min. The sample was then covered with a layer of approximately 500 nm polymethyl methacrylate (PMMA) by spin coating to prevent moisture driven degradation.

These high quality MAPI thin films can achieve a power conversion efficiency of up to 18 % when used in devices with state-of-the-art materials in a planar device configuration consisting of fluorine doped tin oxide (FTO), TiO_2, MAPI, spiro-OMeTAD, and Au-contacts as shown in Figure S2. Figure S3 presents a cross section of such a solar cell, demonstrating the homogeneous material quality. Further studies on the local crystallinity of these thin films were conducted elsewhere.[2]

For the given sample material, no measurable light soaking effect[3] was present, indicating that the PL had already reached its steady-state regime by illumination inside the glove box.

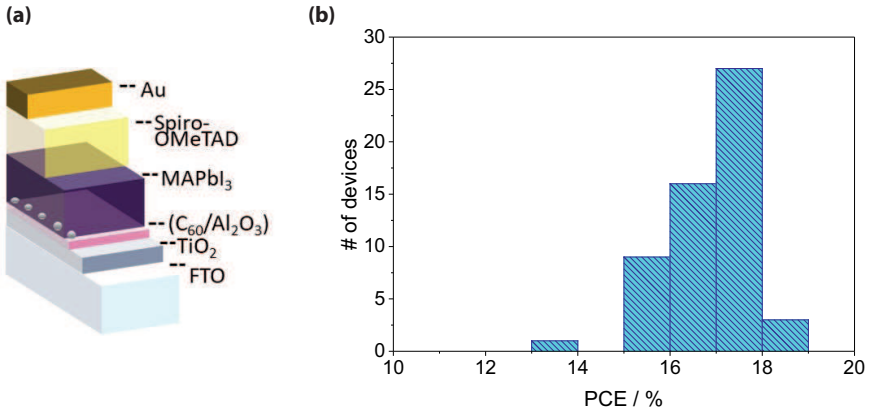

Figure S2: Solar cell device performance. (a) Schematic of the used solar cell architecture. (b) Power conversion efficiency statistic.

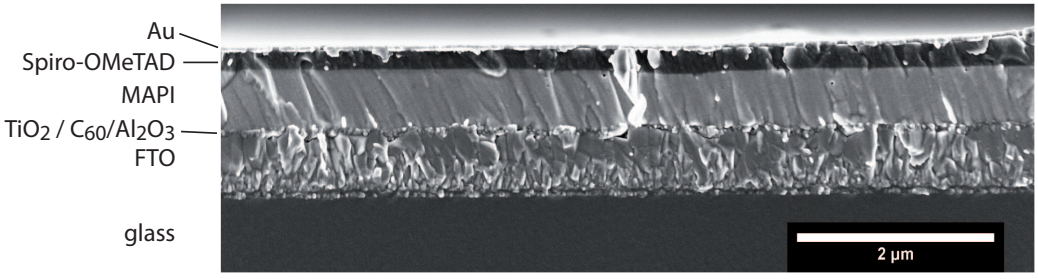

Figure S3: SEM Cross section of a MAPI based solar cell as described in Figure S2. The MAPI thin film is homogeneous in the vertical direction.

S3 Additional data sets

We used two different samples (S1 and S2) of large crystal MAPI thin films which were produced as described in the previous section and measured a total of four individual crystall grains on them. Due to experimental restrictions, the accessible temperature range for the four positions varied. Figure S4 presents the fit results for the diffusion constant D and the extinction length σ from the individual sets of transients. Near the phase transition, it is not possible to fit our model to the data in a reliable fashion because of the coexistence of the two PL bands, therefore the range of 150 K to 170 K has been omitted. We note, that the absolute values of the diffusion constant for the two samples differ by a factor of two, which lies within the typical range of different batches, the temperature depencende, however, is identical. Within the orthorhombic crystal phase, the extinction length increases again when the temperature is further reduced. As discussed in the main manuscript, the extinction length represents an average penetration depth in the spectral range of the PL emission with losses in the film due to scattering and re-absorption. Since the evolution of the PL lineshape in the orthorhombic crystal phase is more complicated than in the tetragonal phase,[4] the trend cannot be interpreted in terms of a Stokes-shift only. Figure S5 presents the derived mobilities of all four positions.

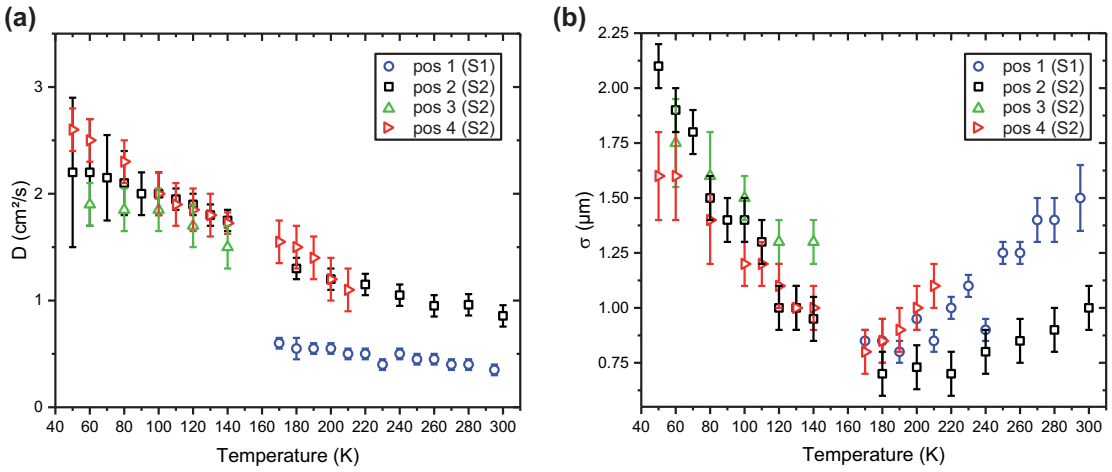

Figure S4: (a) Diffusion constant D and (b) extinction length σ of the PL emission for two different samples (S1 and S2) on four different crystallites (pos. 1...4) in the temperature range of 50 K to room temperature.

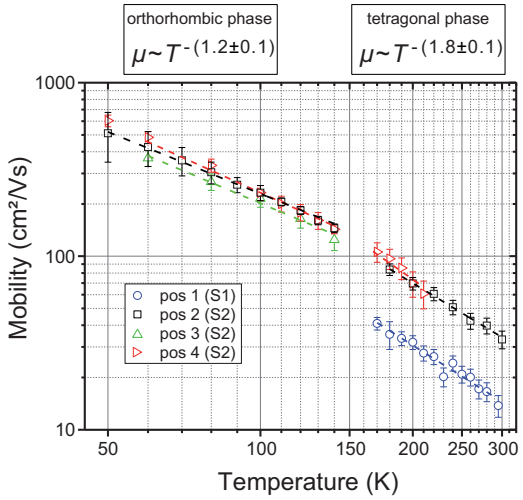

Figure S5: Temperature dependent mobility for two different samples (S1 and S2) on four different crystallites (pos. 1...4) in the temperature range of 50 K to room temperature. The data was derived from the temperature dependent diffusion constants D in Figure S4(a).

Figure S6 presents confocal and remote detection PL scans of a single crystal grain at different temperatures ranging from 70 K to 300 K. In the tetragonal crystal phase, the same behavior as in the main manuscript is observed (c.f. Figure 3a of the main manuscript).

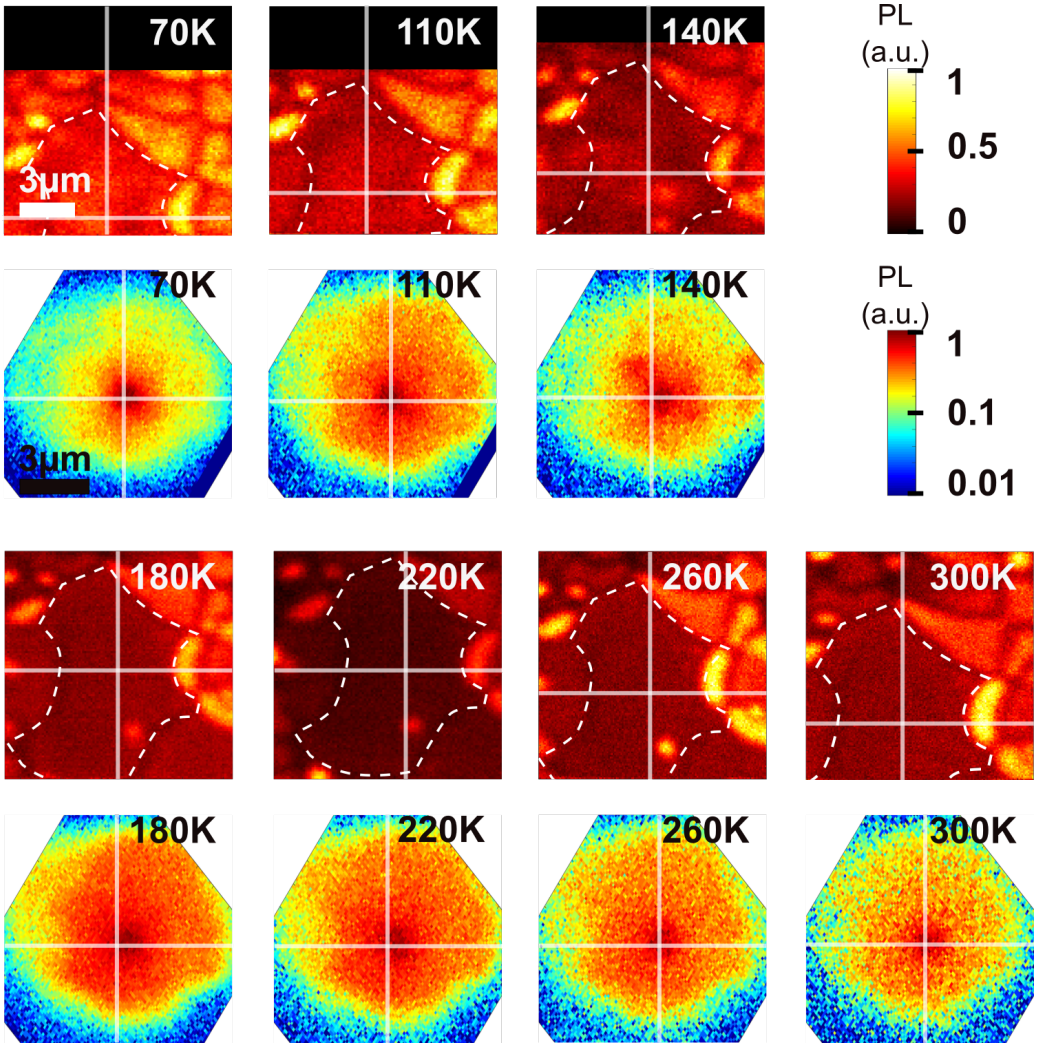

Figure S6: Confocal and remote detection scans of a crystallite from 70 K to 300 K.

References

(1) Giesbrecht, N.; Schlipf, J.; Oesinghaus, L.; Binek, A.; Bein, T.; Müller-Buschbaum, P.; Docampo, P. Synthesis of Perfectly Oriented and Micrometer-Sized MAPbBr3 Perovskite Crystals for Thin-Film Photovoltaic Applications. *ACS Energy Lett.* **2016**, *1*, 150–154.

(2) Giesbrecht, N.; Schlipf, J.; Grill, I.; Rieder, P.; Dyakonov, V.; Bein, T.; Hartschuh, A.; Müller-Buschbaum, P.; Docampo, P. Single–Crystal–Like Optoelectronic–Properties of MAPbI3 Perovskite Polycrystalline Thin Films. *J. Mater. Chem. A* **2018**, *6*, 4822–4828.

(3) Handloser, K.; Giesbrecht, N.; Bein, T.; Docampo, P.; Handloser, M.; Hartschuh, A. Contactless Visualization of Fast Charge Carrier Diffusion in Hybrid Halide Perovskite Thin Films. *ACS Photonics* **2016**, *3*, 255–261.

(4) Wright, A. D.; Verdi, C.; Milot, R. L.; Eperon, G. E.; Pérez-Osorio, M. A.; Snaith, H. J.; Giustino, F.; Johnston, M. B.; Herz, L. M. Electron–Phonon Coupling in Hybrid Lead Halide Perovskites. *Nat. Commun.* **2016**, *7*, 11755.

THE JOURNAL OF PHYSICAL CHEMISTRY C

pubs.acs.org/JPCC Article

Local Disorder at the Phase Transition Interrupts Ambipolar Charge Carrier Transport in Large Crystal Methylammonium Lead Iodide Thin Films

Alexander Biewald, Nadja Giesbrecht, Thomas Bein, Pablo Docampo, Achim Hartschuh,* and Richard Ciesielski*

Cite This: J. Phys. Chem. C 2020, 124, 20757−20764 Read Online

ACCESS | Metrics & More | Article Recommendations | Supporting Information

ABSTRACT: The low-temperature transition from a tetragonal to an orthorhombic crystal phase in methylammonium lead iodide (MAPI) is accompanied by drastic changes in the charge carrier mobility around a critical temperature of approximately 164 K. This transition is studied here using photoluminescence (PL) microscopy on large crystal MAPI thin films, which is extremely sensitive to modifications of the charge carrier dynamics and can resolve physical properties on a single-grain level. The key observation is that ambipolar charge carrier diffusion suddenly stops when the temperature falls below the phase transition temperature. From coexisting PL bands and their spatial distribution, it is concluded that the temperature range from just below the phase transition until about 150 K is determined by a mixed phase where small orthorhombic and tetragonal domains coexist. This results in local disorder, which hinders ambipolar charge carrier diffusion.

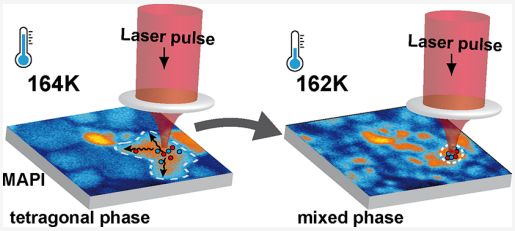

INTRODUCTION

Metal halide perovskite materials show an ever-increasing number of optoelectronic applications,[1] ranging from photovoltaics,[2−4] light detectors,[5,6] light-emitting diodes, and lasers[7,8] to piezo-electric energy harvesting[9] and more. A route to an improved understanding of the material's properties is the study of its behavior at low temperatures, which helps to distinguish the different charge carrier scattering channels.[10−12] Due to their favorable electrooptic properties at low temperatures, perovskite materials have even been proposed for applications in space technology.[13,14] Especially, the prototypical methylammonium lead triiodide (MAPI) is still at the focus of interest as a model system to study the fundamental properties of perovskites. One of these is a change in the crystal structure at a temperature of about 163 K,[15] which heavily influences the optoelectronic properties. Literature reports of temperature-dependent charge carrier transport phenomena that cross this phase transition typically either leave out the area around the transition temperature or use large temperature steps of ≥5 K.[11,12,16,17] It is, for example, known that the charge carrier mobility follows a different power law for the two crystal phases[11,12] and that the band gap differs,[17] but the implications regarding charge carrier dynamics at the phase transition temperature are still unknown. In this context, Dobrovolsky et al. assumed that the existence of nanodomains should hinder charge carrier diffusion in MAPI crystals.[18] Therefore, we focus on temperatures very close to the phase transition to get a better picture of the nature of the changes in charge carrier transport.

Below $T \approx 163$ K, the crystal structure of MAPI changes from the tetragonal to the orthorhombic phase in a first-order phase transition of the PbI_3 lattice.[19,20] During the transition, the MA^+ ions move from an orientational disordered state in the tetragonal phase to an ordered state in the orthorhombic phase.[21] The transition has been investigated using neutron diffraction, X-ray diffraction, and other methods.[19,20,22] Current reports agree that, below the phase transition temperature, there is a temperature range of about 30 K in which the properties of the crystal are in a transitional state.[18,23−25] Two distinct PL peaks are usually attributed to the two crystal phases where the low energy peak at around 1.58 eV belongs to the tetragonal high-temperature phase and the high energy peak at 1.68 eV is indicative of the orthorhombic low-temperature phase. Some studies attribute the existence of two peaks in the spectrum to submicron-sized domains of different crystal phases in the samples,[18,23] whereas others claim that the reason for the double-peak spectrum lies in domains of different degrees of order and disorder of the MA ions.[24] The use of very high fluence shows that this coexistence is a metastable state.[26] The phase transition

Received: July 8, 2020
Revised: August 24, 2020
Published: August 25, 2020

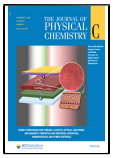

https://dx.doi.org/10.1021/acs.jpcc.0c06240
J. Phys. Chem. C 2020, 124, 20757−20764

temperature itself is known to depend on factors such as the substrate, strain,[25] and crystal size.[27] Larger crystals generally exhibit a clearer trend in the PL energy, which reflects smaller total variations of composition and crystal orientation[27] and underlines that microscopic measurements contain information that ensemble-type experiments cannot yield.

In this manuscript, we investigate large crystal MAPI thin films, which can be implemented in solar cells with an efficiency of up to 18%[12,28] and combine single-crystal properties with thin-film technology. We utilize low-temperature photoluminescence (PL) microscopy as a versatile and sensitive tool to investigate this phase transition in MAPI. Hyperspectral and time-resolved PL microscopy help us to shine new light on the optoelectronic behavior of this material in the presence of disorder related to the phase transition. Our results contribute to the understanding of the transition process from the tetragonal to the orthorhombic crystal phase and for the first time show a complete breakdown of the diffusive charge carrier transport in the orthorhombic crystal phase due to small tetragonal inclusions.

METHODS

The sample is a 400 nm-thick large crystal MAPI film on glass, prepared by spin coating and annealing,[29] and covered with PMMA to prevent degradation. The individual crystal grains reached sizes of 10 μm and more, which makes the sample an ideal platform for lateral transport measurements[28] (see also the Supporting Information, Section S2). It was placed inside a homebuilt confocal low-temperature microscope setup based on a closed cycle helium flow cryostat. An individual crystal grain of the thin film was optically excited using a tightly focused pulsed laser at a wavelength of 635 nm, as schematically illustrated in Figure 1a and Section S2 of the Supporting Information. In addition to confocal scans, a scanning mirror within a detection beam path can be used to selectively collect the signal from outside the point of excitation. This mode of operation with a fixed laser position at the sample is called detection beam scan. For PL detection, we used either an avalanche photon diode (APD) with fast electronics for time-correlated single-photon counting (TCSPC) or a grating-based spectrometer with a sensitive charge-coupled device (CCD) detector. Laser light was removed from the PL signal by spectral longpass filters.

RESULTS

PL Spectra. We first investigate the temperature dependence of MAPI's PL spectra around the phase transition. Figure 1b presents a confocal PL scan of the sample at 164 K in the tetragonal crystal phase with grains of different brightness, separated by dark lines at the grain boundaries. Smaller grains tend to show brighter PL because of restricted carrier diffusion at grain boundaries leading to higher average carrier densities within the individual grains.[30] In Figure 1c, we compare the PL spectrum from the tetragonal (top) with that from the orthorhombic (bottom) crystal phase and those from the mixed phase regime (middle), all recorded at the position marked in Figure 1b. In the tetragonal phase, the spectrum consists of a single, broad peak centered at 770 nm (1.61 eV). Below 164 K, the PL spectrum changes significantly: a second peak at 740 nm (1.68 eV) occurs, which is commonly associated with the orthorhombic crystal phase.[18,23,27] This new peak is a direct indication that the crystal phase has

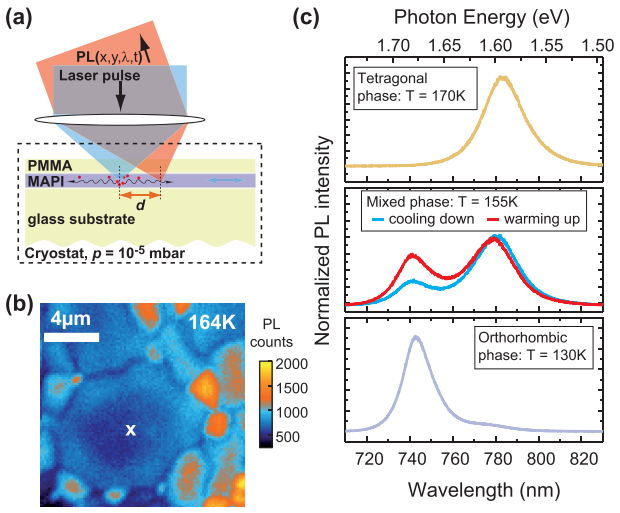

Figure 1. (a) Schematic of the experimental setup. Confocal photoluminescence (PL) images are recorded by raster-scanning the sample with overlapping excitation and detection position. Detection beam scans are obtained after local excitation at a fixed position while scanning the detection point d. PL is detected as a function of position x, y (distance d), wavelength λ, time delay t, and temperature T. (b) PL raster scan of a large crystal MAPI thin film, covered with PMMA at 164 K. "x" denotes the position where spectra are recorded. (c) Spectra from the tetragonal (top) and orthorhombic (bottom) crystal phase. At intermediate temperatures, there is a mixed phase (middle) with both characteristic PL bands visible. A hysteresis of the relative intensities is observed between cooling down and warming up the sample.

changed, but the coexistence of both PL peaks also indicates a coexistence of the two crystal phases.[18,23−25] We observe a dependence of the spectral amplitudes on the direction of the temperature change in the mixed phase regime at 155 K (Figure 1c, middle).

Transition Temperature and Hysteresis. We now study the evolution of the PL spectrum around 163 K at the same position in greater detail, running slow temperature ramps while recording emission spectra. Figure 2a presents the corresponding results for the cooling (top) and the heating process (bottom), normalized to the maximum at each temperature. Near the phase transition temperature, the orthorhombic PL peak (O-peak) has a relatively small amplitude, which steadily increases when the temperature is reduced. At much lower temperatures, it finally dominates the spectrum and the tetragonal PL peak (T-peak) vanishes completely (see Figure 1c, bottom). We report here that, in addition to the occurrence of the O-peak,[23,24,27] the T-peak shows a sudden step of +5 meV toward a slightly higher central energy when the sample is cooled down below a certain temperature, as shown in the top panel of Figure 2a. A rapid change of the PL spectrum at the phase transition had been reported before,[10,31] but close observation demonstrates a discontinuity of the PL spectrum's evolution. There is no observable transition range, but the characteristics of the PL spectrum change in between two individual measurements. At a cooling speed of 1 K/min, about 10 spectra are recorded every minute, which defines our precision to 0.1 K. Despite this, we note that some experimental uncertainty exists about the absolute temperature at the sample because the temperature sensor is separated from the perovskite thin film by the

https://dx.doi.org/10.1021/acs.jpcc.0c06240
J. Phys. Chem. C 2020, 124, 20757−20764

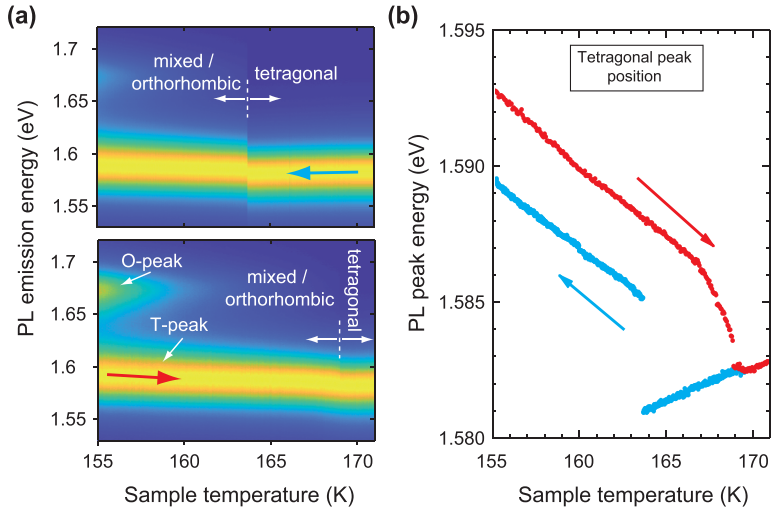

Figure 2. Spectral evolution of the PL of MAPI in the temperature range around the phase transition. (a) PL shows a distinct transition from the tetragonal phase to the mixed phase detected as a sudden jump of the emission (T-peak) from 1.581 to 1.585 eV upon cooling down (top). In the heating process, the transition is less pronounced and at higher temperature (bottom). Experiments were conducted at a speed of about 1 K/min. (b) Hysteresis of the PL energy of the T-peak, extracted from the spectra in panel (a).

glass substrate so that the sample could be slightly warmer than the value given by the sensor. In the reversed process of heating the sample, as shown in the bottom panel of Figure 2a, the step is observed at a higher temperature. The differences between cooling down and warming up the sample are best seen in the trend of the T-peak energy in Figure 2b. In the (pure) tetragonal phase, the peak energy is proportional to the temperature due to an increase of crystal disorder at increasing temperature.[24,32] Interestingly, we see the opposite trend in the mixed phase regime, which indicates that the local disorder initially increases below the transition. Defining the phase transition temperature as the temperature where the step in the PL peak energy occurs, we find that this transition happens at a temperature that is about 5 K higher in the heating process as compared to the cooling process. Hysteresis of the crystal phase transition in MAPI is a known phenomenon,[18,23] and its magnitude of only 5 K is a consequence of the large grain size within the film as the hysteresis effect is reported to be weaker in larger crystals than in smaller ones.[27] Furthermore, in the orthorhombic/mixed phase, we observe an offset for the two directions such that, during the heating process, the PL peak energy is blue-shifted by 3 meV with respect to the cooling process, which can also be seen in the steady-state spectra in Figure 1c at 155 K. It is worth noting at this point that the process is fully reversible and shows the exact same trend and transition temperature of 163 K when the cycle is repeated. The exact value of the transition temperature shows some sample-to-sample and grain-to-grain variation, an effect that is discussed in the next section. It is, however, not influenced by the history of the sample, including previous temperature cycles or moderate sample aging.

Local Transition Temperature. The spectra that were presented until now were recorded in the center of a single crystal grain. This allowed us to determine a phase transition temperature with very high precision from the observed sudden step in the PL peak energy. When the measurement is repeated in an ensemble-type sample averaging over many crystal grains, the results are much less pronounced and there is no sudden step in the PL spectrum but a smooth transition (see the Supporting Information). The reason for this is that every crystal grain features a slightly different transition temperature as we show in the following. We performed a series of hyperspectral microscopic PL images cooling down the sample across the phase transition to then determine the local phase transition temperature from the respective change in the peak energy. Since hyperspectral images take more time than individual spectra, a proportional−integral−derivative (PID) controller had to be used to keep the sample temperature at a constant level, which limited our step size to 1 K in this experiment. Using an arctangent as a fitting function to the peak energy evolution, we determined the transition temperature with an accuracy of 0.5 K (see the Supporting Information for more details). Figure 3 presents

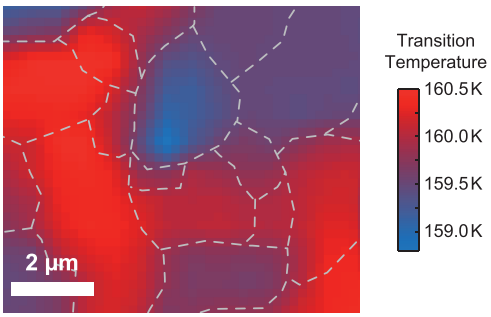

Figure 3. Phase transition temperature for various crystal grains within one thin-film sample with outlined grain boundaries. The transition temperatures are extracted from a series of hyperspectral PL images at different temperatures.

the local transition temperature of a 10 × 10 μ^2/m area, which shows a spread of about 1.5 K from grain to grain. Within the individual grains, on the other hand, we find that the transition temperature is completely uniform, so grains switch their phase at once. The distribution of temperatures across the different crystal grains seems to be random such that there is no obvious correlation between the temperature and any other property, including size or shape. This result is surprising since a

https://dx.doi.org/10.1021/acs.jpcc.0c06240
J. Phys. Chem. C 2020, 124, 20757−20764

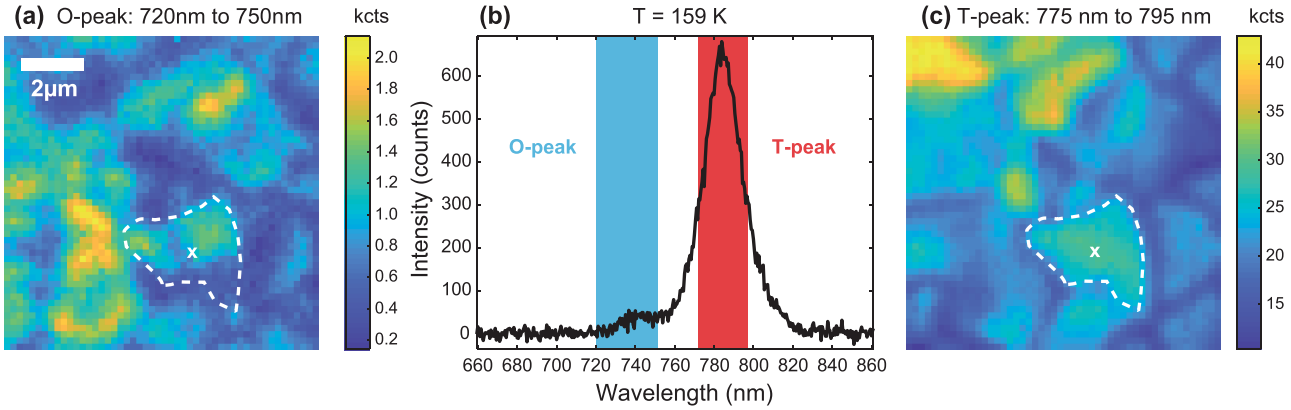

Figure 4. Spectrally resolved PL scan of a MAPI thin film in the mixed phase regime below the phase transition temperature. (a) Integrated PL counts of the orthorhombic O-peak, (b) spectrum at the center of the large, marked crystal grain, and (c) integrated PL counts of the tetragonal T-peak. The ratio of the two peaks fluctuates even within a single crystal grain.

correlation between the average grain size and the transition temperature was reported earlier for grain sizes ranging from few nanometers up to a micron.[27] However, the total range of 1.5 K in our case is not very large, so variations can be caused by small, local differences in strain or surface contamination. This result underlines the necessity to use high-resolution techniques when probing the material's properties of perovskite thin films because, otherwise, important features can be missed. It also shows that, even though the transition temperature can locally be determined very precisely, a thin-film sample changes its crystal phase over a range of about 1.5 K. The Supporting Information presents further data in the form of a video where the sample temperature was tuned across the phase transition slowly, while fast PL scans were performed. These scans also show that the transition temperature is grain-dependent but is homogeneous within an individual crystal grain.

The Mixed Phase Regime. Figure 4 shows PL data in the mixed phase at 159 K for the two PL bands that represent the orthorhombic and the tetragonal crystal phase. Their relative intensities show that tetragonal and orthorhombic domains do not appear at the same positions inside the thin film. The two spectral bands exhibit a very different intensity distribution throughout the MAPI film, which is in accordance with the results of other groups[18,23,26,33] who explained the fragmented PL landscape in the mixed phase regime by the existence of small domains of both phases. These differences are not constrained to the individual crystal grains but show feature sizes much smaller than the individual grains. While our previous measurements, conducted on individual spots within a single grain, showed the coexistence of the PL bands in the mixed phase, the hyperspectral images provide insight into the spatial distribution of the two crystal phases. In contrast to the fact that the individual crystal grains switch from the tetragonal to the mixed phase and back at once, the local mixture of tetragonal and orthorhombic domains forming the mixed phase varies on a smaller scale, which can also be seen from the ratio of the two PL bands, as shown in the Supporting Information, Section S6.

Charge Carrier Diffusion at the Phase Transition. The primary mechanism of charge transport through MAPI is diffusion of free electrons and holes.[34−36] The formation of excitons becomes relevant for the charge transport only at temperatures much lower than the phase transition temperature where it is well known that they coexist with free charge carriers.[36−40] The ambipolar diffusion constant of free charge carriers in the material can be determined by various methods and has a typical value of up to $D = 1\ \mathrm{cm}^2/\mathrm{s}$ ($\mu_{eh} = 39\ \mathrm{cm}^2/\mathrm{Vs}$) in this thin film at room temperature.[34,41] In combination with the long lifetimes of up to microseconds, the diffusion length reaches micrometers, which exceeds the device thickness.[42,43] In a confocal microscope, this means that a substantial part of the photogenerated charge carriers will move out of the excitation volume within tens of nanoseconds.

Figure 5a,b presents confocal PL scans above and below the phase transition within a narrow window of only 2 K. Their main features show a dramatic change: the outline of the individual crystals, visible by the dark grain boundaries at 164 K, becomes indistinguishable in the mixed phase at 162 K. Instead, the image is broken up into many small spots with a highly nonuniform intensity distribution. We note that there was no indication of the crystal grains physically breaking into smaller pieces because, when warming up the sample, the original PL distribution was restored, and the dark grain boundaries became visible again (see Video S1 in the Supporting Information). Our microscope enables us to additionally perform detection beam scans where the point of excitation is kept fixed, and the point of detection is scanned across the sample (see Figure 1a). This method is useful to investigate lateral charge carrier diffusion.[12,30,44,45] We find that, together with the confocal PL images, also, the detection beam images transform completely, as shown in Figure 5c,d. In the tetragonal phase, the entire crystal grain emits light upon local excitation at the grain center, stopped only at the grain boundary due to inhibited charge carrier diffusion.[12,30] Below the phase transition, the emission appears far more localized around the excitation spot. This localization indicates significant changes in the charge carrier diffusion length, calculated from the carrier lifetime τ and the diffusion constant D by $L_D = \sqrt{\tau \cdot D}$. It can have two different origins: either the carrier lifetime τ is strongly reduced or the charge carrier diffusion is strongly hindered altogether. The first option can be ruled out from the confocal PL transients presented in Figure 5e, which show that the PL lifetime changes only by about 20% from 630 ns at 164 K to 514 ns at 162 K. Therefore, we can conclude that, below a temperature of 162 K, the diffusion constant is strongly reduced. Further evidence for this comes from remotely detected PL transients, as shown in

https://dx.doi.org/10.1021/acs.jpcc.0c06240
J. Phys. Chem. C 2020, 124, 20757−20764

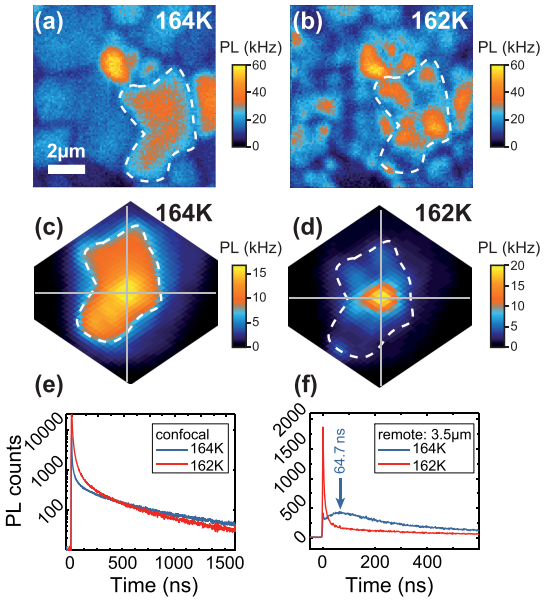

Figure 5. Confocal PL maps of a large crystal MAPI thin film show a change in image features at the phase transition. (a) At a temperature of 164 K, the entire thin film is in the tetragonal crystal phase where the individual crystals are separated by dark lines. (b) Cooling down the sample to 162 K below the phase transition temperature leads to a speckled image with unclear grain boundaries. (c, d) Detection scans at a fixed laser position (crosshair): (c) while PL emission is detected from the whole excited grain upon local excitation at T = 164 K, indicating efficient diffusive transport, (d) below the phase transition at 162 K transport is substantially suppressed; PL transients detected at the point of excitation (e, confocal) and at a distance of 3.5 μm between excitation and the detection point (f, remote), respectively. The PL transients at T = 164 K show the characteristic features of an efficient diffusive transport: a very fast initial decay due to transport of carriers out of the excitation spot (e) and a delayed peak at the remote position (f). Below the phase transition, these features are not observed in the corresponding transients.

Figure 5f. If there is diffusion, then a temporally delayed maximum in the transient appears, which originates from the fact that the charge carriers need some time to travel from the laser excitation spot to the detection spot.[30,45] At 164 K, this maximum appears at a temporal delay of Δt = 64.7 ns for a distance of d = 3.5 μm, independent of the in-plane direction (c.f. Figure 5f). The diffusion constant at this temperature can be estimated using the solution of the two-dimensional diffusion equation[12,30] $D = d^2/(4\Delta t)$ = 0.5 cm^2/s and yields a diffusion length of L_D = 5.6 μm. Below the transition temperature, there is no maximum visible; hence, the charge carriers do not travel that far. It is important to notice that the delayed maximum reappears at about 150 K, which indicates that, at lower temperatures, the diffusion is not inhibited anymore. This is in accordance with the literature that has reported on the electrical transport in the orthorhombic crystal phase, being even more efficient than in the tetragonal phase.[11,12,17,46] Therefore, we interpret our measurements such that, in the temperature region just below the transition, diffusive transport of charge carriers is strongly hindered but sets in again when the temperature is further reduced to reach a homogeneous, orthorhombic phase.

DISCUSSION

Our results shine new light onto the low-temperature phase transition in methylammonium lead iodide thin films that, as a prototypical material system for perovskites, holds particular interest. The soft crystal lattice of MAPI results in several properties that are otherwise atypical for semiconductors and therefore need special attention. Our spectrally resolved PL maps show that small islands of the tetragonal phase survive in the orthorhombic phase, forming instantaneously when crossing the transition temperature. This induces a high degree of local disorder because both crystal phases are in a mixed state, forming microscopic domains and an inhomogeneous energy landscape. An earlier study had shown that the individual grains of this type of thin-film samples have got a homogeneous crystal structure at room temperature;[28] therefore, the observed low-temperature features are a result of the phase transition. As assumed previously,[18] the charge carrier mobility is stopped by this effect such that no spontaneous diffusion of free carriers is observable directly below the transition temperature, while the PL lifetime is nearly unaffected by the change. Therefore, these domains behave distinctly different than the crystal grains within the thin film at other temperatures. Only once the temperature is further reduced and the material reaches a more homogeneous orthorhombic phase, the typical behavior is restored, which means that the crystallites become visible again and a finite charge carrier mobility is observed.[12] The inhibited diffusion occurs correlated with spectral changes in the PL emission, so both effects can serve as a measure of the local transition temperature.

It is known that strained[25] and small[20,27] MAPI crystals have a lower transition temperature than unstrained or larger ones, and the reported range of temperatures reaches from about 130 to 165 K in these cases. The random shape of the grain boundaries in our thin films can lead to local strain variations that can explain the grain-to-grain variations of up to 1.5 K, which we observed. The lateral size of the grains, on the other hand, is probably not the reason for these variations because we observed no correlation between the size and transition temperature, visible in Figure 3. The room temperature synthesis of the MAPI thin films results in a high degree of alignment of the c axis of the tetragonal crystal structure with the substrate;[28] therefore, we do not expect local strain variations to originate from substrate effects here, as reported previously.[25]

We observe that the rapid transition occurs both while cooling and heating the sample but that there is a substantial hysteresis, leading to a higher transition temperature in the heating process. This behavior can be explained by the coexistence of phases below the transition, reflected in local phase islands, as observed in the spectral PL maps. In the heating process, the transition occurs at a temperature of about 5 K higher than in the cooling process and the step in the PL spectrum is less sudden and dramatic (see Figure 2b). This suggests an energy barrier that must be overcome to get to the mixed phase, which is a less-ordered state than the pure tetragonal crystal phase. Coming from the tetragonal phase regime, the original crystal structure can be retained for a longer time before it becomes energetically favorable to switch to the mixed phase region, like the nucleation barrier in droplet formation in supersaturated vapor. When the sample is heated up, the opposite effect occurs, and it becomes energetically

https://dx.doi.org/10.1021/acs.jpcc.0c06240
J. Phys. Chem. C 2020, 124, 20757−20764

favorable to transform completely to the tetragonal phase at a higher temperature. Furthermore, we observe a spectral offset in the PL peak position's hysteresis of 3 meV (see Figure 2b). Such an offset indicates a memory effect in the material, depending on the direction of temperature change and is different from the previously discussed hysteresis of the transition temperature.

CONCLUSIONS

We studied the effects of the tetragonal-to-orthorhombic phase transition in large crystal MAPI thin films on PL emission and charge carrier transport. When cooling the sample below a temperature of about 164 K, the tetragonal crystal phase changes to a mixed phase regime with varying amounts of orthorhombic and tetragonal crystallinity and then gradually converts into the pure orthorhombic crystal phase. Both phases have a characteristic PL band, which can be used to identify them. We found a very sudden peak shift of the PL band from the tetragonal crystal phase upon cooling down; during the heating cycle, the shift occurs at a higher temperature and its magnitude is smaller. Using time-resolved, remote detection PL microscopy, we directly imaged the diffusive charge carrier transport around the transition temperature and observed that it completely stops in the mixed regime because of its inhomogeneous crystal structure. This implies that the local disorder, caused by microscopic domains, inhibits ambipolar charge carrier diffusion and leads to carrier trapping, while the carrier lifetime stays constant. Our microscopic study showed variations of the transition temperature throughout the thin film but proved that individual crystal grains switch their phase at once. The PL spectral shift and the inhibited carrier diffusion can both serve as a very sensitive measure for the crystal phase transition.

ASSOCIATED CONTENT

Supporting Information

The Supporting Information is available free of charge at https://pubs.acs.org/doi/10.1021/acs.jpcc.0c06240.

Experimental setup (Section S1), sample preparation and characterization (Section S2), XRD patterns of the sample (Section S3), extracting the local transition temperature (Section S4), the phase transition in ensemble PL (Section S5), temperature-dependent ratio of PL intensities (Section S6), and temperature-dependent transport dynamics (Section S7) (PDF)

Confocal PL scans across the phase transition (Video S1) (MP4)

AUTHOR INFORMATION

Corresponding Authors

Achim Hartschuh − *Department of Chemistry and Center for NanoScience (CeNS), LMU Munich, 81377 Munich, Germany*; Email: achim.hartschuh@lmu.de

Richard Ciesielski − *Department of Chemistry and Center for NanoScience (CeNS), LMU Munich, 81377 Munich, Germany*; orcid.org/0000-0002-7780-2904; Email: richard.ciesielski@ptb.de

Authors

Alexander Biewald − *Department of Chemistry and Center for NanoScience (CeNS), LMU Munich, 81377 Munich, Germany*

Nadja Giesbrecht − *Department of Chemistry and Center for NanoScience (CeNS), LMU Munich, 81377 Munich, Germany*

Thomas Bein − *Department of Chemistry and Center for NanoScience (CeNS), LMU Munich, 81377 Munich, Germany*; orcid.org/0000-0001-7248-5906

Pablo Docampo − *School of Chemistry, University of Glasgow, Glasgow G12 8QQ, U.K.*; orcid.org/0000-0001-6164-4748

Complete contact information is available at: https://pubs.acs.org/10.1021/acs.jpcc.0c06240

Notes

The authors declare no competing financial interest.

ACKNOWLEDGMENTS

The authors acknowledge the financial support from the German Federal Ministry of Education and Research (BMBF) via CISOVSKIT (03SF0516B), the Deutsche Forschungsgemeinschaft through the Excellence Cluster e-conversion, and from the Bavarian research network SolTech as well as the UK's EPSRC, projects EP/S031103/1 and EP/P03148X/1. The authors would like to thank Markus Döblinger and Steffen Schmidt for valuable discussions.

REFERENCES

(1) Fu, Y.; Zhu, H.; Chen, J.; Hautzinger, M. P.; Zhu, X.-Y.; Jin, S. Metal Halide Perovskite Nanostructures for Optoelectronic Applications and the Study of Physical Properties. *Nat. Rev. Mater.* **2019**, *4*, 169−188.

(2) Petrus, M. L.; Schlipf, J.; Li, C.; Gujar, T. P.; Giesbrecht, N.; Müller-Buschbaum, P.; Thelakkat, M.; Bein, T.; Hüttner, S.; Docampo, P. Capturing the Sun: A Review of the Challenges and Perspectives of Perovskite Solar Cells. *Adv. Energy Mater.* **2017**, *7*, 1700264.

(3) Song, Z.; Chen, C.; Li, C.; Awni, R. A.; Zhao, D.; Yan, Y. Wide-Bandgap, Low-Bandgap, and Tandem Perovskite Solar Cells. *Semicond. Sci. Technol.* **2019**, *34*, No. 093001.

(4) Leijtens, T.; Bush, K. A.; Prasanna, R.; McGehee, M. D. Opportunities and Challenges for Tandem Solar Cells Using Metal Halide Perovskite Semiconductors. *Nat. Energy* **2018**, *3*, 828.

(5) Dou, L.; Yang, Y. M.; You, J.; Hong, Z.; Chang, W.-H.; Li, G.; Yang, Y. Solution−Processed Hybrid Perovskite Photodetectors with High Detectivity. *Nat. Commun.* **2014**, *5*, 5404.

(6) Shen, L.; Fang, Y.; Wang, D.; Bai, Y.; Deng, Y.; Wang, M.; Lu, Y.; Huang, J. A Self−Powered, Sub−nanosecond−Response Solution−Processed Hybrid Perovskite Photodetector for Time−Resolved Photoluminescence−Lifetime Detection. *Adv. Mater.* **2016**, *28*, 10794−10800.

(7) Tan, Z.-K.; Moghaddam, R. S.; Lai, M. L.; Docampo, P.; Higler, R.; Deschler, F.; Price, M.; Sadhanala, A.; Pazos, L. M.; Credgington, D.; et al. Bright Light−Emitting Diodes Based on Organometal Halide Perovskite. *Nat. Nanotechnol.* **2014**, *9*, 687.

(8) Sutherland, B. R.; Sargent, E. H. Perovskite Photonic Sources. *Nat. Photonics* **2016**, *10*, 295.

(9) Jella, V.; Ippili, S.; Eom, J.-H.; Pammi, S. V. N.; Jung, J.-S.; Tran, V.-D.; Nguyen, V. H.; Kirakosyan, A.; Yun, S.; Kim, D.; et al. A Comprehensive Review of Flexible Piezoelectric Generators Based on Organic-Inorganic Metal Halide Perovskites. *Nano Energy* **2019**, *57*, 74−93.

(10) Wright, A. D.; Verdi, C.; Milot, R. L.; Eperon, G. E.; Pérez-Osorio, M. A.; Snaith, H. J.; Giustino, F.; Johnston, M. B.; Herz, L. M. Electron−Phonon Coupling in Hybrid Lead Halide Perovskites. *Nat. Commun.* **2016**, *7*, 11755.

(11) Shrestha, S.; Matt, G. J.; Osvet, A.; Niesner, D.; Hock, R.; Brabec, C. J. Assessing Temperature Dependence of Drift Mobility in

Methylammonium Lead Iodide Perovskite Single Crystals. *J. Phys. Chem. C* **2018**, *122*, 5935−5939.
(12) Biewald, A.; Giesbrecht, N.; Bein, T.; Docampo, P.; Hartschuh, A.; Ciesielski, R. Temperature-Dependent Ambipolar Charge Carrier Mobility in Large-Crystal Hybrid Halide Perovskite Thin Films. *ACS Appl. Mater. Interfaces* **2019**, *11*, 20838−20844.
(13) La-o-vorakiat, C.; Salim, T.; Kadro, J.; Khuc, M.-T.; Haselsberger, R.; Cheng, L.; Xia, H.; Gurzadyan, G. G.; Su, H.; Lam, Y. M.; Marcus, R. A.; et al. Elucidating the Role of Disorder and Free-Carrier Recombination Kinetics in $CH_3NH_3PbI_3$ Perovskite Films. *Nat. Commun.* **2015**, *6*, 7903.
(14) Cardinaletti, I.; Vangerven, T.; Nagels, S.; Cornelissen, R.; Schreurs, D.; Hruby, J.; Vodnik, J.; Devisscher, D.; Kesters, J.; D'Haen, J.; et al. Organic and Perovskite Solar Cells for Space Applications. *Sol. Energy Mater. Sol. Cells* **2018**, *182*, 121−127.
(15) Onoda-Yamamuro, N.; Matsuo, T.; Suga, H. Calorimetric and IR Spectroscopic Studies of Phase Transitions in Methylammonium Trihalogenoplumbates (II). *J. Phys. Chem. Solids* **1990**, *51*, 1383−1395.
(16) Karakus, M.; Jensen, S. A.; D'Angelo, F.; Turchinovich, D.; Bonn, M.; Cánovas, E. Phonon−Electron Scattering Limits Free Charge Mobility in Methylammonium Lead Iodide Perovskites. *J. Phys. Chem. Lett.* **2015**, *6*, 4991−4996.
(17) Milot, R. L.; Eperon, G. E.; Snaith, H. J.; Johnston, M. B.; Herz, L. M. Temperature−Dependent Charge−Carrier Dynamics in $CH_3NH_3PbI_3$ Perovskite Thin Films. *Adv. Funct. Mater.* **2015**, *25*, 6218−6227.
(18) Dobrovolsky, A.; Merdasa, A.; Unger, E. L.; Yartsev, A.; Scheblykin, I. G. Defect-Induced Local Variation of Crystal Phase Transition Temperature in Metal-Halide Perovskites. *Nat. Commun.* **2017**, *8*, 34.
(19) Weller, M. T.; Weber, O. J.; Henry, P. F.; Di Pumpo, A. M.; Hansen, T. C. Complete Structure and Cation Orientation in the Perovskite Photovoltaic Methylammonium Lead Iodide Between 100 and 352 K. *Chem. Commun.* **2015**, *51*, 4180−4183.
(20) Li, D.; Wang, G.; Cheng, H.-C.; Chen, C.-Y.; Wu, H.; Liu, Y.; Huang, Y.; Duan, X. Size-Dependent Phase Transition in Methylammonium Lead Iodide Perovskite Microplate Crystals. *Nat. Commun.* **2016**, *7*, 11330.
(21) Yang, B.; Ming, W.; Du, M.-H.; Keum, J. K.; Puretzky, A. A.; Rouleau, C. M.; Huang, J.; Geohegan, D. B.; Wang, X.; Xiao, K. Real-Time Observation of Order-Disorder Transformation of Organic Cations Induced Phase Transition and Anomalous Photoluminescence in Hybrid Perovskites. *Adv. Mater.* **2018**, *30*, 1705801.
(22) Whitfield, P. S.; Herron, N.; Guise, W. E.; Page, K.; Cheng, Y. Q.; Milas, I.; Crawford, M. K. Structures, Phase Transitions and Tricritical Behavior of the Hybrid Perovskite Methyl Ammonium Lead Iodide. *Sci. Rep.* **2016**, *6*, 35685.
(23) Osherov, A.; Hutter, E. M.; Galkowski, K.; Brenes, R.; Maude, D. K.; Nicholas, R. J.; Plochocka, P.; Bulović, V.; Savenije, T. J.; Stranks, S. D. The Impact of Phase Retention on the Structural and Optoelectronic Properties of Metal Halide Perovskites. *Adv. Mater.* **2016**, *28*, 10757−10763.
(24) Dar, M. I.; Jacopin, G.; Meloni, S.; Mattoni, A.; Arora, N.; Boziki, A.; Zakeeruddin, S. M.; Rothlisberger, U.; Grätzel, M. Origin of Unusual Bandgap Shift and Dual Emission in Organic-Inorganic Lead Halide Perovskites. *Sci. Adv.* **2016**, *2*, No. e1601156.
(25) Shojaee, S. A.; Harriman, T. A.; Han, G. S.; Lee, J.-K.; Lucca, D. A. Substrate Effects on Photoluminescence and Low Temperature Phase Transition of Methylammonium Lead Iodide Hybrid Perovskite Thin Films. *Appl. Phys. Lett.* **2017**, *111*, No. 023902.
(26) Panzer, F.; Baderschneider, S.; Gujar, T. P.; Unger, T.; Bagnich, S.; Jakoby, M.; Bässler, H.; Hüttner, S.; Köhler, J.; Moos, R.; et al. Reversible Laser-Induced Amplified Spontaneous Emission from Coexisting Tetragonal and Orthorhombic Phases in Hybrid Lead Halide Perovskites. *Adv. Opt. Mater.* **2016**, *4*, 917−928.
(27) Stavrakas, C.; Zelewski, S. J.; Frohna, K.; Booker, E. P.; Galkowski, K.; Ji, K.; Ruggeri, E.; Mackowski, S.; Kudrawiec, R.; Plochocka, P.; et al. Influence of Grain Size on Phase Transitions in Halide Perovskite Films. *Adv. Opt. Mater.* **2019**, *9*, 1901883.
(28) Giesbrecht, N.; Schlipf, J.; Grill, I.; Rieder, P.; Dyakonov, V.; Bein, T.; Hartschuh, A.; Müller-Buschbaum, P.; Docampo, P. Single−Crystal−Like Optoelectronic−Properties of $MAPbI_3$ Perovskite Polycrystalline Thin Films. *J. Mater. Chem. A* **2018**, *6*, 4822−4828.
(29) Giesbrecht, N.; Schlipf, J.; Oesinghaus, L.; Binek, A.; Bein, T.; Müller-Buschbaum, P.; Docampo, P. Synthesis of Perfectly Oriented and Micrometer-Sized $MAPbBr_3$ Perovskite Crystals for Thin-Film Photovoltaic Applications. *ACS Energy Lett.* **2016**, *1*, 150−154.
(30) Ciesielski, R.; Schäfer, F.; Hartmann, N. F.; Giesbrecht, N.; Bein, T.; Docampo, P.; Hartschuh, A. Grain Boundaries Act as Solid Walls for Charge Carrier Diffusion in Large Crystal MAPI Thin Films. *ACS Appl. Mater. Interfaces* **2018**, *10*, 7974−7981.
(31) Fang, H.-H.; Raissa, R.; Abdu-Aguye, M.; Adjokatse, S.; Blake, G. R.; Even, J.; Loi, M. A. Photophysics of Organic−Inorganic Hybrid Lead Iodide Perovskite Single Crystals. *Adv. Funct. Mater.* **2015**, *25*, 2378−2385.
(32) Quarti, C.; Mosconi, E.; Ball, J. M.; D'Innocenzo, V.; Tao, C.; Pathak, S.; Snaith, H. J.; Petrozza, A.; De Angelis, F. Structural and Optical Properties of Methylammonium Lead Iodide Across the Tetragonal to Cubic Phase Transition: Implications for Perovskite Solar Cells. *Energy Environ. Sci.* **2016**, *9*, 155−163.
(33) Galkowski, K.; Mitioglu, A. A.; Surrente, A.; Yang, Z.; Maude, D. K.; Kossacki, P.; Eperon, G. E.; Wang, J. T.-W.; Snaith, H. J.; Plochocka, P.; et al. Spatially Resolved Studies of the Phases and Morphology of Methylammonium and Formamidinium Lead Tri-Halide Perovskites. *Nanoscale* **2017**, *9*, 3222−3230.
(34) Herz, L. M. Charge−Carrier Mobilities in Metal Halide Perovskites: Fundamental Mechanisms and Limits. *ACS Energy Lett.* **2017**, *2*, 1539−1548.
(35) Hill, A. H.; Smyser, K. E.; Kennedy, C. L.; Massaro, E. S.; Grumstrup, E. M. Screened Charge Carrier Transport in Methylammonium Lead Iodide Perovskite Thin Films. *J. Phys. Chem. Lett.* **2017**, *8*, 948−953.
(36) Jiang, Y.; Wang, X.; Pan, A. Properties of Excitons and Photogenerated Charge Carriers in Metal Halide Perovskites. *Adv. Mater.* **2019**, *31*, 1806671.
(37) D'innocenzo, V.; Grancini, G.; Alcocer, M. J. P.; Kandada, A. R. S.; Stranks, S. D.; Lee, M. M.; Lanzani, G.; Snaith, H. J.; Petrozza, A. Excitons Versus Free Charges in Organo-Lead Tri-Halide Perovskites. *Nat. Commun* **2014**, *5*, 3586.
(38) Miyata, A.; Mitioglu, A.; Plochocka, P.; Portugall, O.; Wang, J. T.-W.; Stranks, S. D.; Snaith, H. J.; Nicholas, R. J. Direct Measurement of the Exciton Binding Energy and Effective Masses for Charge Carriers in Organic−Inorganic Tri-Halide Perovskites. *Nat. Phys.* **2015**, *11*, 582−587.
(39) Wang, W.; Li, Y.; Wang, X.; Lv, Y.; Wang, S.; Wang, K.; Shi, Y.; Xiao, L.; Chen, Z.; Gong, Q. Density-Dependent Dynamical Coexistence of Excitons and Free Carriers in the Organolead Perovskite C $H_3NH_3PbI_3$. *Phys. Rev. B* **2016**, *94*, 140302.
(40) Ruf, F.; Magin, A.; Schultes, M.; Ahlswede, E.; Kalt, H.; Hetterich, M. Excitonic Nature of Optical Transitions in Electroabsorption Spectra of Perovskite Solar Cells. *Appl. Phys. Lett.* **2018**, *112*, No. 083902.
(41) Shi, D.; Adinolfi, V.; Comin, R.; Yuan, M.; Alarousu, E.; Buin, A.; Chen, Y.; Hoogland, S.; Rothenberger, A.; Katsiev, K.; et al. Low Trap-State Density and Long Carrier Diffusion in Organolead Trihalide Perovskite Single Crystals. *Science* **2015**, *347*, 519−522.
(42) Reid, O. G.; Yang, M.; Kopidakis, N.; Zhu, K.; Rumbles, G. Grain-Size-Limited Mobility in Methylammonium Lead Iodide Perovskite Thin Films. *ACS Energy Lett.* **2016**, *1*, 561−565.
(43) Stranks, S. D.; Eperon, G. E.; Grancini, G.; Menelaou, C.; Alcocer, M. J. P.; Leijtens, T.; Herz, L. M.; Petrozza, A.; Snaith, H. J. Electron-Hole Diffusion Lengths Exceeding 1 Micrometer in an Organometal Trihalide Perovskite Absorber. *Science* **2013**, *342*, 341−344.
(44) Tian, W.; Zhao, C.; Leng, J.; Cui, R.; Jin, S. Visualizing Carrier Diffusion in Individual Single-Crystal Organolead Halide Perovskite

https://dx.doi.org/10.1021/acs.jpcc.0c06240
J. Phys. Chem. C 2020, 124, 20757−20764

Nanowires and Nanoplates. *J. Am. Chem. Soc.* **2015**, *137*, 12458−12461.
(45) Guo, Z.; Manser, J. S.; Wan, Y.; Kamat, P. V.; Huang, L. Spatial and Temporal Imaging of Long-Range Charge Transport in Perovskite Thin Films by Ultrafast Microscopy. *Nat. Commun.* **2015**, *6*, 7471.
(46) Oga, H.; Saeki, A.; Ogomi, Y.; Hayase, S.; Seki, S. Improved Understanding of the Electronic and Energetic Landscapes of Perovskite Solar Cells: High Local Charge Carrier Mobility, Reduced Recombination, and Extremely Shallow Traps. *J. Am. Chem. Soc.* **2014**, *136*, 13818−13825.

https://dx.doi.org/10.1021/acs.jpcc.0c06240
J. Phys. Chem. C 2020, 124, 20757−20764

Supporting Information: Local Disorder at the Phase Transition Interrupts Ambipolar Charge Carrier Transport in Large Crystal Methylammonium Lead Iodide Thin Films

Alexander Biewald,[†] Nadja Giesbrecht,[†] Thomas Bein,[†] Pablo Docampo,[‡] Achim Hartschuh,[*,†] and Richard Ciesielski[*,†,¶]

[†]*Department of Chemistry and Center for NanoScience (CeNS), LMU Munich, Butenandtstr. 5-13, 81377 Munich*

[‡]*School of Chemistry, University of Glasgow, Joseph Black Building, University Pl, Glasgow, G12 8QQ, United Kingdom*

[¶]*Current address: Physikalisch-Technische Bundesanstalt (PTB), Abbestrae 212, 10587 Berlin, Germany*

E-mail: achim.hartschuh@lmu.de; richard.ciesielski@ptb.de

S1 Experimental Setup: Cryogenic Photoluminescence Microscope

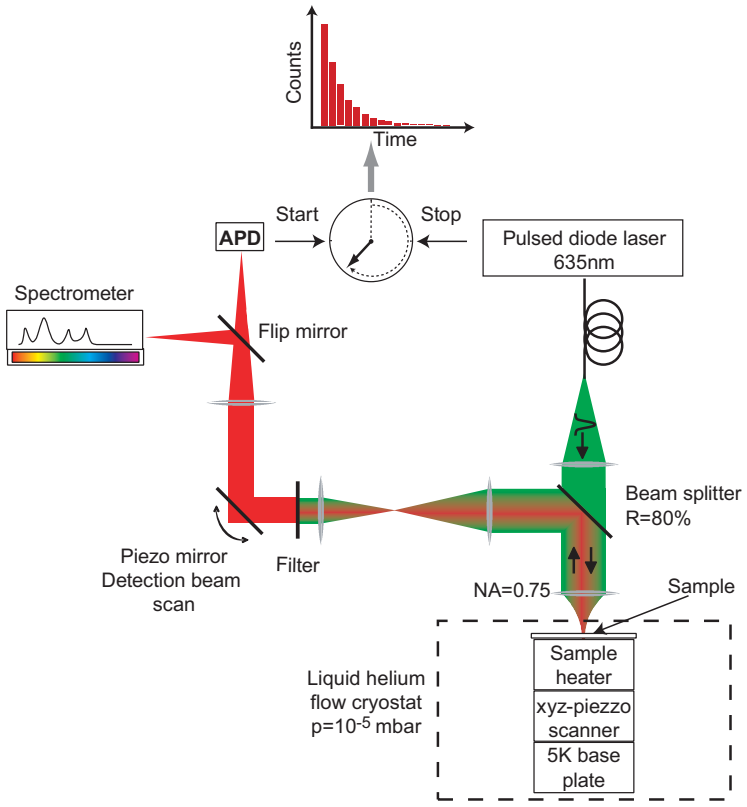

Figure S1: Schematic of the setup

A homebuilt confocal microscope setup based on a closed cycle helium flow cryostat is used, see figure S1. The laser is a pulsed diode laser with a central wavelength of 635 nm at a repetition rate of 250 kHz and a pulse length of below 1 ns. The laser intensity is kept on a low level corresponding to a carrier concentration of $n < 10^{17}/\mathrm{cm}^2$ in the center of the laser spot. This way, a significant contribution of nonlinear effects like bimolecular recombination, Auger recombination or light soaking to the PL decay curves is suppressed. A microscope objective with a numerical aperture of 0.75 and a 100x magnification focuses the laser beam onto the sample and collects the emitted light. Scattered laser light is suppressed by a longpass filter with an edge at 650 nm. A 4f configuration with a piezo-driven double axis scanning

mirror is used to spatially offset the detection area from the laser spot exciting the sample. As detector, either a grating spectrometer with a sensitive CCD camera, or an avalanche photon diode (APD), coupled to fast electronics (time-correlated single photon counting, TCSPC), is used. That way, localized PL spectra and PL transients can be recorded at the point of excitation (confocal case) or at a defined distance from it (remote detection case).

The sample is placed inside a vacuum chamber that can be cooled down to about 5 K through a closed-cycle liquid helium flow cryostat. A heater below the sample allows to access the full temperature regime from 5 K to 300 K.

S2 Sample Preparation and Characterization

The sample preparation follows the route of Giesbrecht et al.[1] with modifications for methylammonium lead iodide[2] and was carried out in a glove box under nitrogen atmosphere. We used 160 μm thick borosilicate microscope cover slips as substrates which we covered for better wetting[3] with a 0.2 wt% solution of Al_2O_3 nanoparticles (Sigma Aldrich <50 nm particle size, 20 wt%) in isopropanol by spin-coating at 2000 rpm for 30 s. This resulted in about 10 % coverage of the substrate. A 62 wt% perovskite precursor solution with lead acetate ($PbAc_2 \times 3H_2O$, Sigma Aldrich 99.999 %) and methylammonium iodide (MAI, Dyesol) in a 1:3 ratio was prepared in a solvent mixture of tetrahydrothiophene 1-oxide (THTO, Alpha Aesar, 97 %) / dimethylformamide (DMF, Sigma Aldrich anhydrous) with 13 vol% THTO and was spin-coated for 3 min at 5000 rpm. After spin-coating, the film appears yellow and transparent and after 5 min turns orange-brown when it pre-crystallizes at room temperature to the perovskite. After pre-crystallization, the substrate was transferred to a hotplate and annealed at 130 °C for 5 min. The sample was then covered with a layer of approximately 500 nm polymethyl methacrylate (PMMA) by spin coating to prevent moisture driven degradation.

These high quality MAPI thin films can achieve a power conversion efficiency of up to

18 % when used in devices with state-of-the-art materials in a planar device configuration consisting of fluorine doped tin oxide (FTO), TiO_2, MAPI, spiro-OMeTAD, and Au-contacts as shown in Figure S2. Figure S3 presents a cross section of such a solar cell, demonstrating the homogeneous material quality. Further studies on the local crystallinity of these thin films were reported elsewhere.[2]

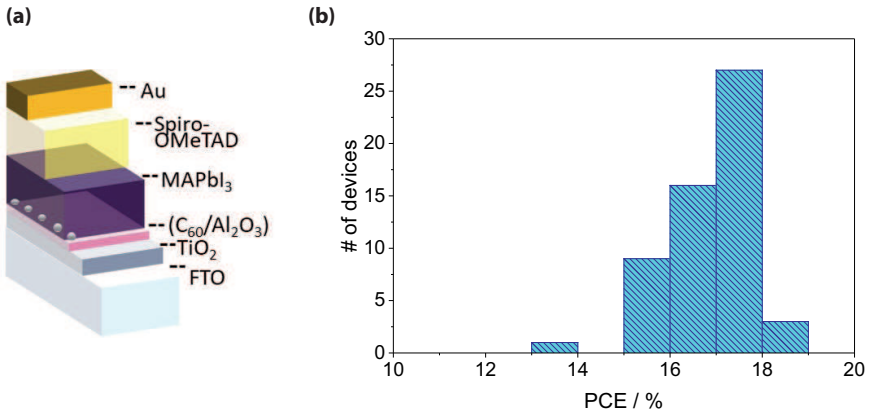

Figure S2: Solar cell device performance. (a) Schematic of the used solar cell architecture. (b) Power conversion efficiency statistics.

For the given sample material, no measurable light soaking effect[4] was present, indicating that the PL had already reached its steady-state regime by illumination inside the glove box.

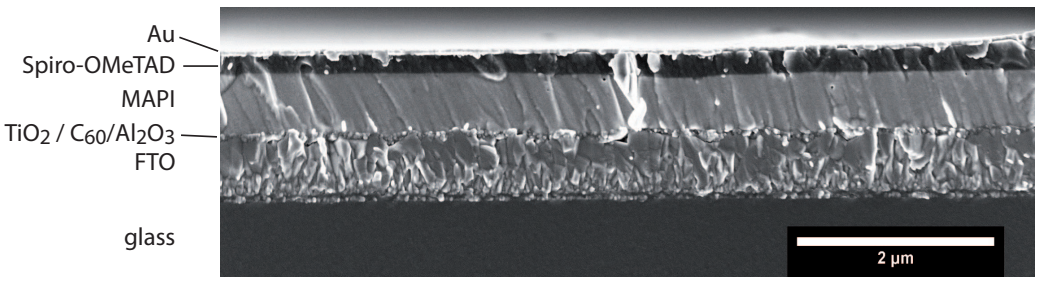

Figure S3: SEM cross section of a MAPI based solar cell as described in Figure S2. The MAPI thin film is homogeneous in the vertical direction.

S3 XRD Patterns of the Sample

Powder XRD was measured of MAPI thin-films which were scraped off the glass substrates and collected in a capillary. XRD diffraction was measured at different temperatures starting with a cooling cycle from 300 K to 10 K and a following heating cycle to 300 K. Afterwards, XRD data was acquired from the same sample in an additional cooling and heating cycle to confirm the reproducibility of the data, see figure S4. The change of the tetragonal phase to the orthorhombic phase mainly appears with peak splitting in the XRD pattern due to a decrease of crystal symmetry. During the cooling process, the formation of the orthorhombic phase is retarded to lower temperatures compared to the phase transition back to the tetragonal phase during the heating cycle (see the red arrows indicating most pronounced reflection splitting). These results are reproducible in the 2nd measurement cycle.

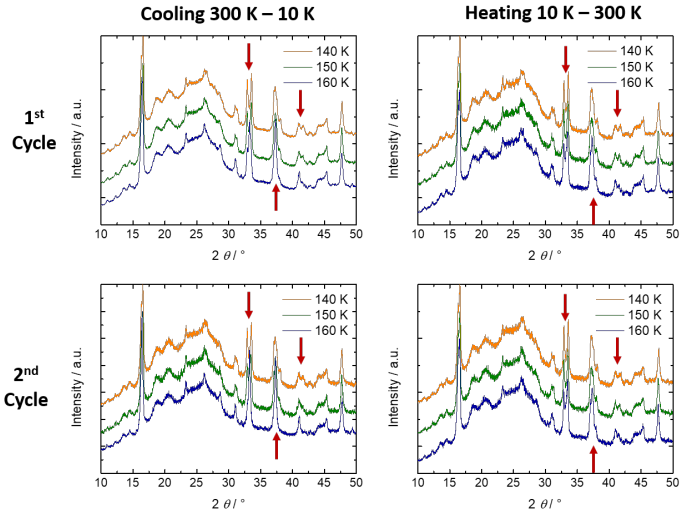

Figure S4: Powder XRD of large crystal MAPI samples. The phase transition from tetragonal to orthorhombic and back is visible through the peak splitting (arrows).

S4 Extracting the Local Transition Temperature

Evaluation of the temperature-dependent hyperspectral images was done independently for every image pixel as illustrated in figure S5. Seven hyperspectral image scans are recorded for temperatures between 157 K and 163 K. First, the peak wavelength is determined by a Gaussian fit to each spectrum taken at one pixel (figure S5(a)), then the transition temperature is determined by a fit of the peak wavelength data to a stretched step function, here an arctangent (figure S5(b)), where the transition temperature is taken as the middle point of the step. The fit has an error bar of ±0.5 K.

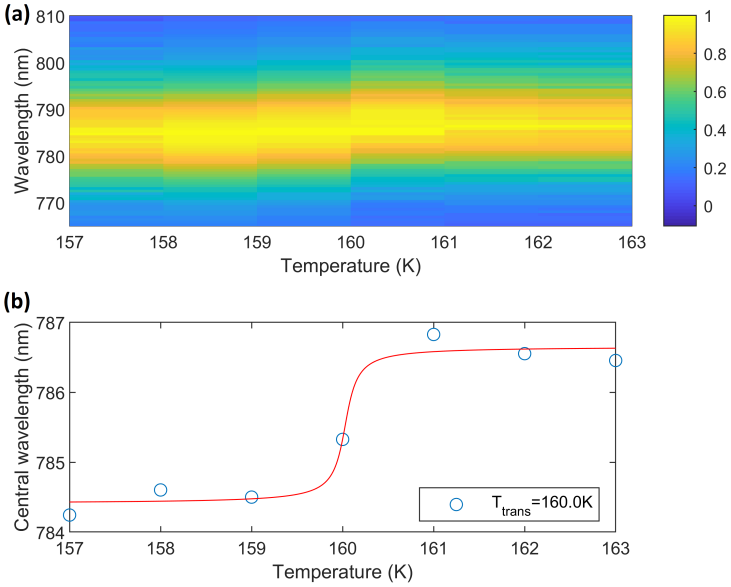

Figure S5: Illustration of the procedure used to determine the local phase transition temperature: (a) Temperature dependent PL spectra taken at a given image pixel. (b) Peak wavelength vs. temperature and fit to the data to determine the local phase transition temperature for the image pixel which is taken as the middle point of the fit function.

S5 The Phase Transition in Ensemble PL

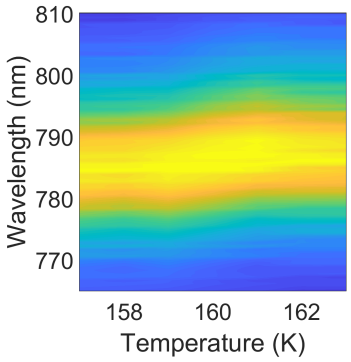

Figure S6: Evolution of the PL spectra detected from a large sample area (diameter 10 μm) during the cooling process near the phase transition. The change in the peak energy is much less pronounced than for the localized measurements shown in figure 2 of the main manuscript.

S6 Temperature dependent ratio of PL intensites

Figure 4 of the main manuscript presents a spectrally resolved PL scan of a large-crystal MAPI thin film at 159 K in the mixed phase. For comparison, figure S7(a,b,c) shows the ratio of the spectrally integrated orthorhombic vs. the tetragonal PL intensity for different temperatures. The orthorhombic peak is integrated from 720 nm to 750 nm and the tetragonal peak is integrated from 770 nm to 790 nm as indicated in figure 4(b) of the main manuscript. At 164 K (figure S7(a)), the sample is in the tetragonal phase and the ratio is homogeneously at zero. At 159 K (figure S7(b)), the sample is in the mixed phase, showing strong, localized fluctuations of the PL ratio. At 141 K (figure S7(c)), the sample is mostly in the orthorhombic phase. Figures S7(d,e,f) show the spectrally integrated PL signal for both peaks as a comparison. The outlines of the grain structure are not visible in the ratio plots, showing the local nature of the phase mixing on a sub-grain level.

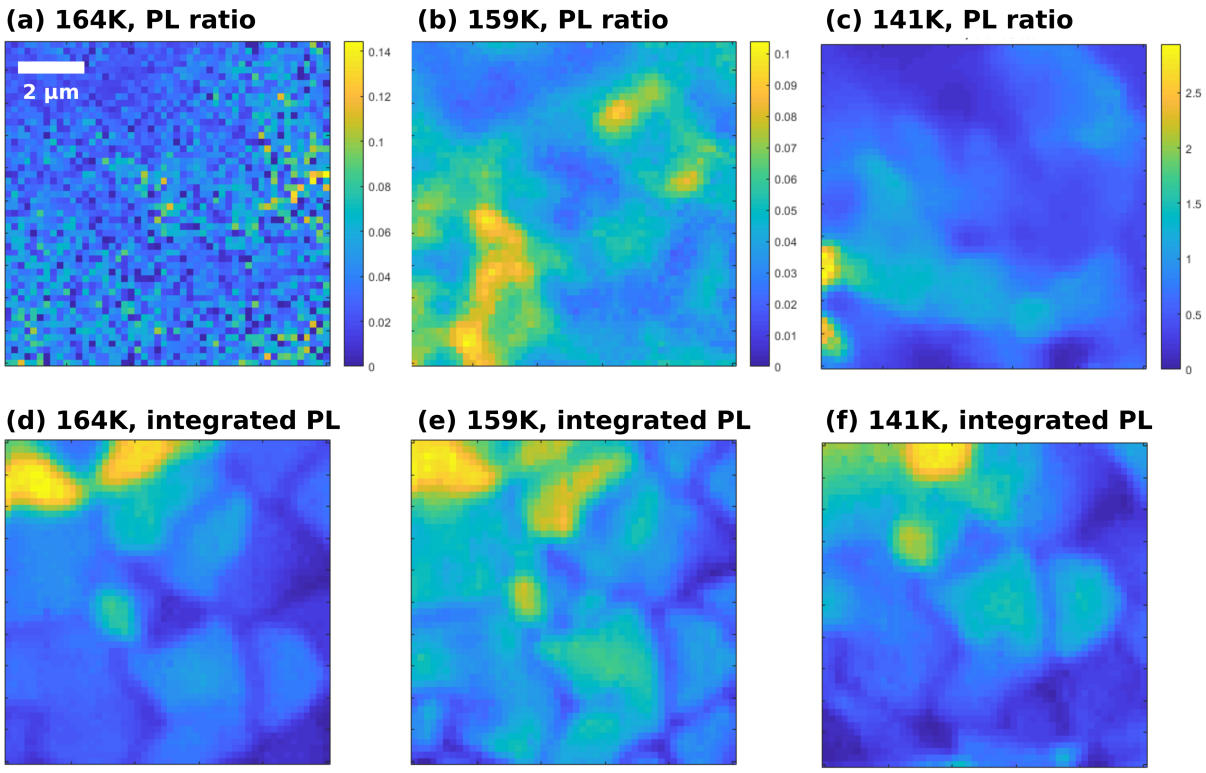

Figure S7: (a,b,c) Integrated signal of the orthorhombic PL peak, divided by the integrated signal of the tetragonal PL peak in the tetragonal (a), mixed (b) and orthorhomic (c) crystal phase. (d,e,f) Integrated signal of both PL peaks for comparison (arbitrary units). The sample area and spectral region is identical to that of figure 4 in the main manuscript.

S7 Temperature dependent transport dynamics

Figure S8 presents PL snapshots of a detection beam scan after pulsed laser excitation that show how charge carriers spread out through the crystal grain in time. Ambipolar charge carrier diffusion leads to a continuous spread of PL light within the excited crystal grain in the tetragonal phase (figure S8(a)), whereas the detected emission in the mixed phase (figure S8(b)) remains mostly in the center of excitation due to inhibited carrier diffusion. Smaller visible deviations from this behaviour at later times ($t > 30\,\mathrm{ns}$) are artifacts due to light scattering effects within the sample.

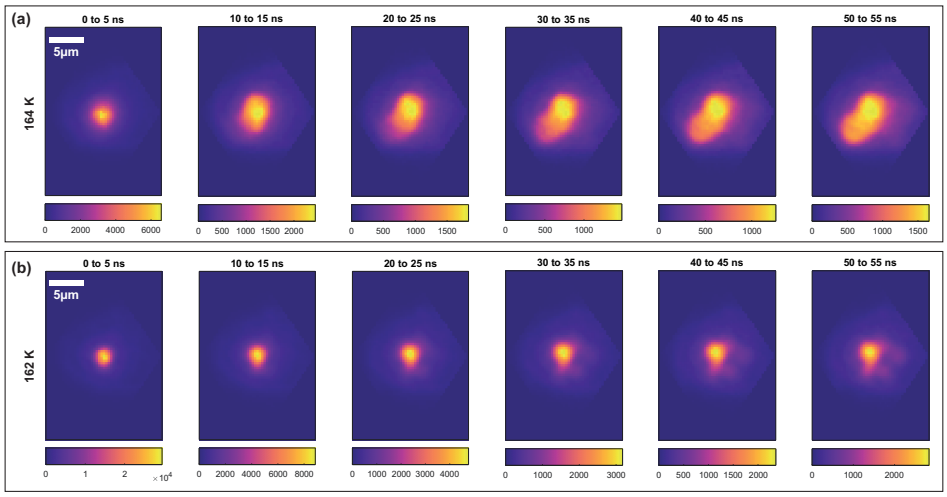

Figure S8: PL snapshots in a detection beam scan after pulsed laser excitation within a single crystal grain above and below the phase transition temperature.

References

(1) Giesbrecht, N.; Schlipf, J.; Oesinghaus, L.; Binek, A.; Bein, T.; Müller-Buschbaum, P.; Docampo, P. Synthesis of Perfectly Oriented and Micrometer-Sized MAPbBr3 Perovskite Crystals for Thin-Film Photovoltaic Applications. *ACS Energy Lett.* **2016**, *1*, 150–154.

(2) Giesbrecht, N.; Schlipf, J.; Grill, I.; Rieder, P.; Dyakonov, V.; Bein, T.; Hartschuh, A.; Müller-Buschbaum, P.; Docampo, P. Single–Crystal–Like Optoelectronic–Properties of MAPbI3 Perovskite Polycrystalline Thin Films. *J. Mater. Chem. A* **2018**, *6*, 4822–4828.

(3) Schultes, M.; Giesbrecht, N.; Kuüffner, J.; Ahlswede, E.; Docampo, P.; Bein, T.; Powalla, M. Universal Nanoparticle Wetting Agent for Upscaling Perovskite Solar Cells. *ACS Appl. Mater. Interfaces* **2019**, *11*, 12948–12957.

(4) Handloser, K.; Giesbrecht, N.; Bein, T.; Docampo, P.; Handloser, M.; Hartschuh, A. Contactless Visualization of Fast Charge Carrier Diffusion in Hybrid Halide Perovskite Thin Films. *ACS Photonics* **2016**, *3*, 255–261.

Spatiotemporal Spectroscopy of Fast Excited-State Diffusion in 2D Covalent Organic Framework Thin Films

Laura Spies[1#], Alexander Biewald[1#], Laura Fuchs[2], Konrad Merkel[2], Marcello Righetto[3], Zehua Xu[1], Roman Guntermann[1], Rik Hooijer[1] Laura M. Herz[3,4], Frank Ortmann[2], Jenny Schneider[1], Thomas Bein[1], Achim Hartschuh[1*]*

[1]Department of Chemistry and Center for NanoScience (CeNS), University of Munich (LMU), Butenandtstraße 5-13, 81377 Munich, Germany

[2]TUM School of Natural Sciences, Department of Chemistry, Technische Universität München, 85748 Garching, München, Germany

[3]Clarendon Laboratory, University of Oxford, Department of Physics, Oxford OX1 3PU, UK

[4]Institute for Advanced Study, Technische Universität München, Lichtenbergstr. 2a, 85748 Garching, München, Germany

Introduction

The diffusion of excitons is one of the most fundamental properties of semiconducting materials, characterizing their ability to transport energy.[1–3] Large diffusion coefficients D and long diffusion lengths L_D of excited states are crucial for applications in optoelectronic and photocatalytic devices.[4–6] In the quest for novel, more efficient photoactive materials, a long-standing goal has been to link the energy transport ability of a material to its molecular structure, thereby understanding the relationship between electronic properties and structural features.[7,8]

Two-dimensional covalent organic frameworks (2D COFs) are an emerging class of highly ordered, crystalline porous materials build solely from organic molecules.[9] Due to their structural versatility, they allow for precise control over their optical and electronic features.[10] Through covalent linking of organic building blocks, an extended π-conjugation is forged, leading to a delocalized electron system throughout the crystalline and periodic framework, often imparting semiconducting properties to the 2D COF.[11] As a result, COFs have been successfully implemented into optoelectronic devices such as light-emitting diodes[12,13], sensors[14] or photovoltaic cells[15,16], and used as photocatalysts [17–19], e.g. for hydrogen evolution and CO_2 reduction. Due to the atomically precise structural control, COFs are highly interesting materials for studying the structure-property relationship in photogenerated energy transport.[20–25] So far, excitonic processes in 2D COFs have been studied mostly in colloidal suspensions using transient absorption spectroscopy. Diffusion coefficients in the range of 10^{-5}-10^{-2} cm^2 s^{-1} and diffusion lengths of tens of nm have been reported for bulk 2D COF powders.[23,25]

Commonly used techniques to study charge transport in semiconductors include photo[26–29]- and cathodoluminescence[30], terahertz spectroscopy[31,32], microwave conductivity[33,34] or Hall effect measurements[35,36], generally coupled with band structure calculations. However, these methods only shed light on particular, often spatially limited aspects of the transport process and fail to provide a full picture

of the macroscopic transport properties of emerging semiconducting materials, as these can be strongly affected by structural defects and disorder, interfaces between components and grain boundaries. Acknowledging the impact of structural inhomogeneities on energy transport phenomena is key to understanding and developing novel electronic and optoelectronic materials. In recent years, new optical methods imaging the spatiotemporal evolution of photogenerated energy carriers have been developed, providing a more complete picture[37]. The three main spatiotemporal characterization techniques are time-resolved photoluminescence (TRPL)[38], transient scattering (TS)[39] and transient absorption (TA)[40,41], all of which are based on an incipient laser pulse triggering the formation of photogenerated energy carriers and the subsequent imaging of their spatial propagation as a function of time.

In this study, we employ a non-destructive remote-detected time-resolved photoluminescence (RDTR PL) technique to study the temperature-dependent charge carrier diffusion in two-dimensional covalent organic framework (COF) thin films. RDTR PL has already been successfully employed to study large-crystal thin films of methylammonium lead iodide (MAPI), a semiconducting material commonly implemented as active layer in perovskite-based solar cells.[38] The extracted diffusion coefficient decreases with increasing temperature, providing crucial information on the dominant charge transport regime in this material. In semiconductors, a description of charge transport is commonly based on two paradigms: coherent *band-like* vs. incoherent *hopping* transport.[42] As seen in MAPI thin films, prevalent *band-like* transport results in a decrease of diffusion coefficient with an increase of temperature, whereas *hopping* transport shows the opposite trend. A comprehensive study of the charge carrier diffusion in COF thin films is still lacking and the powerful RDTR PL technique has not yet been applied to this materials class. Given that COFs are fully organic are fully organic, yet crystalline and periodic polymers, both types of transport are crucial for accurately describing the prevailing diffusion regime. The coexistence of *band-like* and *hopping* transport of charge carriers is observed in some organic semiconductors and organic crystals. [43–45] Furthermore, structural and electronic disorder in the system can have significant and non-intuitive influences on the diffusion of charges in a semiconductor and must therefore be considered when interpreting experimental data and drafting a charge transport model. [46]

The herein studied imine-linked 2D COF thin films comprise the organic building blocks benzodithiophene-dialdehyde **BDT** and *N,N,N',N'*-tetra(4-aminophenyl)benzene-1,4-diamine **W**. This **WBDT COF**, first published by our group in 2020, was chosen for this study because of its significant intrinsic conductivity (1.64×10^{-3} S cm^{-2}) and its tendency to form highly crystalline thin films.[47] We use confocal microscopy to detect remote photoluminescence (RDTR PL), helping us to understand intrinsic properties of the radiative excited state energy transport in this material. We extracted an exceptionally high diffusion coefficient of 4 cm s^{-1} (at 200K) and diffusion lengths of several hundreds of nm for the lateral transport.

Through thorough analysis of the RDTR PL data in combination with theoretical simulations and optical-pump terahertz probe (OPTP) spectroscopy, we elucidate the diffusion mechanism in **WBDT** thin films involving excitons as the majority energy carriers. For the first time, the use of RDTR PL enables direct access to large-scale diffusion in 2D COFs, allowing for a correlation of the excited state dynamics to the highly crystalline 2D network. Efficient long-range exciton transport can be observed in this **WBDT** COF thin film, with D and L_D values exceeding those of other COFs and organic semiconducting materials by several orders of magnitude.[1,23,25]

Results

In this study, we combined advanced spectroscopic techniques with in-depth theoretical investigations to understand the diffusion dynamics in 2D COF thin films comprised of **BDT** and **W**. Thin films of this fully conjugated COF are highly crystalline and porous, with a Kagomé-like pore structure introduced by the tetra-functionalized **W** node. Both **W** and **BDT** are electron-rich molecules with the former being the more dominant π-donor.

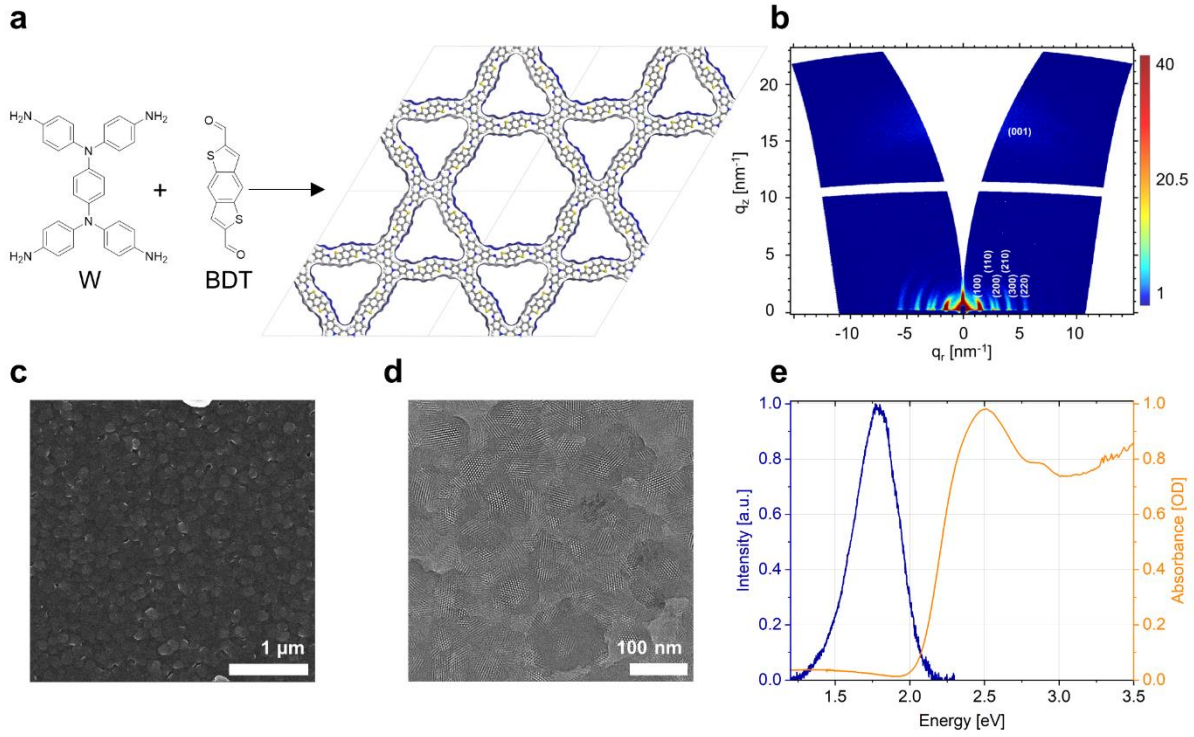

Figure 1. (**a**) Chemical structure of the two molecular building blocks **W** and **BDT** together with the top view onto a 2×2 supercell, illustrating the Kagomé-like pore structure of the **WBDT** COF. (**b**) GIWAXS pattern of the **WBDT** thin film on glass with the corresponding *hkl* indices for in-plane (100, 110, 200, 210, 300, 220) and out of plane reflexes (001). (**c**) SEM top view of the thin film surface. (**d**) TEM image of the thin film, confirming the preferential crystal orientation within the grains. (**e**) Steady-state PL and UV-Vis absorption spectrum of the **WBDT** thin film.

The COF was synthesized according to the literature[47] under solvothermal conditions *via* the acid-catalysed imine condensation of **W** and **BDT** (**Figure 1**a). Thin films were grown on glass or quartz substrates under similar solvothermal conditions as for the bulk material (see section **S3** in the Supporting Information for characterization of the bulk material). The 100, 110, 200, 210, 300, 220 and 001 reflections of the COF crystal lattice are clearly visible in the GIWAXS pattern in **Figure 1**b and appear at identical scattering vectors in the PXRD pattern of the bulk material (**Figure S1**). The intensity of the *hkl* reflections is concentrated in the q_y direction, indicating a predominant orientation of the *a*-*b* plane of the 2D COF sheets parallel to the substrate with the pores extending vertically from the substrate. Scanning electron micrographs in **Figure 1**c show a dense and uniformly covered thin film with quasi-spherical grains of 100 - 200 nm in size and a thickness of ~120 nm, which is further confirmed by atomic force microscopy (AFM) (**Figure S7**). TEM images (**Figure 1**d) confirm the preferential parallel orientation of the COF within the grains. The absence of a defined crystal structure at the grain boundaries implies an amorphous character in this region. It is likely that the 2D COF sheets at the grain boundaries are still oriented parallel to the surface but with a defective stacking order.

Steady-state UV Vis absorption and photoluminescence (PL) spectra are shown in **Figure 1**e. The bright red COF thin film exhibits a maximum absorption at 2.51 eV (494 nm) and an emission peak at 1.78 eV (697 nm) with a full width at half maximum (FWHM) of 0.35 eV. Fitting of the absorption onset using a Tauc plot gives a direct band gap of 2.1 eV (**Figure S6**a). Confocal scanning and hyperspectral imaging of a 10×10 μm^2 section show negligible changes in the normalised intensity, central energy, and spectral width of the PL signal, confirming the homogeneity of the spectral response from the thin film (**Figure S9**).

The calculated band structure of **WBDT** is shown in **Figure 2**a. Both the valence and conduction bands exhibit triplet arrangements, typical of structures based on the Kagomé lattice. **WBDT** displays moderate *in-plane* and strong *out-of-plane* band dispersions, which is highest for the valence bands. A Dirac Cone is only 0.1 eV away from the top of the valence band. The projection of the states on the atoms of **W** and **BDT** indicates that the frontier electronic levels in the valence band are primarily formed by the atomic orbitals of **W**. The lowest unoccupied bands show a balanced contribution from the atomic orbitals of both fragments.

Time-resolved measurements. In this work, we employ a spatiotemporal characterization technique termed remote detected time-resolved photoluminescence (RDTR PL). This method allows for fully contactless access to intrinsic diffusive transport characteristics of crystalline thin-film samples. Herein, a confocal microscope is used for the time-resolved PL measurements, enabling access to the micrometre length scale. The detection segment of the microscope comprises a spectrometer and time correlated single photon counting (TCSPC) electronics for the temporal resolution. For the spatial resolution, a tiltable mirror is implemented in the back focal plane of the detection part, allowing for scanning around

the fixed confocal spot. The aperture of the microscope is defined by the chip of an avalanche photo diode (APD), which, used as a single photon detector, is overfilled by the light emitted from the confocal spot. The studied material is excited with a pulsed laser (510 nm), triggering the formation and subsequent diffusion of photoexcited states from the confocal excitation spot to a remote position, where they recombine whilst emitting a photon. A timestamp is assigned to each of the detected photons, creating a transient. A schematic representation of the methodology is depicted in Figure 2b.

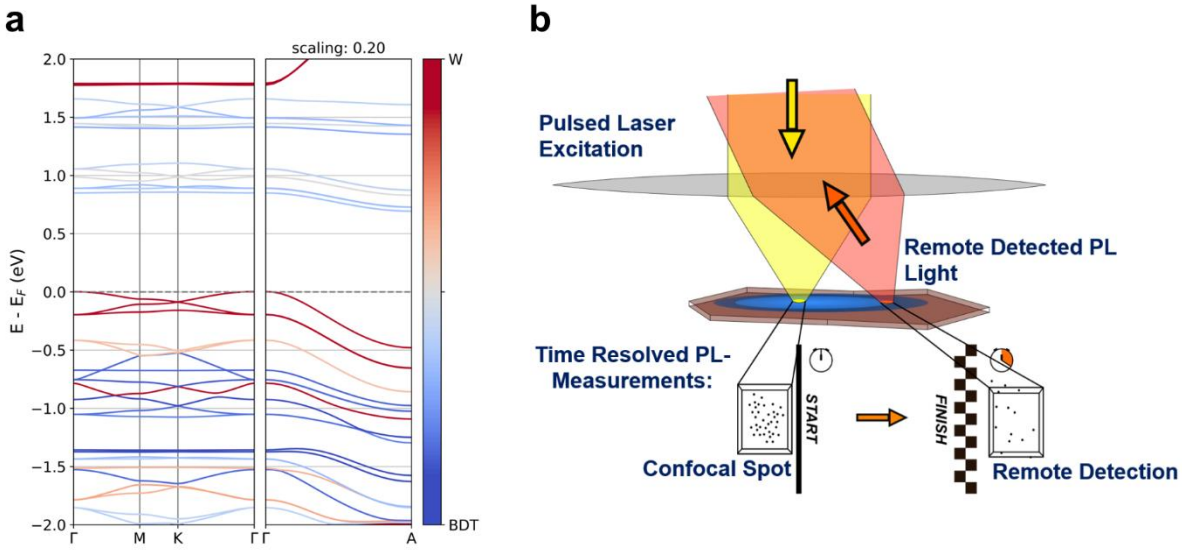

Figure 2. (**a**) Projected band structure of **WBDT**. Projection on the W-based atomic orbitals in red and BDT atomic orbitals in blue, calculated using the PBE functional and empirical scissors shift[48] of +0.49 eV to estimate the band gap at Hybrid-DFT (HSE06) level (see section S8 for more details). Darker colors indicate higher weight of states in certain bands on the fragment's atomic orbitals. The distance between Γ and A points has been scaled by 0.2 for illustration purpose. (**b**) Scheme of the remote detected time-resolved photoluminescence measurement technique. The pulsed laser (yellow) excites the sample at the confocal spot. Photoluminescence emitted from the confocal spot as well as at remote distances from the confocal spot can be detected (red). The temporal resolution is realised via TCSPC.

In these transients, lateral broadening of the confocal PL spot can be observed (**Figure 3**a). This broadening is caused by two-dimensional diffusion of the excited states in the film. While diffusion in the third dimension (*z*-direction) is likely to be present, it cannot be accessed through RDTR PL. Since the Rayleigh length of the excitation laser is longer than the thickness of the film, at the laser spot, the thin film is excited across its entire thickness. Therefore, the diffusion extracted from this RDTR PL measurement can be treated as a two-dimensional process. To analyse the spatial broadening of the RDTR PL signal and to determine the temperature dependent diffusion coefficient $D(T)$ two different methods were used: In method I, a Gaussian peak function is fitted to the RDTR PL data for each time step resulting in the time dependent spatial broadening $\sigma(t)$. As a result of the analysed spatial broadening $\sigma(t)$ of the confocal PL spot, the diffusion coefficient D can be extracted *via* the following relation:

$$\sigma(t) = \sqrt{2Dt}$$

Alternatively, in method II the complete time-dependent data set (**Figure 3**a) is fitted using the analytical solution to the 2D diffusion problem to determine *D* (see section **S5** in SI for details on the analysis and fitting). Due to the finite width of the excitation focus, a Gaussian distribution is assumed as initial condition for both methods. Also, a Gaussian peak function is added with time-independent width attributed to an immobile species in both cases (**Figures S11** and **S12**). All measurements were analysed using both methods for cross-verification and resulted in the same values for the diffusion coefficients within the experimental error (section **S5**). RDTR PL data were collected stepwise across a temperature range from 5 to 300 K.

From the RDTR PL measurements of the **WBDT** film, two diffusion processes at different timescales can be distinguished, visible as two different slopes in the spatial broadening. In the first picoseconds, still within the rise of the PL signal, fast transport process is observed with diffusion coefficient $D \sim 10$ cm^2/s in **Figure 3**b (termed *fast species*). On the longer nanosecond timescale, a slower temperature-dependent diffusion is detected (**Figure 3**c) with significantly lower diffusion coefficient (termed *slow species*). Together with the immobile contribution used in the analysis of the RDTR PL data, the slow and fast species, at least three different species need to be considered in a comprehensive model description of the excited state dynamics in the studied **WBDT** film.

Immobile species: In general, immobile species can result from defect or disorder-related trap states. Remarkably, the steady-state PL spectrum of the **WBDT** film shows no significant narrowing of the PL band for lower temperatures (**Figure S6**b). This indicates the presence of such lower lying states[49], which would dominate the red side of the PL spectrum. Indeed, limiting the detection range to the red side of the PL spectrum, no significant spatial broadening of the PL spot in the RDTR PL measurements is observed. Instead, spatial broadening indicative of excited state diffusion of a mobile species can be clearly seen while detecting the blue side of the RDTR PL spectrum (2.03 - 2.10 eV, data set 1 in **Figure 3**b, c). Detecting the whole spectrum (1.25 – 2.20 eV, data set 2 in **Figure 3**b, c) results in the same diffusion coefficient but with a larger fraction of the immobile contribution (0.3 *vs.* 0.2, respectively).

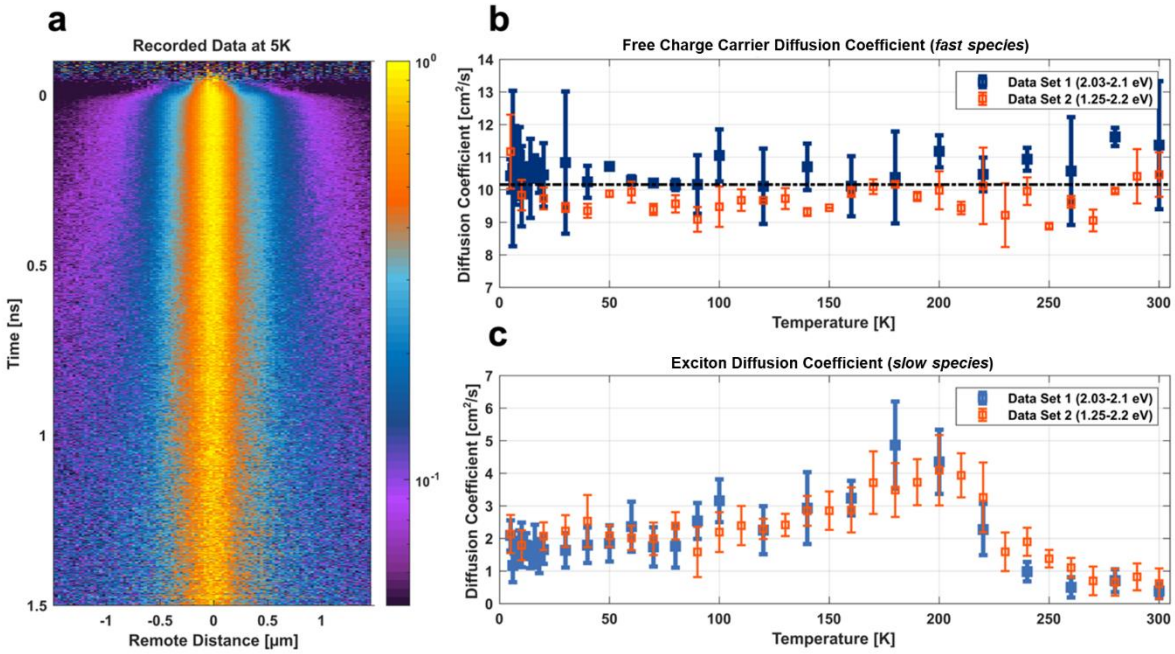

Figure 3. (a) RDTR-PL data at 5K. PL intensity as a function of time (y-axis) and distance (x-axis) from the excitation spot. (**b)** Temperature independent diffusion coefficient of the free charge carriers (*fast species*) during the first picoseconds after excitation. (**c)** Exciton (*slow species*) diffusion coefficient as a function of the temperature. For data set 1 and 2, the diffusion coefficient is determined for the blue side of the PL spectrum and for the whole spectrum, respectively.

Free charge carriers in WBDT COF: To identify the highly diffusive (*fast*) species observed above **(Figure 3**b) optical pump terahertz probe (OPTP) measurements on the picosecond timescale were conducted. **Figure 4** shows a fluence-independent transient THz signal rising within the first 250 fs upon above band gap excitation (3.1 eV) at three different fluences (100, 80, 60 µJ cm^{-2}). We note that an analogous response has been reported for different types of COFs,[50,51] and can be safely attributed to the presence of free charge carriers in the COF film. Here, OPTP measurements cannot exclude the simultaneous formation of bound exciton states which would give rise to resonances outside of our THz probing range (0.5-2.5 THz) because of the high exciton binding energies of COFs.[52] From the initial value of the photoconductivity right after excitation, the effective mobility μ of the free ambipolar charge carriers is extracted as $\varphi\mu \sim 0.12 \pm 0.05\ cm^2V^{-1}s^{-1}$, containing the photon-to-free-charge branching ratio φ. The measured photoconductivity signal decays by ~ 90% of its initial value with a rate of $k_1 \sim 0.7$ ps^{-1}, thus indicating a minimal remaining fraction of free charge carriers, which subsequently decay more slowly ($k_2 \sim 0.05$ ps^{-1}). We interpret the initial decay as a rapid formation of bound exciton states, whose resonance either lies outside the probing window and / or show significantly lower mobility. The slower decay of the residual photoconductivity component indicates the presence of alternative decay channels for the surviving free charge-carrier population, such as trapping or bi-molecular recombination. The formation of bound electron-hole pairs as the main species dominating **WBDT** COFs photophysics is

further supported by the RDTR PL data, which show significantly longer-lived excited states with lifetimes ranging from ~0.9 to 1.2 ns (**Figure S13**).

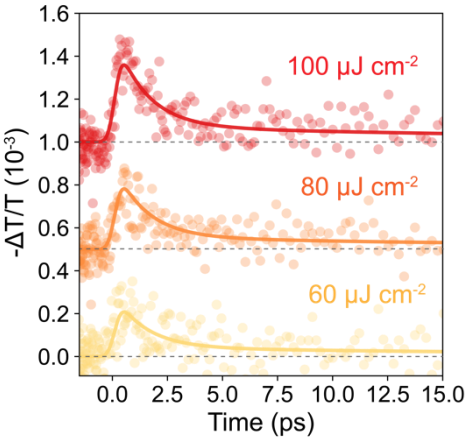

Figure 4. Optical pump terahertz probe measurements. THz photoconductivity transients of **WBDT** COF thin film, measured following a 3.1 eV excitation pulse, for three different excitation fluences (100, 80, 60 µJ/cm^2). For clarity, transients measured at different fluences are vertically shifted and the measurement zero is indicated by the dashed line. Solid lines correspond to a bi-exponential fit to the experimental data.

Consequently, the initial local broadening of the excitation spot within the first picosecond in the RDTR PL measurements is very likely caused by the diffusion of free charge carriers. Both OPTP and RDTR PL data show that on a fast picosecond timescale, a highly mobile species occurs that rapidly relaxes into bound excitons with lower mobility.

Exciton diffusion in WBDT COF: Exciton (*slow species*) diffusion within the COF thin film is detected by RDTR PL measurements over the nanosecond timescale (**Figure 3**Error! Reference source not found.c). To understand and describe the diffusive transport of the excitons, theoretical DFT-based calculations are carried out. Since complete excited state calculations of periodic COF structures are computationally extremely demanding, we have opted for a hybrid approach that considers the essential ingredients while being computationally feasible. As illustrated in Figure 5 the COF unit cell was disassembled into molecular fragments, six **BDT** and three **W** fragments, respectively. The **W** fragments were H-terminated, while the **BDT** fragments included the imine bonds at the peripheral positions. Time dependent DFT (TDDFT) calculations of the **BDT** and **W** fragments were carried out, including the lowest excitons (at least five per molecule), and provided both localized and delocalized transition densities with variable dipole characteristics of the excited states. The calculated transition dipole moments of **BDT** and **W** fragments have a dominating *in-plane* dipole orientation with moderately large oscillator strengths and asymmetric transition densities (see section **S8** in SI for details on the theoretical calculations). Subsequent re-substitution of the calculated excited states back into the COF structure at the respective fragment position allows for the simulation of exciton interaction between all fragments.

This interaction based on the transition charges is dominated by mutually neighbouring pairs, leading to an energy dispersion in the COF lattice. The *in-plane* distance between excitons is much larger than the *out-of-plane* distance (51 Å *vs*. 4 Å), therefore the exciton coupling, although present in the *x*-*y* plane, is larger in the *z*-direction. For the diffusion coefficient, this anisotropy is partially compensated by the geometry prefactor, *i.e.* the lattice constant, which is larger *in-plane*, enabling the diffusive transport in different directions. The different contributions from both **BDT** and **W** molecules in some of the excited states may well result in a superposition of molecularly localized and partially delocalized states. RDTR PL data confirm the mixing of localized and delocalized states as for every time step, the diffusion signal consists of a static component with a constant width and a diffusive component with an increasing spatial width $\sigma(t)$ (**Figure 3**a, **S11** and **S13**).

The overall largest calculated exciton coupling adds up to a moderate value of ε ≅ 50 meV, leading to the hypothesis that the excitons indeed couple to vibrational modes of the crystal lattice, making them polaronic excitons. We hypothesize that the COF lattice can be deformed in the surrounding area of the exciton. The diffusion of the excitons along the 2D COF layers (*in-plane*) is observed in the RDTR PL measurements. The diffusion in *z*-direction across the COF layers will likely be present but cannot be accessed through RDTR PL and is limited by the thickness of the film (~ 120 nm, **Figure S7**).

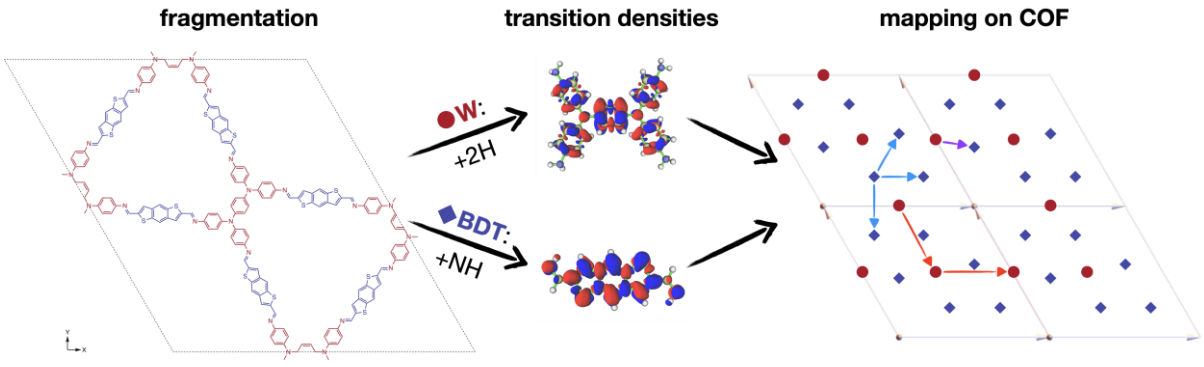

Figure 5. Schematic representation of the hybrid exciton approach: the COF unit cell is divided into molecular fragments of the building blocks **W** and **BDT** (3 and 6 fragments per unit cell, respectively). The transition charges and exciton couplings of these molecular fragments are calculated and the exciton states are placed at the respective positions within the unit cell (red dots indicate centers of mass of **W**, blue diamonds indicate the centers of mass of **BDT**) to carry out exciton interaction and dispersion simulations in-plane and out-of-plane.

Discussion of the temperature-dependent diffusive transport

The temperature dependence of the diffusion coefficient of excitons contains information on the underlying transport processes in semiconducting materials.[38] Exciton transport in highly ordered, crystalline inorganic semiconductors is typically described as coherent *band-like* transport, where excitons are scattered by phonons and defects.[53,54] For organic polymers, incoherent *hopping* transport is commonly assumed, where excited states hop from one electronically favorable state to another, which is described by a hopping rate.[2,53,54] *Band-like* transport is accelerated with decreasing temperature due to reduced phonon scattering while for thermally activated *hopping* transport, the opposite trend is observed. Due to their highly ordered crystalline structure made from building blocks and a delocalized electron system, COFs can often be described as organic semiconductors, where a combination of both transport phenomena is possible.[11,43,44]

The free charge carriers, dominating the dynamics in the first few picoseconds, diffuse almost temperature independently with $D \sim 10$ cm^2 s^{-1}. Due to above-band-gap excitation and a laser pulse duration of ≤ 1 ps, the free charge carriers contain excess energy and are thus not in thermal equilibrium with the surrounding environment. With the extracted lifetime $\tau = 1.4$ ps from the OPTP measurements, free carriers appear to be converted into bound states before temperature dependent phonon scattering can effectively limit transport. The diffusion length L_D of the free carriers can be estimated using values from the two independent measurements: the lifetime extracted from OPTP and the diffusion coefficient from RDTR PL (see section **S7** in SI for details).[55] A value of $L_D = \sqrt{2D\tau} \approx 50$ nm corresponds roughly to the grain size of the **WBDT** film (**Figure 1**c). Hence, we suspect that the free charge carriers stay within one grain without being lost by scattering events.

The combination of the observed and analysed data supports the hypothesis that these mobile free charge carriers relax into a diffusive exciton state within the first picoseconds (**Figure 4**). While the initial transient relaxation phase (free charge carriers) is not in the focus of the simulations, diffusion is considered here for the subsequent phase (diffusive excitons). For calculated values of the exciton coupling of $\varepsilon \cong 50$ meV and an estimated reduced reorganization energy of $\Lambda \cong 0.1$ eV[56], a combination of *band-like* and *hopping* transport in the **WBDT** COF thin film can be expected.[43] This suggests a rather flat or a non-monotonous temperature-dependence of the diffusivity. Also, in this crossover regime *band-like* and *hopping* diffusivities are likely to be comparable in magnitude. Therefore, we apply the simpler hopping ansatz for calculations at room temperature (290 K)[57]. A diffusion coefficient of $D = 0.2$ cm^2 s^{-1} is estimated for the exciton diffusion, which is in good agreement with the experimentally derived value of 0.2 to 0.4 cm^2 s^{-1} at room temperature (**Figure 3**c).

Considering the theoretical model, we tentatively assert that the experimentally observed exciton diffusion coefficient results from a combination of both incoherent (phonon-assisted) *hopping* and

coherent *band-like* contributions. Disorder can lead to a complex interplay of these mechanisms, resulting in a non-intuitive temperature dependence, as observed in organic crystals.[46] **Figure 3**c shows that, when the temperature decreases below 300 K, the diffusion coefficient *D* increases until it reaches a maximum value of 4 $cm^2\ s^{-1}$ at approximately 200 K. This suggests that carrier-phonon scattering dominates the temperature dependence of *D* in this regime, where scattering is enhanced with temperature. This results in a gradual suppression of coherent transport at high temperatures (around room temperature) and an increasing dominance of phonon-assisted incoherent over coherent transport, justifying the use of the hopping model for room temperature calculations. As the temperature lowers, we propose that the coupled phonons start freezing out at 200 K. Consequently, for temperatures below 200 K, an increase in the diffusion coefficient with cooling would be expected for a band regime. However, the opposite is observed, with a gradual decay to 2 $cm^2\ s^{-1}$ at the lowest measured temperatures. We propose that the disorder in the COF crystal lattice significantly influences exciton transport at low temperatures, thereby impeding further acceleration of diffusion. Given that incoherent transport is strongly thermally driven, it is suppressed at low temperatures, and we expect the observed diffusion at low temperatures to be mainly coherent and limited by disorder. The remarkably large values observed here indicate the relevance of the third transport direction in the diffusion process, suppressing possible weak/strong localization effects of lower dimensions.

A schematic model illustrating the excited state diffusion in the **WBDT** COF thin film summarizing the discussion above is shown in Figure 6. Free charge carriers are created within the first picoseconds after excitation and quickly relax into excitons at a rate of $k_1 \sim 0.7\ ps^{-1}$ (lifetime of 1.4 ps). A diffusion length of ~ 50 nm suggests that the free charge carriers stay within one grain. The excitons with longer lifetimes of up to 1.2 ns, diffusive over several grains (L_D = 200 – 800 nm, **Figure S14**), implying that the COF crystallite size is not the limiting factor for diffusion. In addition to the mobile diffusive species, a non-mobile contribution arising from localized states is visible in the RDTR PL data.

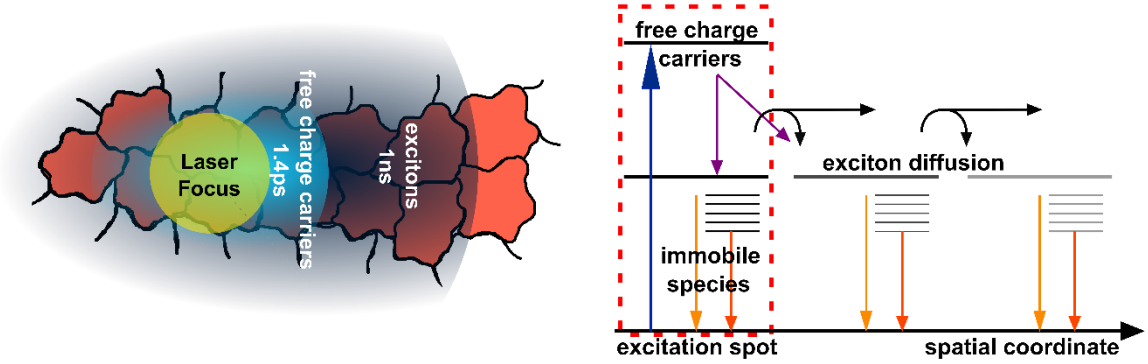

Figure 6. Schematic illustration of the excited state diffusion in 2D **WBDT** COF thin films.

Since RDTR PL measures over several grains, impurities like defect states, or grain boundaries as well as lattice disorder will all affect the experimental observed transport dynamics. We state that the preferential orientation of the COF layers parallel to the substrate throughout the whole thin film is crucial for efficient lateral diffusion of excitons. In other words, the *z*-axis of each grain is perpendicular to the substrate's plane. To support this statement, we grew **WBDT** thin films with random crystallite orientation (see section **S6** in SI for details), where the angle between *z*-axis and substrate plane varies for every grain. RDTR PL measurements in those films show substantially reduced exciton diffusion coefficients, that decrease with decreasing temperature (**Figure S20**). This change in the diffusion characteristics is due to the anisotropy of the COF crystallites with no extension of the two-dimensional COF structure with the same preferential orientation outside the crystallites, hence promoting mainly the *hopping*-type transport.

Finally, we compare the derived diffusion coefficients and lengths for the **WBDT** COF thin films to those reported for other 2D COFs in the literature. To date, excited state diffusion in 2D COFs has been mostly studied using transient absorption spectroscopy of colloidal solutions. [23,25] A direct comparison of the reported diffusion coefficients with those obtained here, however, will thus be of limited use due to differences between sample materials and the methodologies of TA and RDTR PL. We note however, that exciton diffusion in the **WBDT** COF films reaches unprecedented values for D and L_D, exceeding those of other COFs and organic semiconducting materials by several orders of magnitude.[1,23,25] We assume that the extended crystallinity of the framework and the uniform orientation of the crystallites in the thin film play a major role for efficient excited state transport within this **WBDT** COF.

Conclusion

We visualized the spatiotemporal evolution of photogenerated excited states in 2D COF thin films using remote detected time-resolved PL measurements. We directly accessed the lateral exciton diffusion within oriented and crystalline thin films of **WBDT** COF thin films. Remarkably high diffusion coefficients of 4 $cm^2\ s^{-1}$ (200K) and diffusion lengths of several hundreds of nanometers and across grain boundaries were extracted. Furthermore, we analyzed the temperature-dependent exciton transport regime. Phonon-assisted exciton transport prevails above 200 K, while disorder in the system significantly limits the diffusion at temperature below 200 K. Theoretical simulations suggest that the observed diffusion coefficient arise from contributions of incoherent *hopping* and coherent *band-like* transport. This coexistence of the two regimes was also observed before in organic semiconductors and organic crystals.[43–45] We suggest a dominating coherent transport at low temperatures and a prevailing incoherent transport at room temperature. High crystallinity and preferential orientation of COF thin films allows for a precise definition of the nanoscale structure of the material. Hence, it is evident that energy transport processes are influenced not only by the choice of building units but also significantly by the (dis)order

in the system. In the future, broad complementary efforts are required to gain a deeper understanding of the extent to which order and disorder influence energy transport processes in this material's class.

References

(1) Mikhnenko, O. V.; Blom, P. W. M.; Nguyen, T.-Q. Exciton diffusion in organic semiconductors. *Energy Environ. Sci.* **2015**, *8* (7), 1867–1888. DOI: 10.1039/C5EE00925A.

(2) Morab, S.; Sundaram, M. M.; Pivrikas, A. Review on Charge Carrier Transport in Inorganic and Organic Semiconductors. *Coatings* **2023**, *13* (9), 1657. DOI: 10.3390/coatings13091657.

(3) Menke, S. M.; Holmes, R. J. Exciton diffusion in organic photovoltaic cells. *Energy Environ. Sci.* **2014**, *7* (2), 499–512. DOI: 10.1039/C3EE42444H.

(4) Tamai, Y.; Ohkita, H.; Benten, H.; Ito, S. Exciton Diffusion in Conjugated Polymers: From Fundamental Understanding to Improvement in Photovoltaic Conversion Efficiency. *The journal of physical chemistry letters* **2015**, *6* (17), 3417–3428. DOI: 10.1021/acs.jpclett.5b01147. Published Online: Aug. 18, 2015.

(5) Hodes, G.; Kamat, P. V. Understanding the Implication of Carrier Diffusion Length in Photovoltaic Cells. *The journal of physical chemistry letters* **2015**, *6* (20), 4090–4092. DOI: 10.1021/acs.jpclett.5b02052.

(6) Bisquert, J. Interpretation of electron diffusion coefficient in organic and inorganic semiconductors with broad distributions of states. *Physical chemistry chemical physics : PCCP* **2008**, *10* (22), 3175–3194. DOI: 10.1039/b719943k. Published Online: Mar. 25, 2008.

(7) Lunt, R. R.; Benziger, J. B.; Forrest, S. R. Relationship between crystalline order and exciton diffusion length in molecular organic semiconductors. *Advanced materials (Deerfield Beach, Fla.)* **2010**, *22* (11), 1233–1236. DOI: 10.1002/adma.200902827.

(8) Rim, S.-B.; Fink, R. F.; Schöneboom, J. C.; Erk, P.; Peumans, P. Effect of molecular packing on the exciton diffusion length in organic solar cells. *Applied Physics Letters* **2007**, *91* (17). DOI: 10.1063/1.2783202.

(9) Tan, K. T.; Ghosh, S.; Wang, Z.; Wen, F.; Rodríguez-San-Miguel, D.; Feng, J.; Huang, N.; Wang, W.; Zamora, F.; Feng, X.; Thomas, A.; Jiang, D. Covalent organic frameworks. *Nat Rev Methods Primers* **2023**, *3* (1), 1–19. DOI: 10.1038/s43586-022-00181-z.

(10) Keller, N.; Bein, T. Optoelectronic processes in covalent organic frameworks. *Chem. Soc. Rev.* **2021**, *50* (3), 1813–1845. DOI: 10.1039/D0CS00793E.

(11) Huang, W.; Luo, W.; Li, Y. Two-dimensional semiconducting covalent organic frameworks for photocatalytic solar fuel production. *Materials Today* **2020**, *40*, 160–172. DOI: 10.1016/j.mattod.2020.07.003.

(12) Ding, H.; Li, J.; Xie, G.; Lin, G.; Chen, R.; Peng, Z.; Yang, C.; Wang, B.; Sun, J.; Wang, C. An AIEgen-based 3D covalent organic framework for white light-emitting diodes. *Nat Commun* **2018**, *9* (1), 5234. DOI: 10.1038/s41467-018-07670-4. Published Online: Jul. 12, 2018.

(13) Xu, S.; Zhang, Q. Recent progress in covalent organic frameworks as light-emitting materials. *Materials Today Energy* **2021**, *20*, 100635. DOI: 10.1016/j.mtener.2020.100635.

(14) Guo, L.; Yang, L.; Li, M.; Kuang, L.; Song, Y.; Wang, L. Covalent organic frameworks for fluorescent sensing: Recent developments and future challenges. *Coordination Chemistry Reviews* **2021**, *440*, 213957. DOI: 10.1016/j.ccr.2021.213957.

(15) Calik, M.; Auras, F.; Salonen, L. M.; Bader, K.; Grill, I.; Handloser, M.; Medina, D. D.; Dogru, M.; Löbermann, F.; Trauner, D.; Hartschuh, A.; Bein, T. Extraction of photogenerated electrons and holes from a covalent organic framework integrated heterojunction. *Journal of the American Chemical Society* **2014**, *136* (51), 17802–17807. DOI: 10.1021/ja509551m. Published Online: Dec. 15, 2014.

(16) Yildirim, O.; Bonomo, M.; Barbero, N.; Atzori, C.; Civalleri, B.; Bonino, F.; Viscardi, G.; Barolo, C. Application of Metal-Organic Frameworks and Covalent Organic Frameworks as (Photo)Active Material in Hybrid Photovoltaic Technologies. *Energies* **2020**, *13* (21), 5602. DOI: 10.3390/en13215602.

(17) Carmo, M. E. G.; Spies, L.; Silva, G. N.; Lopes, O. F.; Bein, T.; Schneider, J.; Patrocinio, A. O. T. From conventional inorganic semiconductors to covalent organic frameworks: advances and opportunities in heterogeneous photocatalytic CO 2 reduction. *J. Mater. Chem. A* **2023**, *11* (26), 13815–13843. DOI: 10.1039/D3TA01470C.

(18) Liu, S.; Wang, M.; He, Y.; Cheng, Q.; Qian, T.; Yan, C. Covalent organic frameworks towards photocatalytic applications: Design principles, achievements, and opportunities. *Coordination Chemistry Reviews* **2023**, *475*, 214882. DOI: 10.1016/j.ccr.2022.214882.

(19) Bag, S.; Sasmal, H. S.; Chaudhary, S. P.; Dey, K.; Blätte, D.; Guntermann, R.; Zhang, Y.; Položij, M.; Kuc, A.; Shelke, A.; Vijayaraghavan, R. K.; Ajithkumar, T. G.; Bhattacharyya, S.; Heine, T.; Bein, T.; Banerjee, R. Covalent Organic Framework Thin-Film Photodetectors from Solution-Processable Porous Nanospheres. *Journal of the American Chemical Society* **2023**, *145* (3), 1649–1659. DOI: 10.1021/jacs.2c09838. Published Online: Sep. 1, 2023.

(20) Streater, D.; Hu, W.; Kelley, M. S.; Yang, S.; Kohlstedt, K. L.; Huang, J. Wavelength-Dependent Excitonic Properties of Covalent Organic Frameworks Explored by Theory and Experiments. *J. Phys. Chem. C* **2023**, *127* (25), 12321–12332. DOI: 10.1021/acs.jpcc.3c02296.

(21) Jakowetz, A. C.; Hinrichsen, T. F.; Ascherl, L.; Sick, T.; Calik, M.; Auras, F.; Medina, D. D.; Friend, R. H.; Rao, A.; Bein, T. Excited-State Dynamics in Fully Conjugated 2D Covalent Organic Frameworks. *Journal of the American Chemical Society* **2019**, *141* (29), 11565–11571. DOI: 10.1021/jacs.9b03956. Published Online: Jul. 15, 2019.

(22) Helweh, W.; Flanders, N. C.; Wang, S.; Phelan, B. T.; Kim, P.; Strauss, M. J.; Li, R. L.; Kelley, M. S.; Kirschner, M. S.; Edwards, D. O.; Spencer, A. P.; Schatz, G. C.; Schaller, R. D.; Dichtel, W. R.; Chen, L. X. Layered structures of assembled imine-linked macrocycles and two-dimensional covalent organic frameworks give rise to prolonged exciton lifetimes. *J. Mater. Chem. C* **2022**, *10* (8), 3015–3026. DOI: 10.1039/D1TC05840A.

(23) Zhang, X.; Geng, K.; Jiang, D.; Scholes, G. D. Exciton Diffusion and Annihilation in an sp2 Carbon-Conjugated Covalent Organic Framework. *Journal of the American Chemical Society* **2022**, *144* (36), 16423–16432. DOI: 10.1021/jacs.2c04742. Published Online: Aug. 23, 2022.

(24) Ghosh, S.; Tsutsui, Y.; Kawaguchi, T.; Matsuda, W.; Nagano, S.; Suzuki, K.; Kaji, H.; Seki, S. Band-like Transport of Charge Carriers in Oriented Two-Dimensional Conjugated Covalent Organic Frameworks. *Chem. Mater.* **2022**, *34* (2), 736–745. DOI: 10.1021/acs.chemmater.1c03533.

(25) Flanders, N. C.; Kirschner, M. S.; Kim, P.; Fauvell, T. J.; Evans, A. M.; Helweh, W.; Spencer, A. P.; Schaller, R. D.; Dichtel, W. R.; Chen, L. X. Large Exciton Diffusion Coefficients in Two-Dimensional Covalent Organic Frameworks with Different Domain Sizes Revealed by Ultrafast Exciton Dynamics. *Journal of the American Chemical Society* **2020**, *142* (35), 14957–14965. DOI: 10.1021/jacs.0c05404. Published Online: Aug. 24, 2020.

(26) Banappanavar, G.; Saxena, R.; Bässler, H.; Köhler, A.; Kabra, D. Impact of Photoluminescence Imaging Methodology on Transport Parameters in Semiconductors. *The journal of physical chemistry letters* **2024**, *15* (11), 3109–3117. DOI: 10.1021/acs.jpclett.4c00169. Published Online: Dec. 3, 2024.

(27) Kirchartz, T.; Márquez, J. A.; Stolterfoht, M.; Unold, T. Photoluminescence-Based Characterization of Halide Perovskites for Photovoltaics. *Advanced Energy Materials* **2020**, *10* (26). DOI: 10.1002/aenm.201904134.

(28) Crooker, S. A.; Hollingsworth, J. A.; Tretiak, S.; Klimov, V. I. Spectrally resolved dynamics of energy transfer in quantum-dot assemblies: towards engineered energy flows in artificial materials. *Physical review letters* **2002**, *89* (18), 186802. DOI: 10.1103/PhysRevLett.89.186802. Published Online: Oct. 14, 2002.

(29) Kholmicheva, N.; Moroz, P.; Bastola, E.; Razgoniaeva, N.; Bocanegra, J.; Shaughnessy, M.; Porach, Z.; Khon, D.; Zamkov, M. Mapping the exciton diffusion in semiconductor nanocrystal solids. *ACS nano* **2015**, *9* (3), 2926–2937. DOI: 10.1021/nn507322y. Published Online: Feb. 19, 2015.

(30) Coenen, T.; Haegel, N. M. Cathodoluminescence for the 21st century: Learning more from light. *Applied Physics Reviews* **2017**, *4* (3). DOI: 10.1063/1.4985767.

(31) Johnston, M. B.; Herz, L. M. Hybrid Perovskites for Photovoltaics: Charge-Carrier Recombination, Diffusion, and Radiative Efficiencies. *Accounts of chemical research* **2016**, *49* (1), 146–154. DOI: 10.1021/acs.accounts.5b00411. Published Online: Oct. 12, 2015.

(32) Motti, S. G.; Kober-Czerny, M.; Righetto, M.; Holzhey, P.; Smith, J.; Kraus, H.; Snaith, H. J.; Johnston, M. B.; Herz, L. M. Exciton Formation Dynamics and Band-Like Free Charge-Carrier Transport in 2D Metal Halide Perovskite Semiconductors. *Adv Funct Materials* **2023**, *33* (32). DOI: 10.1002/adfm.202300363.

(33) Kunst, M.; Beck, G. The study of charge carrier kinetics in semiconductors by microwave conductivity measurements. *Journal of Applied Physics* **1986**, *60* (10), 3558–3566. DOI: 10.1063/1.337612.

(34) Hu, Y.; Hutter, E. M.; Rieder, P.; Grill, I.; Hanisch, J.; Aygüler, M. F.; Hufnagel, A. G.; Handloser, M.; Bein, T.; Hartschuh, A.; Tvingstedt, K.; Dyakonov, V.; Baumann, A.; Savenije, T. J.; Petrus, M. L.; Docampo, P. Understanding the Role of Cesium and Rubidium Additives in Perovskite Solar Cells: Trap States, Charge Transport, and Recombination. *Advanced Energy Materials* **2018**, *8* (16). DOI: 10.1002/aenm.201703057.

(35) Yi, H. T.; Gartstein, Y. N.; Podzorov, V. Charge carrier coherence and Hall effect in organic semiconductors. *Scientific reports* **2016**, *6*, 23650. DOI: 10.1038/srep23650. Published Online: Mar. 30, 2016.

(36) Karl, N. Charge carrier transport in organic semiconductors. *Synthetic Metals* **2003**, *133-134*, 649–657. DOI: 10.1016/s0379-6779(02)00398-3.

(37) Ginsberg, N. S.; Tisdale, W. A. Spatially Resolved Photogenerated Exciton and Charge Transport in Emerging Semiconductors. *Annual review of physical chemistry* **2020**, *71*, 1–30. DOI: 10.1146/annurev-physchem-052516-050703. Published Online: Nov. 22, 2019.

(38) Biewald, A.; Giesbrecht, N.; Bein, T.; Docampo, P.; Hartschuh, A.; Ciesielski, R. Temperature-Dependent Ambipolar Charge Carrier Mobility in Large-Crystal Hybrid Halide Perovskite Thin Films. *ACS applied materials & interfaces* **2019**, *11* (23), 20838–20844. DOI: 10.1021/acsami.9b04592. Published Online: May. 28, 2019.

(39) Weaver, H. L.; Went, C. M.; Wong, J.; Jasrasaria, D.; Rabani, E.; Atwater, H. A.; Ginsberg, N. S. Detecting, Distinguishing, and Spatiotemporally Tracking Photogenerated Charge and Heat at the Nanoscale. *ACS nano* **2023**, *17* (19), 19011–19021. DOI: 10.1021/acsnano.3c04607. Published Online: Sep. 18, 2023.

(40) Cabanillas-Gonzalez, J.; Grancini, G.; Lanzani, G. Pump-probe spectroscopy in organic semiconductors: monitoring fundamental processes of relevance in optoelectronics. *Advanced Materials* **2011**, *23* (46), 5468–5485. DOI: 10.1002/adma.201102015. Published Online: Oct. 24, 2011.

(41) Grumstrup, E. M.; Gabriel, M. M.; Cating, E. E.; van Goethem, E. M.; Papanikolas, J. M. Pump–probe microscopy: Visualization and spectroscopy of ultrafast dynamics at the nanoscale. *Chemical Physics* **2015**, *458*, 30–40. DOI: 10.1016/j.chemphys.2015.07.006.

(42) Ortmann, F.; Bechstedt, F.; Hannewald, K. Charge transport in organic crystals: interplay of band transport, hopping and electron–phonon scattering. *New J. Phys.* **2010**, *12* (2), 23011. DOI: 10.1088/1367-2630/12/2/023011.

(43) Giannini, S.; Carof, A.; Blumberger, J. Crossover from Hopping to Band-Like Charge Transport in an Organic Semiconductor Model: Atomistic Nonadiabatic Molecular Dynamics Simulation. *The journal of physical chemistry letters* **2018**, *9* (11), 3116–3123. DOI: 10.1021/acs.jpclett.8b01112. Published Online: May. 29, 2018.

(44) Troisi, A. Charge transport in high mobility molecular semiconductors: classical models and new theories. *Chem. Soc. Rev.* **2011**, *40* (5), 2347–2358. DOI: 10.1039/C0CS00198H. Published Online: Mar. 15, 2011.

(45) Yavuz, I. Dichotomy between the band and hopping transport in organic crystals: insights from experiments. *Physical chemistry chemical physics : PCCP* **2017**, *19* (38), 25819–25828. DOI: 10.1039/c7cp05297a.

(46) Ortmann, F.; Roche, S. Polaron transport in organic crystals: Temperature tuning of disorder effects. *Phys. Rev. B* **2011**, *84* (18). DOI: 10.1103/PhysRevB.84.180302.

(47) Rotter, J. M.; Guntermann, R.; Auth, M.; Mähringer, A.; Sperlich, A.; Dyakonov, V.; Medina, D. D.; Bein, T. Highly conducting Wurster-type twisted covalent organic frameworks. *Chemical science* **2020**, *11* (47), 12843–12853. DOI: 10.1039/d0sc03909h. Published Online: Oct. 27, 2020.

(48) Bechstedt, F. *Many-body approach to electronic excitations*:*Concepts and applications*, Vol. 181; Springer, 2015. DOI: 10.1007/978-3-662-44593-8.

(49) Ghosh, R.; Paesani, F. Unraveling the effect of defects, domain size, and chemical doping on photophysics and charge transport in covalent organic frameworks. *Chemical science* **2021**, *12* (24), 8373–8384. DOI: 10.1039/d1sc01262b. Published Online: May. 13, 2021.

(50) Wang, M.; Ballabio, M.; Wang, M.; Lin, H.-H.; Biswal, B. P.; Han, X.; Paasch, S.; Brunner, E.; Liu, P.; Chen, M.; Bonn, M.; Heine, T.; Zhou, S.; Cánovas, E.; Dong, R.; Feng, X. Unveiling Electronic Properties in Metal-Phthalocyanine-Based Pyrazine-Linked Conjugated Two-Dimensional Covalent Organic Frameworks. *Journal of the American Chemical Society* **2019**, *141* (42), 16810–16816. DOI: 10.1021/jacs.9b07644. Published Online: Oct. 8, 2019.

(51) Wang, M.; Wang, M.; Lin, H.-H.; Ballabio, M.; Zhong, H.; Bonn, M.; Zhou, S.; Heine, T.; Cánovas, E.; Dong, R.; Feng, X. High-Mobility Semiconducting Two-Dimensional Conjugated Covalent Organic Frameworks with p-Type Doping. *Journal of the American Chemical Society* **2020**, *142* (52), 21622–21627. DOI: 10.1021/jacs.0c10482. Published Online: Dec. 17, 2020.

(52) Rahman, M.; Tian, H.; Edvinsson, T. Revisiting the Limiting Factors for Overall Water-Splitting on Organic Photocatalysts. *Angewandte Chemie (International ed. in English)* **2020**, *59* (38), 16278–16293. DOI: 10.1002/anie.202002561. Published Online: Jul. 16, 2020.

(53) Franchini, C.; Reticcioli, M.; Setvin, M.; Diebold, U. Polarons in materials. *Nat Rev Mater* **2021**, *6* (7), 560–586. DOI: 10.1038/s41578-021-00289-w.

(54) Kittel, C.; McEuen, P. *Introduction to solid state physics*, Global edition; Wiley, 2022.

(55) Wagner, K.; Zipfel, J.; Rosati, R.; Wietek, E.; Ziegler, J. D.; Brem, S.; Perea-Causín, R.; Taniguchi, T.; Watanabe, K.; Glazov, M. M.; Malic, E.; Chernikov, A. Nonclassical Exciton Diffusion in Monolayer WSe_{2}. *Physical review letters* **2021**, *127* (7), 76801. DOI: 10.1103/PhysRevLett.127.076801.

(56) Vandewal, K.; Benduhn, J.; Schellhammer, K. S.; Vangerven, T.; Rückert, J. E.; Piersimoni, F.; Scholz, R.; Zeika, O.; Fan, Y.; Barlow, S.; Neher, D.; Marder, S. R.; Manca, J.; Spoltore, D.; Cuniberti, G.; Ortmann, F. Absorption Tails of Donor:C60 Blends Provide Insight into Thermally Activated Charge-Transfer Processes and Polaron Relaxation. *Journal of the American Chemical Society* **2017**, *139* (4), 1699–1704. DOI: 10.1021/jacs.6b12857. Published Online: Jan. 24, 2017.

(57) Marcus, R. A. Relation between charge transfer absorption and fluorescence spectra and the inverted region. *J. Phys. Chem.* **1989**, *93* (8), 3078–3086. DOI: 10.1021/j100345a040.

Supporting Information

Spatiotemporal Spectroscopy of Fast Excited-State Diffusion in 2D Covalent Organic Framework Thin Films

Laura Spies[1#], Alexander Biewald[1#], Laura Fuchs[2], Konrad Merkel[2], Marcello Righetto[3], Zehua Xu[1], Roman Guntermann[1], Rik Hooijer[1], Laura M. Herz[3,4], Frank Ortmann[2], Jenny Schneider[1], Thomas Bein[1], Achim Hartschuh[1*]*

[1]Department of Chemistry and Center for NanoScience (CeNS), University of Munich (LMU), Butenandtstraße 5-13, 81377 Munich, Germany

[2]TUM School of Natural Sciences, Department of Chemistry, Technische Universität München, 85748 Garching, München, Germany

[3]Clarendon Laboratory, University of Oxford, Department of Physics, Oxford OX1 3PU, UK

[4]Institute for Advanced Study, Technische Universität München, Lichtenbergstr. 2a, 85748 Garching, München, Germany

Table of Content

Table of Figures

S1. Materials and Synthesis

All solvents were purchased from *Sigma Aldrich, Acros* or *TCI Europe* in the common purities *purum, puriss* or *reagent grade*. The materials were used as received without additional purification and handled in air unless otherwise noted. *N,N,N',N'*-tetra(4-aminophenyl)benzene-1,4-diamine **W** was purchased from Carbosynth/BLDpharm. Benzo[1,2-b:4,5-b']dithiophene-2,6-dicarboxaldehyde **BDT** was synthesized according to the literature.[1]

COF bulk material was synthesized according to the literature in an Argon filled glove box.[2] In a culture tube, a solid mixture of W (0.013mmol, 6 mg) and BDT (0.025 mmol, 6.26 mg) was suspended in 1 mL mesitylene and benzyl alcohol (500 µL each). Subsequently, 50 µL of acetic acid (aqueous, 6M) was added. The culture tube was tightly sealed and heated at 100°C for 72h. The resulting dark red suspension was filtrated hot and the isolated powder thoroughly washed with THF (~10 mL). The obtained red powder was dried under vacuum, followed by activation in supercritical CO_2 at 110 bar and 40°C for 1 hour.

COF thin films were synthesized according to the literature in autoclaves equipped with a teflon liner holding the substrate in a horizontal position.[2] Glass and quartz substrates were cleaned in detergent solution (Hellmanex III, 1% *v/v*, water, acetone and isopropanol). The substrate was immersed into a suspension of W (2.5 µmol, 1.2 mg) and BDT (5 µmol, 1.25 mg) in 2 mL mesitylene and benzyl alcohol (v:v 1:1) and 100 µL of acetic acid (aqueous, 6M). The autoclave was sealed under Argon and heated at 100°C for 1 day. After cooling to room temperature, the COF film was rinsed with dry THF and dried under reduced pressure. **Unoriented COF thin films** were grown on a SiO_2 inverse opal structure. The inverse opal structure was grown on a glass substrate following a published procedure.[3] In order to grow an unoriented film with comparable thickness on top of the substrate and account for the COF material growing within the inverse opal structure, the amount of precursor for the film synthesis was increased to 6 mg (12.5 µmol) and 6.25 mg (25 µmol) for W and BDT, respectively. The synthetic procedure remained unchanged.

S2. Methods

2D grazing-incidence wide angle X-ray scattering (GIWAXS) data were recorded with an Anton Paar SAXSpoint 2.0 system equipped with a Primux 100 micro Cu K_α source and a Dectris EIGER R 1M detector. The oriented (unoriented) COF films were positioned at a sample-detector distance of 140 mm (156 mm) and were measured with an incidence angle of 0.2° (0.3°).

Powder X-ray diffraction (PXRD) measurements were performed using a Bruker D8 Discover with Ni-filtered Cu K_α radiation and a LynxEye position-sensitive detector.

Scanning electron microscopy (SEM) micrographs were obtained with a FEI Helios NanoLab G3 UC microscope equipped with a Schottky field-emission electron source operated at 1 – 30 kV.

Transmission electron microscopy (TEM) was performed on a FEI Titan Themis instrument equipped with a field emission gun operated at 300 kV.

Nitrogen Sorption isotherms were recorded with a Quantachrome Autosorb 1 and Autosorb iQ instrument at 77K. The sample was outgassed for 24h at 120°C under high vacuum prior to the measurements. Pore size distributions were calculated using the QSDFT model with a carbon kernel for cylindrical pores.

UV-Vis-NIR spectra were recorded on a Perkin-Elmer Lambda 1050 spectrometer equipped with a 150 mm integrating sphere, photomultiplier tube (PMT) and InGaAs detectors. **Diffuse reflectance spectra** were collected with a Praying Mantis (Harrick) accessory and were referenced to barium sulfate powder as 100%R standard. The specular reflextion of the sample surface was removed from the signal using apertures that allow only light scatter at angles > 20° to pass.

Atomic force microscopy was measured using a NANOINK AFM setup. A standard tapping mode silicon AFM tip from NANO WORLD was used. The aperture is 20 to 40 nm and the force constant of the cantilever is ~42N/m (length= 125µm, resonance frequency~330kHz). All measurements are performed in tapping mode.

Confocal Photoluminescence Measurements. For Photoluminescence (PL) measurements, hyperspectral images and time resolved PL images, a home-built confocal laser scanning microscope was used. It is based on a microscope body (NIKON) which is combined with a *xyz*-piezo-scanning stage (PHYSIK INSTRUMENTE) for the room temperature (RT) measurements. Herein, the samples are measured upside down in epi-direction using an oil objective with 1.4 NA (NIKON). All low temperature (LT) measurements are performed on a self-built microscope with a commercial cryostat system from ATTOCUBE including scanner, positioner, vacuum chamber and pumps and the cooling apparatus. The microscope around this system is self-built and uses a long-working-distance with 0.75NA (ZEISS). Both microscopes are connected to the same detection path. A beamsplitter (MELLES

GRIOT 03BTL005 for RT-setup, THORLABS BSW29R for the LT-setup) and a spectral 490 or 550nm long pass filter is used to separate the laser from the PL-light. A sub picosecond laser (ichrome TOPTICA) tunable from 476 nm to 645 nm is used for excitation. Here, the excitation wavelengths of 476nm and 510nm laser light is additionally filtered by a 473/10 nm (CHROMA) or 510/10 nm (THORLABS) band pass respectively, which is positioned in the excitation arm. The detection side consists of two parts, which are separated by a rotatable mirror. Additionally, a tiltable mirror in the back focal plane is installed for the diffusion measurements scanning around the confocal spot. One arm in the detection has an avalanche photo diode (APD, type: MPD PDM, detector size 50 x 50 µm), which can be combined with a Time Correlated Single Photon Counting (TCSPC) electronics (BECKER UND HICKEL) measuring time resolved PL- transients. The second part consists of a spectrometer (ANDOR SHAMROCK SRi303) combined with an open electrode CCD camera (ANDOR NEWTON DU920) recording spectra. The data is recorded using a customized LABVIEW (NATIONAL INSTRUMENTS) program that combines the manufacturers' software with our desired measurements. Further processing and analysis are carried out using MATLAB (MATHWORKS) to obtain the PL spectra, TCSPC transients and the images.

S3. WBDT bulk powder characterization

Characterization of the bulk COF powder of WBDT was conducted including PXRD, FTIR, Nitrogen Sorption, steady-state PL and UV-Vis as well as SEM measurements. PXRD of the WBDT COF shows distinct reflexes at 2θ = 2.00°, 3.50°, 4.04°, 5.38°, 6.11°, 7.36°, 8.14°, 8.96°. Pawley refinement of the powder x-ray diffractogram yielded the unit cell parameters, with R_{wp} = 4.20% and R_p = 3.40% (**Figure S1**)

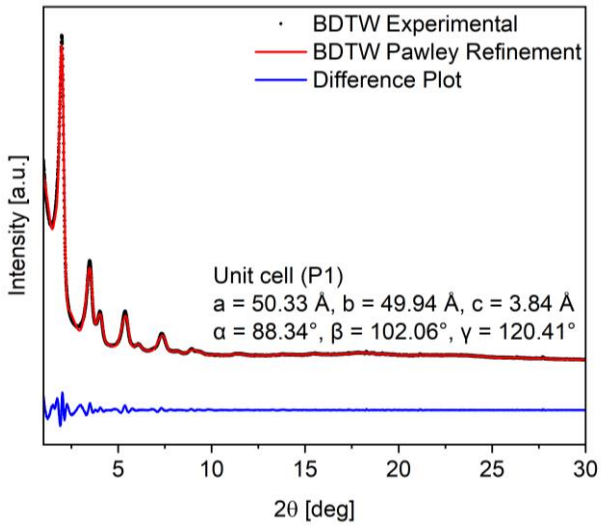

Figure S1. Experimental PXRD of the WBDT COF powder together with the Pawley refinement and the resulting difference plot. Unit cell lengths and angles are indicated.

FTIR measurements confirm the successful formation of the COF network by the disappearance of the -NH (3342 cm^{-1}) and -CO (1664 cm^{-1}) vibrational modes and the appearance of the vibrational mode of the imine bond (1609 cm^{-1}) in the IR spectrum of the WBDT COF (**Figure S2**).

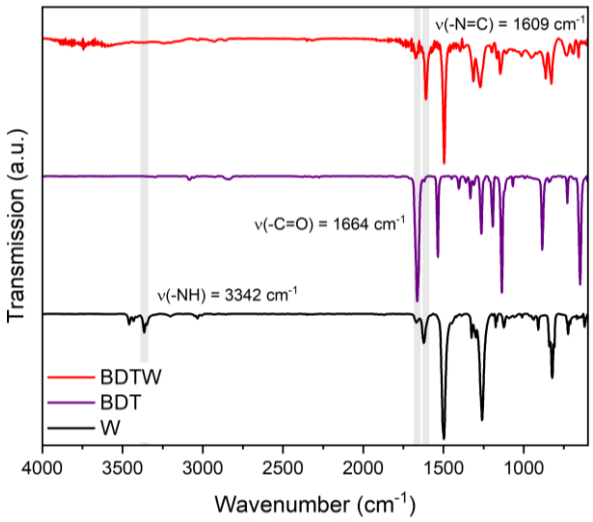

Figure S2. FTIR spectra of the two linker molecules W and BDT and of the WBDT COF.

Surface area and pore sizes of the WBDT COF were determined by nitrogen sorption measurements. The sorption isotherm is a mixture of type I and type IVb with two nitrogen uptake steps. The first step at low partial pressures is characteristics for microporous materials, whilst the second step reveals additional capillary condensation, typical for the presence of mesopores. The calculated Brunauer-Emmet-Teller surface area is 635 $m^2 g^{-1}$ and the two pore sizes of the Kagomé-like structure, are 1.9 nm and 3.4 nm (**Figure S3**).

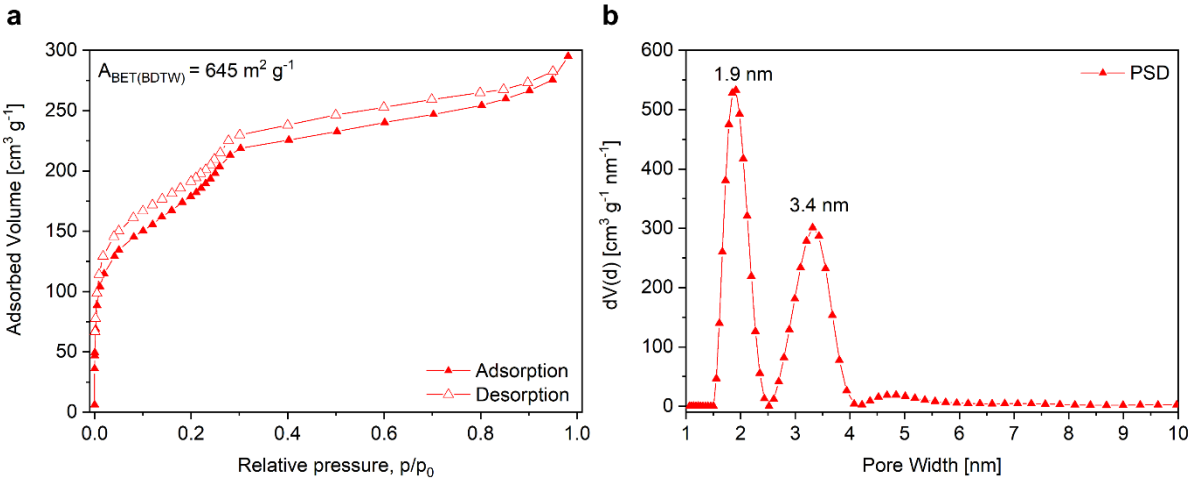

Figure S3. (**a**) Sorption isotherm of the WBDT COF with a BET surface area of 645 $cm^2 g^{-1}$. (**b**) Pore size distribution (PSD) with two pore sizes, 1.9 nm and 3.4 nm, consistent with the dual-pore shape of the Kagomé-like structure.

Steady-state PL and UV-Vis measurements were conducted to optically characterize the WBDT COF powder. The dark red COF powders emits 1.83 eV (677 nm) and has a maximum absorption at 2.41 eV (514 nm). Fitting of the absorption onset using Tauc plot gives a direct band gap of 1.98 eV (**Figure S4**).

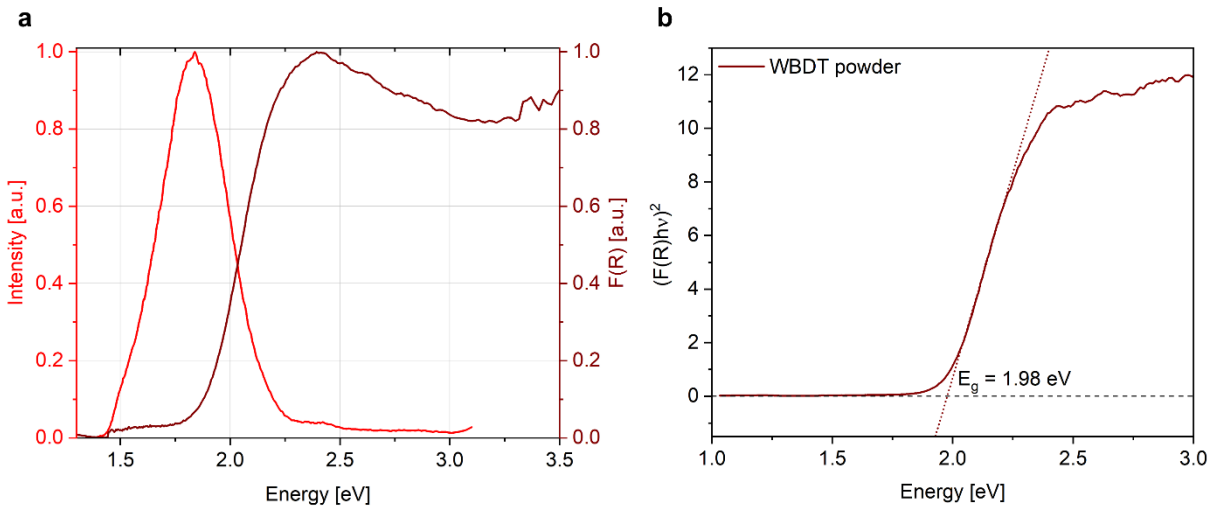

Figure S4. (**a**) Steady-state PL and UV-Vis (Kubelka-Munk, diffuse reflection) of the WBDT COF powder. (**b**) Fitting of the absorption onset using Tauc plot.

Scanning electron micrographs reveal a uniform, spherical morphology of the WBDT COF particles. Transmission electron microscopy confirms the crystallinity of the COF. Detection of crystal domains with the *z*-axis oriented parallel to the incident electron beam visualize the pseudo-hexagonal pattern generated by the dual-pore Kagomé-like structure (**Figure S5**).

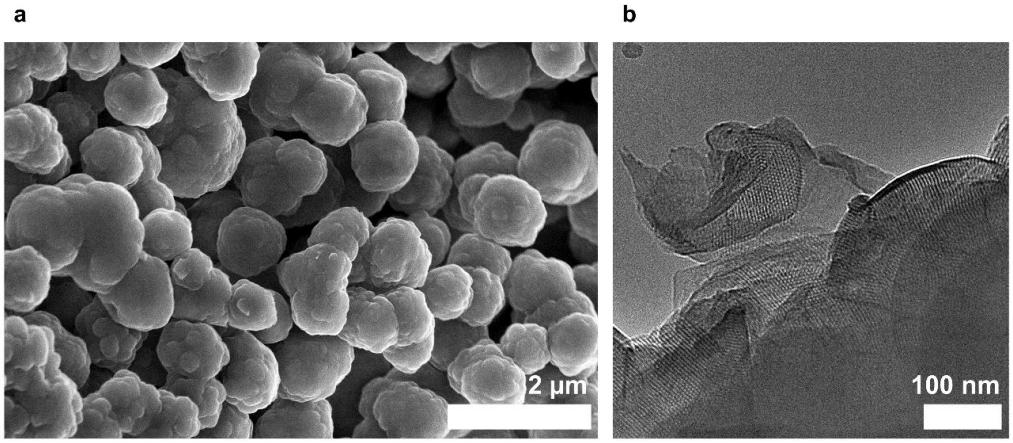

Figure S5. (**a**) SEM micrograph visualizing the spherical morphology of the WBDT COF powder. (**b**) TEM image confirming the crystalline nature of the COF.

S4. WBDT thin film characterization

Fitting of the absorption onset of the WBDT COF thin film using a Tauc plot gives an indirect band gap of 2.16 eV as indicated in **Figure S6**a.

No significant broadening of the PL spectrum is visible upon decrease of the temperature. This is illustrated in **Figure S6**b, depicting the PL spectrum of the thin film at 5 K and at 300 K.

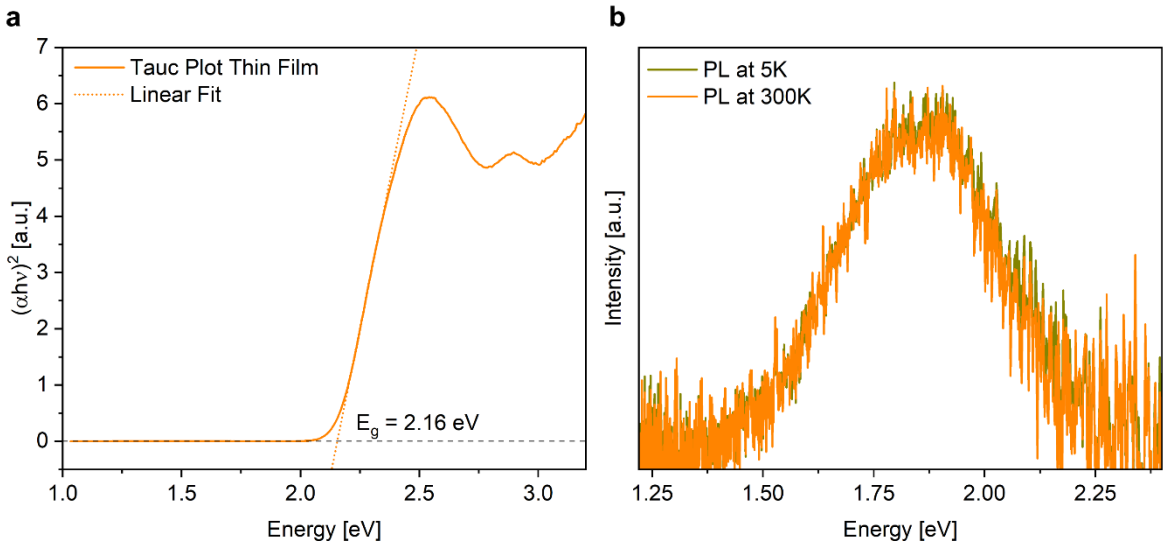

Figure S6. (**a**) Fitting of the absorption onset of the WBDT COF thin film using Tauc plot. (**b**) PL spectra of the thin film at 5 K and 300 K.

The thickness of the film is determined *via* SEM cross-section analysis (~120 nm) and as well as by scanning over a thin scratch on the film's surface using AFM (~130 nm) (**Figure S7**).

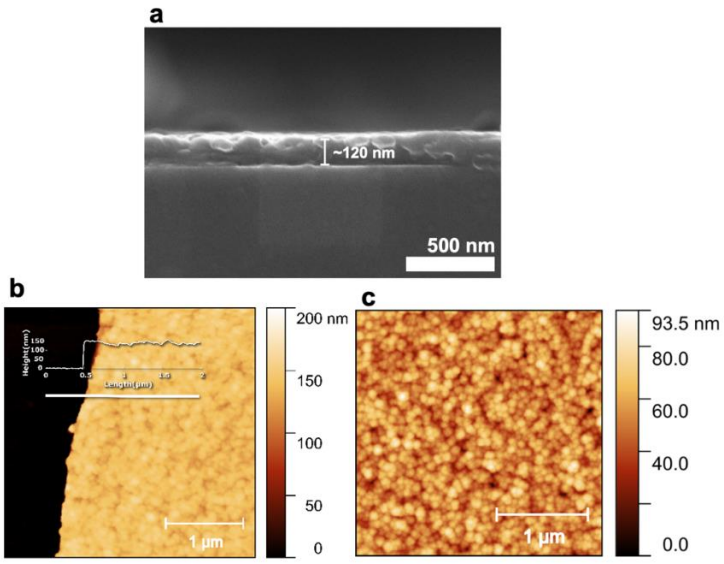

Figure S7. (**a**) SEM cross-section of the WBDT COF thin film. (**b**) AFM image of the measured scratch with the difference in height as inset. (**c**) AFM image of a 2.5 x 2.5 µm^2 section the film surface.

Linear Power Dependency. For the steady-state PL and RDTR PL measurements, it is crucial that the response to the incident laser power is linear in the range of the used laser power, assuring that the number of excited states *n* is proportional to the measured intensity. **Figure S8** confirms the linear power dependency of the PL signal up to ~50 µJ/cm^2. In order to guarantee the stability of the COF throughout the optical measurements, the laser power was chosen accordingly. All RDTR PL measurements were performed under vacuum, steady-state PL was performed under argon atmosphere.

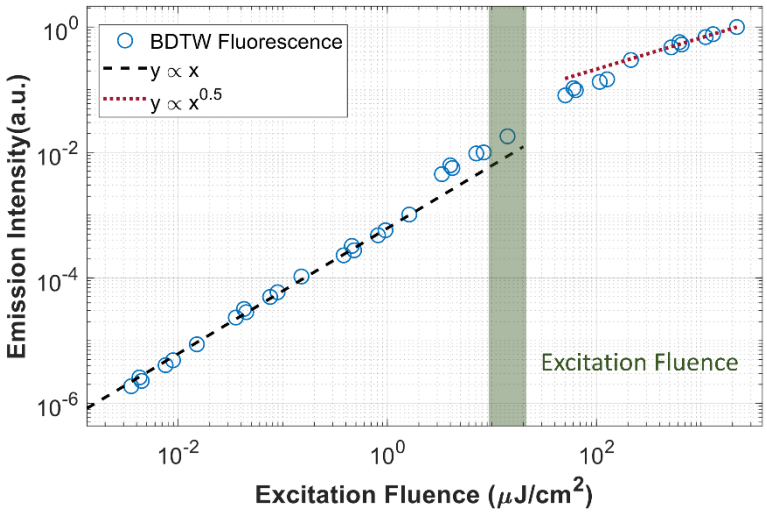

Figure S8. The excitation fluence dependency of the PL signal. The gray range shows the excitation fluence used in the experiments.

Confocal Scan and Hyperspectral Images. To confirm the homogeneity of the spectral response from the thin film, confocal scanning and hyperspectral imaging of a 10 x 10 µm^2 section of the WBDT thin film were conducted, showing neglectable changes in normalized intensity, central energy and spectral width of the PL signal (**Figure S9**a, b and c, respectively).

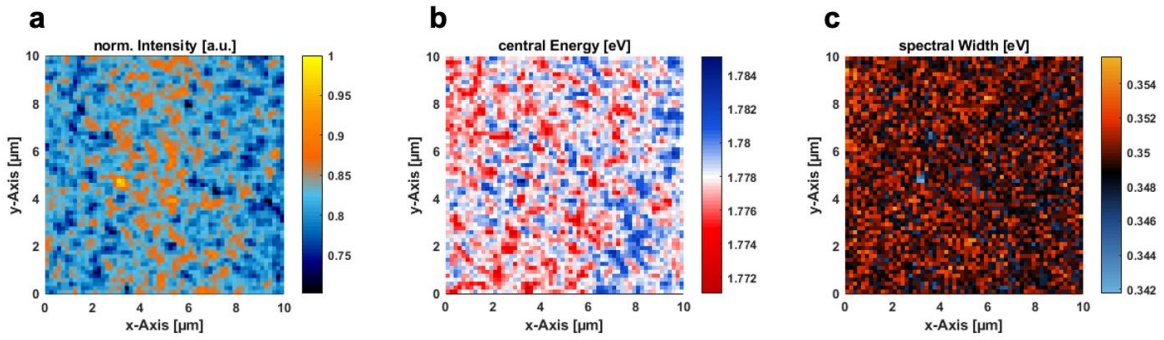

Figure S9. Confocal scan and hyperspectral images of the WBDT thin film, mapping differences in (**a**) normalized intensity, (**b**) central energy and (**c**) spectral width of the PL signal.

S5. RDTR PL measurements – Analysis and Fitting

The data is collected in the form of a TCSPC transient for every remote position of the tiltable mirror. For each temperature step, transients from two different directions through the confocal spot were recorded. Furthermore, two temperature series were measured to guarantee the reproducibility of the observed diffusive transport. Data set 1 is integrated over the blue part of the PL spectrum (590-610nm, 2.03 – 2.10 eV) and Data Set 2 is integrated over the whole PL signal. In both sets the same trend of the diffusive transport is observed. Since the spectrum contains not only a mobile species but also a localized radiative state, the diffusive transport is more visible in the blue data set (Data Set 1). An exemplary data set at 40K is shown in **Figure S10**:

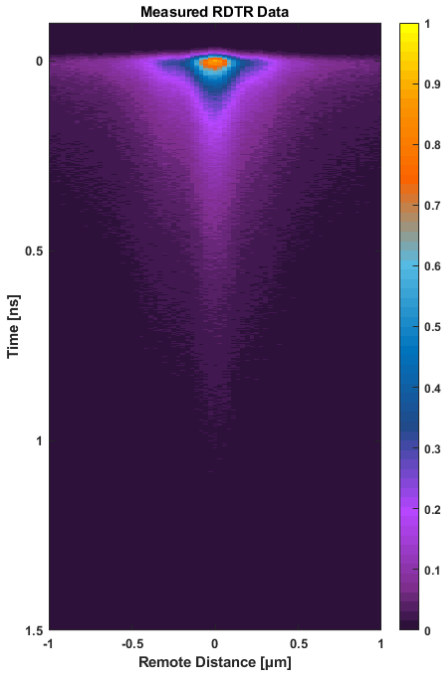

Figure S10. RDTR PL Data at 40K.

As the COF film is thin (~ 100 nm), and the Rayleigh length is around a micrometer, the focus penetrates the whole film in the direction perpendicular to the substrate (*z*-direction). This measuring setup only allows for the observation of the in-plane 2D diffusive transport in the thin film.

The observed diffusive species has a limited lifetime, leading us to the following differential equation (S1):

$$\frac{dn(x,y,t)}{dt} = D\Delta n(x,y,t) - k_1 n(x,y,t) \qquad \text{(S1)}$$

In equation S1, *n* is the number of excited states that are proportional to the measured PL intensity. This is confirmed by linear power dependency (**Figure S8**). *D* is the diffusion coefficient and k_1 is the lifetime of the diffusive species. Assuming a Gaussian starting distribution of excited states, this differential equation can be analytical solved by

$$n(x,y,t) = \frac{N_0 2\sigma^2}{2\sigma^2+4Dt}\, exp\left(\frac{-x^2-y^2}{2\sigma^2+4Dt}\right) \cdot \exp(-k_1 t), \tag{S2}$$

where the spatial integration over $N_0\ exp\left(\frac{-x^2-y^2}{2\sigma^2}\right)$ is the total number of excited states at $t = 0$ and σ is the width of the starting Gaussian distribution. To analyse the RDTR PL data, two different methods are used and subsequently compared for cross-verification. For the first method (method I in the main text), we fit two Gaussians, one with a fixed width corresponding to the initial signal width determined by the excitation focus and the optical resolution of the setup and the other with a variable width (**Figure S11**a). The results show that the variable width follows a linear change in time, as expected from the following relation (equation S3), derived from the 2D diffusion equation S2:

$$\sigma^2 \sim 2Dt \tag{S3}$$

This linear relation is shown in **Figure S11**b. The contribution with fixed (time-independent) width is attributed to a localized, immobile excited species, presumably related to defect trap states.

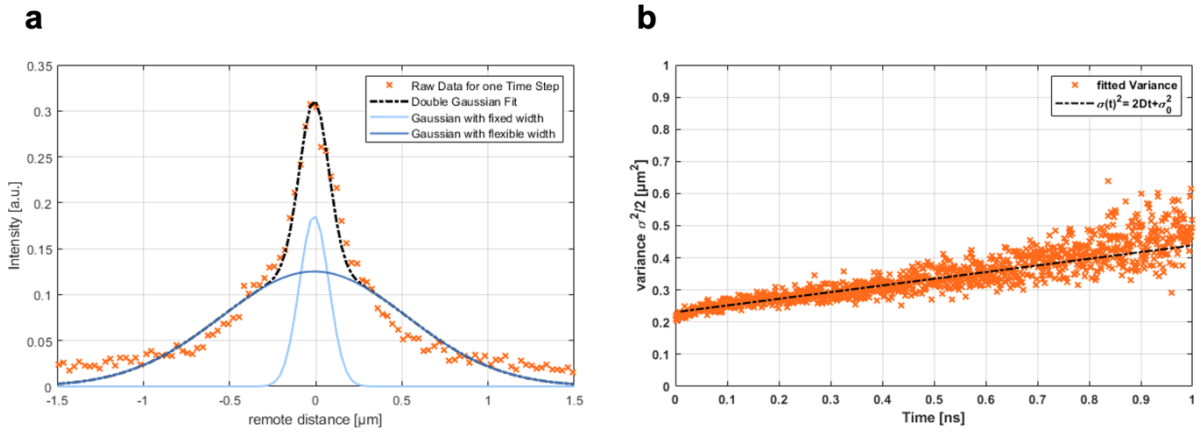

Figure S11. (**a**) Double Gaussian Fit (fixed and flexible width) of the raw RDTR PL data for one time step. (**b**) Linear Fit of the variance of the width as a function of time.

The second method (method II in the main text) involves analysing the full data set using the analytical solution (equation S2) and fitting the whole two-dimensional data with a single diffusion coefficient.

This analysis is split into two parts according to the two different timescales observed. **Figure S12** visualizes and compares the diffusion coefficients obtained by the two methods.

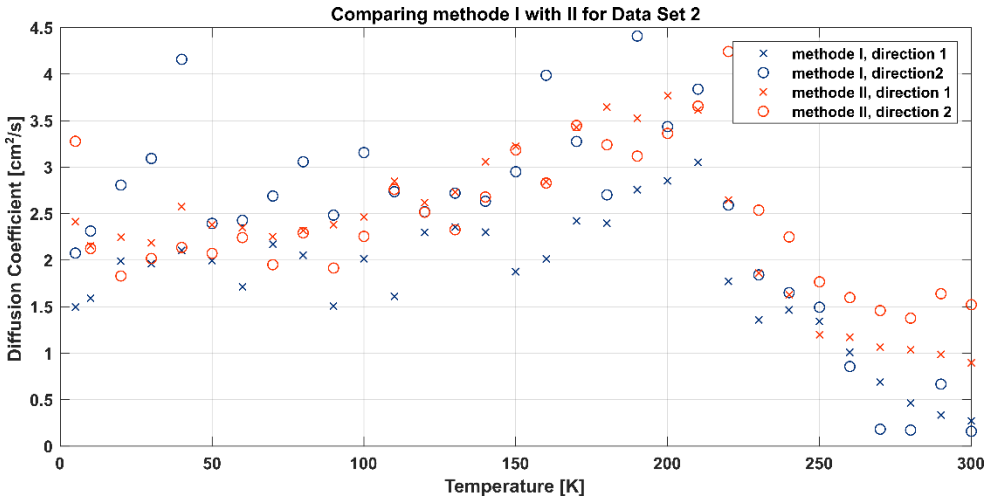

Figure S12. Comparison of the two methods I and II for the determination of the diffusion coefficient for data set 2 (full spectral range). Data are collected in two different scanning directions through the confocal spot, perpendicular to each other (direction 1 and 2).

For the free charge carrier diffusion coefficient, the time interval from -0.025 to 0.005 ns is used. Additionally, the calculated data are convoluted with the instrument response function (IRF, FWHM of 28 ps). The time-zero is defined by the maximum and the overlap of the initial rise of the IRF at the centre of the confocal spot (remote distance = 0 µm). An additional Gauss distribution with a mono-exponential decay is added, representing the localized excited states.

For the free charge carrier diffusion, only method I is used, and the data is averaged over both directions (**Figure S13**a). The time interval between 0.1 and 1 ns is used for the exciton diffusion coefficient. Here, both methods I and II are applied, and the data is averaged over both directions (**Figure S13**b).

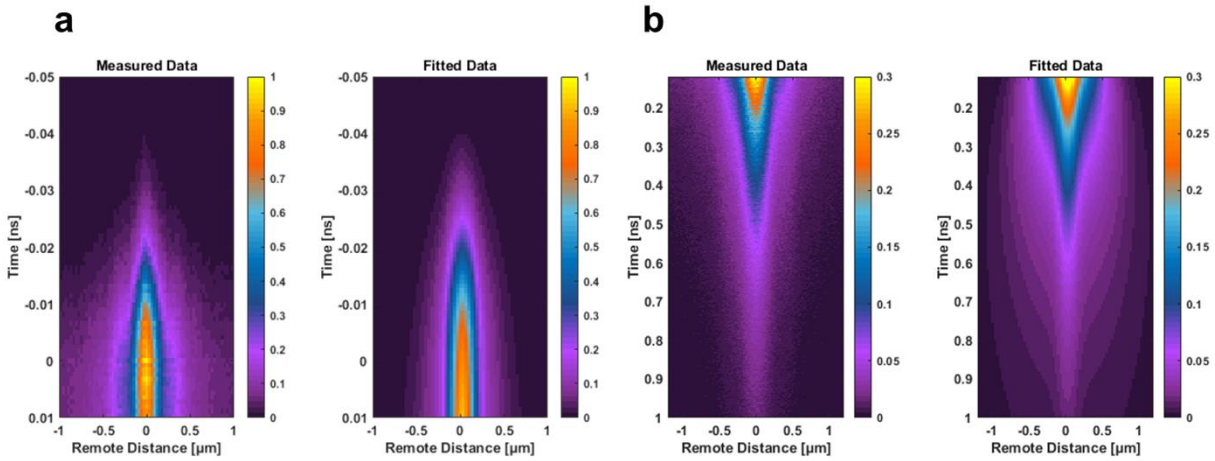

Figure S13. Measured and fitted data for the diffusion coefficient of the (**a**) free charge carriers and (**b**) excitons.

According to the fits, the lifetimes τ of the excitons are in the order of 0.9 - 1.2 ns. Using τ, the diffusion length L_D can be approximated:

$$L_D = \sqrt{2D\tau} \tag{S4}$$

The diffusion length of the polarons as a function of temperature is depicted in **Figure S14**.

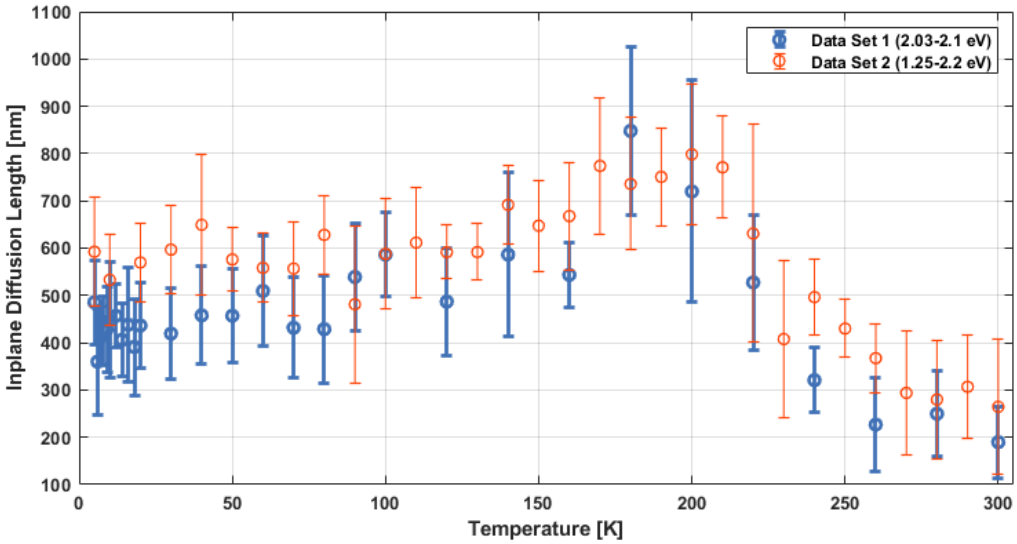

Figure S14. Diffusion length of the excitons as a function of temperature.

S6. WBDT unoriented thin film characterization and diffusion dynamics

Characterization

The WBDT COF has a strong tendency to grow highly oriented thin films on most substrates, even when incorrect ratios of building blocks are used or different solvents are chosen for the COF synthesis. Therefore, we changed the substrate's morphology drastically from a smooth surface to a meso-structured SiO_2 inverse opal with a thickness of ~ 4 µm and pores with 300 nm diameter. WBDT COF grows interconnected spherical grains of around 150-200 nm size similar to the bulk powder, both into and on top of the structure. **Figure S15**a and b show SEM top views of the inverse opal structure, c and d show the WBDT COF@SiO_2 grown on top the macro-structured substrate.

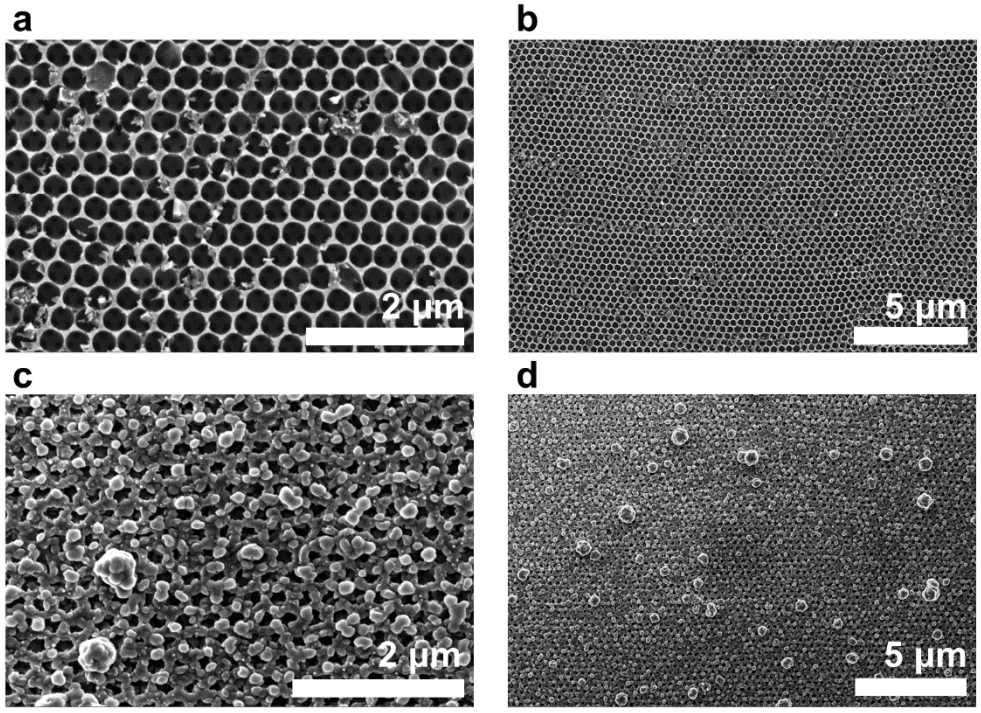

Figure S15. (**a**) and (**b**) Top view of the SiO_2 inverse opal structure at different magnifications. (**c**) and (**d**) WBDT COF@SiO_2 inverse opal structure.

Figure S16a and c show cross sections of the WBDT COF@SiO_2, illustrating the COF growth both into the mesopores and on top of the structure. Figure b and d show the same section of the film, looking only at the backscattered electrons. This method has a higher contrast for the inorganic SiO_2, revealing the SiO_2 structure below the COF grains.

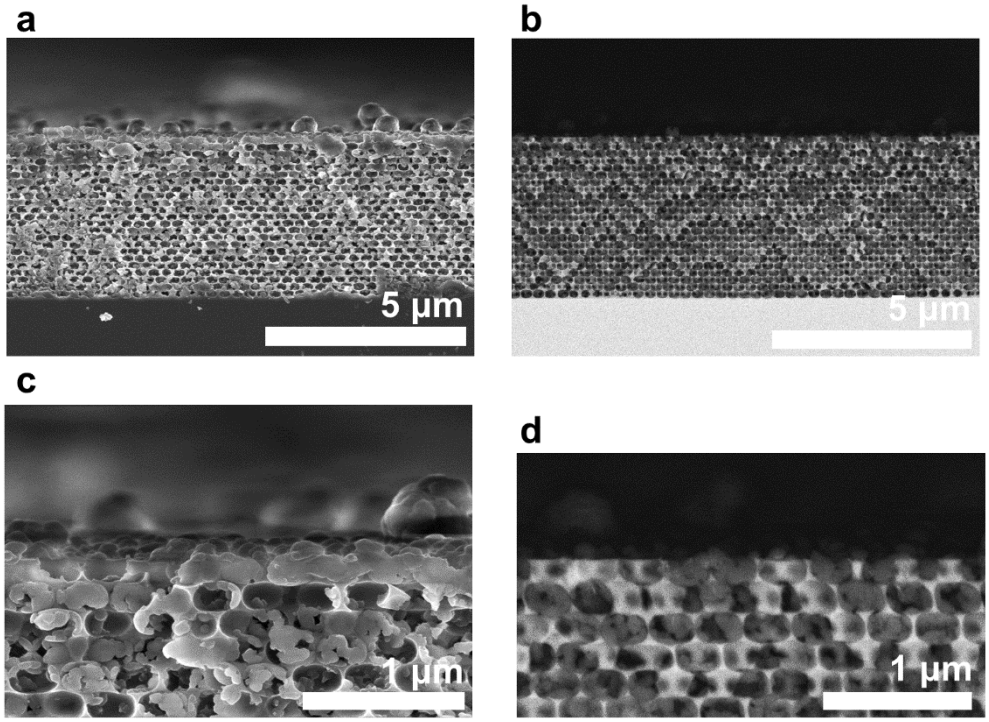

Figure S16. (**a**) and (**c**) Cross section of WBDT COF@SiO_2 with different magnifications, showing the growth of the COF both into the structure as well as on top of it. (**b**) and (**d**) Backscattered electron image of the same film sections as (**a**) and (**c**), revealing the SiO_2 structure below the COF.

Additionally, AFM was conducted on a 2.5 x 2.5 µm^2 section of the unoriented thin film to better illustrate the difference in morphology compared to the oriented WBDT film (**Figure S17**)

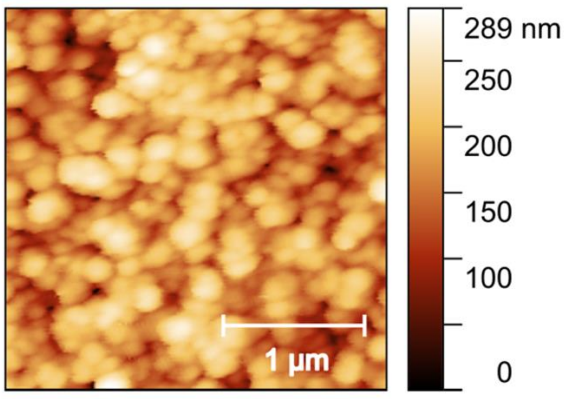

Figure S17. AFM image of a 2.5 x 2.5 µm^2 section of the unoriented WBDT thin film.

In **Figure S18**, the reflections in the GIWAXS pattern of the unoriented film appear at identical scattering vectors in the GIWAXS pattern of the oriented film and in the PXRD pattern of the bulk material, confirming the formation of a crystalline COF. The intensity of the *hkl* reflections is uniformly distributed in q_z and q_r direction, forming a semi-circle. The scattering pattern indicates a random orientation of the COF crystallites.

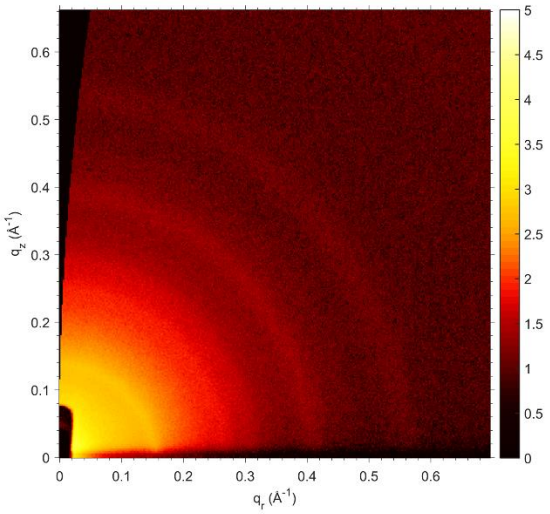

Figure S18. GIWAXS pattern of the unoriented WBDT COF grown on an SiO_2 inverse opal structure. The colour map was chosen differently to the main text to improve the visibility of the reflexes at low q_r values.

Steady-state PL and UV-Vis measurements were conducted to optically characterize the WBDT COF@SiO_2 film. The dark red film emits at 1.88 eV (660 nm) and has a maximum absorption at 2.48 eV (500 nm). Fitting of the absorption onset using Tauc plot gives an indirect band gap of 2.08 eV (**Figure S19**)

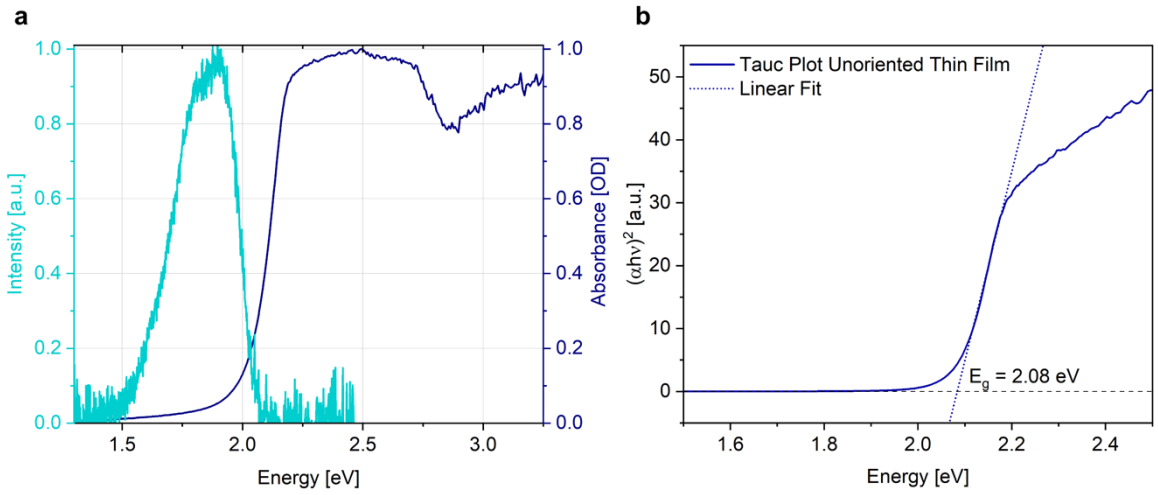

Figure S19. (**a**) Steady-state PL and UV-Vis of the unoriented WBDT COF thin film. (**b**) Tauc plot of the absorption onset.

Diffusion Dynamics

The analysed RDTR PL data for the unoriented WBDT COF thin film is shown in **Figure S20**. With $D_{unoriented} \approx 11$ cm^2 s^{-1}, the diffusion coefficient for the free charge carrier in the shorter timescale is comparable to the oriented thin film ($D_{oriented} = 10$ cm^2 s^{-1}). This is in line with our interpretation of the carriers diffusing within one grain and the grain size not significantly changing from oriented to unoriented film. The exciton diffusion coefficient is decreasing with decreasing temperature, indicating a *hopping* type transport. It is also overall lower, suggesting that the high degree of orientation of the crystallites on the film plays a major role in the diffusive transport.

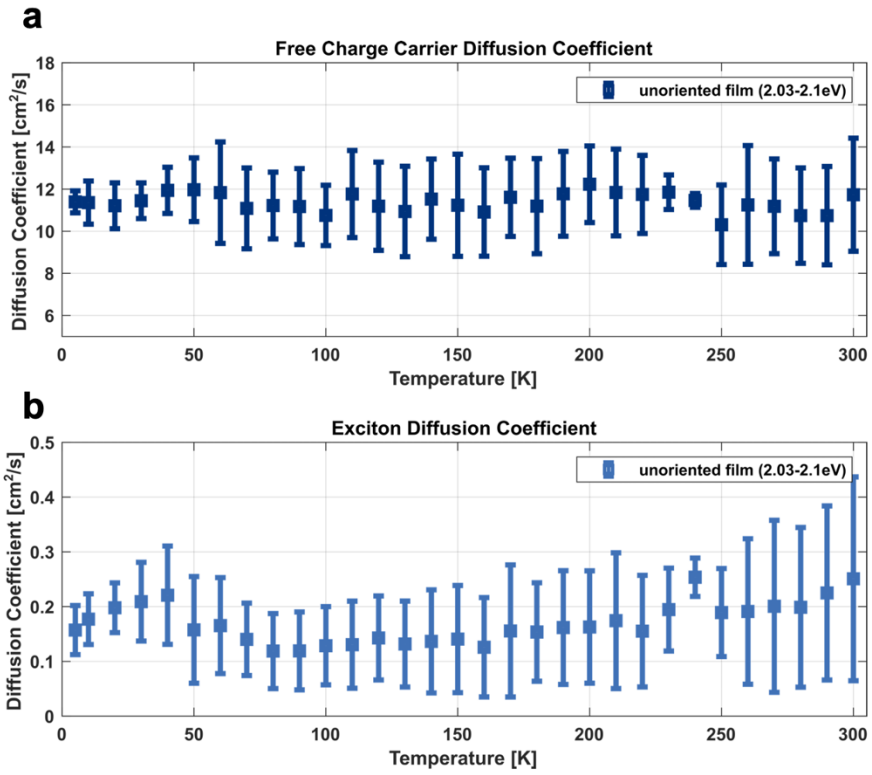

Figure S20. Diffusion coefficient as a function of temperature of the (**a**) free charge carriers and (**b**) excitons in the unoriented WBDT COF thin film.

S7. Optical Pump Terahertz Probe Spectroscopy (OPTP)

The setup used for optical pump terahertz probe (OPTP) transients is described in full detail elsewhere.[4] Briefly, an amplified Ti:sapphire laser system (Spitfire ACE, Spectra-Physics) provides 800-nm light pulses (35 fs) with 5-kHz repetition rate. The fundamental output of the amplified Ti:sapphire laser is used to generate single-cycle THz radiation pulses in a W/$Co_{40}Fe_{40}B_{20}$/Pt multilayer film on quartz (spintronic emitter) through the inverse spin Hall effect.[5] Furthermore, the optical excitation pulses (400 nm) used to photoexcite the samples are generated by second-harmonic generation in a beta-barium-borate (BBO) crystal. During OPTP measurements, the fractional changes in the THz transmission (0.5-2.5 THz) following the 400-nm photoexcitation are monitored by using free-space electro-optic sampling (EOS) in a 1-mm-thick (110)-ZnTe crystal. BDTW COF thin films were deposited onto 2 mm thick z-cut quartz. During OPTP measurements, the THz emission and detection optics and samples are kept under vacuum at pressures below 0.1 mbar.

Extraction of charge-carrier mobility from OPTP measurements

We extracted effective charge-carrier mobility following the method developed by Wehrenfennig et al..[6] Briefly, for semiconductor thin films materials with thicknesses smaller than the wavelength of the incident THz radiation, the sheet photoconductivity can be estimated from the fractional change in the transmitted THz electric field $\Delta T/T$, and expressed as

$$\Delta S = -\epsilon_0 c(n_q + n_v)\left(\frac{\Delta T}{T}\right) \quad \text{(S6)}$$

where $n_q = 2.13$ and $n_v = 1$ are the refractive indexes of quartz and vacuum, respectively.[7]

To extract the effective charge-carrier mobility from the sheet photoconductivity, the number of initially photogenerated carriers is estimated as

$$N = \phi\frac{E\lambda}{hc}\left(1 - R_p - T_p\right) \quad \text{(S7)}$$

Where φ is the photon-to-charge branching ratio (i.e., the fraction of generated charges per absorbed photon absorbed), E is the pump pulse energy, λ is the excitation wavelength, and R_p and T_p are the reflectance and transmittance of the sample at the excitation wavelength (3.1 eV, 400 nm). The charge-carrier mobility μ can be calculated as

$$\mu = \frac{\Delta S\, A_{eff}}{Ne} \quad \text{(S8)}$$

Where A_{eff} is the effective overlap area between THz and pump beam and e is the elementary charge. By substituting Equation S6 and Equation S7 into Equation S8, the effective charge-carrier mobility is obtained as:

$$\varphi\mu = -\epsilon_0 c(n_q + n_v)\frac{A_{eff}hc}{eE\lambda(1 - R_{pump} - T_{pump})}\left(\frac{\Delta T}{T}\right) \quad \text{(S9)}$$

Here, it is worth noting that the sheet photoconductivity signal measured by OPTP arises from the contributions of both photogenerated free electrons and holes. Therefore, the extracted charge-carrier mobility is the effective electron-hole sum mobility.

Calculation of the diffusion length using charge carrier lifetime from OPTP

In this study, we calculated the diffusion length L_D of the free charge carriers (*fast species*) using the lifetime extracted from OPTP measurements τ = 1.4 ps and the diffusion coefficient given by RDTR PL D ~ 10 cm^2 s^{-1}, assuming that the fast-moving species is equal to the free charge carriers. Both methods are independent and generate two different values. OPTP measures only the free charge carriers, formed shortly after excitation. From the absorbed probe signal, an effective mobility is calculated and a lifetime of the free charge carriers can be extracted. The effective mobility $\varphi\mu \sim 0.12 \pm 0.05\ cm^2V^{-1}s^{-1}$contains the photon-to-charge branching ratio φ, since the exact number of contributing free charge carriers is unknown. In RDTR PL measurements however, the PL is generated by a combination of free charge carriers and possible unbound excitons. Here, the diffusive transport is only driven by the chemical potential of the generated excited states, while in OPTP measurements, the excited charge carriers react to the applied THz probing field.

In principle the absolute mobility μ and diffusion coefficient D can be connected *via* the Einstein-Smoluchowski[8,9] relation:

$$D = \frac{\mu k_B T}{e} \quad \text{(S10)}$$

with the Boltzmann constant k_B, the temperature T and the elemental charge e. However, this formula is only valid in the case of a charged particle with a charge e, moving through a neutral medium. In our case, the excited charges are bound to each other (exciton) or move as ambipolar charge carriers (combined movement of electrons and holes) in a dielectric and periodic crystal lattice. This lattice shields the charges. Therefore, the Einstein-Smoluchowski relation cannot be readily applied here. A more accurate model would be needed to contextualize both numbers. Additionally, it is not clear if the disorder in the system has an influence on the fast-moving species.

Hence, the calculated diffusion length of the free charge carriers (*fast species*) in this study, combining values from both OPTP and RDTR PL measurements, should be considered as a qualitative estimation.

S8. Theoretical Calculations

The structure of WBDT is optimized at density functional theory (DFT) level. We use the projector-augmented wave (PAW) method[10,11] in conjugation with Perdew-Burke-Ernzerhof (PBE) exchange and correlation functional[12] as implemented in the Vienna ab-initio simulation package (VASP).[13–15] The atomic positions are relaxed using the conjugate gradient method with an energy convergence value of 10^{-6} eV. The dispersion interactions are described with the nonlocal vdW-DF functionals by Dion et al.[16] The band structure of WBDT shown in Figure 2a has been corrected by a scissors shift[17] of +0.49 eV for all conduction bands to estimate the band gap at Hybrid-DFT (HSE06) level (L. Fuchs et al. unpublished).

The Brillouin zone (BZ) for the relaxation simulations is sampled with a 1x1x6 Γ-centered mesh. The electronic band structure (**Figure 2a**) is calculated along a path connecting high-symmetry points in the primitive hexagonal cell (Γ-M-K-Γ-A) with 20 equally spaced points between two special points. Additionally, atomic projections of the Kohn-Sham states onto W and BDT fragments were calculated.

For the calculation of the transition densities of the excited states, WBDT is divided into two precursor fragments (BDT and W), which are NH- and H-terminal saturated. After a gas phase relaxation of the fragments with VASP, the transition densities describing the excited states are calculated with the software gaussian16[18] and Multiwfn,[19] using M062X as the exchange-correlation functional and a cc-pVTZ basis set. Excitonic transition densities are used to calculate the Coulomb interaction between the exciton states that are placed at the fragment position in the COF as described earlier[20] with an effective screening described by a low relative dielectric permittivity of $\epsilon = 2$. The large electron and hole transfer integrals extracted from the calculated band structure are further taken into account for second-order transfer processes to estimate the resulting effective exciton transfer integrals of $\varepsilon \cong 50$ meV.

A Marcus-type hopping ansatz with exciton coupling of $\varepsilon \cong 50$ meV and an estimated reduced reorganization energy of $\Lambda \cong 0.1$ eV was used to estimate the diffusion coefficient at 300K.

References

(1) Sick, T.; Rotter, J. M.; Reuter, S.; Kandambeth, S.; Bach, N. N.; Döblinger, M.; Merz, J.; Clark, T.; Marder, T. B.; Bein, T.; Medina, D. D. Switching on and off Interlayer Correlations and Porosity in 2D Covalent Organic Frameworks. *Journal of the American Chemical Society* **2019**, *141* (32), 12570–12581. DOI: 10.1021/jacs.9b02800. Published Online: Feb. 8, 2019.

(2) Rotter, J. M.; Guntermann, R.; Auth, M.; Mähringer, A.; Sperlich, A.; Dyakonov, V.; Medina, D. D.; Bein, T. Highly conducting Wurster-type twisted covalent organic frameworks. *Chemical science* **2020**, *11* (47), 12843–12853. DOI: 10.1039/d0sc03909h. Published Online: Oct. 27, 2020.

(3) Hatton, B.; Mishchenko, L.; Davis, S.; Sandhage, K. H.; Aizenberg, J. Assembly of large-area, highly ordered, crack-free inverse opal films. *Proceedings of the National Academy of Sciences of the United States of America* **2010**, *107* (23), 10354–10359. DOI: 10.1073/pnas.1000954107. Published Online: May. 19, 2010.

(4) Buizza, L. R. V.; Wright, A. D.; Longo, G.; Sansom, H. C.; Xia, C. Q.; Rosseinsky, M. J.; Johnston, M. B.; Snaith, H. J.; Herz, L. M. Charge-Carrier Mobility and Localization in Semiconducting Cu2AgBiI6 for Photovoltaic Applications. *ACS energy letters* **2021**, *6* (5), 1729–1739. DOI: 10.1021/acsenergylett.1c00458. Published Online: Apr. 7, 2021.

(5) Seifert, T.; Jaiswal, S.; Martens, U.; Hannegan, J.; Braun, L.; Maldonado, P.; Freimuth, F.; Kronenberg, A.; Henrizi, J.; Radu, I.; Beaurepaire, E.; Mokrousov, Y.; Oppeneer, P. M.; Jourdan, M.; Jakob, G.; Turchinovich, D.; Hayden, L. M.; Wolf, M.; Münzenberg, M.; Kläui, M.; Kampfrath, T. Efficient metallic spintronic emitters of ultrabroadband terahertz radiation. *Nature Photon* **2016**, *10* (7), 483–488. DOI: 10.1038/nphoton.2016.91.

(6) Wehrenfennig, C.; Eperon, G. E.; Johnston, M. B.; Snaith, H. J.; Herz, L. M. High charge carrier mobilities and lifetimes in organolead trihalide perovskites. *Advanced Materials* **2014**, *26* (10), 1584–1589. DOI: 10.1002/adma.201305172.

(7) Joyce, H. J.; Boland, J. L.; Davies, C. L.; Baig, S. A.; Johnston, M. B. A review of the electrical properties of semiconductor nanowires: insights gained from terahertz conductivity spectroscopy. *Semicond. Sci. Technol.* **2016**, *31* (10), 103003. DOI: 10.1088/0268-1242/31/10/103003.

(8) Smoluchowski, M. von. Zur kinetischen Theorie der Brownschen Molekularbewegung und der Suspensionen. *Ann. Phys.* **1906**, *326* (14), 756–780. DOI: 10.1002/andp.19063261405.

(9) Einstein, A. Über die von der molekularkinetischen Theorie der Wärme geforderte Bewegung von in ruhenden Flüssigkeiten suspendierten Teilchen. *Ann. Phys.* **1905**, *322* (8), 549–560. DOI: 10.1002/andp.19053220806.

(10) Blöchl, P. E. Projector augmented-wave method. *Physical review. B, Condensed matter* **1994**, *50* (24), 17953–17979. DOI: 10.1103/physrevb.50.17953.

(11) Kresse, G.; Joubert, D. From ultrasoft pseudopotentials to the projector augmented-wave method. *Phys. Rev. B* **1999**, *59* (3), 1758–1775. DOI: 10.1103/physrevb.59.1758.

(12) Perdew, J. P.; Burke, K.; Ernzerhof, M. Generalized Gradient Approximation Made Simple. *Physical review letters* **1996**, *77* (18), 3865–3868. DOI: 10.1103/physrevlett.77.3865.

(13) Kresse, G.; Hafner, J. Ab initio molecular-dynamics simulation of the liquid-metal-amorphous-semiconductor transition in germanium. *Physical review. B, Condensed matter* **1994**, *49* (20), 14251–14269. DOI: 10.1103/physrevb.49.14251.

(14) Kresse, G.; Furthmüller, J. Efficiency of ab-initio total energy calculations for metals and semiconductors using a plane-wave basis set. *Computational Materials Science* **1996**, *6* (1), 15–50. DOI: 10.1016/0927-0256(96)00008-0.

(15) Kresse, G.; Furthmüller, J. Efficient iterative schemes for ab initio total-energy calculations using a plane-wave basis set. *Phys. Rev. B* **1996**, *54* (16), 11169–11186. DOI: 10.1103/PhysRevB.54.11169.

(16) Dion, M.; Rydberg, H.; Schröder, E.; Langreth, D. C.; Lundqvist, B. I. van der Waals density functional for general geometries. *Phys. Rev. Lett.* **2004**, *92* (24), 246401. DOI: 10.1103/PhysRevLett.92.246401. Published Online: Jun. 16, 2004.

(17) Bechstedt, F. *Many-body approach to electronic excitations*:*Concepts and applications*, Vol. 181; Springer, 2015. DOI: 10.1007/978-3-662-44593-8.

(18) M. J. Frisch, G. W. Trucks, H. B. Schlegel, G. E. Scuseria, M. A. Robb, J. R. Cheeseman, G. Scalmani, V. Barone, B. Mennucci, G. A. Petersson, H. Nakatsuji, M. Caricato, X. Li, H. P. Hratchian, A. F. Izmaylov, J. Bloino, G. Zheng, J. L. Sonnenberg, M. Hada, M. Ehara, K. Toyota, R. Fukuda, J. Hasegawa, M. Ishida, T. Nakajima, Y. Honda, O. Kitao, H. Nakai, T. Vreven, J. A. Montgomery, Jr., J. E. Peralta, F. Ogliaro, M. Bearpark, J. J. Heyd, E. Brothers, K. N. Kudin, V. N. Staroverov, T. Keith, R. Kobayashi, J. Normand, K. Raghavachari, A. Rendell, J. C. Burant, S. S. Iyengar, J. Tomasi, M. Cossi, N. Rega, J. M. Millam, M. Klene, J. E. Knox, J. B. Cross, V. Bakken, C. Adamo, J. Jaramillo, R. Gomperts, R. E. Stratmann, O. Yazyev, A. J. Austin, R. Cammi, C. Pomelli, J. W. Ochterski, R. L. Martin, K. Morokuma, V. G. Zakrzewski, G. A. Voth, P. Salvador, J. J. Dannenberg, S. Dapprich, A. D. Daniels, Ö. Farkas, J. B. Foresman, J. V. Ortiz, J. Cioslowski, and D. J. Fox. *Gaussian 16, Revision B.01*; Gaussian, Inc., 2016.

(19) Lu, T.; Chen, F. Multiwfn: a multifunctional wavefunction analyzer. *Journal of computational chemistry* **2012**, *33* (5), 580–592. DOI: 10.1002/jcc.22885. Published Online: Dec. 8, 2011.

(20) Müller, K.; Schellhammer, K. S.; Gräßler, N.; Debnath, B.; Liu, F.; Krupskaya, Y.; Leo, K.; Knupfer, M.; Ortmann, F. Directed exciton transport highways in organic semiconductors. *Nat Commun* **2023**, *14* (1), 5599. DOI: 10.1038/s41467-023-41044-9. Published Online: Sep. 12, 2023.

Giant rare-earth metal catecholate crystals - morphology control and rapid NIR luminescence response

Marina Schönherr[†,a,b], Alexander Biewald[†,a,b], Andre Mähringer[a,b], Peter Mayer [a,b], Markus Döblinger[a,b], Patricia I. Scheurle[a,b], Achim Hartschuh[a,b*] and Dana D. Medina[,a,b*]

[a]Department of Chemistry, Ludwig-Maximilians-Universität (LMU), Butenandtstr. 11 (E), 81377 Munich, Germany.
[b]Center for NanoScience (CeNS), Schellingstr. 4, 80799 Munich, Germany.
[†] The authors contributed equally to this work. *Corresponding Author.

Abstract

Lanthanide coordination polymers (Ln-CPs) have attracted great attention as an emerging type of near-infrared (NIR) emitting materials. In this work, we report the synthesis and characterization of three semiquinone-based Ln-CPs, namely Ln-DHBQ (Ln= Yb (**1**), Nd (**3**), $C_6H_2O_4^{2-}$ = 2,5-dihydroxy-1,4-benzoquinone) with a chemical formula $[Ln_2(C_6H_2O_4)_3(H_2O)_6]\cdot 18H_2O$ and a novel member of this framework family with a chemical formula $[Ln_2(C_6H_2O_4)_3(H_2O)_4]\cdot 6H_2O$ with (Ln= Yb (**2**), $C_6H_2O_4^{2-}$=2,5-dihydroxy-1,4-benzoquinone) as single crystals. Single-crystal x-ray diffraction analysis shows that the isostructural series of Yb, Nd-DHBQ type I (**1**, **3**) crystallize in the trigonal $R\bar{3}$ space group, whereas for Yb-DHBQ type II (**2**), a second phase was obtained, that crystallizes in the monoclinic *C*2*/m* space group. Both phases of Yb-DHBQ present a (6,3)-2D topology but differ at the coordination number of Yb^{3+} metal centers in both phases. By adjusting the synthesis conditions, we achieve control over the morphology of the single crystals of Yb-DHBQ and Nd-DHBQ, resulting in either disc-like shapes or faceted giant single crystals of sizes up to 500 µm. Moreover, this series of Ln-DHBQ (**1**–**3**) single-crystals features strong photoluminescence in the near-infrared region with a lifetime in the range of tens of nanoseconds. Furthermore, the observation of photon bunching on the timescale of the excited-state lifetime in the second order time correlation function demonstrates a down-conversion process for both Yb-DHBQ CPs.

Introduction

Near-infrared (NIR) emitters, such as rare-earth metal (RE) ions, are attractive functional materials for application in optical thermometry[1], sensing[2], bioimaging and drug delivery[3] up to operation as barcode material[4]. Ordered coordination polymers (CPs) and sub-class metal–organic frameworks (MOFs), consisting of inorganic building units (IBUs), periodically connected by organic linker molecules, can serve as intriguing material platforms for enabling tunable NIR emission[ref]. For example, by applying the principles of reticular chemistry, the chemical properties of framework materials can be predesigned and systematically controlled [ref]. In addition, utilizing building blocks with a specific symmetry grants access to a large variety of crystal structures ranging from 2D layered configurations to complex 3D rigid networks.(ref) An intriguing approach to induce NIR emission in CPs includes the implementation of rare-earth metal ions (REI) into a rigid framework. The most common oxidation state of lanthanide elements is the trivalent state Ln^{3+} with a few exceptions in other oxidation states[5]. Owing to distinct 4*f* orbital configurations, different lanthanide ions exhibit different energetic levels. Photoluminescence (PL) displayed at the near-infrared (NIR) is characteristic for the respective trivalent lanthanide with Nd^{3+}, Er^{3+} and Yb^{3+}.[6] The number of observed bands depends on the particular lanthanide ion and its distinct electronic states. However, for free lanthanide ions, which are not implemented in matrices, low molecular absorption coefficients and a rather weak luminescence are intrinsic.[5] This is related to the forbidden *f-f* electronic/orbital transitions of lanthanide ions.[7] To overcome this limitation, Ln^{3+} ions can be incorporated into well-defined structures held by organic linker molecules, making them controllably and spatially resolved. In this structural paradigm, the organic linkers operate as chromophores absorbing the excitation energy followed by a ligand-to-metal energy transfer process, and subsequent excitation of the Ln^{3+} ion generating a strong luminescence.[7] In the growing field of sensing, luminescent Ln-MOFs have been employed for various analytes, the porous network allows for a reversible uptake and release of guest molecules and lanthanide luminescence can be turned-on and turned-off.[8] For instance, environmental pollutants such as pesticides[9], antibiotics[10], explosives[11], heavy metal ions[12] and toxic gases[13] can be detected with high sensitivity and selectivity. An interesting example is related to temperature sensing using mixed Yb^{3+}/Er^{3+} MOFs serving as contactless sensors. Here, an optical thermometer was established in $[EtNH_3]Yb_{0.79}Er_{0.21}(HCOO)_4]$ MOF by monitoring broadening its NIR emission, where a temperature decrease is associated with the broadening of the Er^{3+}characteristic NIR emission.

In recent years, photo- and electro-induced properties have been added to the property collection of MOFs and CPS, demonstrating their potential as active materials in applications such as energy storage

and conversion, sensing or transistors.(ref) To induced electrical conductivity in framework materials, redox active molecules are often included into the matrix. A well-known redox active organic linker molecule with catecholoid functionality is 2,5-dihydroxy-1,4-benzoquinone (DHBQ) in combination with transition metal-oxo cluster nodes such as iron, copper and nickel, are widely used. For example, quinoid-based $Fe_2(DHBQ)_3$ framework exhibits a remarkable high electrical conductivity of 10^{-2} S cm^{-1}. By exploiting the properties of the high conductivity of DHBQ frameworks and the exceptional luminescent properties of rare earth ions, a growing interest arises in the synthesis of Ln-DHBQ frameworks for electronic devices particularly in the context of sensing.[6] For implementation in application as a sensing material, there is a need for air-, water- and photo- material stability. Additionally, intense emissions with relatively short lifetimes are highly desired targets to enable an efficient photon detection, due to the rapid on and off switching.

Inspired by the rich chemistry provided by rare earth ions (REIs), we set our focus on the synthesis of two rare-earth CPs, using lanthanide metals Nd^{3+} or Yb^{3+} as a metal node and DHBQ as the organic linker. The synthesis of these two Ln-DHBQ CPs has been extensively described in literature, [ref] however the crystallization process in order to obtain single crystals of Nd-DHBQ CP is yet to be reported. Importantly, despite their well-described structures, their photophysical properties remained elusive.

Here, we present the synthesis of single-crystals of Nd-DHBQ with unprecedented size of up to 500 µm with a truncated pseudo-cubic morphology, featuring a trigonal space group $R\bar{3}$ space group, confirmed by single-crystal X-ray diffraction (SXRD) analysis. Moreover, by employing alterations of the synthesis protocol, Yb-DHBQ was isolated as a novel single crystal phase. Taking advantage of the remarkable size of the Ln-DHBQ crystals obtained, a complete structural analysis is enabled. Furthermore, the crystal morphology is rational modified by the crystallisation process ranging from disc-like few micron-sized crystals to faceted large several hundred micron sized single crystals for both Ln-DHBQ (Ln=Yb, Nd) CPs. Upon excitation with a 405 nm laser, emission in the NIR at 1.55 eV (800 nm), 1.38 eV (900 nm) and 1.17 eV (1060 nm) (Nd-DHBQ) and 1.27 eV (980 nm) (Yb-DHBQ) is detected for all RE-ion containing CPs. A strong Stokes shift and a relatively short PL lifetime of 32 ns and 156 ns were measured for Nd-DHBQ and Yb-DHBQ, respectively. Importantly, both Yb-DHBQs show a non-parametric down-conversion process, measured by the photon statistics via a Hanbury Brown Twiss configuration of two photodetectors. This analysis gives access to the second order photon statistics proving non-parametric two photon emission, independently of their quantum yield.[29]

Results and Discussion

Synthesis and characterization of Ln-DHBQ (Ln=Yb, Nd) single crystals

Single crystals play a crucial role in understanding the way in which the building fragments interact and form ordered coordination polymers (CPs). Furthermore, the isolation of single crystal of CPs enables to study their physical properties at the furthest, minimizing effects of grain boundaries and surface defects. A well-known rare-earth metal CP series is the Ln-DHBQ series having the chemical structure formula of $[Ln_2(DHBQ)_3(H_2O)_6]\cdot 18H_2O$.[14] The series comprise the lanthanide metals centres of La, Ce, Gd, Yb, Lu, Ho, Er which are connected by the redox-active 2,5-dihydroxy-1,4-benzoquinone (DHBQ) organic ligand. [14–17] The synthesis of Ln-DHBQ as powders and single crystals has been extensively described in the literature. Although being extensively studied, the control over the crystal morphology and the production of single crystals for some of the representatives i.e., Nd-DHBQ are yet to be reported. Typically, Ln-DHBQ CPs are synthesized by employing metal precursors and the redox active organic building block DHBQ under hydrothermal and ambient conditions which results in crystalline powders with the space group $R\bar{3}$ of the trigonal crystal system (Fig. 1).[14–17] Intrigued by their rich chemistry, we aimed at filling the gaps in their crystallization processes, we thereby choose two members of the series namely Yb- and Nd-DHBQ CP and explore their synthesis and crystallization, utilizing different approaches that provide a modulated crystallization process and the emergence of single crystals. Primarily, we employed the strategy of decreased temperature synthesis, which is associated with monitored chemical reactions and crystallization processes (e.g., super saturation, nucleation). We initiated our endeavours with the synthesis of CP Yb-DHBQ following a reported hydrothermal protocol where we altered the temperature profile.[14] Briefly, ytterbium nitrate and the DHBQ ligand were dissolved in water and kept in a reaction vessel at 0 °C for 24 hours to slow down the chemical reaction and thereby nucleation rate. Then, the reaction vessel was allowed to warm up to room temperature and was kept at this temperature for additional five days. After the given reaction time, a dark red precipitate was isolated by filtration and washed several times with water and dried in air. More information on the synthesis of the Ln-DHBQ CP is given in the Supporting Information. Optical microscopy revealed that the red precipitate obtained consists of uniformly roundish shaped single crystals with up to 100 µm in size (Fig. 2). Scanning electron microscopy (SEM) images of the crystallites revealed a roundish morphology and less pronounced facets, in line with the morphology observed by optical microscope (Fig. 2, Fig. S8). To categorize and compare the single crystal precipitates with the literature known structure, the crystallites were ground and subsequently analysed by powder X-ray diffraction (PXRD). The PXRD pattern obtained features multiple sharp and narrow reflections where the most intense reflections are centered at around 12.3° and 12.6° 2ϑ

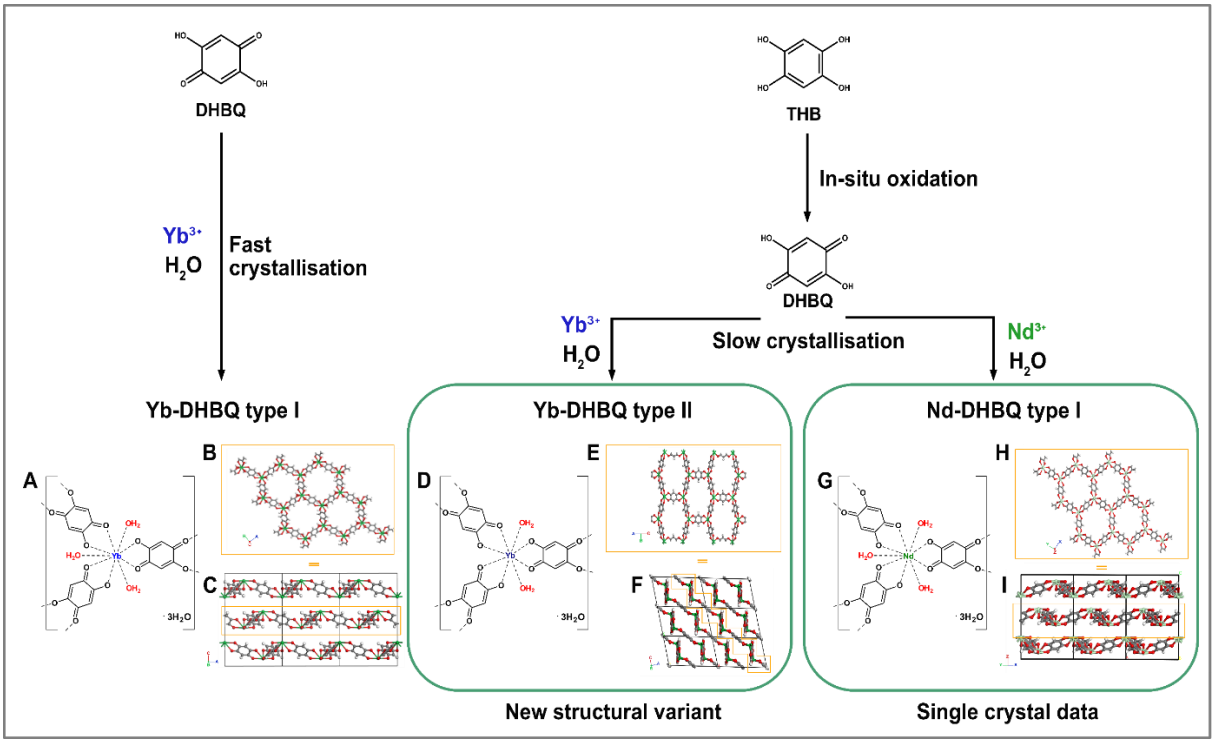

Fig. 1 Schematic overview on the synthesis pathways yielding three Ln-DHBQ CPs (Ln= Yb, Nd). Direct utilizing of DHBQ leads to the literature-known phase type I of Yb-DHBQ. Use of a preliminary in-situ oxidation step of THB to DHBQ, employed in our developed synthesis route, yielded a new structural variant of Yb-DHBQ type II. Using the developed protocol for Nd-DHBQ resulted in the formation of single crystals being isostructural to the Ln-DHBQ type I series. In **A**, **D** and **G**, the asymmetric unit of each crystal structure is displayed, with a view on the 2D sheet providing a visualization of the pore system in the orange inset (**B**, **E** and **H**) and a view along the 2D ribbon-like structure displayed for the three crystal structures (**C**, **F**, **I**). The water molecules are omitted in all images for clarity.

indicating the presence of a highly crystalline material. The experimental PXRD pattern was indexed according to the calculated theoretical XRD pattern of the Yb-DHBQ CP and is in good agreement with the reported structure of Abrahams *et al.* (Fig. S3).[18] In line with the observation of the PXRD analysis, single crystal X-ray diffraction (SXRD) (Fig. 1) of the crystals obtained confirmed the formation of a highly crystalline Yb-DHBQ CP isostructural to the known Ln-DHBQ series with space group $R\bar{3}$ of the trigonal system, denoted as YB-DHBQ type I (**1**). A detailed description of the crystal data is given in the section crystallographic analysis, followed. Based on the successful synthesis of single crystals of YB-DHBQ type I (**1**), we targeted the synthesis of larger single crystals with a more defined morphology of Ln-DHBQ, particularly of CPs that have not been reported yet. In this regard, we studied different synthetic parameters such as different precursor concentrations, temperature ranges, and reaction times to attain control over the crystallization process of this series such that large single crystals of the desired isostructural phase of Ln-DHBQ CPs will emerge as end product.[18] Previously, the oxidation state of DHBQ has been demonstrated to be key for modulating the synthesis of Ln-DHBQ CPs through slower complexation of metal and ligand, enabling the precipitation of single crystals.[19] To control the crystallization process further, we employed in a hydrothermal synthesis the fully

reduced, 1,2,4,5-tetrahydroxybenzene (THB) analogue as the organic building block instead of direct utilization the DHBQ at different temperatures (Fig. 1). Notably, combining the low temperature synthesis approach of Yb-DHBQ type I (**1**) with the presence of THB ligand in the reaction mixture resulted in dark-coloured small crystallites with a size of 75 µm, crystallizing in a crystal phase, which could not be attributed to the Ln-dhbq series by means of powder X-ray diffraction. We therefore aimed for larger single crystals to solve the structure of the new phase with SXRD. Utilizing crystallization modulation through the redox-active organic linker, we developed an adapted reaction protocol, in which ytterbium nitrate as metal salt was added to an aqueous solution of THB and charged into a reaction vessel that was kept at elevated temperatures for 6 days. After the designated reaction time, the reaction product was collected by filtration under reduced pressure. Subsequently, the crystals were resuspended in water and dried in air, revealing dark-red shiny crystals. Strikingly, visualization of the reaction product with an optical microscope revealed the elongated-shaped diopside-like crystals of Yb-DHBQ reaching sizes of 200 µm with distinct morphology and crystal facets (Fig. 2, Fig. S8). SEM images reveal large crystals with distinct facets in line with the optical microscopy results, however seemingly affected by the high vacuum exposed upon handling, recognizable as fissures. In variance with the low temperature crystallization, our developed reaction protocol resulted in a different morphology compared to the crystals when utilizing DHBQ ligand directly. This first indication of a structural variety of the Yb-DHBQ CP was studied examining with PXRD in more detail. The PXRD pattern obtained revealed multiple sharp and narrow distinct reflections with different position compared to YB-DHBQ type I (**1**) with the most intense reflections centered at around 11.1°

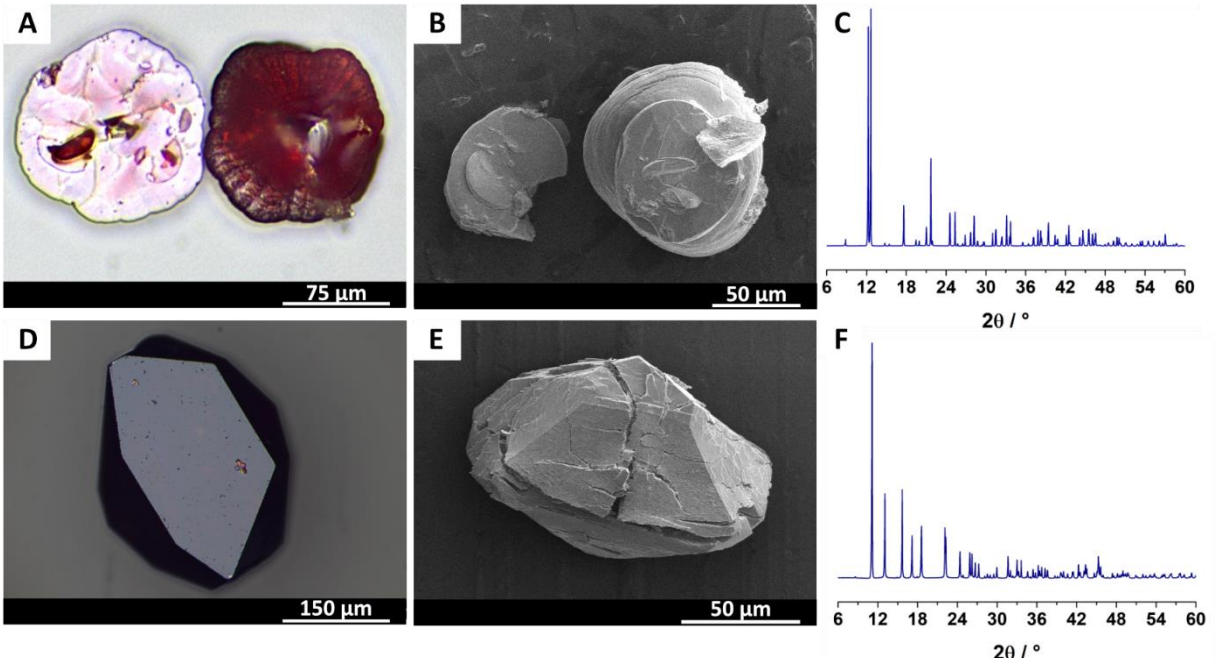

Fig. 2 Optical microscope images of CPs Yb-DHBQ type I (**A**) and type II (**B**) displaying the different morphology and sizes of the single crystals obtained for the different synthesis protocols. SEM images of a respective crystallite of both phases, type I (**B**) and type II (**E**). Comparison of PXRD patterns experimentally obtained for the two Yb-DHBQ type I (**C**) and type II (**F**) demonstrating the presence of a structural variety for Yb-DHBQ obtained with our adapted protocol.

2ϑ suggesting a highly crystalline structure of a different phase (Fig. S4). Contrary to our expectations, SCXRD revealed single crystals of the monoclinic system, a reduced symmetry compared to the known trigonal system in the series of Ln-DHBQ, referred to as Yb-DHBQ type II (**2**).

Next, we delve into the synthesis of another representative of the Ln-DHBQ $[Ln_2(DHBQ)_3(H_2O)_6]\cdot 18H_2O$ CPs series, namely Nd-DHBQ (Fig. 1). In a previous report, Nd-DHBQ framework powder has been assigned to the structural family of Ln-DHBQ CPs by indexing the PXRD pattern obtained with the ones reported for other representatives of this series,[18] however, structure solution by single crystals of this materials have not yet been reported. First, we synthesized Nd-DHBQ applying the same synthesis conditions as for Yb-DHBQ type I (**1**). Briefly, metal salt neodymium nitrate and organic ligand DHBQ were dissolved in water and kept for 1 day at 0°C and for further 5 days at room temperature. A dark red precipitate was isolated by filtration and washed several times with water and dried in air. Optical microscopy (Fig. 3, S8) and SEM revealed disc-like crystallites uniformly formed with sizes of about 10 µm (Fig. 3A, B), unfortunately too small to solve the crystal structure with SXRD. The PXRD pattern of these small crystallites reveals the same isostructural phase to the series of Ln-DHBQ CPs (Fig. 3C). To shed ultimate light on its crystal structure, we applied our developed synthesis protocol for Yb-DHBQ type II (**2**) to the synthesis and crystallization of Nd-DHBQ CP replicating the protocol with neodymium nitrate as metal salt and a longer reaction time of 16 days. After isolation, the powders collected appeared to the naked eye as dark-red shiny crystals. Optical microscopy of the precipitate revealed dark-red single crystals reaching a giant size of 500 µm, one of the largest sizes realized in this

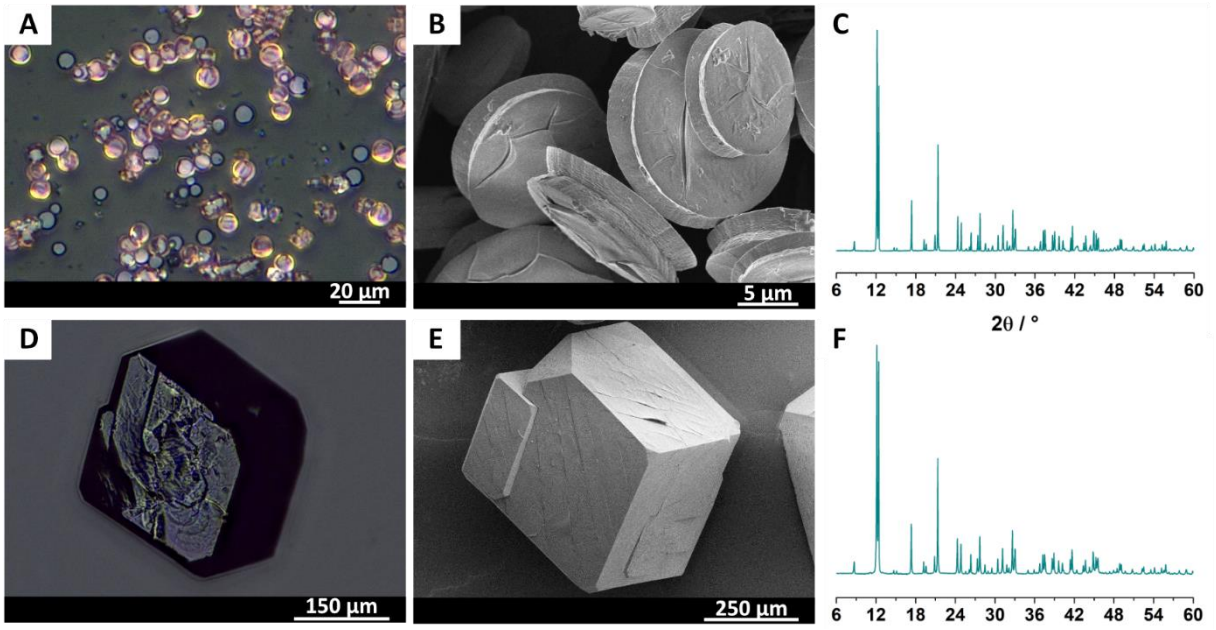

Fig. 3 Optical microscope images of CP Nd-DHBQ displaying the different sizes and morphologies obtained by employing different synthesis approaches, directly utilizing DHBQ (**A**) or use of THB (**D**) as redox-active ligand for the framework formation. SEM images of the resulting crystals (**B**) and (**C**), respectively for the synthesis condition with DHBQ or THB. PXRD pattern of the ground crystals confirm an isostructural compound regardless the diverse morphology and crystal size.

series of Ln-DHBQ CPs. The collected crystals feature truncated pseudo-cubic shapes in line with its crystal symmetry as described in more detail in the crystallographic section. Interestingly, these truncated corners create equilateral triangles having 3-fold rotational symmetry, in line with the trigonal crystal system. To illuminate the crystalline nature of the reaction product obtained, a ground powder of Nd-DHBQ was analysed by means of PXRD and compared to the PXRD of the crystals obtained employing the direct synthesis route with DHBQ (Fig. 3). Analogous to Yb-DHBQ type I (**1**), the PXRD pattern obtained could be indexed according to previous Ln-DHBQ CPs (Fig. S5) with the most intense sharp reflections centered at 12.1° and 12.4° 2ϑ, strongly indicating that the single crystals formed are an isostructural phase to Yb-DHBQ type I (**1**).[18] Despite applying the similar synthesis protocol as for Yb-DHBQ (**2**), where we found the structural variety, for the CP Nd-DHBQ we solely obtain the isostructural phase. On account of the record size of the Nd-DHBQ single crystals obtained with our crystallisation approach, we could determine the precise structure of Nd-DHBQ supported by single crystal data for the first time. Notably, the PXRD reflections of Nd-DHBQ type I (**3**) compared to Yb-DHBQ type I (**1**) are slightly shifted to smaller 2ϑ values, in consequence of the lanthanide contraction effect of larger ion Yb^{3+} compared to Nd^{3+}.

Crystal Structure

By virtue of the single crystals obtained for all three compounds Ln-DHBQ (Ln= Yb, Nd) **1**–**3**, single crystal XRD (SCXRD) was employed providing a conclusive picture of the underlying crystal structure. A summary of the structural data collection and refinement parameters for **1**–**3** is given in Table 1 and in Table S1. First, the novel crystal data for Nd-DHBQ type I (**3**) is discussed, enabling access to precise structural information of the framework. The obtained crystal data is compared to a previously reported structure, which was solved by indexing the experimental PXRD pattern according to the reported representatives of Ln-DHBQ.[18] The new single crystal data for **3**, we report in this manuscript (Fig. 1), confirms the framework structure proposed[18] and follows the Ln-DHBQ series as adequately described by Abrahams *et al.* for Ln= La, Ce, Gd, Y, Yb, and Lu.[15,14] The obtained Nd-DHBQ (**3**) CP, consisting of the larger lanthanide ion radii Nd^{3+}, exclusively crystallizing in the trigonal space group $R\bar{3}$. As such, the lattice paramaters were determined to be $a = b = 14.2962$ Å and $c = 17.9561$ Å (Table 1, Table S1). Similar to the other representatives of Ln-DHBQ, containing tetraoxolone DHBQ ligands, a bis-chelating cluster based on DHBQ ligands with a trigonal prismatic mode can be obtained. The DHBQ ligands are further bridged by adjacent ligands into a honeycomb network structure with a 2D (6,3) topology, meaning that 3-connecting neodymium centers link to form six-membered rings in a two-dimensional network extending in the *ab* plane. Hereby, the neodymium ions adopt a tri-capped trigonal prismatic coordination sphere (Fig. 4). The nine-fold coordination geometry comprises a central Nd^{3+} ion, which is coordinated by three bis-chelating DHBQ ligands and three coordinated aqua

ligands. These coordination units form ribbon-like 2D sheets composed of undulating six-membered rings giving hexagonal pore apertures of 1.4 nm (Fig. 1). In the crystal network, coordinated aqua ligands and crystal water molecules as well as the oxygen from the DHBQ ligands form out hydrogen bonds, establishing various water clusters located between the layers. The hydrogen bonding within the structure stabilizes the sheets and results in an overall three-dimensional network.[15]

In contrast, Yb-DHBQ containing the smaller lanthanide ion Yb^{3+} crystallizes in two different structures with differing space groups (**1**, **2**) (Fig. 1, more information given in the section synthesis SI). Interestingly, we found that the crystal phase can thereby be controlled by the synthesis conditions employed. With direct utilization of DHBQ in the synthesis, Yb-DHBQ type I (**1**) is phase-purely obtained in the trigonal space group $R\bar{3}$ isostructural to Nd-DHBQ type I (**3**). However, at elevated temperatures utilizing a preliminary in-situ oxidation step of THB to DHBQ, the Yb-DHBQ forms a structural variety to **1** and **3**, adopting a monoclinic space group *C*2/*m*. In contrast to the type I structures, the crystal structure of the second phase, type II, is a more compressed network structure (Fig. 2). The coordination sphere of the central Yb^{3+} ions is decreased from nine-folded (**1**) to eight-folded (**2**) by the loss of one coordinated aqua ligand (Fig. 4). A 2D sheet is formed of the undulating six-membered rings of Yb^{3+} ions and bis-chelating DHBQ ligands giving rise to hexagonal pore apertures of 1.2 nm in diameter. However, the loss of one aqua ligand results in a more dense packing in the network and a change in the lattice paramaters determined to be *a* = 14.0778 Å, *b* =15.8986 Å and *c* = 6.1208 Å. The crystal planes are stacked with four coordinated water molecules and six crystal water molecules connecting the 2D layers by hydrogen bonds. The water cluster located between the layers, connecting the 2D layers through hydrogen-bonds are changed in the structure of **2**. The amount of crystal water molecules is reduced from 18 to 6 leading to a denser packing and a reduced cell volume from 3050 to

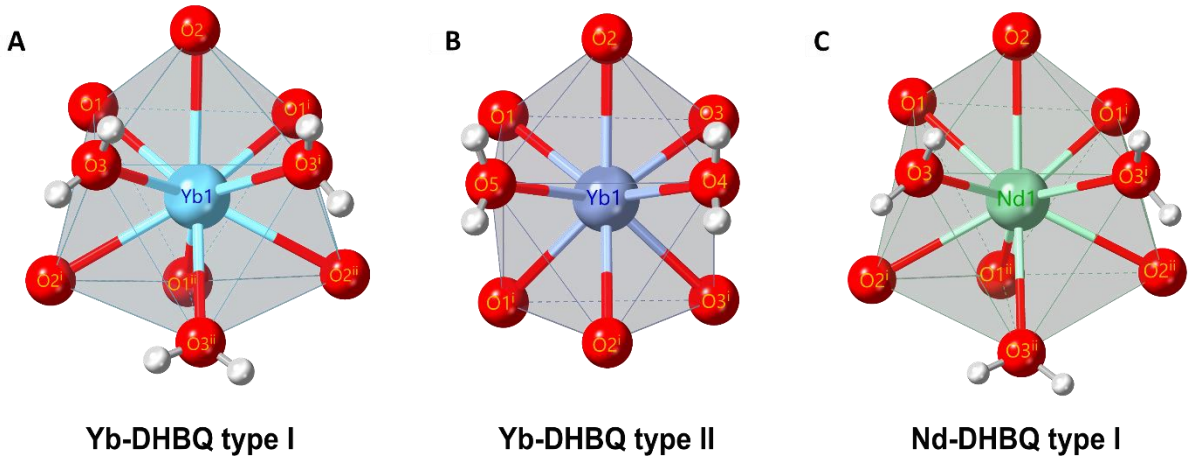

Fig. 4 View of the coordination sphere of Ln-DHBQ CPs. A distorted tricapped trigonal-prismatic geometry with a 3-fold symmetry is obtained for the Yb^{III} (**A**) and Nd^{III} (**C**) central atom in the isostructural Ln-DHBQ CPs. For the structural variety Yb-DHBQ type II, the loss of one coordinated water ligand leads to a 2-fold symmetry and a decrease in coordination number from nine to eight (**B**).

1300 Å^3 (Table 1). We attribute the change of the crystal structure to the different reaction conditions employed, with a prior oxidation step from THB to DHBQ leading to a slower complexation of metals and ligands, enabling a structural variation for the smaller lanthanide Yb^{3+}. Whereas, the existence of at least two different structural types is well-known in the series of chloranilate (CA)[20], a derivative of DHBQ and Ln^{3+} ions, it is so far not reported for DHBQ with Ln^{3+} ions, especially within the same lanthanide CP. Further details on single-crystal growth and structural data are given in the Supporting Information (Table S1).

Table 1 Crystal data for Yb-DHBQ type I (**1**), Yb-DHBQ type II (**2**) and Nd-DHBQ type I (**3**).

Compound	**1**	**2**	**3**
Empirical formula	$[Yb_2(C_6H_2O_4)_3(H_2O)_6]\cdot 18H_2O$	$[Yb_2(C_6H_2O_4)_3(H_2O)_4]\cdot 6H_2O$	$[Nd_2(C_6H_2O_4)_3(H_2O)_6]\cdot 18H_2O$
Crystal size/ mm	0.02 x 0.05 x 0.07	0.03 x 0.03 x 0.04	0.02 x 0.06 x 0.07
Crystal system	Trigonal	Monoclinic	Trigonal
Space group	$R\bar{3}$	$C2/m$	$R\bar{3}$
Unit cell dimensions /Å	a=14.0419(5), b=14.0419(5), c=17.8740(7)	a=14.0778(7) b=15.8986(7) c=6.1208(3)	a=14.2962(5), b=14.2962(5), c=17.9561(7)
Unit cell angles / °	α=90, β=90, γ=120	α=90, β=107, γ=120	α=90, β=90, γ=120
V / Å^3	3052.1(3)	1310.13(11)	3178.2(3)
Z	6	4	6
R[a]	0.0166	0.0136	0.0143
R_W[b]	0.0367	0.0311	0.0357
R_{int}	0.032	0.046	0.039
Goodness-of-fit, S	1.10	1.12	1.10

Furthermore, to confirm phase purity for compounds **1**–**3**, we ground the single crystals and compared the resulting PXRD pattern with the theoretical PXRD pattern calculated from single crystal X-ray data being in good agreement (Fig. S3–5). Furthermore, PXRD measurements of **1**, **2** and **3** show high stability of CPs while stored at room temperature for more than one years (Fig. S6) and long-term treatment in water with a duration of more than 6 months without any structural changes (Fig. S7). To gain information on the chemical composition of the CPs obtained, scanning electron microscopy (SEM) in combination with energy dispersive X-ray spectroscopy (EDX) were employed, indicating the sole presence of oxygen and carbon arising from the DHBQ linker and water molecules and the respective lanthanide metal Nd or Yb (Fig. S9−11). Nitrogen physisorption measurements were

performed at 77 K for **1**–**3**, revealing type II isotherm shapes for examined CPs. In addition, extremely low apparent Brunauer–Emmett–Teller (BET) surface areas (0.05 – 0.2 p/p_0) of 22 $m^2 g^{-1}$ (**1**), 15 $m^2 g^{-1}$ (**2**) and 12 $m^2 g^{-1}$ (**3**) rendering this series as CPs of limited accessible surface area, in accordance with their crystal structure (Fig. S13). The activation of the CP prior to nitrogen physisorption measurements was performed with vacuum treatment at 80 °C, leading to a loss of crystallinity of the CPs. We conclude that the activation of Ln-DHBQ with vacuum treatment beforehand leads to a collapse of the water clusters connecting the 2D layers and therefore to a structural collapse. The crystal water between the layers resembles an elemental part of the structural integrity and cannot be removed without collapsing the network. The major stabilizing role of the hydrogen bonds was already described in literature.[14] Thermogravimetric analysis (TGA) of the CPs reveals a high thermal stability up to 330 °C for all CPs (Fig. S12). All three CPs show several decomposition steps, starting with the release of crystal water molecules around 100 °C and followed by the loss of coordinated water molecules. For **1** and **2**, a plateau was reached at 68, and 61% residual sample mass, respectively. The plateaus can be attributed to the water-free compounds $[Yb_2(DHBQ)_3]$ and $[Nd_2(DHBQ)_3]$. For **3**, the plateau is reached earlier, at 81% residual sample mass and is attributed to $[Yb_2(DHBQ)_3]$, in line with a lower proportion of water in the structure and a lower mass weight of **3**. After decomposition of the frameworks, the lanthanide oxides Nd_2O_3 and Yb_2O_3 were obtained for all three Ln-DHBQ CPs. FTIR vibrational spectroscopy supported further the formation of the respective CPs (Fig. S14). For all investigated samples, the three characteristic vibrational bands of the linker DHBQ in the range between 1600 and 1250 cm^{-1} were observed in the IR spectra containing characteristic bands at 1490 cm^{-1} ν(–C=O), 1370 cm^{-1} ν(–C–C) and 1250 cm^{-1} ν(–C–O). The change in the position of the C=O band for CP **1**–**3** compared to the uncoordinated linker DHBQ (1600 cm^{-1}) is affected by the metal-oxygen coordination by means of framework formation. The disappearance of the band associated with the deformation of the CO-H bond of the DHBQ at around 1200 cm^{-1} occurs due to the newly formed metal-oxygen coordination bond. All three CPs (**1**–**3**) have an identical appearance in the spectrum until 850 cm^{-1}, at lower wavenumbers, the IR spectra of **1** and **3** resemble one another in the so-called fingerprint region. In contrast, in the IR spectra of **1**, the second phase of Yb-DHBQ, can be clearly determined by a different pattern in the fingerprint region compared to **1** and **3** enabling a simple structure distinction between both phases of Yb-DHBQ.

Despite the various descriptions of synthesis and crystal structures of Ln-DHBQ CPs in a more crystallographic context, very less is known about the material properties of this structural family. The photophysical properties are yet to be investigated to further elucidate on the potential of these frameworks to serve as photoactive material for (bio-)sensing applications. The optical properties of the Ln-DHBQ **1**–**3** were measured as ground powders using UV-vis absorption, summarized in Fig. S15. The UV-vis spectra were recorded in diffuse reflectance geometry and obtained from the Kubelka–

Munk equation. For examined samples of **1** to **3**, a strong absorption is located in the UV region with maxima at approximately 3.87 eV (320 nm) and a second one in the visible region at around 2.34 eV (530 nm) see Fig. S15. This broadband absorption can be assigned to the absorbance of the organic component THB/DHBQ (Fig. S15) in the structure. Characteristic absorption bands for each lanthanide metal ion can be found in the visible and near-infrared region as distinct lines, e.g. of Nd-DHBQ (**3**) at 1.69 eV (735 nm), 1.66 eV (745 nm), 1.56 eV (796 nm), 1.54 eV (805 nm) and 1.43 eV (870 nm) and for Yb-DHBQ type I, II (**1**,**2**) at 1.28 eV (965 nm) and 1.25 eV (988 nm) (Fig. S9). The sharp absorption lines observed are connected to the distinct 4*f* electron energy level transitions of Yb and Nd metal ions embbeded in a crystal matrix (Fig. S9).[21] [6] To shed light on the excited state dynamics, we measured time and spectrally resolved photoluminescence (PL) of the synthesized large single crystals. The PL spectra contain mainly the emission bands associated with the rare earth ion metal centers (Fig. 5). For Nd-DHBQ, four different transitions ($^4F_{3/2}\rightarrow{}^4F_{5/2}$/ $^2H_{5/2}$, $^4F_{3/2}\rightarrow{}^4I_{9/2}$, $^4F_{3/2}\rightarrow{}^4I_{11/2}$, $^4F_{3/2}\rightarrow{}^4I_{13/2}$ (1350 nm, Fig. S20) that exhibit additional fine-splitting are detected.[22] Both Yb-DHBQ types show only one transition in which fine-splitting leads to asymmetric peak shapes. All spectral lines can be assigned to transitions between the known energy levels of the REIs.[23,24] Notably, these optical transitions, which are dipole-forbidden for isolated ions[5] become allowed only because of the coupling to the DHBQ matrix. The different observed transitions between the 4*f* electron energy levels

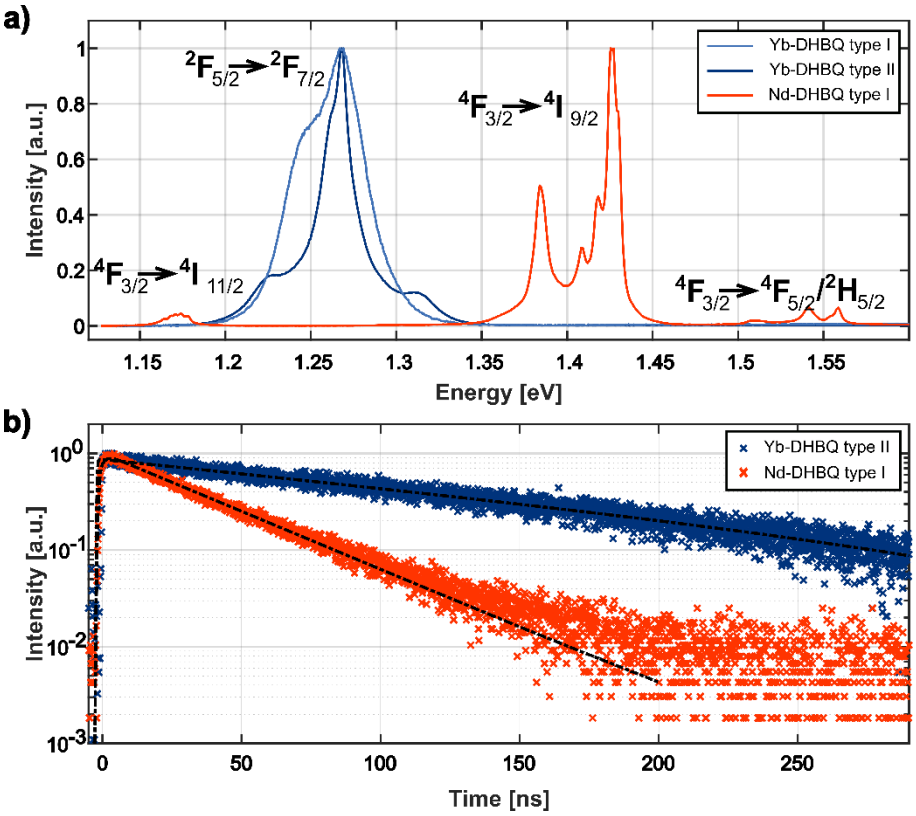

Fig. 5 Time and spectral resolved PL- from the three Ln-DHBQ CPs. The different transitions of the REI states are visible, appearing in the near-infrared region (**a**). The different transients are shown, the Nd-DHBQ CP crystals show a faster decay than the Ytterbium ones (**b**).

occur due to the specific splittings of these states, which originates from Coulomb interactions, spin-orbit coupling and a fine splitting with the crystal matrix. Additionally, a broad weak and weak peak at 1.7 eV appears in the spectrum which is attributed to radiative decay of the CP-matrix itself (Figure S15). The lifetime of this contribution, obtained from PL transients detected in this spectral range, is below 10 ps (Figure S15). The extremely short lifetime can be attributed to energy transfer from the initially excited CP-matrix to the REIs. This is illustrated in the energy level scheme shown in Figure 6e, where the organic-inorganic hybrid coordination polymer framework absorbs the light and transfers the energy to the REIs where the main PL originates.[23]

For the NIR emission of the REIs centers, lifetimes are 32±5 ns for Nd-DHQB, 160±10 ns for Yb-DHQB type I and 156±10ns for Yb-DHQB type II, respectively (Fig. 3). Surprisingly, these lifetimes are significantly shorter than those reported for other REIs-doped materials. Typical Ytterbium glasses[25] exhibit life time of 0.4 to 2.1 ms, whereas for other REI coordination polymers, lifetimes in the range of 0.2 to 17 µs were found.[26] As an example for Neodymium doped systems, the typical laser ceramic Nd:YAG possesses life times in the range of 40 to 240 µs.[27] The strongly reduced emission lifetimes are presumably related to the local density of REIs in the solid matrix. Within this structure, REIs may exchange energy, leading to self-quenching of the excited state.[23] In the Ln-DHBQ crystals, the REIs are bridged by the relatively small molecular (DHBQ) ligand giving rise to a high density of REI emitting centers in the crystal, therefore shorter lifetimes compared with other REI systems are to be expected. Furthermore, the presence of structural coordinating O-H groups resulting from coordinated water molecules may lead to quenching.

A particularly interesting phenomenon observed for REIs doped systems is nonparametric photon down-conversion, also known as photon cutting.[28–31] In this process two NIR-photons are emitted upon absorption of one photon with at least twice their energy (Fig. 4). Hereby, the CP crystal can serve as an absorber which subsequently transfers the energy absorbed to two independent REIs-ions. Since two separated REI excited states are created by energy transfer, we classify this process as a sequential nonparametric down-conversion process. Both simultaneously excited states of the REIs can relax by emitting a photon resulting in an increased probability of the emission of two correlated photons within the excited state lifetime, in other words photon bunching. In the literature, such down-conversion processes are typically investigated by measuring the quantum yield of the emission.[28,29] Having a process which generates 2 photons out of one, a quantum yield of more than 100% is expected assuming dominating radiative decay. For the present materials quantum yield measurements could be misleading and difficult to interpret due to the emission contribution of the CP crystal, the unknown energy transfer efficiency from CP to REI and missing information on the possible non radiative transition rates. Measurements of the second order time correlation function

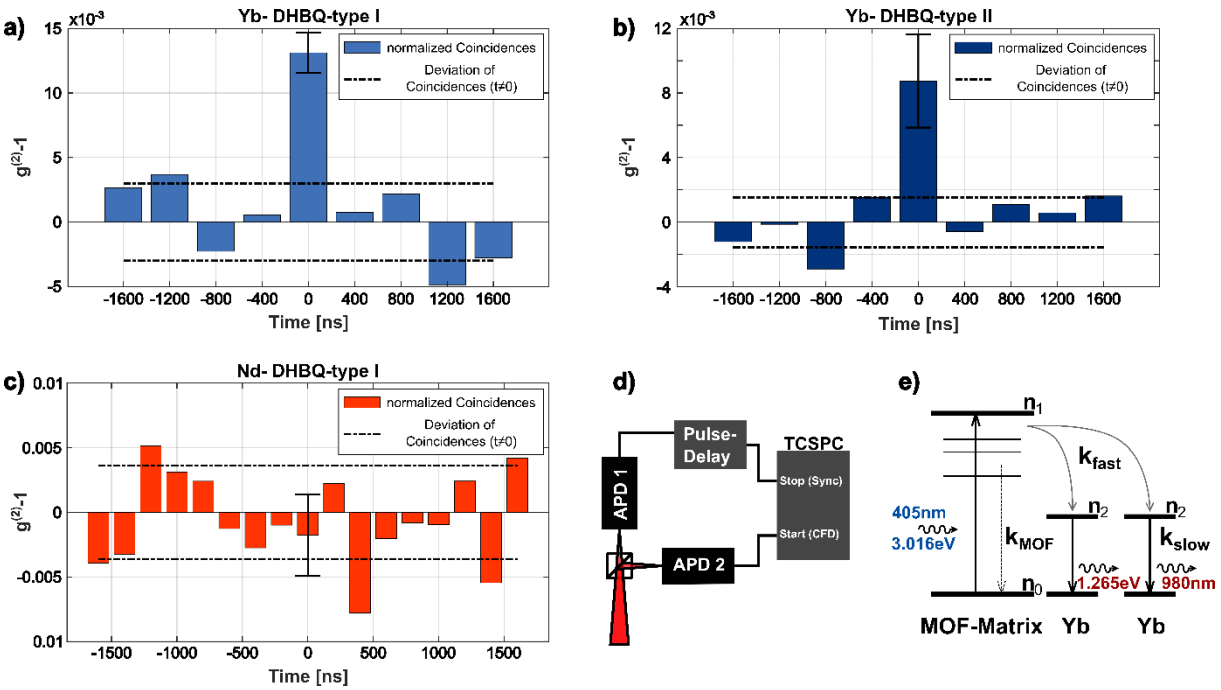

Fig. 6 The second order time correlation statistics are shown of both Yb-DHBQ type I (**a**) and II (**b**) and Nd-DHBQ type I (**c**), using an excitation wavelength of 405nm. In **a**) and **b**) a bunching is observable of 1-1.5 %, which shows a down-conversion process. For the Nd-type crystals **c**) no bunching is observed. All photon statistics are obtained by a Hanbury Brown Twiss configuration (**d**). An energetic scheme of the down-conversion process and the possible decay channels are shown in (**e**).

registering the time-stamps of the emitted photons overcome the challenges associated with quantum yield measurements as demonstrated recently.[31] With two emitted photons per absorbed photon, the probability of detecting two photons within the excited state life time is increased corresponding to a value of the second order time correlation function $g^{(2)}(0)$ larger than 1. Because in the experiment a large number of REIs are excited in the excitation spot and contribute to PL, the observed $g^{(2)}(0)$ will be reduced by 1/N with N being the average number of emitters[31]. For measuring the intensity correlation function we combined our confocal microscope setup with Hanbury Brown Twiss configuration of two avalanche photodiodes (APD). These two APDs are connected to time resolving electronics to register each measured photon with a time stamp (Figure 4 d)). As a result, the detection probability of photons after excitation is measured corresponding to the second order time correlation function. For both Yb-DHBQ crystals we find $g^{(2)}(0)$ ~ 1.010 to 1.015 corresponding to photon bunching of 1-1.5 % for an excitation wavelength of 405 nm (3.06 eV) and detection at 980 nm (Figure 6 a) and b)). Since the number of REIs in the focus is very high a low photon bunching ratio is expected. To confirm the observation of photon bunding we varied the excitation wavelength from 405 nm to 635 nm (1.95eV) while keeping the same laser fluence. No bunching is not observed as expected, because the energy the input photon is smaller than double the emission photon energy. For the Nd-DHBQ system, however, no bunching is detected by exciting the system at 405 nm (3.06 eV). A reason for

that could be the possible $^4F_{3/2} \rightarrow {}^4F_{5/2}/{}^2H_{5/2}$ transition which appears between 1.5 to 1.57 eV (790 to 827 nm), because there are emitted photons with more energy than half of 3.06 eV (405 nm). Nevertheless, blocking the spectral contributions above 1.46 eV (850nm), also no bunching is observed (Figure 4c)). A possible explanation for the absence of photon bunching in the PL detected from the Nd-DHBQ system could be the large number of possible transitions in Nd extending down to 1060 nm and below (ref).

Photon down-conversion makes Ytterbium-doped crystals particularly interesting for optical applications where the short excited state lifetime allows for rapid cycling of the emitting system combined with excellent photo stability.

Conclusion

In our study, we present the successful single-crystal synthesis in the system Nd^{3+} and Yb^{3+} and linker 2,5-dihydroxy-1,4-benzoquinone (DHBQ), respectively 1,2,4,5-tetrahydroxybenzene (THB). Novel single-crystal data was obtained for Nd-DHBQ isolated from aqueous solutions of THB and neodymium nitrate with formula $[Nd_2(DHBQ)_3(H_2O)_6]\cdot 18H_2O$. It crystallizes in the trigonal space group $R\bar{3}$, alike the isostructural series reported by Abrahams *et al.* for $[Ln_2(DHBQ)_3(H_2O)_6]\cdot 18H_2O$ with Ln=Y, La, Ce, Gd, Yb and Lu.[15] Investigation of Yb^{3+} and DHBQ or THB led to the discovery of a novel phase of Yb-DHBQ CPs with composition $[Yb_2(DHBQ)_3(H_2O)_4]\cdot 6H_2O$. Following the literature approach with DHBQ as organic linker, single crystals of the same phase reported by Abrahams *et al.* were obtained, whereas the replacement of DHBQ by THB led to the discovery of the compressed phase of Yb-DHBQ. The structures mainly vary in the coordination sphere of Yb^{3+} that is decreased from nine-folded to eight-folded by the loss of one coordinated aqua ligand. This leads to a tighter packing within the crystal structure and decreases the hexagonal pore apertures slightly by 0.2 nm. Our study highlights also the intriguing photophysical properties of Ln-DHBQ CPs strongly emitting in the near-infared, potentially allowing for the integration in sensor systems. However, short lifetimes in the nanosecond range allow fast switching between on and off mode.

Additionally, it could be shown that the Ytterbium MOFs have a downconversion property. This feature allows by using an excitation energy which is bigger than 2.7 eV (495nm) a higher number of emitting photons, which is beneficial for several applications, especially for bio-sensing. With respect to their high water stability and material stability under ambient conditions, in combination with well-defined REI properties, these MOF crystals can be implemented in novel photo sensing applications.

References

[1] M. Runowski, D. Marcinkowski, K. Soler-Carracedo, A. Gorczyński, E. Ewert, P. Woźny, I. R. Martín, *ACS Applied Materials & Interfaces* **2023**, *15*, 3244.

[2] Y. Cui, B. Chen, G. Qian, *Coordination Chemistry Reviews* **2014**, *273-274*, 76.

[3] a) P. Horcajada, R. Gref, T. Baati, P. K. Allan, G. Maurin, P. Couvreur, G. Férey, R. E. Morris, C. Serre, *Chemical reviews* **2012**, *112*, 1232; b) K. Deng, Z. Hou, X. Li, C. Li, Y. Zhang, X. Deng, Z. Cheng, J. Lin, *Scientific reports* **2015**, *5*, 7851; c) M.-X. Wu, Y.-W. Yang, *Advanced materials (Deerfield Beach, Fla.)* **2017**, *29*.

[4] K. A. White, D. A. Chengelis, K. A. Gogick, J. Stehman, N. L. Rosi, S. Petoud, *Journal of the American Chemical Society* **2009**, *131*, 18069.

[5] J.-C. G. Bünzli, S. V. Eliseeva in *Lanthanide Luminescence: Photophysical, Analytical and Biological Aspects* (Hrsg.: P. Hänninen, H. Härmä), Springer Berlin Heidelberg, Berlin, Heidelberg, **2011**, S. 1–45.

[6] J.-C. G. Bünzli, C. Piguet, *Chemical Society reviews* **2005**, *34*, 1048.

[7] D. Zou, J. Zhang, Y. Cui, G. Qian, *Dalton transactions (Cambridge, England : 2003)* **2019**, *48*, 6669.

[8] M. Gutiérrez, Y. Zhang, J.-C. Tan, *Chemical reviews* **2022**, *122*, 10438.

[9] Y. Li, S. Wu, Y. Zhang, Z. Ma, M. Zhu, E. Gao, *Inorganica Chimica Acta* **2021**, *528*, 120632.

[10] G. Yuan, Z.-Q. Chen, C. Zhang, Z.-Y. Xie, S.-Y. Liu, X.-H. Meng, J.-Y. Sun, X.-M. Li, L.-H. Dong, X.-R. Hao, *Journal of Solid State Chemistry* **2022**, *315*, 123442.

[11] J.-H. Qin, H.-R. Wang, M.-L. Han, X.-H. Chang, L.-F. Ma, *Dalton transactions (Cambridge, England : 2003)* **2017**, *46*, 15434.

[12] L. Li, Q. Chen, Z. Niu, X. Zhou, T. Yang, W. Huang, *J. Mater. Chem. C* **2016**, *4*, 1900.

[13] L. Wang, Y. Chen, *Chemical communications (Cambridge, England)* **2020**, *56*, 6965.

[14] B. F. Abrahams, J. Coleiro, K. Ha, B. F. Hoskins, S. D. Orchard, R. Robson, *J. Chem. Soc., Dalton Trans.* **2002**, 1586.

[15] B. F. Abrahams, J. Coleiro, B. F. Hoskins, R. Robson, *Chem. Commun.* **1996**, 603.

[16] N. Ponjan, K. Kodchasanthong, S. Jiajaroen, K. Chainok, *Acta Crystallographica Section E* **2019**, *75*, 64.

[17] K. Nakabayashi, S. Ohkoshi, *Acta Crystallographica Section E* **2010**, *66*, m1300.

[18] T. K. Sievers, C. Genre, F. Bonnefond, T. Demars, J. Ravaux, D. Meyer, R. Podor, *Phys. Chem. Chem. Phys.* **2013**, *15*, 16160.

[19] a) D. Yamazui, K. Uchida, S. Koyama, B. Wu, H. Iguchi, W. Kosaka, H. Miyasaka, S. Takaishi, *ACS Omega* **2022**, *7*, 18259; b) M. P. M. Poschmann, H. Reinsch, N. Stock, *Zeitschrift anorg allge chemie* **2021**, *647*, 436.

[20] S. Benmansour, A. Hernández-Paredes, C. J. Gómez-García, *Journal of Coordination Chemistry* **2018**, *71*, 845.

[21] J.-Y. Hu, Y. Ning, Y.-S. Meng, J. Zhang, Z.-Y. Wu, S. Gao, J.-L. Zhang, *Chemical science* **2017**, *8*, 2702.

[22] P. R. Nawrocki, T. J. Sørensen, *Physical chemistry chemical physics : PCCP* **2023**, *25*, 19300.

[23] D. A. Atwood, *The rare earth elements*. *Fundamentals and applications*, Wiley, Chichester, **2013**.

[24] M. H. V. Werts, *Science progress* **2005**, *88*, 101.

[25] X. Zou, H. Toratani, *Physical review. B, Condensed matter* **1995**, *52*, 15889.

[26] a) S. Ashoka Sahadevan, N. Monni, A. Abhervé, D. Marongiu, V. Sarritzu, N. Sestu, M. Saba, A. Mura, G. Bongiovanni, C. Cannas et al., *Chemistry of Materials* **2018**, *30*, 6575; b) S. Ashoka Sahadevan, N. Monni, M. Oggianu, A. Abhervé, D. Marongiu, M. Saba, A. Mura, G.

Bongiovanni, V. Mameli, C. Cannas et al., *ACS Appl. Nano Mater.* **2020**, *3*, 94; c) F. Artizzu, M. Atzori, J. Liu, D. Mara, K. van Hecke, R. van Deun, *J. Mater. Chem. C* **2019**, *7*, 11207.

[27] a) J. Lu, M. Prabhu, J. Song, C. Li, J. Xu, K. Ueda, A. A. Kaminskii, H. Yagi, T. Yanagitani, *Applied Physics B: Lasers and Optics* **2000**, *71*, 469; b) C. F. Rapp, J. Chrysochoos, *J. Phys. Chem.* **1973**, *77*, 1016; c) B. C. Tofield, H. P. Weber, *Phys. Rev. B* **1974**, *10*, 4560.

[28] R. Wegh, H. Donker, E. van Loef, K. Oskam, A. Meijerink, *Journal of Luminescence* **2000**, *87-89*, 1017.

[29] Q. Duan, F. Qin, D. Wang, W. Xu, J. Cheng, Z. Zhang, W. Cao, *Journal of Applied Physics* **2011**, *110*.

[30] R. T. Wegh, H. Donker, K. D. Oskam, A. Meijerink, *Science (New York, N.Y.)* **1999**, *283*, 663.

[31] M. de Jong, A. Meijerink, F. T. Rabouw, *Nature communications* **2017**, *8*, 15537.

Supporting Information

Giant rare-earth metal catecholate crystals - morphology control and rapid NIR luminescence response

Marina Schönherr[†,a,b], Alexander Biewald[†,a,b], Andre Mähringer[a,b], Markus Döblinger [a,b], Peter Mayer[a,b], Patricia I. Scheurle[a,b], Achim Hartschuh[a,b*] and Dana D. Medina[,a,b*]

[a]Department of Chemistry, Ludwig-Maximilians-Universität (LMU), Butenandtstr. 11 (E), 81377 Munich, Germany.

[b]Center for NanoScience (CeNS), Schellingstr. 4, 80799 Munich, Germany.

† The authors contributed equally to this work.

* Correspondence to D. Medina: dana.medina@cup.lmu.de

Table of Contents

1. Characterization methods

Nuclear magnetic resonance (NMR)

NMR spectra were recorded on *Bruker AV400* and *AV400 TR* spectrometers. The chemical shifts are expressed in parts per million and calibrated using residual (undeuterated) solvent peaks as an internal reference (^{1}H-NMR: DMSO-d_6: 2.50; ^{13}C-NMR: DMSO-d_6: 39.52). The data for ^{1}H-NMR spectra are written as follows: s = singlet, d = doublet, t = triplet, q = quartet, m = multiplet.

X-ray diffraction

Powder x-ray diffraction (PXRD) analyses were performed on a STOE Stadi MP diffractometer with a Cu Kα1 radiation source (λ = 1.54060 Å) operating at 40 kV and 40 mA. The diffractometer was equipped with a DECTRIS MYTHEN 1 K solid-state strip detector. Single-crystal X-ray diffraction (SXRD) data of CP **1**, **2** and **3** were collected on a Bruker diffractometer D8 Venture TXS system equipped with a multilayer mirror monochromator using Mo Kα radiation (λ = 0.71073 Å). The frames were integrated with the Bruker SAINT software package. Data were corrected for absorption effects using the Multi-Scan method (SADABS). The structure was solved and refined using the Bruker SHELXTL Software Package. All C-bound hydrogen atoms have been calculated in ideal geometry riding on their parent atoms, the O-bound hydrogen atoms have been refined freely. The OH-distances have been restrained to be equal within a standard deviation of 0.01 Å. Crystallographic data for the Nd-DHBQ type I and Yb-DHBQ type II (Nr. X and Y) can be obtained free of charge from The Cambridge Crystallographic Data Centre (CCDC).

Scanning electron microscopy (SEM)

SEM images were recorded on a *FEI Helios NanoLab G3 UC* electron microscope with an acceleration voltage of 2 kV from a field emission gun. For the cross-section analysis substrates were partially cut and broken manually to reveal fresh cross-sections. Prior to SEM analysis the samples were coated with a thin carbon layer by carbon fiber flash evaporation in high vacuum.

Nitrogen sorption

Adsorption and desorption measurements were performed on an Autosorb 1 (Quantachrome instruments, Florida, USA) with nitrogen of 99.9999% purity at 77.3 K. The samples were

activated under high vacuum at 120 °C for at least 12 h. Evaluation of adsorption and desorption isotherms was carried out with the AsiQwin v.3.01 (Quantachrome instruments, Florida, USA) software.

For BET calculations, pressure ranges of the nitrogen isotherms were chosen with the help of the BET assistant in the AsiQwin software. In accordance with the ISO recommendations, multipoint BET tags equal to or below the maximum in V x (1-p/p_0) in the semilogarithmic plot were chosen.

Thermogravimetric analysis (TGA)

Thermogravimetric analysis of the samples was performed using a NETZSCH STA 449C with a heating rate of 10 K min^{-1} and a heating range up to 900°C under a stream of synthetic air with a gas flow rate of 25 mL min^{-1}.

Infrared spectroscopy (FTIR)

ATR-FT-IR spectra were recorded on a Bruker Vertex 70 – RAM II instrument under nitrogen stream. Prior to measurement, the single crystals were ground to a powder.

UV-Vis spectroscopy

UV-Vis spectra were recorded using a Perkin Elmer UV Vis/NIR Lambda 1050 spectrophotometer equipped with a 150 mm InGaAs integrating sphere. Diffuse reflectance spectra were collected with a Praying Mantis (Harrick) accessory and were referenced to barium sulphate powder as white standard.

Confocal Photoluminescence Measurements

For Photoluminescence (PL) measurements, hyperspectral images and time resolved PL images, a home-built confocal laser scanning microscope was used. It based on a microscope body (NIKON) which is combined with a xyz-piezo-scanning stage (PHYSIK INSTRUMENTE). The samples were measured upside down in epi-direction with an air objective (1.4 NA, NIKON). A beamsplitter non-polarizing beam splitter cube, 30:70 THORLABS) and three spectral, 490nm long pass, 650nm long pass, 900 nm long pass filters are used to separate the laser from the PL-light. Two different pulsed diode lasers for excitation are used, a 405 nm and a 635 nm. Both have the advantage of an adjustable repetition rate. For the Ytterbium-MOF a repetition rate of 2.5 MHz and for the Neodymium- MOF 5 MHz were used, which gives a laser to laser

pulse distance of roughly 3 times the lifetime of the MOF crystals. As a clean-up filter a 450 nm short pass and a 635/10 nm band pass (both THORLABS) were used. The detection side consists of two parts, which are separated by a flip-able mirror. One has an avalanche photo diode (APD, type: MPD PDM, detector size 50 x 50 µm,), which can be combined with a Time Correlated Single Photon Counting (TCSPC) electronics (BECKER UND HICKEL) measuring time resolved PL- transients and simple confocal images. Furthermore an additional flip able mirror and a 50:50 non polarizing beamsplitter cube (THORLABS) with further two APDs (LASERCOMPONENTS, one VIS, one NIR enhanced, detector size 150 x 150 µm) are installed in a Hanbury Brown Twiss configuration, which is used to record photon correlations in combination with the TCSPC electronics and a delay generator (STANDFORD RESEARCH SYSTEMS DG535). The second part consists of a spectrometer (ANDOR SHAMROCK SRi303) combined with an open electrode CCD camera (ANDOR NEWTON DU920) recording spectra. The data were recorded using customized LABVIEW (NATIONAL INSTRUMENTS) program that combines the manufacturers' software to our desired measurements. Further processing and analysis were carried out using MATLAB (MATHWORKS) program to obtain the PL spectra, TCSPC transients, photon correlation data and the images.

Raman spectroscopy

For the Raman measurements a Helium-Neon laser is used, which has an excitation wavelength of 632.8nm. A bandpass 633/10 filter (THORLABS) cleans up the laser spectrum. In combination of a thin 50:50 beamsplitter at 633nm (MELLES GRIOT) and a longpass 633 (CHROMA), the actual Raman signal is filtered out from the residual laser light. The rest of the detection remains the same.

2. Experimental

General

All materials were purchased from Sigma Aldrich, Acros or TCI Europe in the common purities purum, puriss or reagent grade. The materials were used as received without additional purification and handled in air unless otherwise noted. Synthesis of the CPs **1**-**3** was conducted under inert conditions. The water utilized in the synthesis was subjected to a Merck-Milipore Mili-Q purification system prior to use.

Synthetic procedures

Synthesis of 1,2,4,5-Tetrahydroxybenzene (THB)

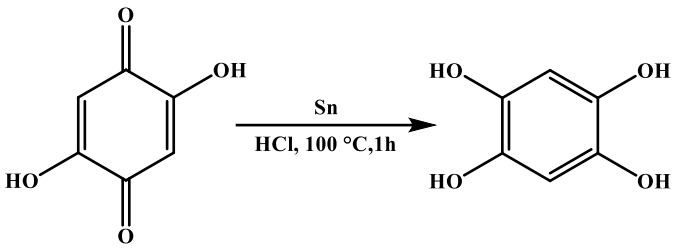

The organic linker 1,2,4,5-tetrahydroxybenzene was synthesized following a procedure reported in literature by Weider *et al*.[1] 2,5-Dihydroxy-1,4-benzoquinone (16.3 g, 115 mmol) was dissolved in 350 mL hydrochloric acid (36 %). Granular tin metal was slowly added to the mixture (16.5 g, 140 mmol), followed by stirring at 100 °C for 1 h until the color of the solution turned from orange to the colorless. The solution was filtered hot through a coarse glass frit and cooled down slowly to room temperature and then even further to 0 °C using an ice bath. The crystals were collected through filtration and recrystallized from tetrahydrofuran (50 mL). The product was dried under vacuum yielding 1,2,4,5-tetrahydroxybenzene (13.1 g, 92.2 mmol, 80 %) as a dark white solid. **IR** (ATR, cm^{-1}): $\tilde{\nu}$ = 3350 (vw), 3222 (w), 1552 (vw), 1536 (vw), 1475 (m), 1370 (vw), 1347 (vw), 1298 (vw), 1218 (vw), 1165 (m), 1027 (vw), 926 (vw), 862 (w), 845 (m), 714 (w); **NMR**: ^{1}H NMR (400 MHz, $(CD_3)_2SO$) δ: 6.20 (s, 2H, 2C*H*, Ar), 7.92 (s, 4H, ArO*H*) ppm; ^{13}C NMR (400 MHz, $(CD_3)_2SO$) δ: 104.7 (s, 2C, 2*C*H, Ar), 137.0 (s, 4C, ArOH) ppm.

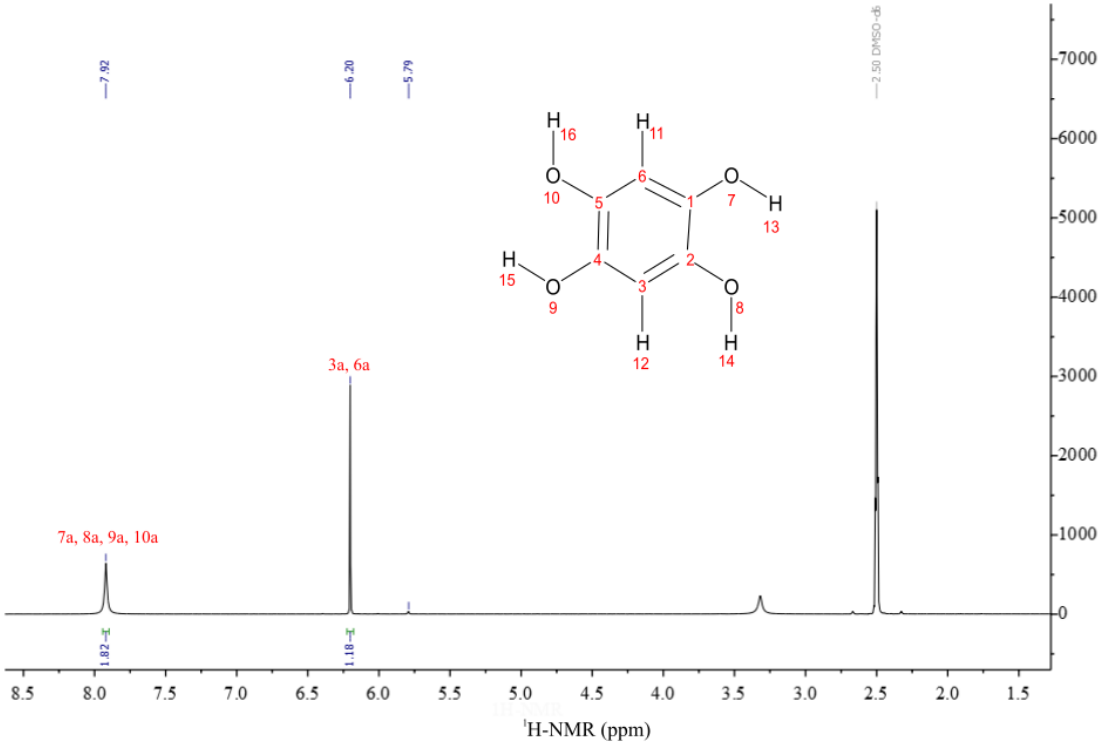

Fig. S1 ^{1}H NMR spectrum of 1,2,4,5-tetrahydroxybenzene in DMSO-d_6 at room temperature.

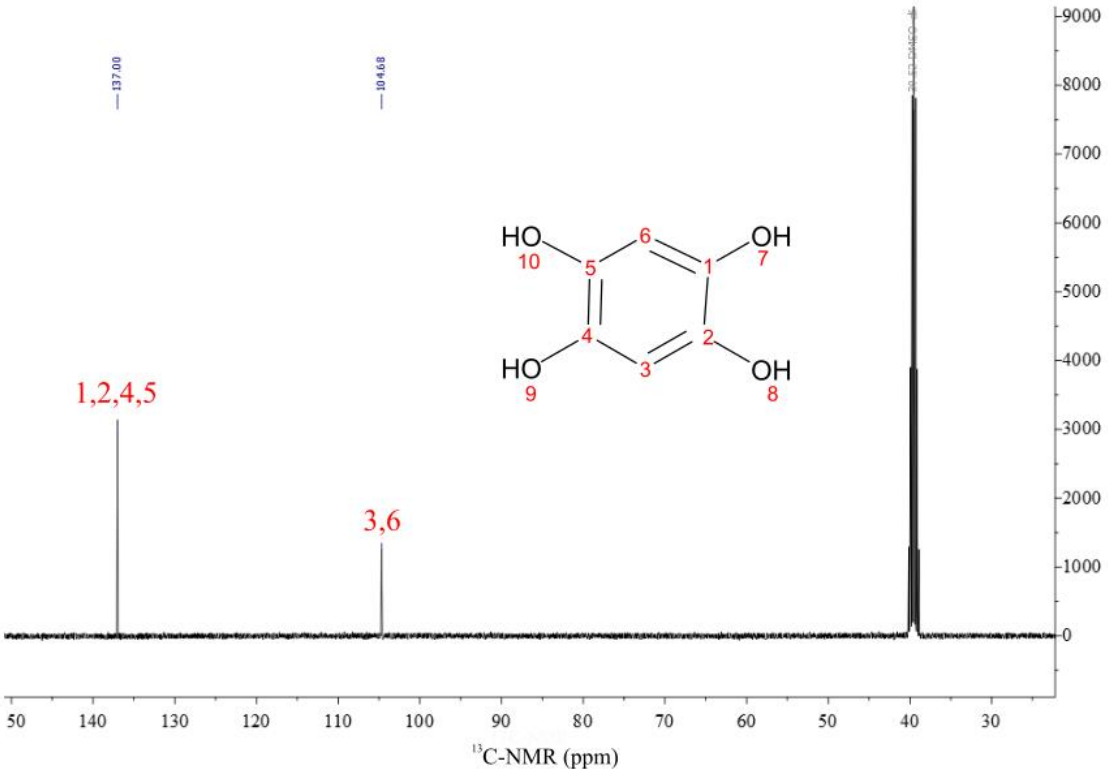

Fig. S2 ^{13}C NMR spectrum of 1,2,4,5-tetrahydroxybenzene in DMSO-d_6 at room temperature.

One-Pot-Synthesis of Ln-DHBQ CPs

Synthesis of $[Yb_2(DHBQ)_3(H_2O)_6]\cdot 18H_2O]_n$ (1)

Synthesis of Yb-DHBQ type I was performed modified to a literature reported synthesis.[3] A glass bottle (Schott Duran, borosilicate 3.3. ISO4796, 250 mL) with a PBT cap equipped with a Teflon seal was used for synthesis. $Yb(NO_3)_3 \cdot 5\ H_2O$ (44.9 mg, 0.1 mmol) dissolved in 25 mL of water was slowly added to a solution of 2,5-dihydroxy-1,4-benzoquinone (21.0 mg, 0.15 mmol) in 50 mL water. The reaction mixture was kept at 0 °C for 1 day and at room temperature for further 5 days. The reaction product was collected by filtration and washed via suspension in water (3 times, 6 mL). Dark-red single crystals of Yb-DHBQ type I (**1**) were obtained.

Synthesis of $[Yb_2(DHBQ)_3(H_2O)_4]\cdot 6H_2O]_n$ (2)

Synthesis of Yb-DHBQ type II was performed similar to **1**. Briefly, $Yb(NO_3)_3 \cdot 5\ H_2O$ (112.3 mg, 0.25 mmol) and 1,2,4,5-tetrahydroxybenzene (142.1 mg, 1.00 mmol) were dissolved in 5 mL water. After 15 minutes of ultrasonication, the solution mixture was placed in a preheated oven at 85 °C and was kept at this temperature for 6 days. Afterwards the reaction vessel was cooled to room temperature and the reaction product was collected by filtration and washed via suspension in water (3 times, 6 mL). Dark-red single crystals of Yb-DHBQ type II (**2**) were obtained.

Synthesis of $[Nd_2(DHBQ)_3(H_2O)_6]\cdot 18H_2O]_n$ (3)

Synthesis of small cylindrical crystals:

Synthesis of Nd-DHBQ as small cylindrical crystallites was performed similar to the reported synthesis of Yb-DHBQ type I. A glass bottle (Schott Duran, borosilicate 3.3. ISO4796, 250 mL) with a PBT cap equipped with a Teflon seal was used for synthesis. $Nd(NO_3)_3 \cdot 5\ H_2O$ (43.8 mg, 0.1 mmol) dissolved in 25 mL of water was slowly added to a solution of 2,5-dihydroxy-1,4-benzoquinone (21.0 mg, 0.15 mmol) in 50 mL water. The reaction mixture was kept at 0 °C for 1 day and at room temperature for further 5 days. The reaction product was collected by filtration and washed via suspension in water (3 times, 6 mL). Dark-red single crystals of Nd-DHBQ type I were obtained.

Synthesis of large pseudo-cubic crystals:

A glass bottle (Schott Duran, borosilicate 3.3. ISO4796, 25 mL) with a PBT cap equipped with a Teflon seal was used for synthesis. $Nd(NO_3)_3 \cdot 6\ H_2O$ (109.6 mg, 0.25 mmol) and 1,2,4,5-tetrahydroxybenzene (142.1 mg, 1.00 mmol) were dissolved in 5 mL water following a modified procedure reported by Nakabayashi *et al.*[2] After 15 minutes of ultrasonication, the solution mixture was placed in a preheated oven at 85 °C and was kept at this temperature for 16 days. Afterwards the reaction vessel was cooled to room temperature and the reaction product was collected by filtration and washed via suspension in water (3 times, 6 mL). Dark-red single crystals of Nd-DHBQ type I (**3**) were obtained.

3. Characterization

Table S1 Crystallographic data of CP 1, 2 and 3.

Crystal data	Yb-DHBQ type I (1)	Yb-DHBQ type II (2)	Nd-DHBQ type I (3)
Formula	$[Yb_2(C_6H_2O_4)_3(H_2O)_6]\cdot 18H_2O$	$[Yb_2(C_6H_2O_4)_3(H_2O)_4]\cdot 6H_2O$	$[Nd_2(C_6H_2O_4)_3(H_2O)_6]\cdot 18H_2O$
Formula weight / g mol^{-1}	596.34	470.23	567.54
Crystal system	trigonal	monoclinic	trigonal
Space group	$R\bar{3}$	*C2/m*	$R\bar{3}$
Color, habit	Colorless block	violet blocks	Colorless block
Size / mm	0.03 x 0.03 x 0.04	0.02 x 0.05 x 0.07	0.10 x 0.37 x 0.50
Unit cell dimensions /Å	*a* = 14.0419(5) *b* = 14.0419(5), *c* = 17.8740(7)	a = 14.0778(7) b = 15.8986(7) c = 6.1208(3)	*a* = 14.2962(5), *b* = 14.2962(5), *c* = 17.9561(7)
Unit cell angles / °	$\alpha = 90, \beta = 90, \gamma = 120$	α = 90, β = 107, $\gamma = 120$	$\alpha = 90, \beta = 90, \gamma = 120$
V / $Å^3$	3052.1(3)	1310.13(11)	3178.2(3)
Z	6	4	6
ρ_{calc} / g cm^{-3}	1.947	2.384	1.779
F(000)	1770	900	1710
Data collection			
Diffractometer	Bruker D8 Venture TXS	Bruker D8 Venture TXS	Bruker D8 Venture TXS
Radiation $\lambda_{MoK\alpha}$ / $Å^3$	0.71073	0.71073	0.71073
T / K	173		102

θ range / °	3.4−28.3	3.5−30.5	3.4−33.1
Absorption correction	multi-scan	multi-scan	multi-scan
μ /mm^{-1}	2.531	7.196	2.531
Dataset	−18: 18; −18: 18; −23: 23	−20: 20; −22: 22; −8: 8	−21: 21; −21: 21; −27: 27
Measured refl.	24939	18221	22637
Independent refl.	1689	2067	2690
Observed refl.[a]	1570	1965	2598
R_{int}	0.046	0.032	0.039
Solution and refinement			
Structure solution	SHELXL	SHELXL	SHELXL
Structure refinement	SHELXS	SHELXS	SHELXS
Refined parameters	117	127	117
R_1 (obs)[b]	0.0166	0.0136	0.0143
wR_2 (all data)[c]	0.0367	0.0311	0.0357
GoF[c]	1.12	1.10	1.10
Res. Dens. / e Å^{-3}	−0.58, 0.56	−0.70, 0.63	−0.80, 1.07

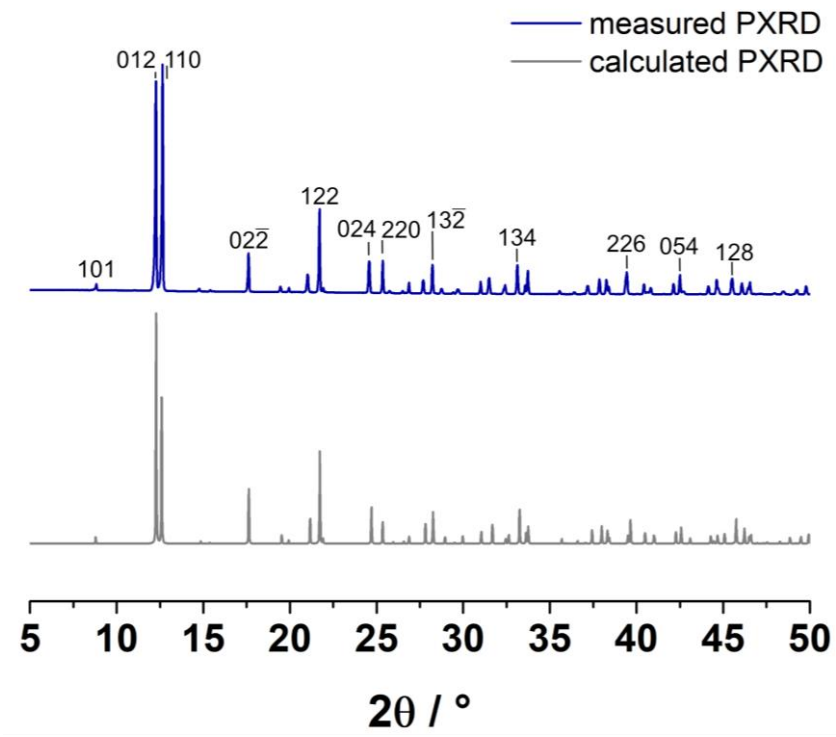

Fig. S3 Experimental (blue) and calculated (grey) PXRD pattern of Yb-DHBQ (**1**) are shown. The measured PXRD pattern was obtained from a ground sample of single crystals. The calculated PXRD pattern was obtained from single crystal data from the crystal structure of Yb-DHBQ type I CP.

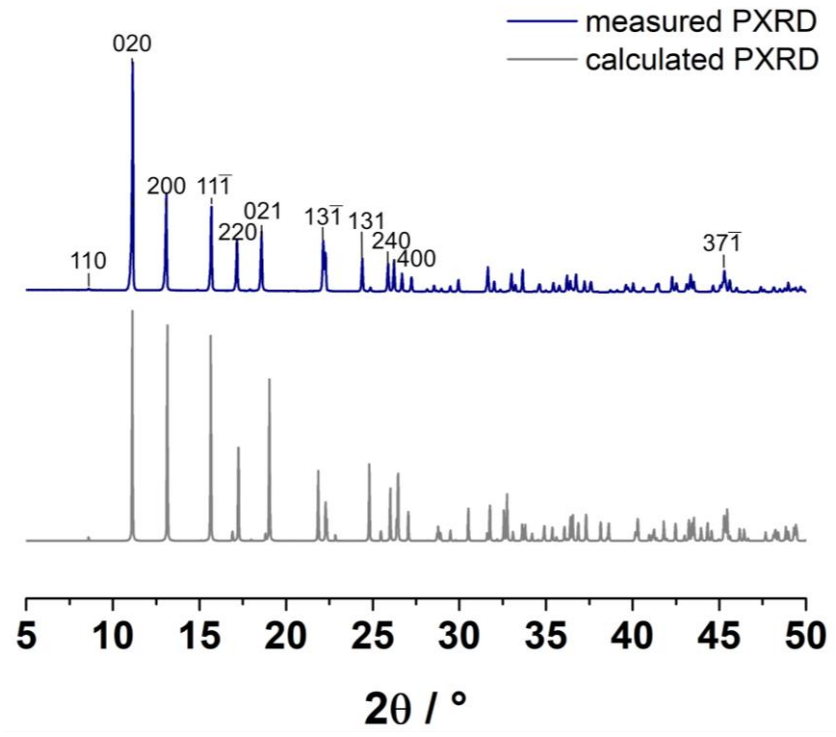

Fig. S4 Experimental (blue) and calculated (grey) PXRD pattern of Yb-DHBQ type II (**2**) are shown. The measured PXRD pattern was obtained from a ground sample of single crystals. The calculated PXRD pattern was obtained from single crystal data from the crystal structure of Yb-DHBQ type II CP.

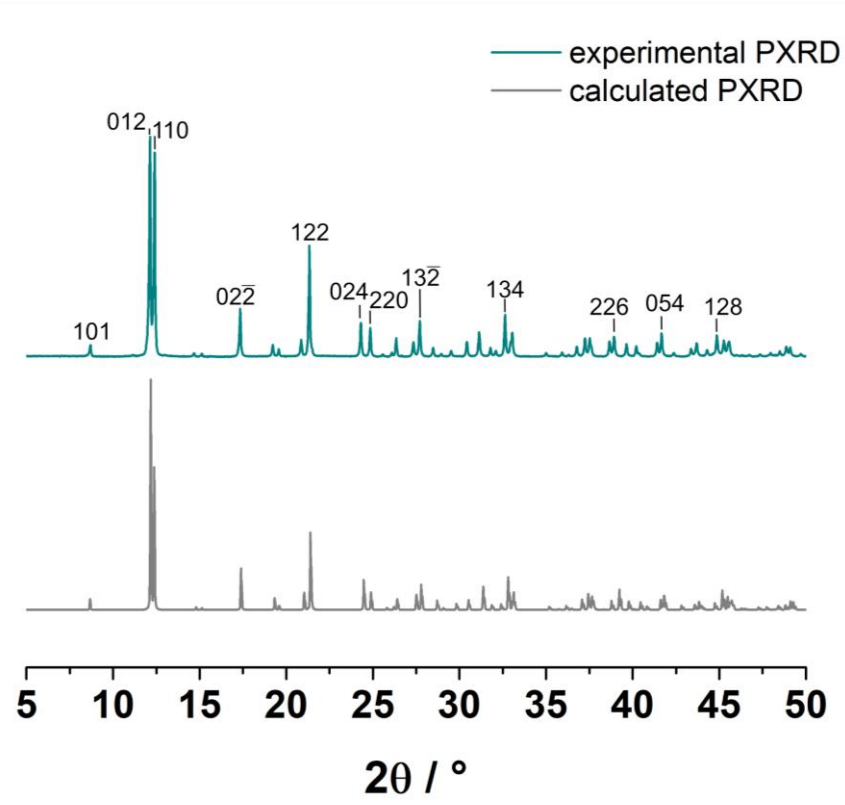

Fig. S5 Experimental (cyan) and calculated (grey) PXRD pattern of Nd-DHBQ type I (**3**) are shown. The measured PXRD pattern was obtained from a ground sample of single crystals. The calculated PXRD pattern was obtained from single crystal data from the crystal structure of Nd-DHBQ type I CP.

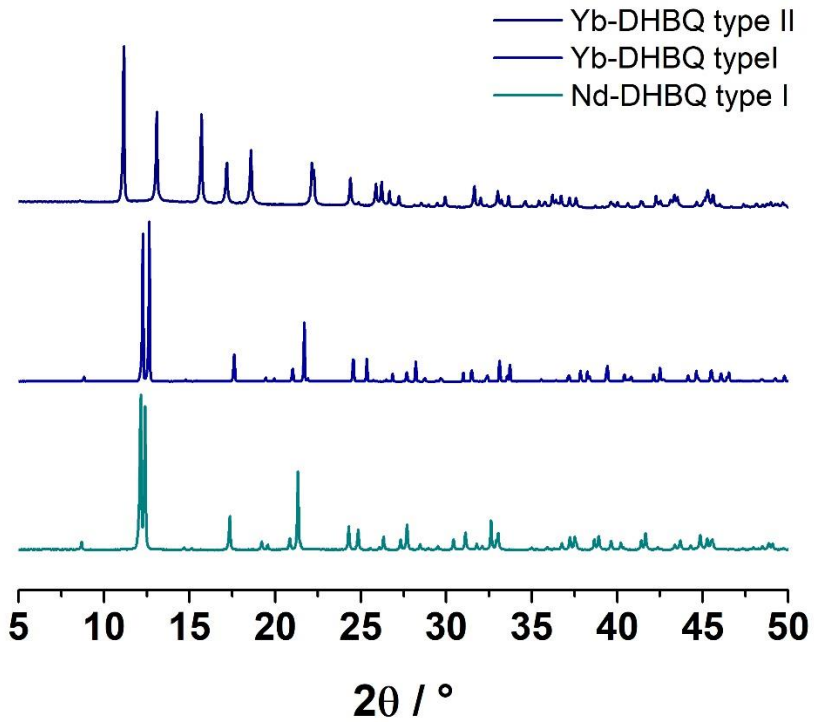

Fig. S6 PXRD pattern of ground Ln-DHBQ CPs **1**–**3** aged under ambient air in a closed vessel for more than 1 year showing the chemical stability of the CPs.

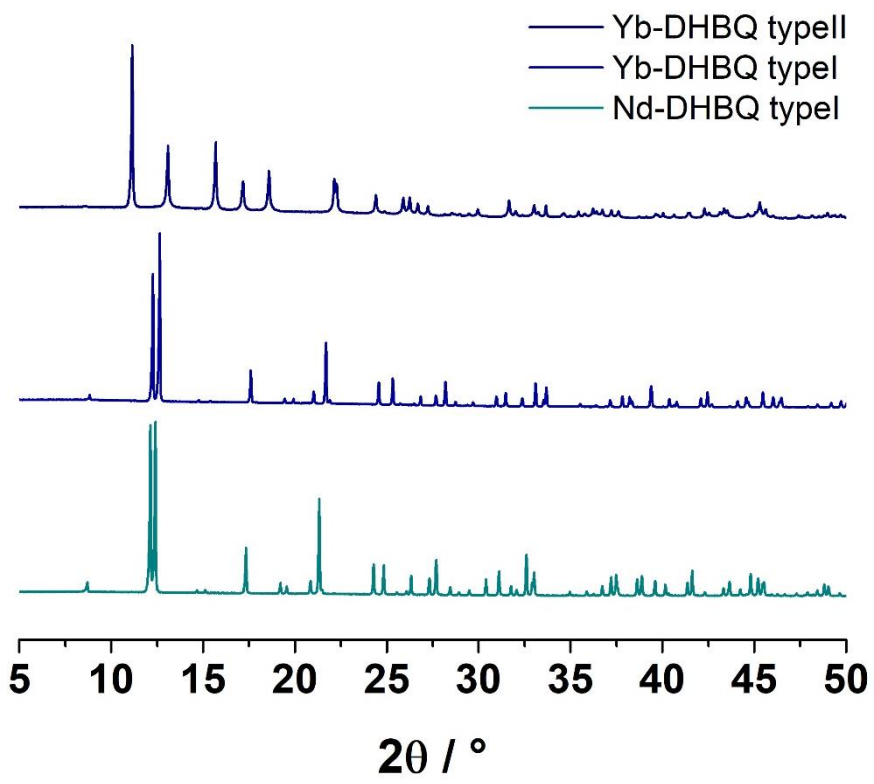

Fig. S7 PXRD pattern of ground Ln-DHBQ CPs **1**–**3** stored in water in a closed vessel for more than 6 months.

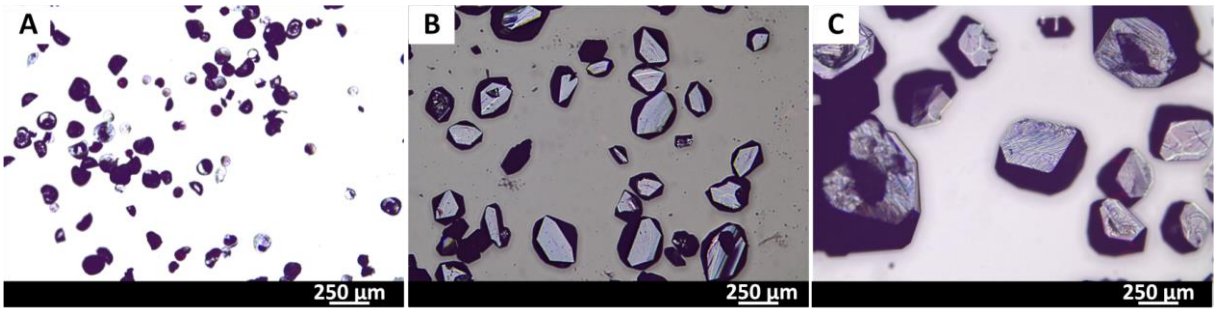

Fig. S8 Light microscope images of Yb-DHBQ type I (**A**),Yb-DHBQ type II (**B**) and Nd-DHBQ type I (**C**) in low magnification showing the overall homogeneity of the single crystals.

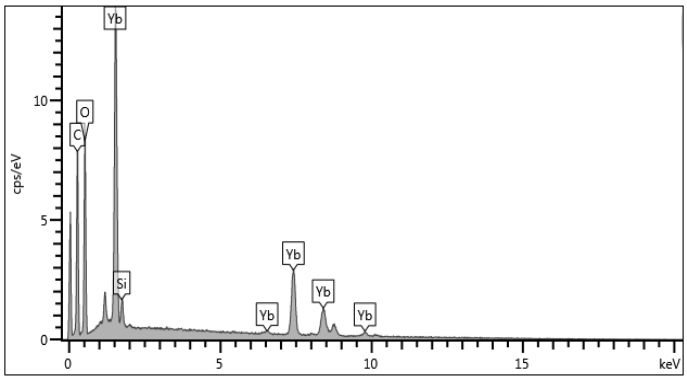

Element	Atom %
O	78.27
Yb	21.73

Fig. S9 EDX spectra of Yb-DHBQ type I showing the presence of Yb and O.

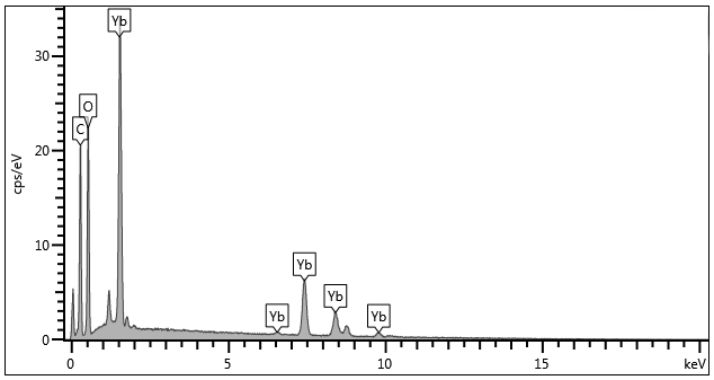

Element	Atom %
O	86.22
Yb	13.78

Fig. S10 EDX spectra of Yb-DHBQ type II showing the presence of Yb and O.

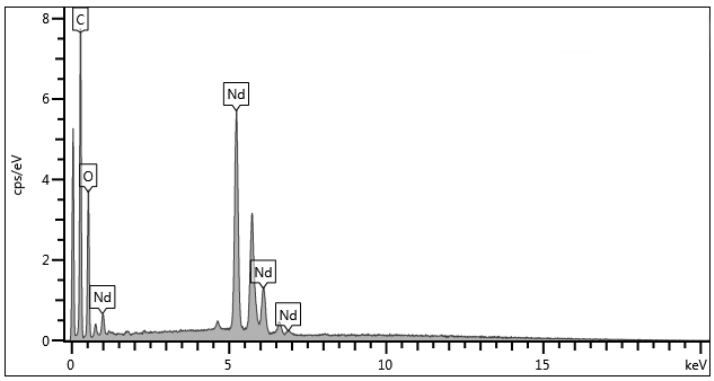

Element	Atom %
O	62.63
Nd	37.37

Fig. S11 EDX spectra of Nd-DHBQ type I showing the presence of Nd and O.

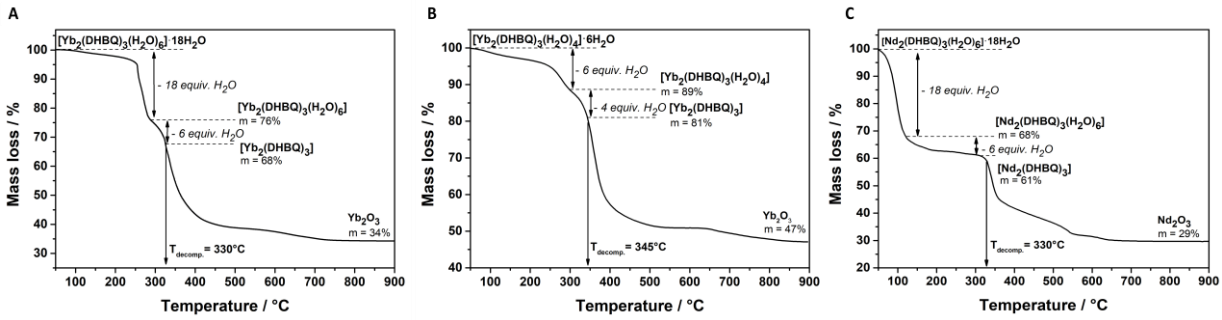

Fig. S12 Thermogravimetric analysis of CPs Yb-DHBQ type I (**A**), Yb-DHBQ type II (**B**) and Nd-DHBQ type I (**C**) in the range between 25 and 900 °C. The measurements were performed with a constant flow of synthetic air and a heating rate of 1 K min^{-1}.

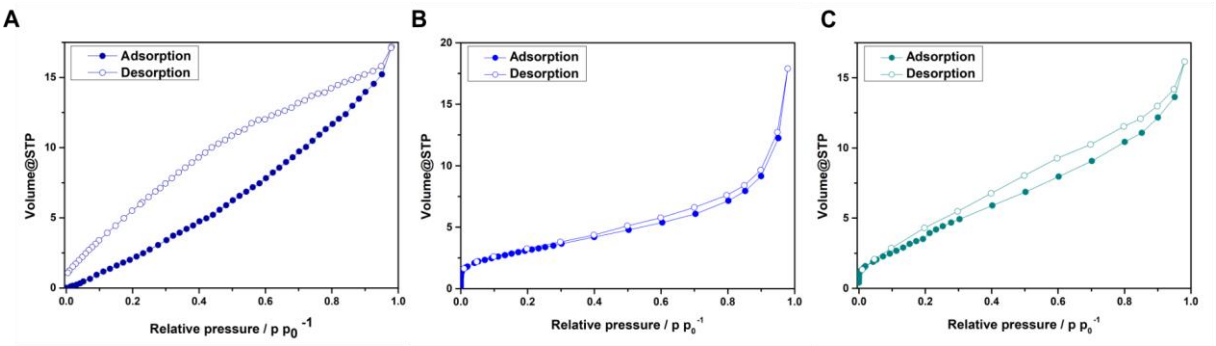

Fig. S13 Nitrogen physisorption isotherms of Yb-DHBQ type I (**A**), Yb-DHBQ type II (**B**) and Nd-DHBQ type I (**C**), showing low porosity of the three CPs.

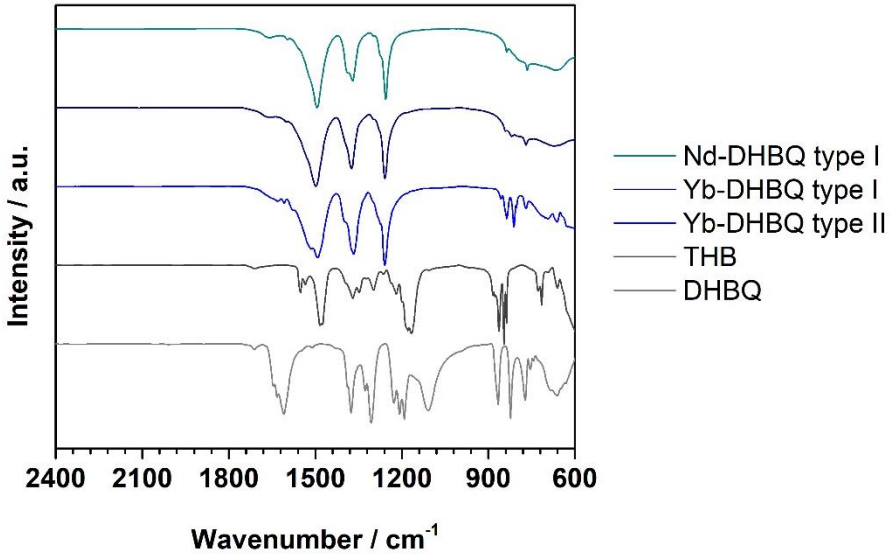

Fig. S14 Fourier-transform infrared spectrum (FTIR) of the DHBQ (light grey) and THB (dark grey) ligand and the CPs **1**–**3** measured as powder samples. Three characteristic IR bands are observed at all three CPs at 1490 cm^{-1} ν(–C=O), 1370 cm^{-1} ν(–C–C) and 1250 cm^{-1} ν(–C–O).

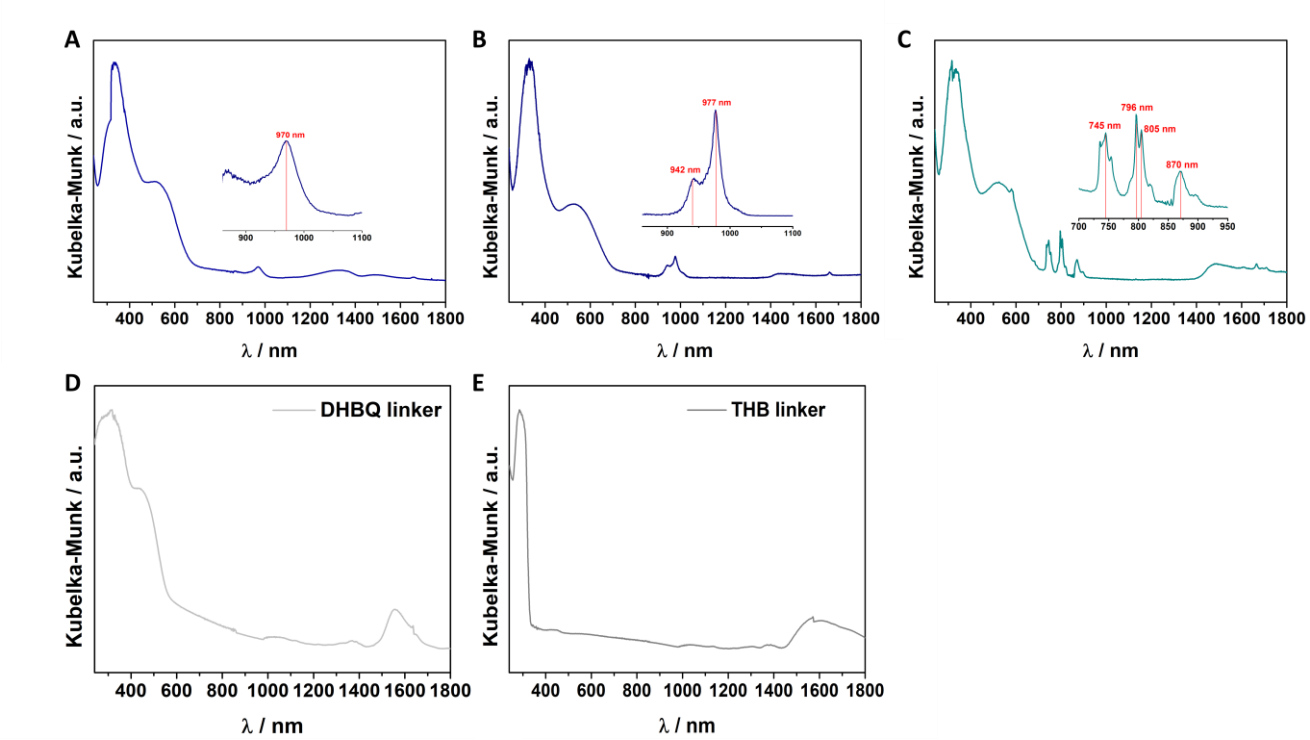

Fig. S15 UV-Vis-NIR spectrum of Yb-DHBQ type I (**A**), Yb-DHBQ type II (**B**) and Nd-DHBQ type I (**C**) with insets at spectral regions between 700 and 1000 nm. The characteristic narrow absorption bands arise from the REI states in the CPs. UV-Vis spectrum of the linker molecules DHBQ (**D**) and THB (**E**) showing absorption in the ultraviolet region and infrared region.

Raman spectra

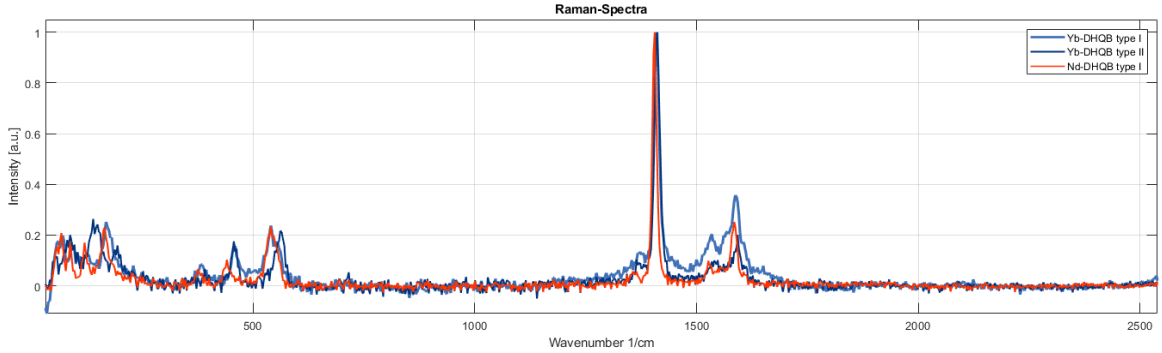

Fig. S16 Raman spectrum of the Ln-DHBQ CPs. In the Raman spectra, several bands are visible. In the spectral region below 250 cm^{-1} lattice phonon bands become appearant. Between 300 and 650 cm^{-1}, the metal-oxygen coordination band is visible. The phonon band at around 550 cm^{-1} characterizes the two different crystal structures obtained, type I and type II. The phonon bands above 1300 cm^{-1} belong to C-C, C-O and C-H vibrational modes.

Analysis of Photon statistic data

In Figure S17, the raw data of the recorded photon statistics of the measurement of Yb-DHBQ type II is displayed. In the Hanbury Brown Twiss configuration installed for the measurements, one APD is the starting the clock and the other is stopping the clock of the TCSPC card, which measures the time between two events occuring. Furthermore, the one APD is connected to a delay generator, which is routed to the Sync channel and stops the time. This allows to reach negative times. Since the generated signal comes from a pulsed laser source, the actual signal appears as individual peaks with the decay time on each slope. Every peak was fitted by an autocorrelation of a monoexponential decay function. Hereby two of three parameters, decay time and offset, were fixed and only the amplitude for every peak was varied. The mean value of all amplitude values excluding that at time zero, are used to normalize them to 1 and compare it to the time zero amplitude value. For a downconversion process, an amplitude value bigger than 1 is expected, because the probability is higher to measure two correlated photons at the same time. Since the focus of the laser is diffraction limited (about 200nm) and the measured crystals have a micrometer size, more than one emitter pair gets excited. All bunching measurements are measured with a fluence of ca. 1 mJ cm^{-2} at 2.5 MHz and an absolute detected photon count rate of 6000 Hz per APD channel. One measurement took between 24 and 36 hours. To confirm that these correlation measurements are dependent on the number of excited states, the same measurements is performed with the double photon count rate, which leads to no bunching. Furthermore, by changing the excitation wavelength from 405 nm to 635 nm no bunching is measured as well (Fig. S18).

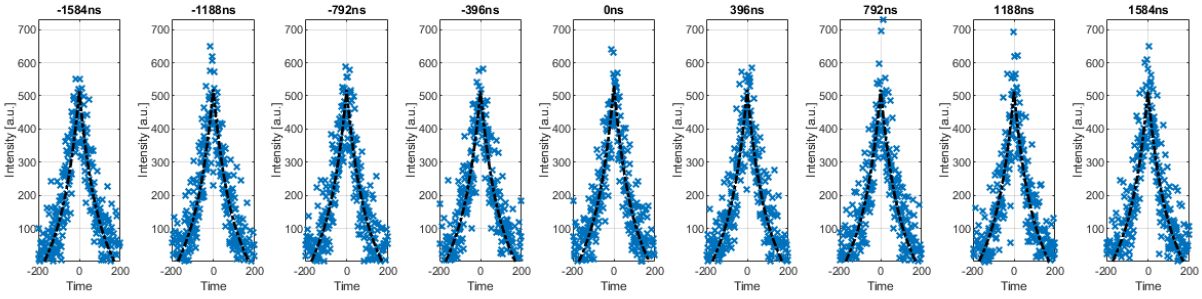

Fig. S17 Recorded photon statistics of the PL measurement of Yb-DHBQ type II. The measured raw data from the autocorrelation experiment (blue dots) is displayed with the monoexponential autocorrelation (black lines).

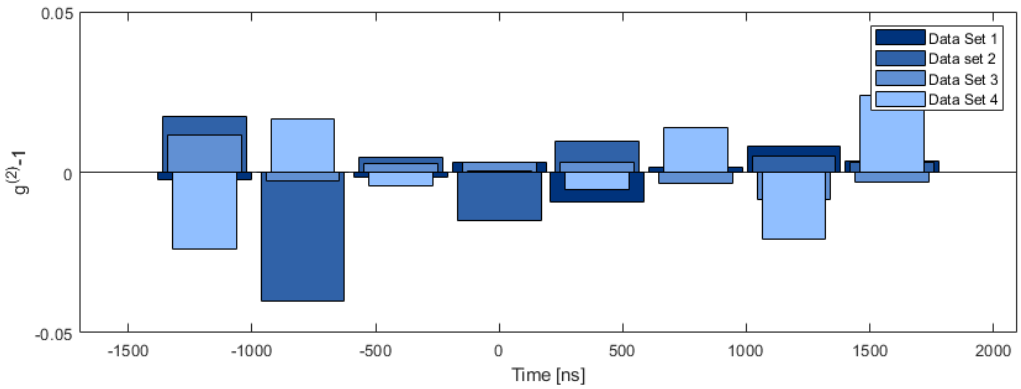

Fig. S18 Second order time correlation function for the Yb-DHBQ type II crystals measured by 635 nm excitation with similar laser fluence and count rates on the APDs. No bunching is detectable.

Spectra and Time Resolved PL

The complete emission spectrum of Yb DHBQ type I CP and the time resolved PL measurements are shown in Fig. S19. In the logarithmic intensity scale of the spectrum, the weak blue emission from the CP matrix is visible (between 1.4 to 2 eV). It has a very short lifetime, below 10 ps. This transient was recorded with a 476 nm sub ps pulsed laser, which gives a 1/e instrument response function width of 27 ps. Below 1.4 eV, the emission of the rare earth ion Yb^{3+} becomes appearant, which possesses a much longer lifetime of several ns. The blue emission as seen for Yb-DHBQ type I, is visible for all three CP crystals Ln-DHBQ (Ln = Yb, Nd) and possesses a decay time below 10 ps, close to the time resolution of the setup. However, for all three Ln-DHBQ CPs, the emission of the rare earth ions is characteristic for each crystal system and differs for Yb-DHBQ type I (**1**) and type II (**2**) and Nd-DHBQ type I (**3**).

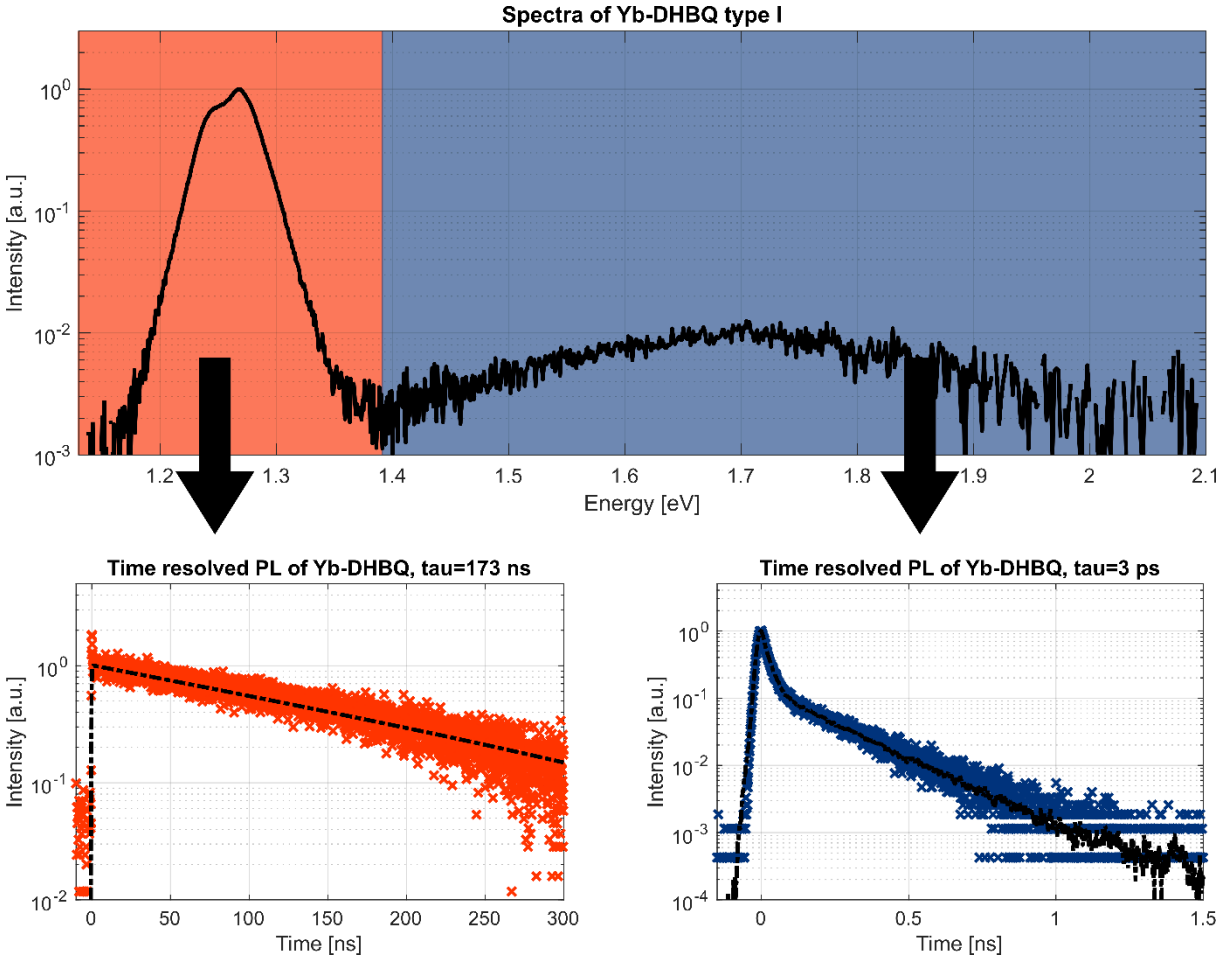

Fig. S19 Photoluminescence of Yb-DHBQ type I and time resolved PL measurements.

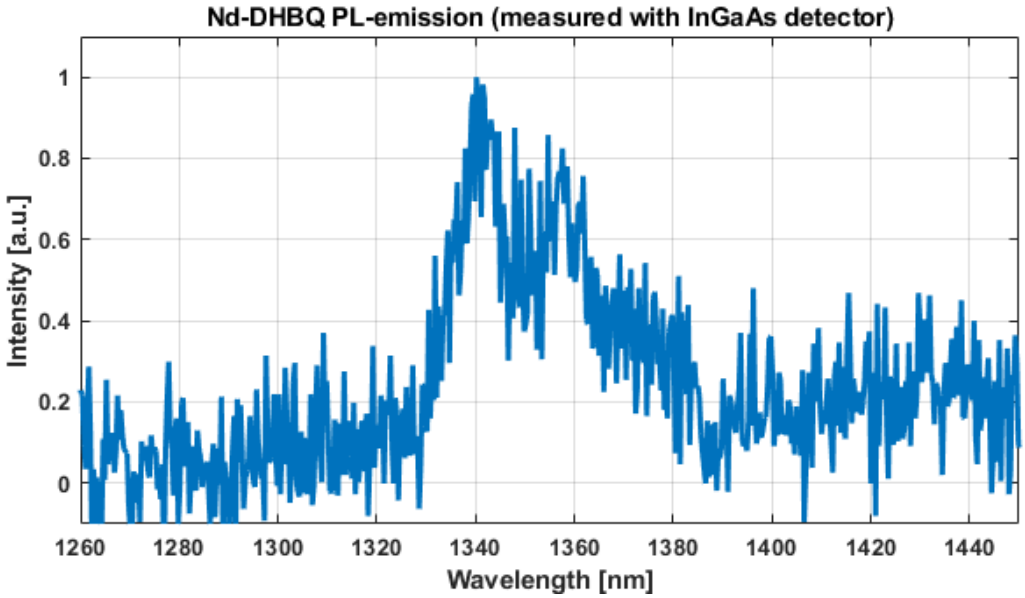

Fig. S20 PL spectrum for the transition $^4F_{3/2} \rightarrow {}^4I_{13/2}$ in the emission of Nd-DHBQ type I at 1350 nm. The measurement was performed with an InGaAs detector.

References

[1] P. R. Weider, L. S. Hegedus, H. Asada, *J. Org. Chem.* **1985**, *50*, 4276.

[2] K. Nakabayashi, S. Ohkoshi, *Acta Crystallographica Section E* **2010**, *66*, m1300.

[3] B. F. Abrahams, J. Coleiro, B. F. Hoskins, R. Robson, *Chem. Commun.* **1996**, 603.

7 Acknowledgment

In this part, I want to thank all the people involved in the projects, as well as my friends who have been with me all the time and helped me through.

First, I want to thank Professor Achim Hartschuh. He gave me the opportunity and freedom to carry out all the scientific work in his labs. It was always a very constructive and productive working atmosphere and I always enjoyed the fruitful scientific discussions.

Thank you to all the members of the Hartschuh group over the years. Veit was always in a good mood in our office, initiating Soup Tuesdays, organizing group get-togethers, and fostering great discussions. Luquinhas always found the right words to lift the mood, and we had many productive scientific discussions that led to great ideas. Richard led the lead perovskite projects, resulting in two excellent publications. I also want to express my appreciation to Irene, Nicolai, Meltem, Lucas, Hari, Sean, Veit, Luquinhas, Olli, and Zehua, who shared the office with me. I deeply value the good working atmosphere and the fun we had together.

I want to thank Professor Bein and his group for all the fruitful collaborations. Nadja consistently produced the highly crystalline MAPI films, which served as the foundation for our work on MAPI perovskite studies. Andi, Max, Shize, Tianhao, Flo, Andre, Patricia, Marcella, Julian, and Roman produced several different exciting samples that I characterized spectroscopically, resulting in numerous publications and great collaborations. I especially want to mention Rik and Laura, with whom I had many valuable scientific discussions. Special thanks to Laura and Jenny, who collaborated on the 2D COF project from the initial idea to the final manuscript. I also want to express my gratitude to Marina and Dana for their contributions to our REI MOF manuscript. The scientific exchange and working atmosphere with all of you have been amazing.

Thank you to Professor Philip Tinnefeld and his group for always making me feel welcome in your kitchen. We had amazing soup Tuesdays before the pandemic, deep discussions, fruitful scientific exchange and always enjoyed good "after work beer" meetings.

I want to thank all the external collaborators I had the privilege of working with. None of these projects would have been possible without the input of so many great people. Thank you to Manuel and Professor Müller Buschbaum, as well as Anna and Professor Deschler, for realizing two great scientific projects.

I want to thank CeNS and Susanne for organizing all the great scientific meetings, events, and conferences. The CeNS Venice workshop was always a highlight.

Thanks to Econversion and Soltech for funding part of my research and for organizing many nice conferences.
Thank you to the whole SFBeer group for organizing amazing events on campus. It was always a very nice social atmosphere and the coolest connection in the physical chemistry department.

I want to thank the physical chemistry football group for having amazing games alongside the scientific work.

Desweiteren möchte ich meiner Mama danken, die mich immer unterstützt hat und an mich geglaubt hat, dass ich mein Studium und auch meine Doktorarbeit schaffe. Danke

Zum guten Schluss möchte ich meiner Familie und all meinen guten Freunden danken, die mich auf dem Weg begleitet haben. Hier möchte ich meine Münchner Freunde erwähnen: Max, Steffen, Yvie, Alex, Anna, Vero mit Familie, Terence mit Familie und allen vom RSV. Dann gibt es die ganzen Freunde, die ich an der Uni kennen gelernt habe und auch sehr wichtig geworden sind: Sarah, Katya, Viki, Lennart, Flo und Flo, Andres, Meltem, Frank, Veit und Luquinhas. Einen speziellen Dank an Iza, für deine Unterstützung. Und zu guter Letzt möchte ich mich bedanken bei Yvonne, danke dir für jegliche mentale Unterstützung.